

# First Antihydrogen Production within a Combined Penning-Ioffe Trap

A thesis presented

by

David Anthony Le Sage

to

The Department of Physics

in partial fulfillment of the requirements

for the degree of

Doctor of Philosophy

in the subject of

Physics

Harvard University

Cambridge, Massachusetts

October 2008

©2008 - David Anthony Le Sage

All rights reserved.

Thesis advisor

Author

**Gerald Gabrielse**

**David Anthony Le Sage**

## **First Antihydrogen Production within a Combined Penning-Ioffe Trap**

### **Abstract**

The long-term goal of the ATRAP collaboration is to perform precision laser spectroscopy on antihydrogen, the simplest atom made entirely of antimatter. Comparing this to the hydrogen spectrum would be a direct test CPT and Lorentz invariance. Antihydrogen has been produced by ATRAP both during the positron cooling of antiprotons and by a laser-controlled charge-exchange process. Antihydrogen spectroscopy will first require confining the atoms produced in a Penning ion trap within the magnetic confining field of a superimposed Ioffe trap. A new experimental zone was established at the CERN Antiproton Decelerator facility, and a combined Penning-Ioffe trap was constructed for the trapping and spectroscopy of antihydrogen. Significant advances were made in the methods of accumulating the constituent particles necessary for antihydrogen formation, including a factor of 400 improvement of the positron loading rate using buffer-gas accumulation, the demonstration of a new electron loading method via the photoelectric effect using UV laser pulses, and efficient antiproton trapping using magnetic fields that were much lower than previously demonstrated, as required to maximize antihydrogen trapping depths. The loss of particles from the Penning trap caused by the radial magnetic field of a quadrupole-Ioffe trap was measured, and found to be suitably low for antihydrogen

production. Following this, antihydrogen production in a combined Penning-Ioffe trap was demonstrated for the first time. A new method of antihydrogen production via positron-cooling of antiprotons was utilized that prolonged the interaction time of the positrons and antiprotons, while minimizing the mixing-energy of the antiprotons. Larger amounts of antihydrogen were produced in the presence of the Ioffe field than without it, assuaging reasonable fears that the magnetic confining field would restrict antihydrogen formation. Searches for antihydrogen confined in the magnetic trap yielded null results, likely due to the velocity and state distribution of the antihydrogen produced, although present experiments would not be sensitive to very small numbers of confined atoms. A number of production methods that may lead to trapped antihydrogen are presently in development, and this new trap will provide a versatile and robust platform for these experiments.

# Contents

Title Page . . . . .	i
Abstract . . . . .	iii
Table of Contents . . . . .	v
List of Figures . . . . .	viii
List of Tables . . . . .	xii
Publications . . . . .	xiii
Acknowledgments . . . . .	xiv
<b>1 Introduction</b>	<b>1</b>
1.1 CPT Symmetry . . . . .	7
1.2 Antihydrogen Production Methods . . . . .	11
1.2.1 Three-Body Recombination . . . . .	11
1.2.2 Other Antihydrogen Formation Methods . . . . .	15
1.2.3 Antihydrogen Production within a Penning-Ioffe Trap . . . . .	16
<b>2 Apparatus</b>	<b>18</b>
2.1 The Penning Trap . . . . .	18
2.1.1 Penning Trap Theory . . . . .	18
2.1.2 Penning Trap Electrode Geometries . . . . .	21
2.1.3 The A-TRAP and B-TRAP Penning Traps . . . . .	24
2.2 The Ioffe Trap . . . . .	29
2.3 The Full Penning-Ioffe Trap Apparatus . . . . .	33
2.3.1 The Superconducting Solenoid . . . . .	34
2.3.2 The Insert Dewar . . . . .	34
2.3.3 The A-TRAP Vacuum Hat . . . . .	42
2.3.4 The A-TRAP Cryogenic and Thermal Isolation System . . . . .	43
2.3.5 Thermal Cycling of the Penning-Ioffe Trap . . . . .	48
2.3.6 The Cryogenic, Two-Dimensional Translation Stage . . . . .	52
2.3.7 Vacuum Inside the Cryogenic Penning Trap . . . . .	58

<b>3</b>	<b>Particle Manipulations and Measurements</b>	<b>63</b>
3.1	Particle Transfer . . . . .	63
3.1.1	Adiabatic Transfer . . . . .	63
3.1.2	Pulse Transfer . . . . .	65
3.2	Particle Counting . . . . .	72
3.2.1	Destructive Charge Counting . . . . .	73
3.2.2	Annihilation Detection . . . . .	80
3.2.3	Comparing Annihilation and Charge Counts . . . . .	88
3.2.4	Nondestructive RF Detection . . . . .	92
3.3	Particle Cooling . . . . .	95
3.3.1	Radiative Cooling . . . . .	95
3.3.2	Sideband Cooling . . . . .	99
<b>4</b>	<b>Particle Loading</b>	<b>101</b>
4.1	Electrons . . . . .	101
4.1.1	Previous Methods for Loading Electrons . . . . .	102
4.1.2	Electrons Loaded from Photoemission . . . . .	103
4.2	Positrons . . . . .	110
4.2.1	Previous Method of Loading Positrons . . . . .	111
4.2.2	Buffer Gas Positron Accumulation and Transfer . . . . .	112
4.3	Antiprotons . . . . .	121
4.3.1	Antiproton Production and Delivery at CERN . . . . .	121
4.3.2	Antiproton Steering and Energy Tuning . . . . .	122
4.3.3	Antiproton Trapping . . . . .	126
4.3.4	Antiproton Cooling and Accumulation . . . . .	136
4.3.5	Future Improvements to Antiproton Loading . . . . .	146
<b>5</b>	<b>Non-neutral Plasmas</b>	<b>148</b>
5.1	Plasmas in a Cylindrical Trap . . . . .	149
5.2	Plasmas in a Quadratic Electric Potential . . . . .	155
5.3	Spheroidal Plasma Dynamics . . . . .	156
5.4	Plasmas in Non-ideal Potentials . . . . .	158
5.5	Plasma Mode Frequency Detection . . . . .	163
<b>6</b>	<b>Particle Stability in a Combined Penning-Ioffe Trap</b>	<b>167</b>
6.1	Single Particle Stability . . . . .	168
6.2	Diffusive Losses in Plasmas . . . . .	175
6.3	Comparing Quadrupole to Higher-Order Ioffe Traps . . . . .	177
6.4	ATRAP Experimental Results . . . . .	181

---

<b>7</b>	<b>Antihydrogen Production within a Penning-Ioffe Trap</b>	<b>192</b>
7.1	Antihydrogen Production Procedure . . . . .	193
7.2	Effects of the Ioffe Field on the Antiprotons . . . . .	202
7.3	Experiment Results . . . . .	207
7.4	Future Prospects for Antihydrogen Confinement . . . . .	210
<b>8</b>	<b>Conclusion</b>	<b>213</b>
	<b>Bibliography</b>	<b>220</b>

# List of Figures

1.1	A comparison of possible antihydrogen spectroscopy accuracy with the most accurate tests of CPT. . . . .	11
2.1	The three distinct motions of a charged particle in a Penning trap. . .	19
2.2	a) Hyperbolic and b) cylindrical ring electrode geometries. . . . .	21
2.3	The confinement potential within a radius-length electrode, in comparison to the corresponding ideal quadrupole potential. . . . .	24
2.4	The A-TRAP Penning trap electrode stack. . . . .	25
2.5	The lower A-TRAP electrode stack wiring diagram. . . . .	27
2.6	The upper A-TRAP electrode stack wiring diagram. . . . .	28
2.7	The Zeeman splitting of the ground states of an antihydrogen atom. .	29
2.8	The ATRAP superconducting quadrupole Ioffe trap. . . . .	31
2.9	The magnetic potential contours of the Ioffe trap. . . . .	33
2.10	The full Penning-Ioffe trap experimental apparatus. . . . .	35
2.11	Cross section view of the insert dewar. . . . .	36
2.12	Temperatures within the insert dewar during a typical cool-down cycle.	37
2.13	Comparison of the insert dewar temperatures before and after a complete rebuild. . . . .	40
2.14	The temperatures in the insert dewar during the warm-up process. . .	41
2.15	The A-TRAP vacuum hat. . . . .	42
2.16	The A-TRAP cryogenic and thermal isolation system. . . . .	44
2.17	The thermal coupling of the isolation baffles and the helium dewar to the insert dewar as it cools. . . . .	45
2.18	Operation of the Penning-Ioffe trap under adverse conditions. . . . .	47
2.19	The typical cool-down procedure for the Penning-Ioffe trap. . . . .	49
2.20	The Penning-Ioffe trap warm-up procedure using heaters. . . . .	51
2.21	The cryogenic, two-dimensional translation stage used to line up a variety of different windows with the central axis of the Penning trap.	53
2.22	The potentiometer resistance and photodiode response measurements used to determine the position of the X-Y stage. . . . .	56
2.23	The Penning trap vacuum enclosure. . . . .	59

2.24	The electrical feed-throughs into the Penning trap vacuum space. . . . .	61
3.1	The potentials used to adiabatically transfer particles. . . . .	64
3.2	The potentials used to pulse transfer particles. . . . .	65
3.3	Electronics used to apply fast voltage pulses to the trap electrodes. . . . .	66
3.4	The energy and temporal distribution of pulse-launched electrons. . . . .	69
3.5	The potentials used to pulse separate positrons from ions. . . . .	70
3.6	Pulse-transfer efficiency of 8 million electrons. . . . .	71
3.7	Electronics used to measure currents and charges of particles within the trap. . . . .	74
3.8	Charge-sensitive amplifier signal. . . . .	75
3.9	Potentials used for particle charge counting. . . . .	76
3.10	An example of incremental charge counting for electrons. . . . .	78
3.11	Scintillating fibers and paddles used to detect antiproton annihilations. . . . .	82
3.12	Demonstration that the detection fibers are sensitive to positron annihilations, but the paddle detectors are not. . . . .	88
3.13	Positron detector efficiency calibration curve. . . . .	89
3.14	Comparison of detector channel counts with the net antiproton charge detected. . . . .	90
3.15	The relative detection efficiency of the fiber and paddle detectors at 1 T and 2 T. . . . .	92
3.16	Nondestructive rf particle counting circuit and signal. . . . .	94
4.1	The photoelectron-loading apparatus. . . . .	104
4.2	The potentials typically used to load and count electrons. . . . .	106
4.3	Potential energy distribution of trapped electrons. . . . .	108
4.4	Typical number and energy of emitted electrons as a function of accelerating bias. . . . .	109
4.5	Linearity of electron loading. . . . .	110
4.6	The positron accumulation and transfer system. . . . .	113
4.7	The buffer-gas pressures and electric potentials used to trap positrons in the positron accumulator. . . . .	114
4.8	The positron-admitting aperture into the cryogenic Penning trap. . . . .	116
4.9	The number of positrons striking the degrader as a function of the position of a 1 mm diameter aperture. . . . .	118
4.10	The potentials used for loading positrons into the Penning trap. . . . .	119
4.11	Positrons loaded into the Penning trap as a function of the number of positron bunches stacked. . . . .	120
4.12	The Antiproton Decelerator storage ring at CERN. . . . .	122
4.13	The path of antiprotons before entering the trap. . . . .	124
4.14	Optimization of the SF <sub>6</sub> -He gas mixture in the energy-tuning cell for antiproton loading. . . . .	126

4.15	Antiproton catching procedure. . . . .	127
4.16	High voltage switch delay optimization for antiproton loading. . . . .	128
4.17	Trapped antiproton axial energy distribution. . . . .	129
4.18	Antiproton cyclotron diameter as a function of radial energy. . . . .	130
4.19	Cross sections of the antiproton trapping regions. . . . .	131
4.20	Antiprotons loaded as a function of axial trapping voltage in zone one. . . . .	132
4.21	Antiprotons loaded as a function of magnetic field in zone one. . . . .	133
4.22	Comparison of the antiproton loading efficiency in zone one and zone two. . . . .	134
4.23	Antiprotons loaded as a function of axial trapping voltage in zone two. . . . .	135
4.24	Antiprotons loaded as a function of magnetic field in zone two. . . . .	136
4.25	Antiproton stacking procedure. . . . .	137
4.26	Antiprotons loaded as a function of the number of cooling electrons. . . . .	140
4.27	Antiprotons loaded as a function electron confining potentials for various electron numbers. . . . .	141
4.28	Antiprotons loaded as a function electron confining potentials at various magnetic fields. . . . .	142
4.29	Antiproton cooling as a function of time . . . . .	143
4.30	Antiprotons loaded into the X3 trap per bunch from the AD. . . . .	144
4.31	Antiprotons loaded into A-TRAP per bunch from the AD. . . . .	146
5.1	The plasma density as a function of plasma rotation frequency. . . . .	154
5.2	Frequencies of the lowest-order cylindrically-symmetric plasma modes. . . . .	158
5.3	The center-of-mass mode frequency as a function of particle number and plasma aspect ratio. . . . .	160
5.4	The axial confining potential of a radius-length electrode compared to an ideal quadrupole potential. . . . .	161
5.5	Plasma mode frequencies as a function of density. . . . .	162
5.6	The circuit used to detect plasma mode frequencies. . . . .	164
5.7	The plasma mode detection signal. . . . .	165
5.8	The shape of a plasma containing 60 million positrons. . . . .	166
6.1	The distortion of axial magnetic field lines by a quadrupole Ioffe trap. . . . .	169
6.2	Particle motion in a combined Penning-Ioffe trap. . . . .	170
6.3	Projections of stable magnetron orbits in a Penning-Ioffe trap. . . . .	171
6.4	Equipotentials and magnetic field lines in a Penning-Ioffe trap, and the corresponding radial cut-off. . . . .	173
6.5	Critical cut-off radius for quadrupole and octupole Ioffe fields. . . . .	178
6.6	Magnetic field magnitude as a function of radius in quadrupole and octupole Ioffe traps. . . . .	179
6.7	The Penning-Ioffe apparatus used for particle stability measurements. . . . .	182
6.8	The fraction of antiprotons that survived a quadrupole Ioffe field. . . . .	183

---

6.9	Antiproton losses while turning on the quadrupole Ioffe field. . . . .	184
6.10	Electron loss as a function of time in a quadrupole Ioffe trap field. . .	185
6.11	Electron loss as a function of well depth in a quadrupole Ioffe trap field.	188
6.12	Electron loss as a function of well depth in a quadrupole Ioffe trap field with a 5 minute hold time. . . . .	189
7.1	The Penning-Ioffe apparatus used to produce antihydrogen. . . . .	194
7.2	The potentials used for antihydrogen production and detection. . . .	196
7.3	The effect of the positron space charge on the axial energy of the an- tiprotons. . . . .	197
7.4	The energy distribution of antiprotons in the nested well cooled by decreasing the positron confining well depth. . . . .	199
7.5	The antihydrogen detection well. . . . .	200
7.6	The equipotential contours and field lines governing the motion of an- tihydrogen atoms and charged particles. . . . .	202
7.7	Energetically allowed trajectories of antiprotons within the Penning- Ioffe trap. . . . .	204
7.8	The energy distribution of antiprotons released from the nested well after antihydrogen formation at various Ioffe trap depths. . . . .	207
7.9	Number of antihydrogen atoms detected within the Ioffe trap at various trap depths. . . . .	208

# List of Tables

2.1	Typical particle motion frequencies in our Penning trap. . . . .	20
2.2	Confinement potential expansion coefficients for the three typical electrode configurations used in the Penning trap. . . . .	23
3.1	The solid angle acceptance of the detectors for a single particle originating at the indicated annihilation position [1]. . . . .	83
3.2	Monte Carlo simulation predictions for the probability that a single antiproton annihilation at the indicated location in a 1 T field will be registered on the indicated detector or coincidence of detectors [1]. . . . .	84
3.3	Absolute detector channel efficiencies, derived from the relative detector efficiencies and the assumption that the paddle detector efficiencies are equal to the derived Monte Carlo values. Also listed are the typical background count rates for each detector channel, and the antiproton annihilation rate that is required to equal the background noise rate (labeled S/N). . . . .	86
3.4	Radiative damping time constants for particles in the Penning trap, assuming a 100 V confining potential in a radius-length electrode and a 1 T magnetic field. . . . .	96

# Papers and Publications

1. *Antihydrogen Production within a Penning-Ioffe Trap*  
G. Gabrielse, P. Laroche, D. Le Sage, B. Levitt, W.S. Kolthammer, R. McConnell, P. Richerme, J. Wrubel, A. Speck, M.C. George, D. Grzonka, W. Oelert, T. Seifick, Z. Zhang, A. Carew, D. Comeau, E.A. Hessels, C.H. Storry, M. Weel, and J. Walz, Phys. Rev. Lett. 100, 113001 (2008).
2. *Single-Component Plasma of Photoelectrons*  
B. Levitt, G. Gabrielse, P. Laroche, D. Le Sage, W.S. Kolthammer, R. McConnell, J. Wrubel, A. Speck, D. Grzonka, W. Oelert, T. Seifick, Z. Zhang, D. Comeau, M.C. George, E.A. Hessels, C.H. Storry, M. Weel, and J. Walz, Phys. Lett. B 656, 25-29 (2007).
3. *Density and Geometry of Single Component Plasmas*  
A. Speck, G. Gabrielse, P. Laroche, D. Le Sage, B. Levitt, W.S. Kolthammer, R. McConnell, J. Wrubel, D. Grzonka, W. Oelert, T. Seifick, Z. Zhang, D. Comeau, M.C. George, E.A. Hessels, C.H. Storry, M. Weel, and J. Walz, Phys. Lett. B 650, 119-123 (2007).
4. *Antiproton Confinement in a Penning-Ioffe Trap for Antihydrogen*  
G. Gabrielse, P. Laroche, D. Le Sage, B. Levitt, W.S. Kolthammer, I. Kujanishvili, R. McConnell, J. Wrubel, F.M. Esser, H. Glueckler, D. Grzonka, G. Hansen, S. Martin, W. Oelert, J. Schillings, M. Schmitt, T. Seifick, H. Soltner, Z. Zhang, D. Comeau, M.C. George, E.A. Hessels, C.H. Storry, M. Weel, A. Speck, F. Nillius, J. Walz and T.W. Haensch, Phys. Rev. Lett. 98, 113002 (2007).
5. *First Laser-Controlled Antihydrogen Production*  
C.H. Storry, A. Speck, D. Le Sage, N. Guise, G. Gabrielse, D. Grzonka, W. Oelert, G. Scheppers, T. Seifick, J. Walz, H. Pittner, M. Herrmann, T.W. Haensch, D. Comeau, E. A. Hessels, Phys. Rev. Lett. 93, 263401 (2004).
6. *First Measurement of the Velocity of Slow Antihydrogen Atoms*  
G. Gabrielse, A. Speck, C.H. Storry, D. Le Sage, N. Guise, D. Grzonka, W. Oelert, G. Schepers, T. Seifick, H. Pittner, J. Walz, T.W. Haensch, D. Comeau, E.A. Hessels, Phys. Rev. Lett. 93, 073401 (2004).

# Acknowledgments

I am grateful for the opportunity to have worked on an exceptionally interesting and challenging project over the last few years. It has been a very rewarding and educational experience that I shall remember for the rest of my life. I would like to thank my advisor, Jerry Gabrielse, for his support, motivation, and knowledgeable guidance throughout the process. I would also like to acknowledge the many other members of the ATRAP collaboration, without whom this work would not have been possible.

In particular, I am exceedingly grateful to the grad students and post-docs that I spent many long hours working with in the AD at CERN, to: Andrew Speck, Daniel Comeau, Phil Larochelle, Ben Levitt, Jonathan Wrubel, Matt Weel, Matt George, Adam Carew, Zhongdong Zhang, Rob McConnell, Steve Kolthammer, and Phil Richerme. In addition to being talented researchers, the camaraderie gained through long hours facing shared challenges was absolutely essential for me to maintain motivation and good humor during the mentally draining beam runs at CERN. I would like to thank Prof. Eric Hessels and Prof. Cody Storry of York University for their knowledgeable insights and hands-on help with the experiments. Thanks to Prof. Walter Oelert and Dr. Dieter Grzonka of Forschungszentrum Jülich for their indispensable contributions, good natures, and willingness to help out in any way possible. I would also like to acknowledge Heiko Pittner and Max Herrmann from the Max Planck Institute at Garching, and Fabian Nillius, Andreas Müllers, Frank Markert, and Prof. Jochen Walz from the University of Mainz for their work on the laser systems.

I would like to thank my family for their love and support.

I would like to thank my friends throughout grad school for all of the fond memories and continuing support.

# Chapter 1

## Introduction

Antihydrogen is the simplest atom made entirely of antimatter. While a hydrogen atom ( $\text{H}$ ) is the bound state of a proton ( $\text{p}$ ) and an electron ( $\text{e}^-$ ), an antihydrogen atom ( $\bar{\text{H}}$ ) is the bound state of an antiproton ( $\bar{\text{p}}$ ) and a positron ( $\text{e}^+$ ). If antihydrogen can be created and studied, it would allow some interesting measurements that would test the fundamental symmetries between matter and antimatter. A precise comparison of the spectrums of hydrogen and antihydrogen would be a direct test of CPT invariance, a fundamental symmetry believed to be obeyed in nature. A test of whether hydrogen and antihydrogen experience the same acceleration due to gravity [2, 3], as is expected, would be the first direct test of the equivalence principle for antimatter.

The research presented here was carried out within the ATRAP collaboration, which has the long-term goal of confining antihydrogen for precise laser spectroscopy [4] as a test of CPT and Lorentz invariance. Significant progress has recently been made toward this goal with the construction of an apparatus compatible with anti-

hydrogen confinement and spectroscopy, and the first reported production of antihydrogen within a magnetic field capable of confining cold, ground-state antihydrogen atoms [5].

Antihydrogen was first observed in 1996, when 9 antihydrogen atoms traveling near the speed of light were detected at CERN [6]. However, precision measurement of the spectrum of antihydrogen atoms would require a drastically different procedure that produces cold antihydrogen atoms that can be confined and observed for long periods of time. A significant challenge for any form of antimatter confinement is that antiparticles will annihilate if they come in contact with their particle counterparts. This requires that antimatter be kept away from all of the objects used to confine it, and within an exceptionally good vacuum environment free of background gas that can also cause annihilation loss. There is no available source of antihydrogen atoms, but the constituents of antihydrogen can be produced within a laboratory. Positrons are emitted during some beta decay processes from radioactive isotopes, and antiprotons can be produced during high-energy particle collisions at particle accelerator facilities.

A cryogenic Penning trap makes an ideal environment for long-term confinement of the constituent particles used to form antihydrogen. The TRAP collaboration that preceded ATRAP demonstrated the first confinement [7] and cooling [8] of antiprotons within a cryogenic Penning trap. Positron accumulation within a cryogenic Penning trap has been achieved with a number of methods, including field ionization of Rydberg positronium [9] and buffer gas accumulation of positrons in an external accumulator [10]. Simultaneous confinement and mixing of oppositely-charged positrons and

antiprotons for antihydrogen production can be achieved using a nested Penning trap [11, 12]. ATRAP demonstrated the first cooling of antiproton motion by positrons within a nested Penning trap [13]. It was later demonstrated that antihydrogen atoms are formed during this process [14, 15, 16].

The neutral antihydrogen atoms produced are not confined within the Penning trap, and rapidly annihilate on the surrounding electrodes. Precision spectroscopy of the antihydrogen will first require magnetically confining the atoms to allow enough time for measurements. The most straightforward approach to doing this is to superimpose the magnetic confining field of a Ioffe trap over the Penning trap fields used to produce the atoms. Ioffe traps have previously been used to confine hydrogen atoms [17] for spectroscopy [18]. A critical step for loading hydrogen atoms into those Ioffe traps was to cool the atoms through collisions with liquid-helium-coated walls, which would cause immediate annihilation for antihydrogen atoms. Instead, we must rely upon producing trappable antihydrogen atoms directly from constituent particles that are individually cooled to cryogenic temperatures within the Penning trap.

We desire slow-moving, tightly-bound antihydrogen atoms that can be trapped. Initial measurements by ATRAP demonstrated that the antihydrogen atoms detected were predominately in very highly-excited states [16, 19], and had velocities that were too large to be magnetically confined [20]. However, the detection technique used was insensitive to any antihydrogen atoms in tightly-bound states that may have been produced. In addition, Monte Carlo simulations of the antihydrogen formation process recently gave a more favorable interpretation of this data [21]. These simulations suggested that slow antihydrogen atoms are formed as antiprotons slowly pass through

the positron plasma, with the detected atoms converted into fast-moving antihydrogen atoms via a charge-exchange process with the fast-moving antiprotons in the nested Penning trap on either side of the positron plasma. This work also closely reproduced the experimentally-observed antihydrogen state distribution, including the power law scaling for loosely-bound atoms and enhanced production for tightly-bound atoms. This leaves open the possibility that some of the antihydrogen atoms produced that do not undergo the charge exchange process may be slow-moving and tightly-bound. Furthermore, an alternate antihydrogen production technique demonstrated by ATRAP [22], which utilizes a double resonant charge-exchange process with stationary antiprotons, may potentially give more favorable antihydrogen velocity and state distributions, although the number of atoms produced with this method thus far have been insufficient for measuring these distributions.

Although the Penning traps used for the results just outlined were extremely useful, they were not compatible with a Ioffe trap required to trap antihydrogen atoms for spectroscopy. A combined Penning-Ioffe trap was thus constructed and installed into a newly-commissioned experimental zone at CERN. This apparatus was much larger than those previously used, as required to accommodate a superconducting Ioffe trap, laser access space, and larger Penning trap electrodes for increased Ioffe trap depth and antiproton loading efficiency. The Penning-Ioffe trap has a flexible design to allow a versatile range of experiments. There is radial access into the center of the Penning-Ioffe trap through four ports, for either laser beams or instrumentation. A two-dimensional cryogenic translation stage above the Penning trap allows access to the central axis of the Penning trap for lasers and a range of particle loading and

diagnostic capabilities. The Penning trap itself is 0.8 m long, and divided into 36 electrodes that are each connected to independent DC voltage supplies and also to RF voltage sources, making a flexible platform for antihydrogen experiments that can employ complicated and dynamic potential structures that span large portions of the Penning trap.

This thesis will focus upon the design and performance of this new apparatus (Chapter 2) and the recent progress achieved with it toward the goals of antihydrogen confinement and spectroscopy. This trap was used to make critical progress in the methods used to load particles into the Penning trap (Chapter 4). These include a new method of rapidly loading up to a billion electrons via the photoelectric effect using short UV laser pulses [23], a buffer gas positron accumulator that was constructed to increase the positron accumulation rate in the the trap by a factor of 400 over the best accumulation rates previously achieved by ATRAP, and the most efficient antiproton accumulation rate demonstrated by ATRAP, in spite of the requirement that antiprotons be loaded at an unprecedented low magnetic field. Previously proven techniques were used to transport, count, and cool particles within the Penning trap (Chapter 3), while the geometry of plasmas within our Penning trap can be determined using a slight variant on the previous mode diagnostic method (Chapter 5).

The Penning-Ioffe trap apparatus was first used to demonstrate that positrons and antiprotons could be confined within a quadrupole Ioffe field for a sufficiently long time to form antihydrogen (Chapter 6) [24]. This was in spite of the fact that the radial Ioffe field breaks the cylindrical symmetry that is required for long-term

particle confinement within the Penning trap. We demonstrated that the resulting radial loss of particles, which was shown to be quite dramatic under somewhat different experimental conditions [25], was not a grave challenge for our intended experiments. The next step was to demonstrate the first reported formation of antihydrogen within a combined Penning-Ioffe trap (Chapter 7) [5]. This required dealing with the diminished positron and electron cyclotron cooling rates at reduced magnetic fields, and a method of prolonging antiproton-positron interaction times while minimizing the antiproton interaction energy. The observed antihydrogen production was actually enhanced when the Ioffe field was turned on, presumably due to the increase in the magnetic field within the antihydrogen production region generated by the axial confinement coils. Although no trapped antihydrogen atoms have yet been observed, future results that will become possible with modified antihydrogen formation procedures and an improved Ioffe trap seem very promising.

The work presented here was made possible through the combined effort of many members of the ATRAP collaboration. When appropriate, credit is given to those groups within the collaboration primarily responsible for construction and operation of certain portions of the apparatus. My contributions to the experiment began during the antiproton beam runs at CERN during the summers of 2003 and 2004, when I ran antihydrogen production experiments, helped to maintain the Penning traps, and optimized particle loading and transfer procedures during off-shift hours. Several important developments happened during this time, including the only measurement to date of the velocity of highly-excited antihydrogen atoms produced during the positron cooling of antiprotons [20], and the first demonstration of laser-controlled

antihydrogen production using a double resonant charge-exchange process [22].

Following that, I played a primary role in designing the two new Penning traps used for the experiments outlined in this thesis, with two postdoctoral researchers in the group also making contributions. I was responsible for the design and testing of the trap cryogenic system, the trap vacuum enclosures, and the two-dimensional cryogenic translation stage. The experimental results presented in this thesis were from the antiproton beam runs at CERN during the summers of 2006 and 2007. As the senior graduate student on the project, I played an important role in designing and performing the experiments, analyzing the data, and maintaining and modifying the Penning-Ioffe trap to meet the experimental goals. The demonstrated confinement of particles [24] and production of antihydrogen [5] within the fields of a combined Penning-Ioffe trap mark significant steps toward the goal of confining antihydrogen atoms for spectroscopy.

The remainder of this introductory chapter will first summarize the motivation for these experiments. The previously demonstrated methods of forming antihydrogen will then be briefly discussed.

## 1.1 CPT Symmetry

Symmetries play an important role in our understanding of physics. By Noether's theorem, each symmetry in a system is directly linked to a corresponding conserved quantity. For example, rotation invariance leads to conservation of angular momentum, and time invariance leads to conservation of energy. This fundamental interrelation of symmetry and conservation laws is an important tool in theoretical physics,

both as a computational tool and a route to better fundamental understanding. As such, characterizing the fundamental symmetries of nature is of great intrinsic importance to our theoretical understanding of the universe.

For many years, it was believed that the physical laws of nature were independently invariant under the transformations: parity (P), charge conjugation (C), and time reversal (T). A parity transformation inverts the spatial coordinate system ( $x \rightarrow -x, y \rightarrow -y, z \rightarrow -z$ ), converting the right-handed system to a left-handed system. Charge conjugation converts particles into their antiparticles, thereby reversing the fundamental charge of the particle. Time reversal reverses the direction of all motions. Phrased in simple terms, it was originally believed that if we observe any process in nature, and then observed the same process either through a “mirror” that inverts all three coordinates, or after exchanging particles with antiparticles, or in a movie played in reverse, or any combination of these transformations, then the physical laws governing the evolution of the transformed process should be indistinguishable from the physical laws governing the original process.

Although these symmetries are obeyed under most circumstances, it was eventually revealed that none of these individual transformations were fundamental symmetries of nature. In 1956, Lee and Yang observed that parity conservation had not been tested for weak interactions [26], and an experiment by Wu soon discovered that electrons are preferentially emitted in the direction of the nuclear spin of a  $^{60}\text{Co}$  atom during  $\beta$  decay [27], violating parity for the weak interaction. This violation of parity for the weak interaction is associated with the fact that all observed neutrinos have left-handed helicity and all observed antineutrinos have right-handed helicity.

The result of a parity transformation or a charge conjugation transformation on a neutrino or antineutrino would result in a neutrino or antineutrino with a helicity that is not observed in nature. Consequently, although parity and charge conjugation appear to be conserved for strong and electromagnetic interactions, neither of them are individually valid symmetries for the weak interaction.

After this discovery, it was assumed that the combined transformations of parity and charge conjugation (CP) was a valid symmetry of nature. In 1964 however, Cronin and Fitch, following previous work by Gell-Mann and Pais [28], discovered CP violation within the neutral  $K$  meson system [29]. CP violation allows us for the first time to make a clear distinction between how particles and antiparticles are treated in physics. It has been suggested that this may be responsible for why the modern universe is predominately made of matter, while it is believed that matter and antimatter were formed in equal quantities in the early universe [30]. However, this is only a qualitative speculation so far.

It is presently believed that the combination of the operations of parity, charge conjugation, and time reversal (CPT) is a fundamental symmetry of nature. This belief is based upon both experimental observations so far performed, and on a theoretical justification called the CPT theorem. The CPT theorem arises because all local Lorentz invariant quantum field theories obey CPT symmetry [31], which includes all of the accepted theories of particle physics, such as quantum electrodynamics and the standard model. Any observed deviation from CPT symmetry would therefore necessitate new physics beyond our present models. We are aware that our present theories are incomplete however, since gravity has not yet been successfully incor-

porated into quantum field theory. As such, there is certainly room for discoveries beyond our present theories, and history has taught us that belief in fundamental symmetries can only be supported or refuted through extensively testing.

One consequence if the CPT theorem is valid is that particles and their antiparticles must have the same mass and lifetime, and equal magnitude but opposite sign charge and magnetic moment [32]. CPT symmetry has been tested by comparing these properties between particles and antiparticles. The most accurate of these tests is the mass comparison of the neutral K mesons [33], while the most accurate test for leptons compares the electron and positron magnetic moments [34], and the most accurate test for baryons compares the charge-to-mass ratios of protons and antiprotons [35], a measurement made by the TRAP collaboration that was a predecessor of ATRAP. The exact way in which a CPT violation might occur is unknown, so the theory must be tested within different systems.

A further consequence of CPT invariance is that hydrogen and antihydrogen should have precisely the same energy levels, so a comparison of the two spectra could test this symmetry in the new regime of an interacting baryon-lepton system [36]. It has been speculated that CPT violation might be observed in a comparison of hydrogen and antihydrogen under some circumstances if reality were not invariant under Lorentz transformations [36]. A comparison of the 1S-2S transition frequency would be a particularly promising measurement, since the long lifetime of the metastable 2S state in Hydrogen gives the transition a narrow 1.3 Hz natural linewidth, corresponding to an accuracy of 5 parts in  $10^{-16}$ . The best measurement to date of this transition has an accuracy of 1.8 parts in  $10^{-14}$  [37]. Spectroscopy of antihydrogen

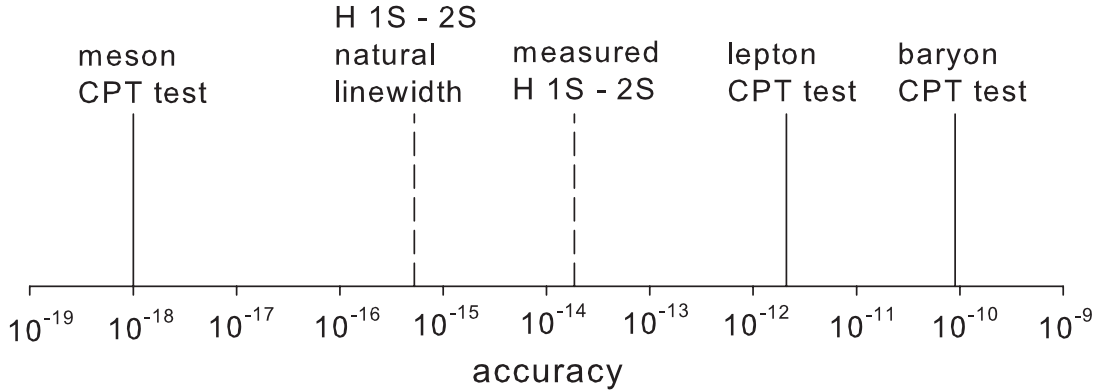


Figure 1.1: A comparison of possible antihydrogen spectroscopy accuracy with the accuracy of the most accurate CPT tests for mesons, leptons, and baryons.

to a similar level would mark tremendous progress in testing CPT invariance. A comparison of the accuracy of such measurements with previous CPT tests is given in Fig. 1.1. Accurate spectroscopy of antihydrogen will have to be performed within a magnetic trap [4, 38], similar in some ways to previous work done with hydrogen [18].

## 1.2 Antihydrogen Production Methods

### 1.2.1 Three-Body Recombination

Most of the antihydrogen observed so far has been produced during the positron cooling of antiprotons within a nested Penning trap [11]. In this process, the antiprotons must be given sufficient energy to overcome the electric potential confining the positrons in order to form antihydrogen within the dense positron plasma. This is done by either injecting the antiprotons into the nested well from an elevated potential [14, 15], or by adding energy to the antiproton axial motion using a resonant

radio-frequency oscillating voltage [16].

The dominant antihydrogen production mechanism is through the three-body recombination process [11]:



where the extra positron is required to conserve energy and momentum. The excited antihydrogen atoms ( $\bar{H}^*$ ) have an average radius that can be estimated by the classical distance of closest approach of the particles,  $\rho_{\text{tbd}} = e^2/(4\pi\epsilon_0 k_b T)$ , which suggests that atoms formed by positrons and antiprotons at 4 K will typically be so weakly bound that they would be ionized by the electric fields within the trap. The atoms can decay to more deeply bound states however, through short-range exchange collisions [39, 40] and long range collisions [41, 42] with other positrons in the plasma. Nonetheless, the state distribution of detected atoms suggests that most of the atoms produced have large radii with barely sufficient binding energy to survive the trap fields [16, 19].

A significant advantage of this three-body recombination process is that it produces antihydrogen atoms very efficiently. One model for three-body antihydrogen production in a strong magnetic field ( $B \rightarrow \infty$ ) suggested that the rate for a single antiproton to form an antihydrogen atom that is sufficiently deeply bound to not be rapidly ionized scales as [39]:

$$\Gamma_{\text{tbr}} = 4 \times 10^{-10} \frac{n_{e^+}^2}{T^{9/2}} \quad (1.2)$$

where  $n_{e^+}$  is the density of the positron plasma and  $T$  is the plasma temperature. A later simulation suggesting that this rate is boosted by about 60 % for fields of just a few Tesla [43]. For typical parameters in our trap,  $n_{e^+} = 5 \times 10^7 / \text{cm}^3$  and  $T = 4.2 \text{ K}$ , we might therefore expect an antiproton to be converted into an antihydrogen atom

typically within 400 microseconds inside the positron plasma. The antiprotons and the excited antihydrogen atoms produced typically spend far less time than this within the positron plasma however. The antiprotons can still be effectively converted into antihydrogen by passing back and forth through the positron plasma many times, but a neutral antihydrogen atom only has a single pass within the plasma in which to undergo de-excitation collisions.

Simulations of antihydrogen formation that included realistic plasma geometries suggested that the antihydrogen atoms did not spend sufficient time within the plasma to undergo many de-excitation collisions with positrons [21, 44, 45]. Consequently, these studies predicted that the antihydrogen produced would be predominantly in highly-excited states, as supported by experimental evidence [16, 19]. The data from these ATRAP experiments was replicated very well by some of the simulations [21]. The small plasma dimensions also caused the antihydrogen production rate to scale much more weakly with temperature than indicated in Eq. 1.2 [45], in agreement with measurements [46].

The initial antihydrogen state distribution observed is unfavorable for antihydrogen confinement and spectroscopy, which requires the atoms to end up in low-field-seeking ground states. The spontaneous emission decay time of these highly excited atoms is believed to be much longer than the typical time that the atoms spend within the trap [47]. Monte Carlo simulations further suggest that only a small percentage of these highly-excited atoms will be in magnetically confinable, low-field-seeking states [44]. However, of the low-field-seeking states produced, the highly excited states tend to have a larger magnetic moment than ground state atoms, and correspondingly ex-

perience a larger Ioffe trap depth. It has been proposed that the spontaneous decay of excited atoms within the Ioffe field can provide a mechanism for cooling the motion of trapped antihydrogen atoms [48, 49].

One recent simulation suggests that the three-body recombination rate does not decrease rapidly with increasing antiproton velocity [43]. This would suggest that most of the antihydrogen produced has kinetic energies significantly larger than  $k_B T$ , for a given positron plasma temperature  $T$  [45], consistent with antihydrogen velocity measurements made by ATRAP [20]. However, a contemporary simulation suggested that the high velocities measured were in part due to charge exchange processes between slow moving antihydrogen atoms and nearby fast-moving antiprotons [21]. In order to have a chance of trapping some non-negligible fraction of the antihydrogen atoms produced, the thermal distribution of the antihydrogen atoms produced must be close to equilibrium with the 4 K trap temperature.

For three-body recombination to be useful for antihydrogen confinement, the antihydrogen formation process must be optimized to maximize the number of slow antihydrogen atoms in tightly-bound, low-field-seeking states. Slower antihydrogen atoms can be produced by minimizing the energy of the antiproton passing through the positron plasma. The rate at which antiprotons slow within the positron plasma is likewise an important parameter, and theoretical models of this process continue to be developed [50]. The geometry and temperature of the positron plasma also plays an important role, although these parameters can have complicated competing effects on the number, velocity, and states of antihydrogen atoms produced. Further experimental and theoretical work is needed to optimize this process for antihydrogen

confinement.

## 1.2.2 Other Antihydrogen Formation Methods

A second method developed by ATRAP involves forming antihydrogen through a laser-controlled two-step charge-exchange process [22]. In this process, Cs atoms from an oven are excited by a pair of laser beams into an excited Rydberg state before passing through the positron plasma. In the first charge exchange process [51], the excited Cs electron and a positron are able to form excited positronium which, being neutral, is not affected by the electric fields in the Penning trap. Some of the positronium passes through the antiprotons stored in a nearby well, and can form antihydrogen via a second charge exchange process. This antihydrogen formation method has the disadvantage that the low cross sections of the two charge exchange processes, and small solid angle factor for positronium to pass through the antiprotons make the overall antihydrogen production efficiency very low. Only a couple of antihydrogen atoms were typically detected per trial, compared to hundreds or thousands for the corresponding three-body recombination experiments, although greater efficiencies are expected with the increased number of positrons now available. The production method does have two advantageous features. First, because the two charge exchange processes tend to conserve binding energy, the antihydrogen produced is expected to be within a much more narrow binding energy range, which is effectively controlled by the initial laser excitation of the Cs atoms. Second, the antiprotons in this process are not heated in order to interact with positrons and form antihydrogen, potentially producing colder antihydrogen atoms as a consequence. Simulations of this process

in a strong magnetic field [52] agreed with previous calculations [53] showing that the binding energy is roughly conserved in the process, and that antihydrogen is produced more efficiently if the Cs atom is initially excited to higher levels. These simulations further suggested that most of the atoms are produced in non-confineable high-field-seeking states, although a larger percentage of the atoms are produced in low-field-seeking states if the antihydrogen atoms are produced in more tightly-bound states, at the expense of the overall number of atoms produced [52].

Another possibility is for an antiproton and a positron to form antihydrogen through radiative recombination, in which a photon is emitted from the formed atom to conserve energy and momentum in the process. This process has a very low production efficiency however because the time that the antiprotons and positrons spend near each other is typically short compared to the spontaneous decay time of the antihydrogen state [11]. However, those atoms that do form via this process are preferentially in tightly bound states, since those states have much shorter decay times. It is unlikely that this favorable feature of radiative recombination can be taken advantage of, however, because the process is completely dominated by the much faster three-body recombination rate. Attempts at stimulating radiative recombination using lasers were made by another group, with negligible boosts to the antihydrogen production observed [54].

### 1.2.3 Antihydrogen Production within a Penning-Ioffe Trap

The first antihydrogen production within a Penning-Ioffe trap (Chapter 7) [5] was accomplished using a variation on methods previously used for antihydrogen pro-

duction via three-body recombination in a nested well. These represent preliminary results with the new Penning-Ioffe trap, and many further studies are expected in the future using both three-body recombination and laser-controlled charge-exchange procedures. It is yet to be determined which method is better suited to produce trapped, ground state antihydrogen atoms for spectroscopy.

# Chapter 2

## Apparatus

### 2.1 The Penning Trap

#### 2.1.1 Penning Trap Theory

Charged-particle confinement in a Penning trap is provided by a combination of an axial magnetic bias field:

$$\vec{B} = B_0 \hat{z} \quad (2.1)$$

and a quadrupole electric field:

$$\phi(r, z) = \frac{C_2 V_0}{2d^2} \left( z^2 - \frac{\rho^2}{2} \right) \quad (2.2)$$

where  $d$  and  $C_2$  are geometric constants. The motion of a charged particle in the fields is governed by the Lorentz force equation:

$$m\ddot{\vec{r}} = q \left( -\nabla\phi + B_0 \dot{\vec{r}} \times \hat{z} \right) \quad (2.3)$$

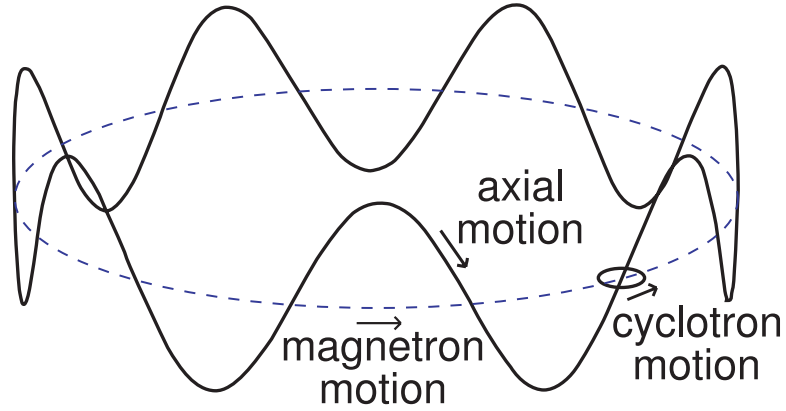


Figure 2.1: The three distinct motions of a charged particle in a Penning trap.

which can be written as

$$m\ddot{z} = \frac{-qC_2V_0}{d^2}z \quad (2.4a)$$

$$m\ddot{x} = \frac{qC_2V_0}{2d^2}x - qyB_0 \quad (2.4b)$$

$$m\ddot{y} = \frac{qC_2V_0}{2d^2}y + qxB_0 \quad (2.4c)$$

The particles undergo harmonic oscillations along the  $\hat{z}$  direction with frequency:

$$\omega_z = \sqrt{\frac{qC_2V_0}{md^2}} \quad (2.5)$$

The radial motion equations can be simplified by making the substitution  $u = x + iy$  and writing the constants in terms of  $\omega_z$  and the cyclotron frequency,  $\omega_c = \frac{qB_0}{m}$ , resulting in:

$$\ddot{u} + i\omega_c\dot{u} - \frac{1}{2}\omega_z^2u = 0 \quad (2.6)$$

The general solution is  $u = e^{-i\omega_{\pm}t}$ , where

$$\omega_{\pm} = \frac{1}{2} \left( \omega_c \pm \sqrt{\omega_c^2 - 2\omega_z^2} \right) \quad (2.7)$$

	e <sup>+</sup>	$\bar{p}$
Magnetic Field	1.0 T	
Trapping Voltage ( $V_0$ )	-100 V	100 V
Electrode Size ( $d$ )	11.0 mm	
Magnetron Frequency	33.5 kHz	33.5 kHz
Axial Frequency	43.3 MHz	1.01 MHz
Cyclotron Frequency	28.0 GHz	15.2 MHz

Table 2.1: Typical particle motion frequencies in our Penning trap.

If  $\omega_{\pm}$  is real, the two solutions describes circular orbits with eigenfrequencies  $\omega_{\pm}$ , while imaginary values of  $\omega_{\pm}$  lead to unstable orbits. There is therefore a requirement that  $\omega_c \geq \sqrt{2}\omega_z$  in order to have stable confinement of charged particles in a Penning trap.

Charged particles in a Penning trap therefore undergo three distinct motions: axial oscillation with frequency  $\omega_z$ , cyclotron motion at the modified cyclotron frequency,  $\omega'_c = \omega_+ = \omega_c - \omega_m$ , and magnetron motion with frequency  $\omega_m = \omega_- = \frac{\omega_z^2}{2\omega'_c}$ , which can be identified as an  $\vec{E} \times \vec{B}$  drift motion [55, 56]. These motions are depicted in Fig. 2.1. The typical particle motion frequencies in our Penning trap are depicted in Table 2.1. The frequencies in general have the hierarchy  $\omega'_c \gg \omega_z \gg \omega_m$ , and can therefore be regarded as independent of each other.

The energies corresponding to the axial, cyclotron, and magnetron motions are respectively:

$$E_a = \frac{m}{2}\omega_z^2 z_{max}^2 \quad (2.8a)$$

$$E_c = \frac{m}{2}\omega_c^2 \rho_c^2 \quad (2.8b)$$

$$E_m = \frac{m}{2} \left( \omega_m^2 - \frac{1}{2}\omega_z^2 \right) \rho_m^2 < 0 \quad (2.8c)$$

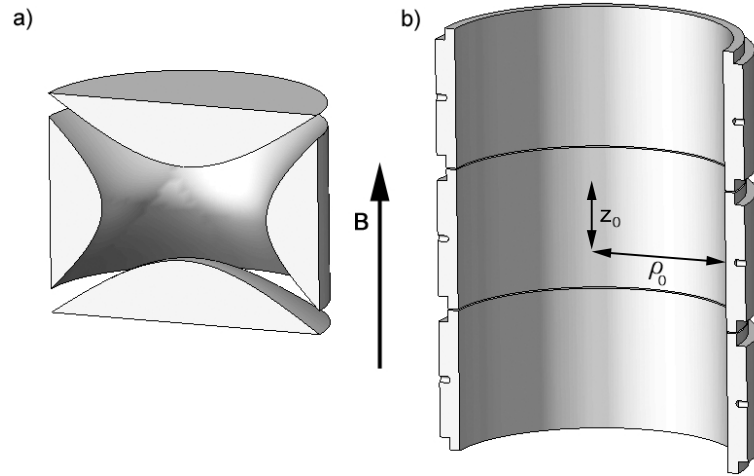


Figure 2.2: a) Hyperbolic and b) cylindrical ring electrode geometries.

where  $z_{max}$  is the amplitude of the axial oscillation,  $\rho_c$  is the cyclotron radius, and  $\rho_m$  is the magnetron radius. If a particle loses axial or cyclotron energy through a damping mechanism, this leads to a reduction in its axial oscillation amplitude or its cyclotron radius. In contrast, the magnetron energy decreases with increasing magnetron radius because the radial electric potential energy has a larger magnitude than the kinetic energy of the magnetron motion. Consequently, energy has to be actively added to the magnetron motion in order to decrease the magnetron radius. These issues will be discussed in more detail in Section 3.3.1 and Section 3.3.2.

### 2.1.2 Penning Trap Electrode Geometries

The quadrupole electric confining potential of an ideal Penning trap can be generated by applying voltages to electrodes with surfaces that have the same shape as the equipotential contours. For a quadrupole potential, the equipotential contours are hyperboloids (Fig. 2.2a). Although hyperbolic trap electrodes can in principle be made,

they are difficult to fabricate, and this electrode geometry makes it difficult to load particles or to link different trapping zones. The simplest and most versatile Penning trap electrode design is to use cylindrical ring electrodes with open ends (Fig. 2.2b) [57]. An arbitrarily large number of cylindrical ring electrodes can be stacked on top of each other and independently biased to different voltages in order to produce multiple particle confinement regions, and particles can be loaded through the open ends of the electrodes or transported from one electrode to another by adjusting the potentials applied to the electrodes.

The electric confining potential produced by cylindrical electrodes is not a perfect quadrupole. If we assume that the voltages applied to the cylindrical electrodes are axially symmetric about the center of the confinement electrode, then the confining potential can be written in spherical coordinates about the center of the electrode as an expansion of even Legendre polynomials,  $P_j(\cos[\theta])$ :

$$\phi(\rho, z) = \frac{V_0}{2} \sum_{\substack{j=0 \\ \text{even}}}^{\infty} C_j \left(\frac{r}{d}\right)^j P_j(\cos[\theta]) \quad (2.9)$$

where  $d^2 = \frac{1}{2}(z_0^2 + \frac{1}{2}\rho_0^2)$ ,  $V_0$  is the voltage applied to the confinement electrode,  $r^2 = z^2 + \rho^2$ ,  $z_0$  is the electrode half-length, and  $\rho_0$  is the electrode radius. A perfect quadrupole potential can be written in terms of the  $C_0$  and  $C_2$  terms alone, while the higher order terms in the expansion describe the anharmonic portions of the potential generated by the cylindrical electrodes.

The specific values of the  $C_n$  terms depend upon the relative geometries and relative voltages applied to the cylindrical electrodes. With an appropriate choice of the dimensions of the confinement electrode and its two nearest neighbors, and the voltages applied to the three electrodes, the  $C_4$  and  $C_6$  terms can be set to zero

	radius-length electrode	“endcap” electrode	“ring-comp” electrode set
$\rho_0$	18.0 mm		
$z_0$	9.0 mm	15.3 mm	2.8 mm
$z_1$	...	...	7.3 mm
$\frac{V_1}{V_0}$	0	0	0.8811
$d$	11.0 mm	14.1 mm	15.3 mm
$C_0$	1.15	1.61	1.55
$C_2$	-0.5092	-0.5734	-0.5449
$C_4$	0.1080	-0.0135	0
$C_6$	-0.0036	0.0486	0
$C_8$	-0.0061	-0.0039	0.0366

Table 2.2: Confinement potential expansion coefficients for the three typical electrode configurations used in the Penning trap. It is assumed that both ends of the electrode stack are closed by a grounded plane.

[57]. This is useful when very precise harmonic potentials are required in order to have a well-defined particle axial oscillation frequency. In most applications, this degree of precision is not required for particle storage or antihydrogen production however, so most of the electrodes in our Penning trap are of identical length to their neighbors. The corresponding Legendre polynomial expansion coefficients are given in Table 2.2 for the three types of confinement electrode geometries typically used to confine particles in our Penning trap, where  $z_1$  and  $V_1$  are the axial half-lengths and voltages of the two electrodes neighboring the confinement electrode. Near the center of the electrodes, the potential can be approximated as a quadrupole, although it deviates from this away from the center. The confinement potential inside a radius-length electrode in comparison with the corresponding ideal quadrupole potential is depicted in Fig. 2.3.

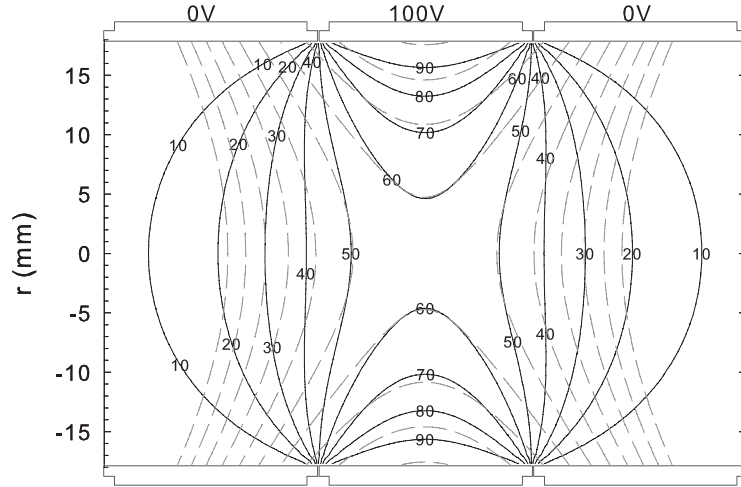


Figure 2.3: The confinement potential within a radius-length electrode (solid contours), in comparison to the corresponding ideal quadrupole potential (dashed contours).

### 2.1.3 The A-TRAP and B-TRAP Penning Traps

Two identical Penning traps were constructed for use in the new experimental zone at CERN, either of which can be used in conjunction with the Ioffe neutral atom trap. Two traps were constructed so that one can be used at any time to perform experiments while the other is being repaired or modified. We refer to these two traps as “A-TRAP” and “B-TRAP”, but I shall typically refer to either experiment as A-TRAP from this point forward for simplicity, since the two traps are nearly identical, although only one of them at a time can be combined with the one Ioffe trap that we presently have. In that case, the other trap is simply a Penning trap, which can still be used for useful particle loading and diagnostic experiments, and antihydrogen production experiments.

The A-TRAP Penning trap is depicted in Fig. 2.4. The “electrode stack” consists of 36 gold-plated copper ring electrodes that are stacked on top of each other, separated

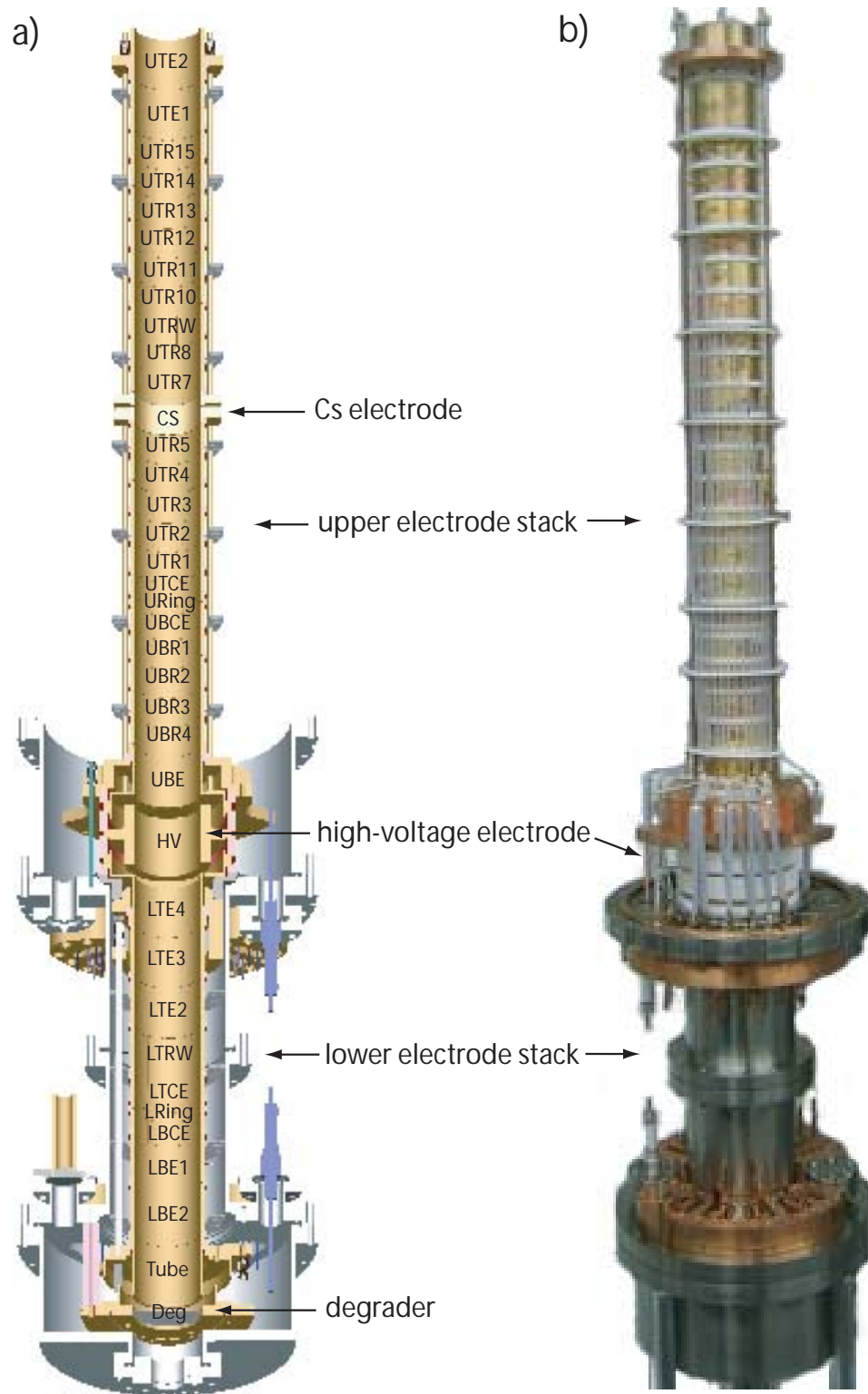


Figure 2.4: The A-TRAP Penning trap electrode stack (a) in cross-section, and (b) in reality. Each label in the cross section view indicates one independently-biased electrode.

by insulated macor spacers so that the electrodes can be independently biased to different potentials. Almost any of these electrodes can be used to confine particles within a single electrode volume, or more complicated potentials can be created within the Penning trap to perform a diverse array of experiments. The electrode stack in Fig. 2.4 can be divided into two main regions, the lower electrode stack, and the upper electrode stack. The lower electrode stack is primarily used for capturing antiprotons, which are initially confined between the high voltage potentials applied to the high-voltage electrode (HV) and the degrader (DEG) after arriving from the Antiproton Decelerator at CERN. The upper electrode stack is the region above the HV electrode, and is used both for the trapping positrons from the positron accumulator and for forming antihydrogen out of the accumulated positrons and antiprotons. This region can either be surrounded by the Ioffe trap, or simply by a vacuum enclosure.

The electrical connections for the electrodes are schematically depicted in Fig. 2.5 and Fig. 2.6. For most of the electrodes, there is both a DC bias voltage connection that passes through a RC filter immediately before reaching the electrode, and also a connection for high-frequency signals or voltage pulses, which are capacitively coupled to the electrodes after passing into the cryogenic Penning trap through stainless-steel micro-coaxial cables. Additionally, some of the electrodes are split into segments which have independent electrical connections so that axially-asymmetric signals can be transmitted or received.

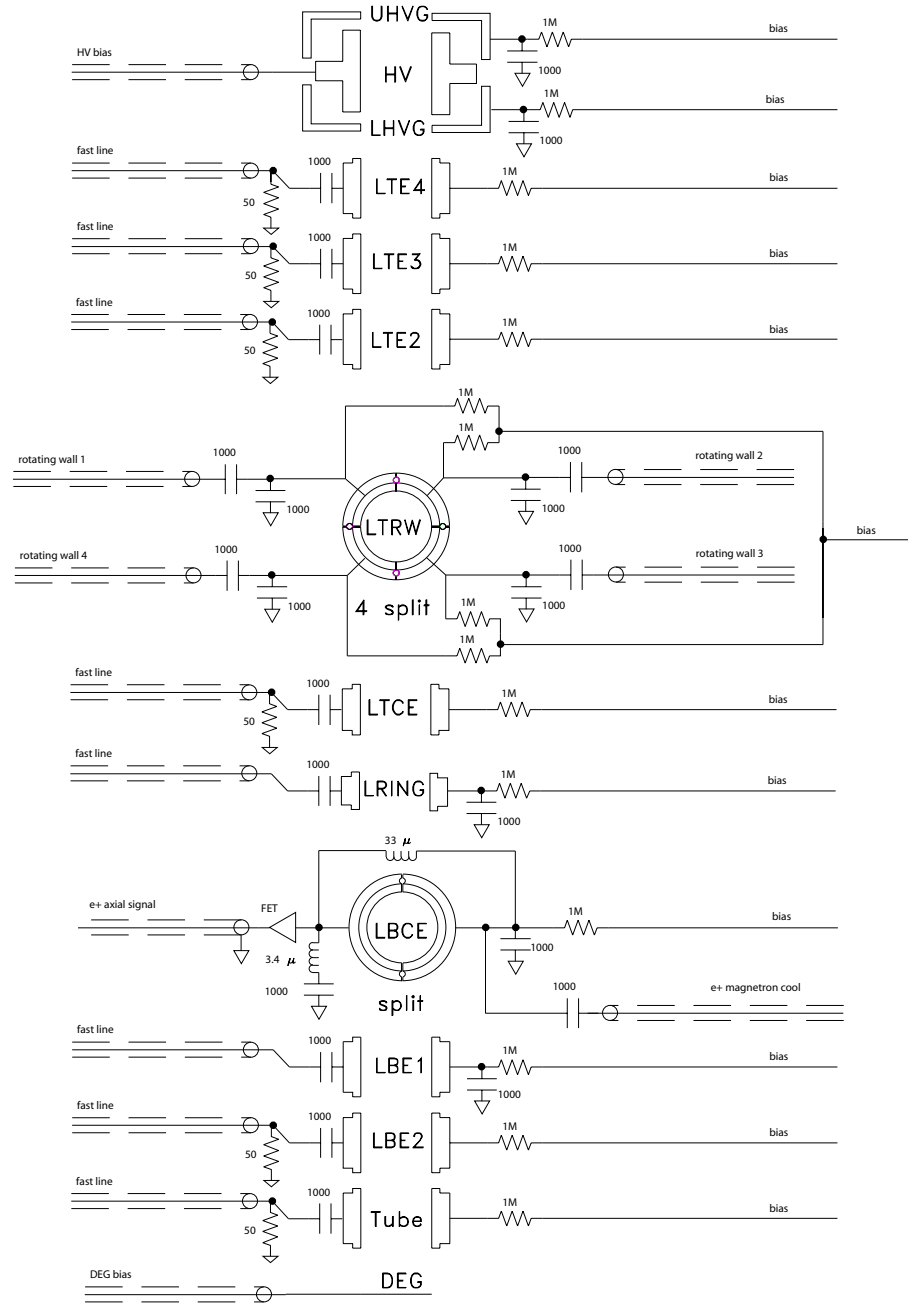


Figure 2.5: The lower A-TRAP electrode stack wiring diagram.

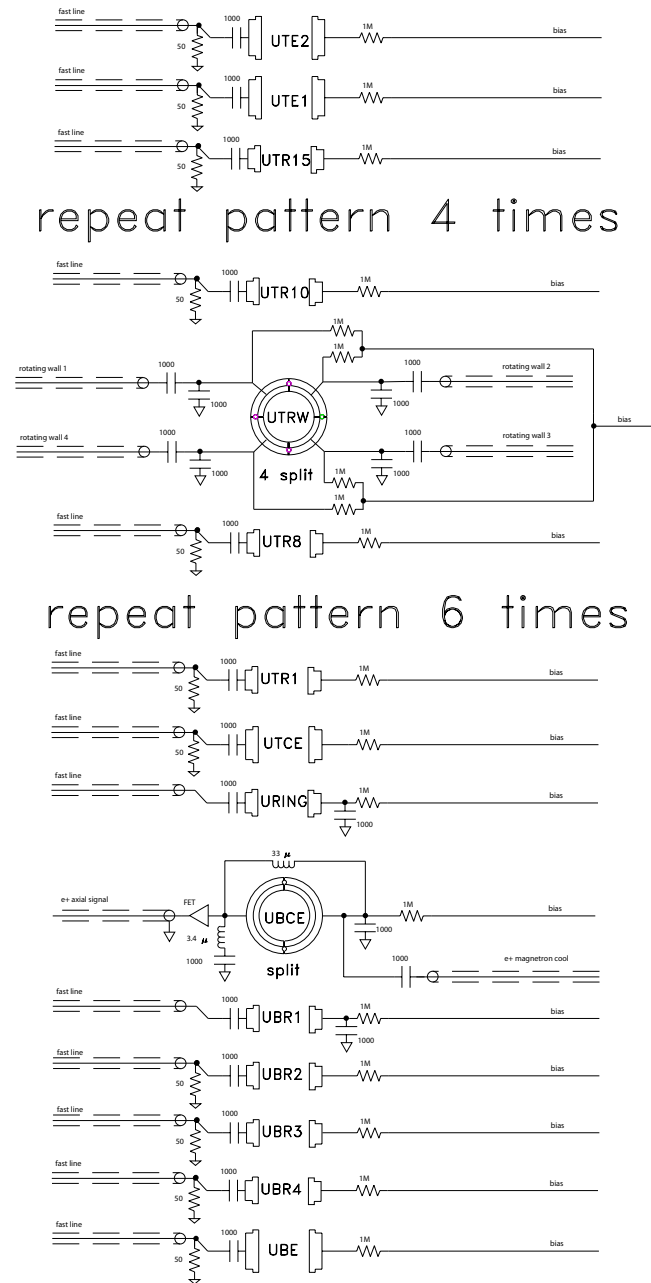


Figure 2.6: The upper A-TRAP electrode stack wiring diagram.

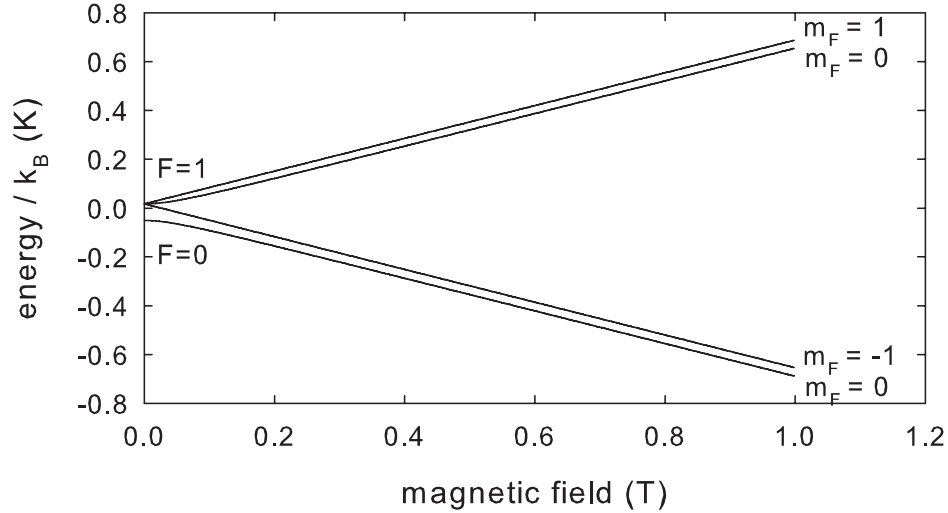


Figure 2.7: The Zeeman splitting of the ground states of an antihydrogen atom.

## 2.2 The Ioffe Trap

When antihydrogen is produced inside a Penning trap, the neutral atom is not confined within the trap, and will annihilate as soon as it comes in contact with the electrode walls. Even 4 K atoms produced in the center of the electrodes will typically drift to a wall and annihilate in approximately 100  $\mu\text{s}$ , which is far too short of a time to perform precise spectroscopy. As such, it will be necessary to magnetically confine the antihydrogen atoms produced before measuring their spectrum [4]. A Ioffe neutral atom trap was constructed to enclose the Penning trap electrode stack, forming a combined Penning-Ioffe trap that is capable of both producing and confining antihydrogen atoms.

An antihydrogen atom has an intrinsic magnetic moment,  $\mu$ , due to the spins of the positron and antiproton, and the orbital motion of the positron. The potential energy

of this magnetic moment within an external magnetic field is given by  $U = -\vec{\mu} \cdot \vec{B}$ . As the atom travels through a region of varying magnetic field, the magnetic moment adiabatically maintains its relative orientation to the magnetic field direction as long as the following condition is satisfied [58]:

$$\omega = \frac{\mu B}{\hbar} \gg \left| \frac{dB}{dt} \right| \frac{1}{B} \quad (2.10)$$

which is easily satisfied for atoms within our magnetic trap. This makes the potential energy of the atom just a function of the magnitude of the magnetic field, as in the example in Fig. 2.7 for the ground states of an antihydrogen atom. The magnetic moment will be either aligned or anti-aligned with the magnetic field, depending upon the quantum state of the atom. The aligned states will have a potential energy that decreases with magnetic field magnitude, and they are therefore attracted toward regions of high magnetic field. In contrast, the anti-aligned states will have a potential energy that increases with magnetic field magnitude, and are attracted toward regions of low magnetic field. Maxwell's equations forbid the existence of a magnetic field maximum in a static field configuration, but it is possible to create a field configuration that has a magnetic minimum. Such a minimum will create a confining potential for anti-aligned, low-field-seeking states.

It makes sense to define the depth of the magnetic-minimum confining potential in terms of the low-field-seeking ground states of the antihydrogen atom. Even if an excited antihydrogen atom is initially confined in the magnetic trap, within a short amount of time, it will have either decayed into a confined ground state or decayed into a high-field-seeking state and be lost. Within a large magnetic field, the potential energy of a confined antihydrogen atom in the ground state is  $U = \mu_B B$ , where  $\mu_B$  is

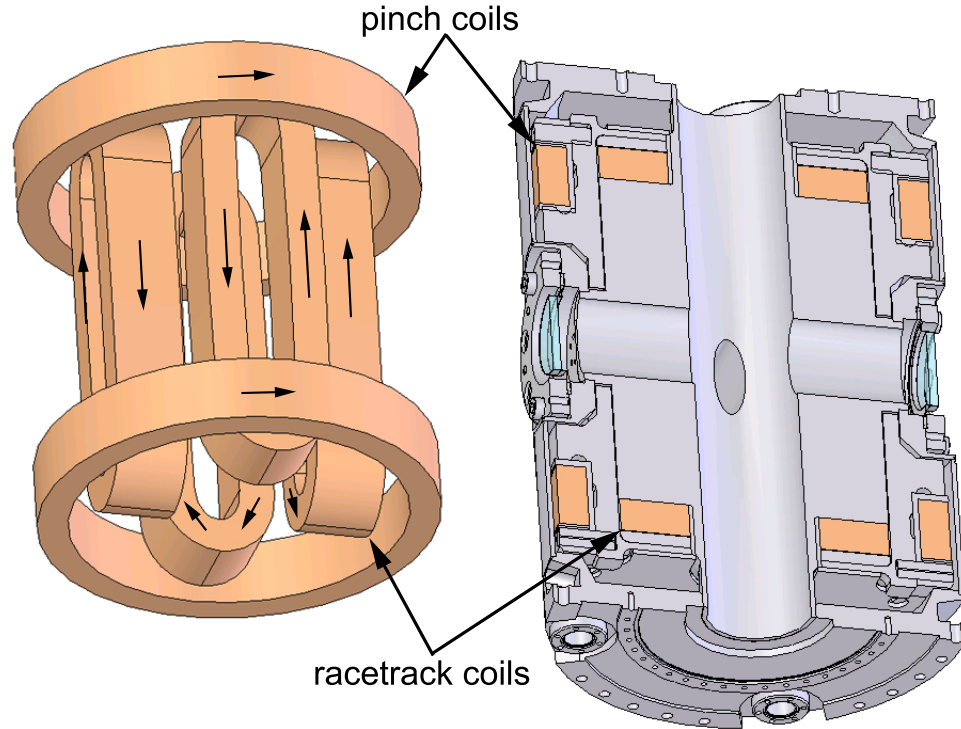


Figure 2.8: The ATRAP superconducting quadrupole Ioffe trap.

the Bohr magneton, and the magnetic moment due to the antiproton spin has been neglected since it is much smaller than the electron spin magnetic moment. The depth of the confining potential in units of temperature is then:

$$T = \frac{\mu_B \Delta B}{k_B} = (0.67 \text{ K/T}) \Delta B \quad (2.11)$$

where  $\Delta B = B_w - B_0$ ,  $B_w$  is the magnetic field magnitude at the wall of the trap, and  $B_0$  is the magnetic field minimum in the center of the trap.

A quadrupole Ioffe trap is the simplest magnetic trap design that is compatible with the axial magnetic field required for charged particle confinement in a Penning trap [59, 60]. The radial field of a quadrupole Ioffe trap has the form:

$$\vec{B} = \beta(x\hat{x} - y\hat{y}) \quad (2.12)$$

If we add this field to the bias field of the Penning trap,  $B_0\hat{z}$ , then the corresponding depth of the confining potential is.

$$T = (0.67 \text{ K/T}) \left( \sqrt{\beta^2 \rho_0^2 + B_0^2} - B_0 \right) \quad (2.13)$$

where  $\rho_0$  is the radius of the trap electrodes. The axial confinement in a Ioffe trap is produced by two current loops at either end of the confinement region (pinch coils), which both produce a magnetic field in the same direction as the Penning trap bias field.

Our superconducting quadrupole Ioffe trap is depicted in Fig. 2.8. It was designed and constructed in a cooperative effort between members of the ATRAP collaboration and staff from Forschungszentrum Jülich and ACCEL Instrument GmbH. Four racetrack coils with alternating current directions produce the radial field, and the axially-confining field is produced by the pinch coils surrounding the ends of the racetracks. The Ioffe trap is constructed from entirely non-magnetic materials. The vacuum enclosure and the majority of the interior parts are constructed from titanium. Multistrand NbTi wire is wound on titanium forms to produce the electromagnet coils, with tight-fitting titanium and aluminum parts to counteract the large repulsive forces on them. The upper electrode stack of the Penning trap (Fig. 2.4) fits within the central bore of the Ioffe trap. Four MgF<sub>2</sub> optical windows allow access for Lyman alpha light through the center of the racetrack coils onto the electrode stack for future laser-cooling and spectroscopy purposes.

The magnetic potential contours of the Ioffe trap field within the electrodes are depicted in Fig. 2.9. A current of 80 A in the pinch coils and 69 A in the racetrack coils produces a 375 mK axial and radial trap depth. This value takes into account

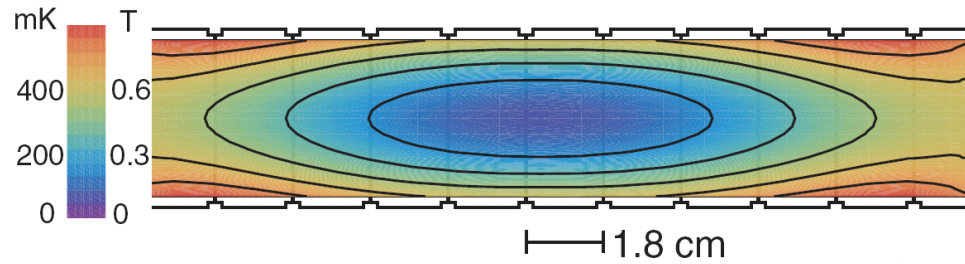


Figure 2.9: The magnetic potential contours of the Ioffe trap.

the fact that the field in the center of the trap is boosted from  $B_0 = 1\text{ T}$  to  $2.2\text{ T}$  by the current in the pinch coils. The total trap depth would be  $650\text{ mK}$  if the  $1\text{ T}$  axial bias field for the Penning trap were turned off, but it takes too long to turn off the magnet producing that field for it to be a practical option.

## 2.3 The Full Penning-Ioffe Trap Apparatus

The combined Penning-Ioffe trap requires a substantial amount of supporting apparatus. The axial magnetic field of the Penning trap is produced by an external superconducting solenoid. The Penning trap requires a vacuum enclosure, including a multitude of electrical connections passing through it to the electrode stack and access for loading particles into the trap. The Penning trap must be maintained at cryogenic temperatures to achieve the exceptional vacuum levels required for antimatter confinement, and to cool the confined particle motion to cryogenic temperatures. The superconducting Ioffe trap also needs to be supplied with cryogens and connected to a current supply. Laser access into the Penning-Ioffe trap will also be required for spectroscopy of trapped antihydrogen apparatus. To satisfy all of these requirements, a new experimental zone was established in the Antiproton Decelerator facility at

CERN, and a completely new experimental apparatus was built. This new experimental apparatus is depicted in Fig. 2.10.

### 2.3.1 The Superconducting Solenoid

The axial bias field for the Penning trap is produced by 2.2 m tall superconducting solenoid with a 20 inch room-temperature bore. The maximum field in the center of the solenoid is 3 T, but it is typically operated at 1 T because this increases the depth of the radial Ioffe trap confining potential. The field is constant to within 1% over the whole length of the Penning trap, and is homogenous to within one part in  $10^4$  along a 20 inch long region surrounding the Ioffe trap.

### 2.3.2 The Insert Dewar

If a cryogenic trap were placed directly within the solenoid, there would be a significant radiative heat load on it from the room-temperature bore of the solenoid. The heat load on the trap is minimized by placing it within a vacuum enclosure that sits inside the magnet bore and has two internal radiation shield layers that are cooled by cryorefrigerators. We refer to this apparatus as the “insert dewar,” which is shown in Fig. 2.11.

The insert dewar is composed of three layers: an outer room-temperature vacuum enclosure, a middle layer cooled to 60 K, and an inner layer cooled to 20 K. The cooling power is provided by both a Cryomech PT405 two-stage pulse tube and a Cryomech PT60 single-stage pulse tube. The primary cooling stages of the PT405 and PT60 are linked together by a copper block, and connected to the middle shield

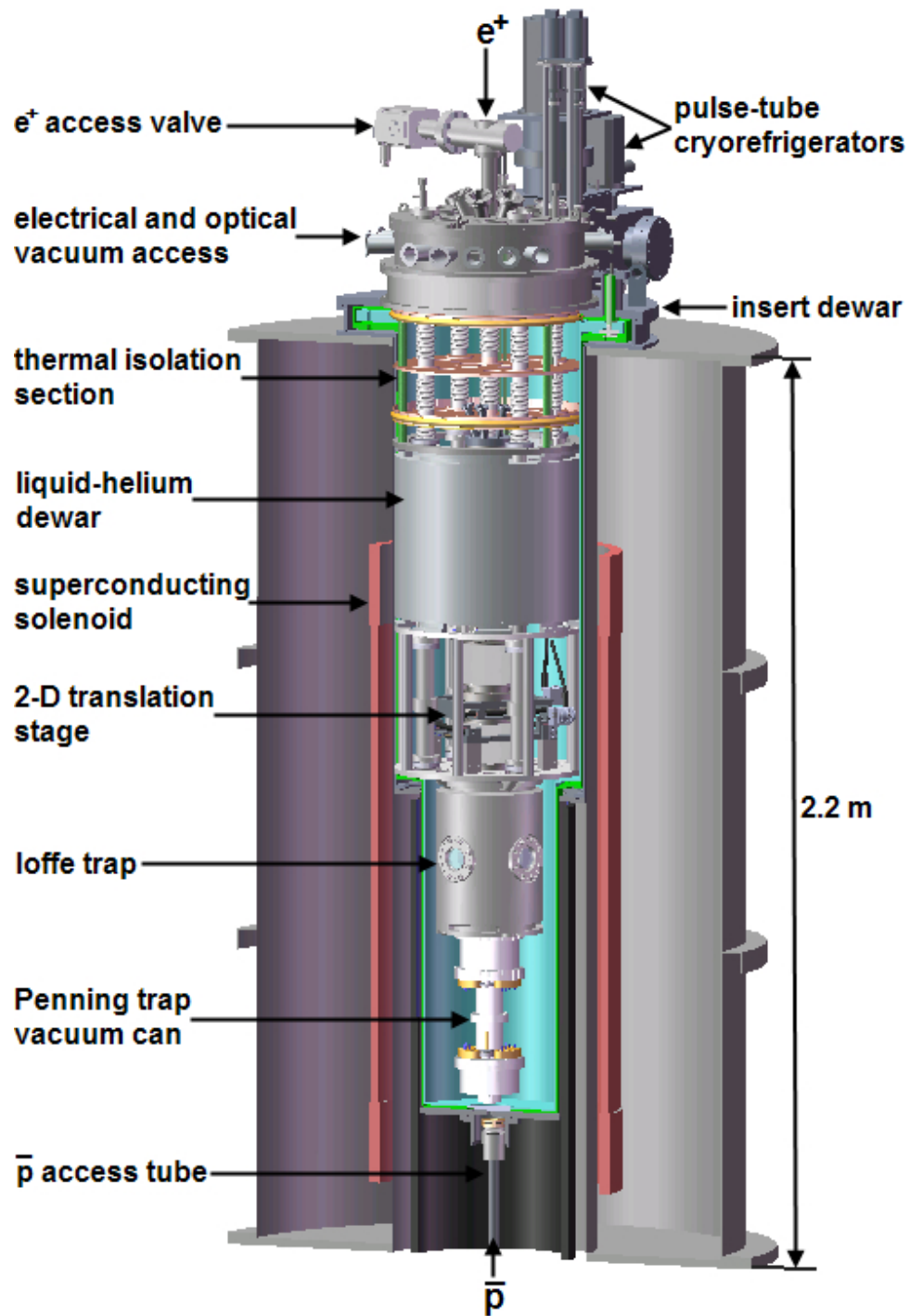


Figure 2.10: The full Penning-Ioffe trap experimental apparatus.

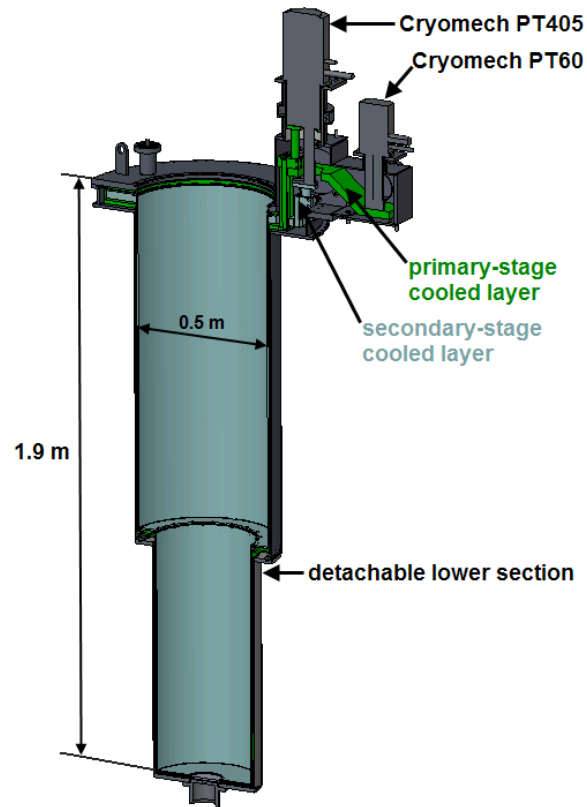


Figure 2.11: Cross section view of the insert dewar.

layer by a set of flexible copper cables that are brazed into copper anchor blocks. The secondary cooling stage of the PT405 is connected to the inner layer by similar copper cables. In each case, a good thermal connection is established by tightly clamping the components together with a small amount of copper-loaded vacuum grease between the joints. The outer vacuum layer is made from a nominally non-magnetic grade of stainless steel, while the inner two layers are constructed from 1100 series (pure) aluminum in order to maximize the thermal conductivity of the layer and minimize temperature gradients.

The insert dewar has a very narrow radial profile, in order to maximize the volume

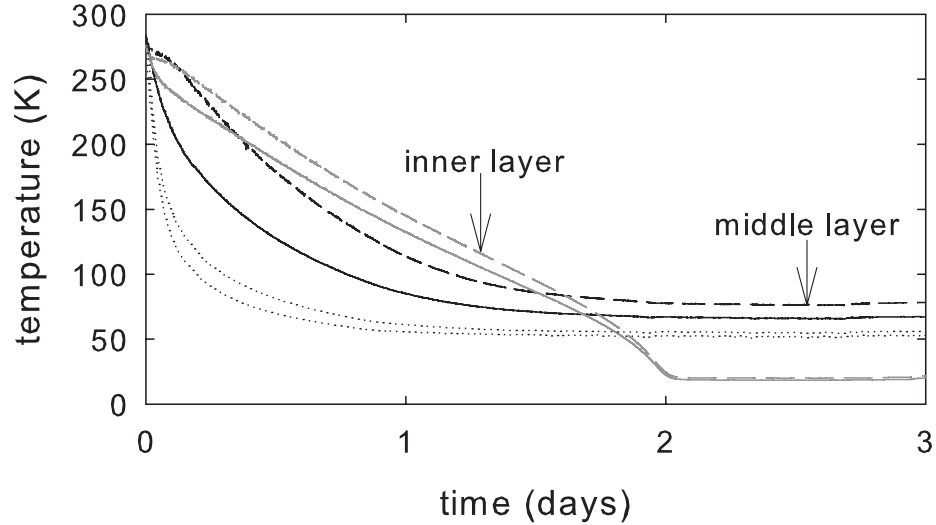


Figure 2.12: Temperatures within the insert dewar during a typical cool-down cycle. The temperatures on the layers indicated are shown for the top of the detachable section (dashed curves), the top of the upper section (solid curves), and at the pulse tubes (dotted curves).

available for the trap. It fits within the 20 inch bore of the solenoid, and has an inside diameter of 18.4 inches. Each of the layers has detachable lower sections that extend the internal length of the insert dewar to 1.9 m. These lower sections are detachable so that either a small-diameter or large-diameter set of extensions can be attached to the insert dewar. The small-diameter extensions are large enough to enclose the vacuum can of the Penning trap, but small enough that two additional sets of scintillating-fiber particle detectors can fit around the exterior of the insert dewar lower section. The large-diameter extension depicted in Fig. 2.10 and Fig. 2.11 is required to fit the Ioffe trap, and in this case, there is only enough room for one set of scintillating fibers around the exterior of the large lower extension. All of the extension layers are made of aluminum.

A number of steps were taken to thermally decouple the layers as much as possible. The middle layer is suspended from the top plate of the insert dewar by a G10 fiberglass tube, and the inner layer is separated from this layer by a second set of long-path-length fiberglass tubes in order to minimize direct thermal conduction between the layers. Each of the outward-facing surfaces of the two inner layers are covered by dozens of layers of highly-reflective aluminized-mylar “super insulation,” which minimizes the radiation heat load from the hot surface onto the cold surface. Additionally, the inner layer is wrapped with a spiral of thin dacron cord on the exterior of the super insulation. This guarantees that any contact between the two layers is through the low-conductance cord rather than a direct metal-on-metal touch.

Any gas within the insert dewar will create a thermal path between the layers. As such, the interior of the insert dewar is kept under high vacuum when it is in use. The entire insert dewar is evacuated through a 6" CF flange on the enclosure that houses the two pulse tubes. The large sections of the outer vacuum layer that are bolted together are sealed by o-rings. The top opening of the insert dewar can either be sealed by the top of the Penning-Ioffe trap apparatus or by a blank plate. The bottom of the insert dewar is sealed by a 10  $\mu\text{m}$  thick titanium foil that allows access for high-energy antiprotons. Because this thin foil is rather fragile to sudden shocks, the dewar is initially pumped down slowly from atmosphere to roughing pressures through an adjustable restriction.

The temperatures inside the insert dewar are constantly monitored by eight carbon-glass temperature sensors that are read out along with the trap temperature on a 16-channel Lakeshore 370 AC resistance bridge. The temperatures achieved during a

typical cool-down are shown in Fig. 2.12. The temperature of the middle layer ranged from 60-67 K, and the temperature of the inner layer ranged from 17-20 K during regular operation. The cool-down takes approximately two days due to the large heat capacity of the insert dewar.

Pulse tubes provide cooling power down to significantly lower temperatures than the ones observed. Although our operating temperatures are off of the cooling curves provided by Cryomech, we can extrapolate to estimate that the heat load on the middle layer of the insert dewar is several tens of Watts, and the heat load on the inner layer is on the order of ten Watts. This is likely in-part due to unexpected thermal contacts between the layers, which are separated by small distances. Over the 2 m length of the insert dewar, the inner layer is separated from the middle layer by only 1.5 mm, while the middle layer is separated from the outer layer by 4 mm. The cooling power of the pulse tubes overpowers these heat loads however, making the insert dewar moderately insensitive to significant heat loads. To measure the response to applied heat loads, we used small test heaters placed inside the insert dewar. The middle layer temperature increased about one K per applied Watt, while the inner layer temperature increased by about 2 K per Watt of power applied to the layer.

When the insert dewar was first received from the company that built it, it did not meet the desired specifications. It was originally designed to be cooled by just the PT405, but the PT60 was later added in series for additional cooling power. This did not entirely solve the problem though. After receiving the insert dewar, we took it apart and rebuilt it in the hopes of reducing its operating temperature. This

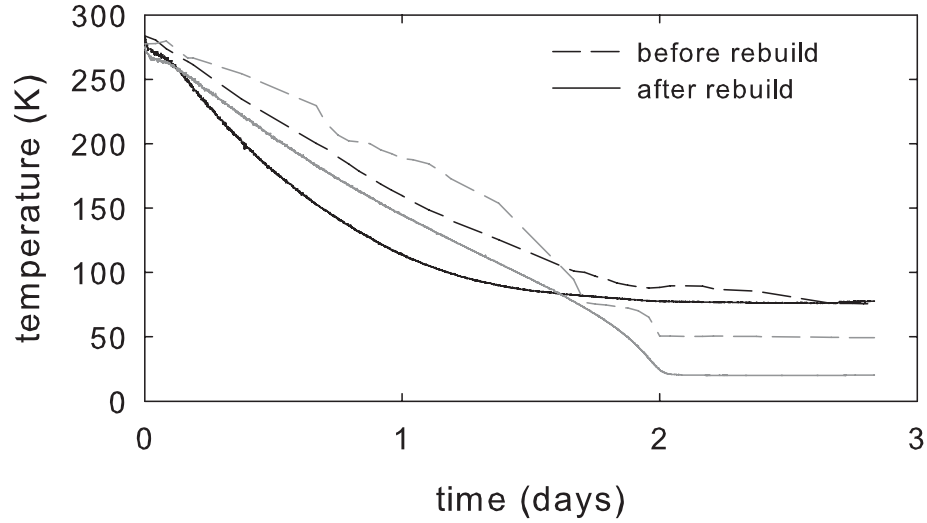


Figure 2.13: Comparison of the temperatures of the middle (black) and inner (gray) insert dewar layers, both before (dashed) and after (solid) a complete rebuild.

rebuild was successful, as seen in Fig. 2.13, which compares the temperatures achieved during a cool-down at the company with a cool-down after the rebuild. Before the rebuild, the lowest temperatures achieved were 74 K on the middle layer and 47 K on the inner layer. Immediately after the rebuild, the corresponding temperatures were 77 K and 20 K, but replenishing the helium gas in the compressors that run the pulse tubes further reduced these temperatures to 62 K and 17 K at a later date. The temperature of the inner layer is the most important, since it determines the heat load on the Penning-Ioffe trap. From the Stefan-Boltzmann law for the power radiated from a blackbody,  $P = A\epsilon\sigma T^4$ , the radiative heat load on the trap after the rebuild was reduced by a factor of nearly 60, making it much less significant than the direct conductive heat loads on the trap. There were a couple of clear changes made during the rebuild. Super insulation was added to the inner layer as

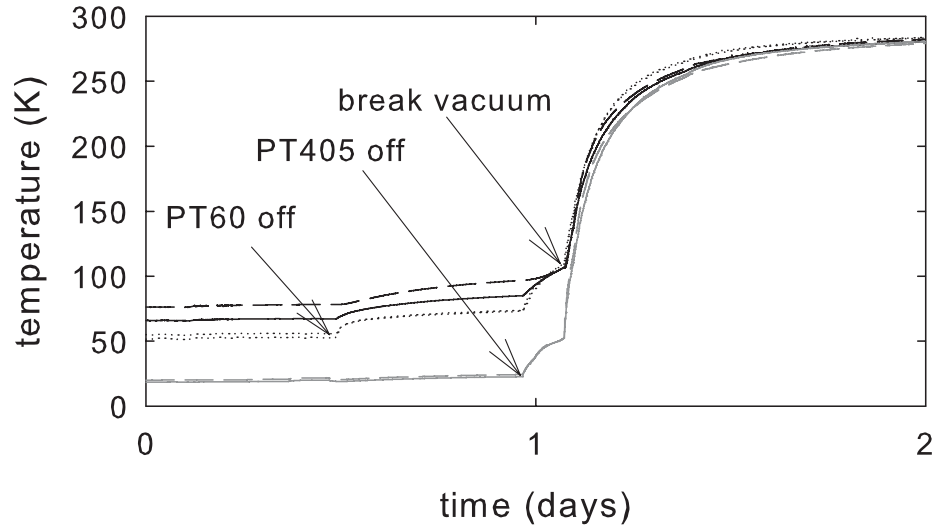


Figure 2.14: The temperatures in the insert dewar during the warm-up process.

well as the dacron cord, while this layer initially had the cord but no super insulation. Additionally, the temperature sensors were better heat-sunk to the dewar to ensure that the temperature measurements were accurate. It is also possible that some potential touches between the layers were avoided when the dewar was reassembled.

When the pulse tubes are turned off, it takes roughly four days for the insert dewar to warm up to room temperature due to the good insulation and large heat capacity of the cold layers. The heaters on the insert dewar can not apply enough power to significantly speed up this process. The most effective way of warming up the insert dewar is to slightly break the vacuum in the insert dewar. Dry nitrogen gas is used to avoid water condensation within the insert dewar. It is important to avoid adding too much gas, since this can lead to a large amount of condensation and ice accumulating on the outer vacuum layer, which can in turn freeze the o-rings

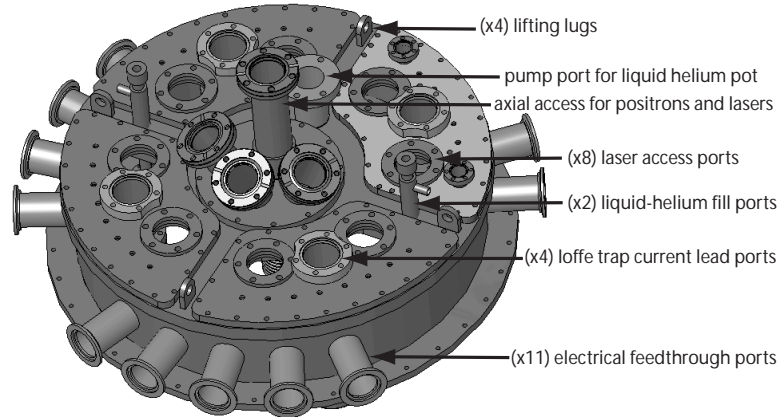


Figure 2.15: The A-TRAP vacuum hat.

and cause vacuum leaks as well. The insert dewar warm-up process is depicted in Fig. 2.14. It typically takes a full day to warm up and vent the insert dewar. The plot in Fig. 2.14 also demonstrates that the PT60 reduces the equilibrium temperature of the middle layer, but turning this pulse tube off does not have a dramatic impact on the temperature of the inner layer.

### 2.3.3 The A-TRAP Vacuum Hat

The top of the insert dewar vacuum space is sealed by the top of the A-TRAP Penning-Ioffe trap apparatus. We refer to this stainless-steel upper portion of the vacuum chamber as the “hat,” which is shown in Fig. 2.15. The entire weight of the apparatus is suspended below the hat using G10 fiberglass tubes, and the apparatus can be picked up and transported on a crane using the lifting lugs on the top of the hat. The hat has a multitude of vacuum flanges, which allow access into the insert dewar vacuum space for electrical connections, laser access, and motion feedthroughs. It also allows access into the helium vacuum space for cryogenic liquids and

the detachable current leads that connect to the superconducting Ioffe trap. Finally, it allows access into the trap vacuum space for positrons coming from the external positron accumulator. The top of the hat has four quadrant plates and a central plate that are sealed with o-rings. If desired, these plates can be removed and replaced by plates with different configurations of vacuum flanges welded into them, allowing for a great deal of flexibility in the design for future unforeseen experiments.

### 2.3.4 The A-TRAP Cryogenic and Thermal Isolation System

The Penning-Ioffe trap is cooled and maintained at cryogenic temperatures using a reservoir of liquid helium, which has a temperature of 4.2 K. It takes only 2.6 kJ of energy to vaporize a liter of liquid helium, so modest heat loads can rapidly cause the helium reservoir to boil away. Liquid helium is very expensive, and time consuming to transport and transfer from one vessel to another, so it is very desirable to minimize the heat load on the liquid helium reservoir, and consequently minimize the amount of liquid helium used to keep the trap cold. To do this, we use the thermal isolation system depicted in Fig. 2.16.

There are three 0.25" thick copper baffle plates between the 4 K helium dewar from the room-temperature vacuum hat. The top of each plate is covered by aluminized-mylar super insulation to minimize the thermal radiation load from the layer above. Each plate is separated from the layer above and below it by three G10 fiberglass-epoxy tubes, which also support the entire weight of the trap. These G10 tubes are strong, but have a very low thermal conductivity. The helium dewar itself is constructed from aluminum. The vacuum connections into the helium space are

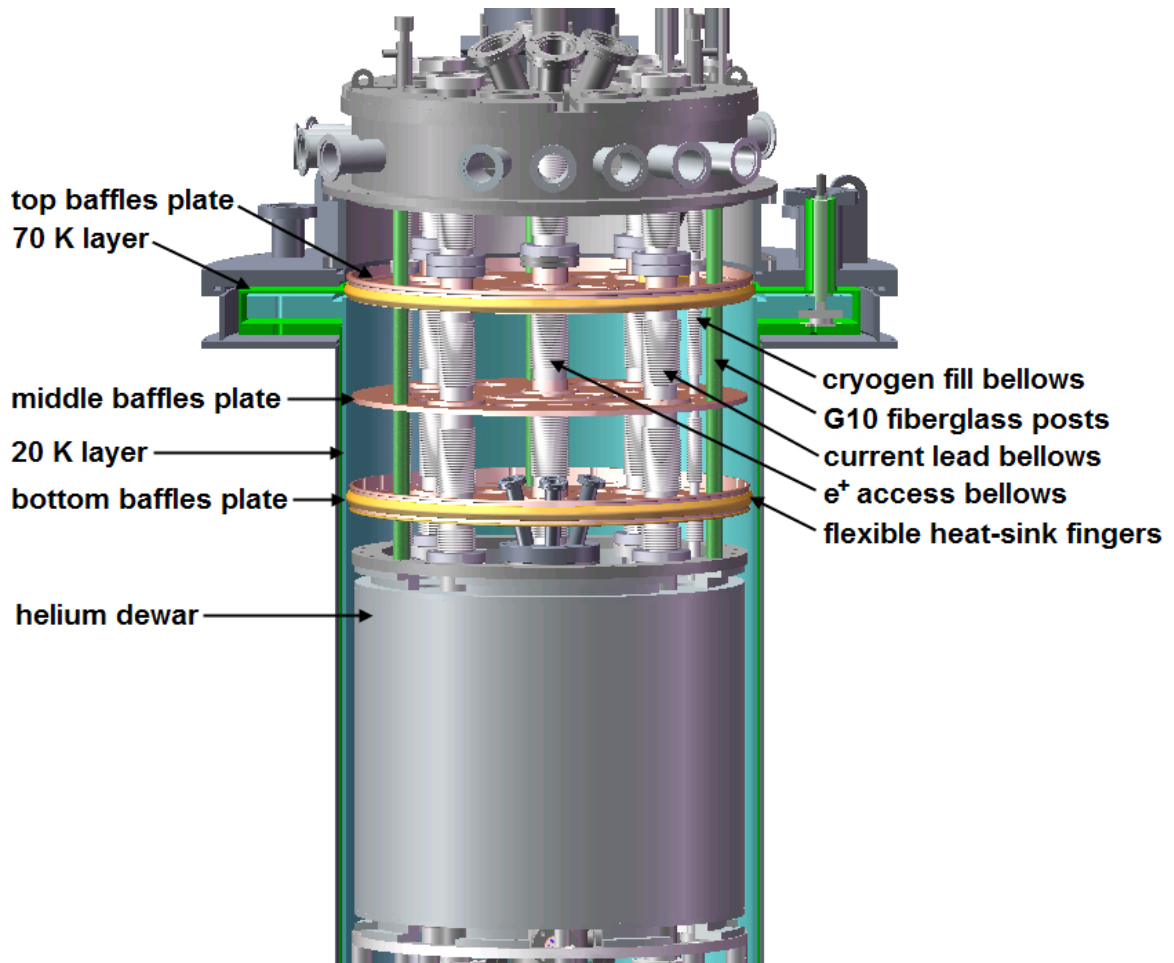


Figure 2.16: The A-TRAP cryogenic and thermal isolation system.

provided by explosively-bonded bimetallic conflat flanges that are welded into the dewar. The bottom half of these flanges are made from aluminum, while the top half is formed from either stainless-steel or titanium, depending upon whether it is welded onto the top of bottom of the dewar respectively. Electrical and laser access from the hat down to the Penning-Ioffe trap is provided by holes through the thermal isolation plates and tubes through the helium dewar that correspond to the flange locations on the top of the hat.

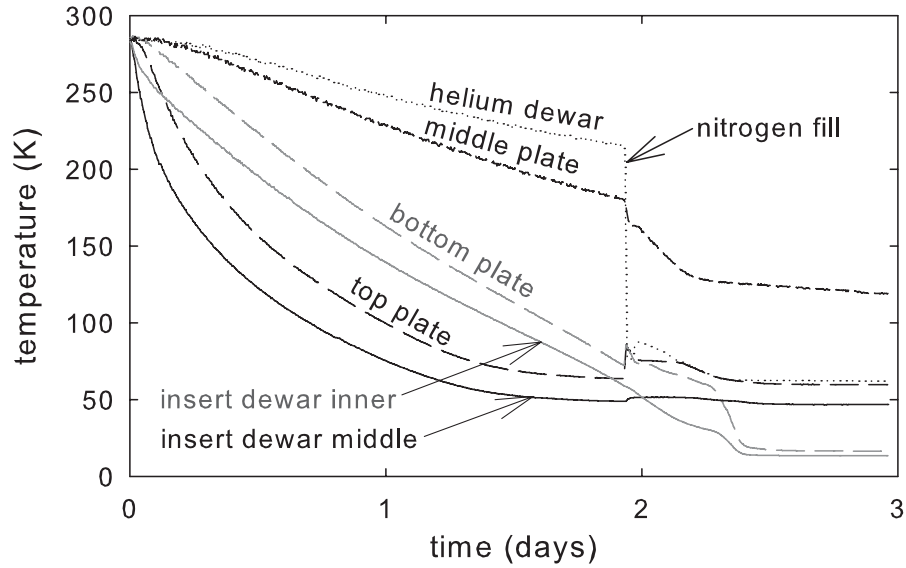


Figure 2.17: The temperature of the thermal isolation baffles and helium dewar (dashed curves indicated) as the insert dewar is cooled. This demonstrates the coupling of the top baffle plate to the insert dewar middle layer (solid black curve) and the bottom plate to the insert dewar inner layer (solid gray curve).

Thin-walled stainless-steel bellows link the exterior of the insert dewar vacuum space to the helium space and with the trap vacuum space for positron access. Stainless-steel has a very low thermal conductivity at cryogenic temperatures compared to other metals. At the location of each plate, the bellows are brazed to a copper flange that is bolted to the corresponding plate, thermally anchoring the bellows to plates at these locations. The top plate is thermally connected to the middle layer of the insert dewar by flexible beryllium copper contact fingers, and is therefore cooled by the insert dewar pulse tubes. The bottom plate is similarly anchored to the inner layer of the insert dewar, while the middle layer has a floating temperature. The heat load on the helium dewar from above is therefore set by the temperature of the bottom baffle plate, and the corresponding heat conducted through the G10

tubes and the thin-walled stainless-steel bellows. The sound thermal connection between the top and bottom baffle plates and their corresponding insert dewar layers is demonstrated by Fig. 2.17. In contrast, the helium dewar and middle baffle plate are only weakly coupled to the insert dewar temperature as it cools down, as desired.

### **The Liquid Helium Hold Time**

The helium dewar holds 44 liters of liquid helium. Under optimal conditions, this helium needs to be refilled once every six days in order to keep the trap cold (0.3 l/h boil-off rate). The helium hold-time is a practical measure of how usable the apparatus is, but it also allows us to estimate and diagnose the total heat load on the dewar. A heat load of 1.3 W would boil away all of the helium within a day. The longest hold time is achieved if the thermal isolation baffles and helium dewar are placed in the insert dewar with no trap below them, and with only the two cryogen fill bellows and three G10 support tubes connected to the helium dewar. In this case, the measured hold time was 28 days, which is on the scale of what one might predict from the known heat loads. The total heat load on the helium dewar is increased from this baseline value when the entire apparatus is in use however. Four additional 1.5" ID bellows are required for current lead access for the Ioffe trap and positron access to the Penning trap, and the electrical connections within the Penning trap require approximately 50 coaxial connections and roughly twice as many wire connections. To minimize the heat load on the trap, stainless-steel micro-coax lines (Microstock UT-20-SS) and constantan wires with a 0.003" conductor diameter are used for the electrical connections. The reduced helium hold time is 6 days, corresponding to a

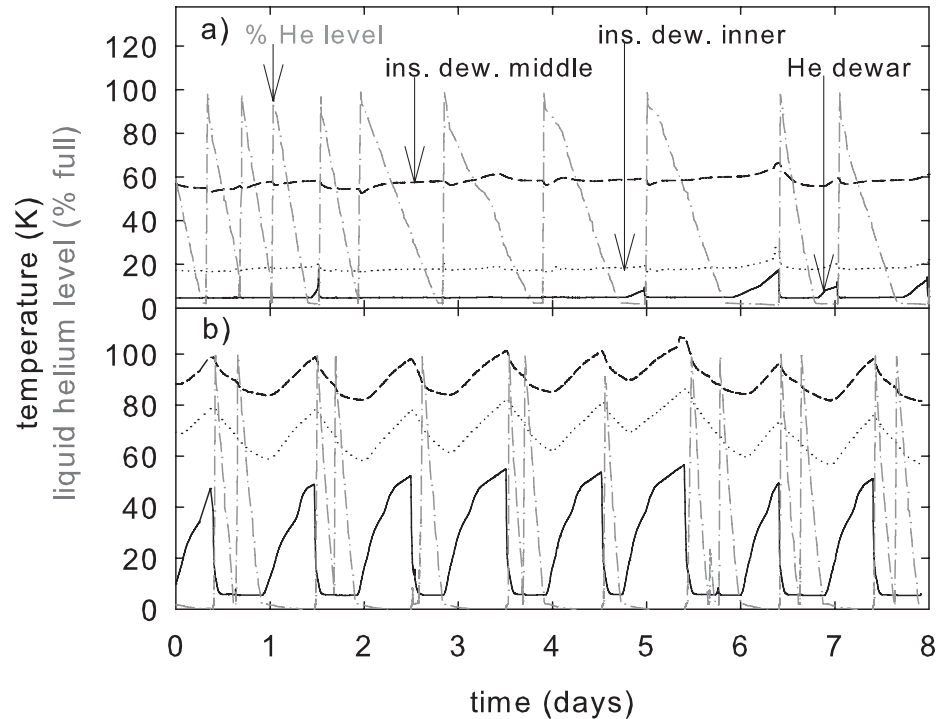


Figure 2.18: Operation of the Penning-Ioffe trap under adverse conditions, (a) when there was a liquid helium leak into the insert dewar vacuum space, and (b) when the PT405 pulse tube stopped working in addition to the liquid helium leak. The plot depicts the liquid helium level (dash-dot), as well as the temperatures of the helium dewar (solid), the insert dewar inner layer (dotted), and the insert dewar middle layer (dashed).

200 mW heat load. When the Ioffe trap is in regular use however, which requires lowering the retractable 100 A current leads into the helium space, then this further decreases the helium hold time.

The Penning-Ioffe trap was operated for several weeks under extremely adverse conditions, when the helium hold time dropped as low as just a few hours. This happened when a leak opened up on the Ioffe trap, leaking liquid helium directly into the insert dewar vacuum space. The leak not only caused a direct loss of helium,

but also raised the pressure within the insert dewar, causing thermal shorts which in turn increased the helium boil-off rate (Fig. 2.18a). Before this problem was fixed, the two-stage PT405 pulse tube stopped working as well (Fig. 2.18b). Although this dramatically decreased the helium hold time, we were still able to continue working with the Penning-Ioffe trap during the antiproton beam run at CERN. Both the helium leak and the PT405 were later fixed.

### 2.3.5 Thermal Cycling of the Penning-Ioffe Trap

Experiments can only be performed while the trap is at cryogenic temperatures. When the trap needs to be repaired or modified, the trap must be warmed up, removed from the insert dewar, repaired, put back, and cooled back down again. Since we usually receive antiproton beam at CERN on a daily basis, this can cause loss of valuable time for experiments. Although we have two Penning traps, so that we can continue performing experiments when lengthy repairs are required on one of them, the warm-up and cool-down times continue to be fundamental limitations. As such, the trap warm-up and cool-down procedures have been streamlined as much as possible.

Cooling a Penning trap typically involves first cooling the trap to 77 K with liquid nitrogen, since liquid nitrogen is cheaper and has a much larger cooling capacity per liter than liquid helium. Once this step is done, the liquid nitrogen must be removed before filling the dewar with liquid helium. This can be done by extending a tube down to the bottom of the dewar and pressurizing the dewar from the top with nitrogen gas, which forces the liquid up the tube and out of the dewar. The dewar can then be

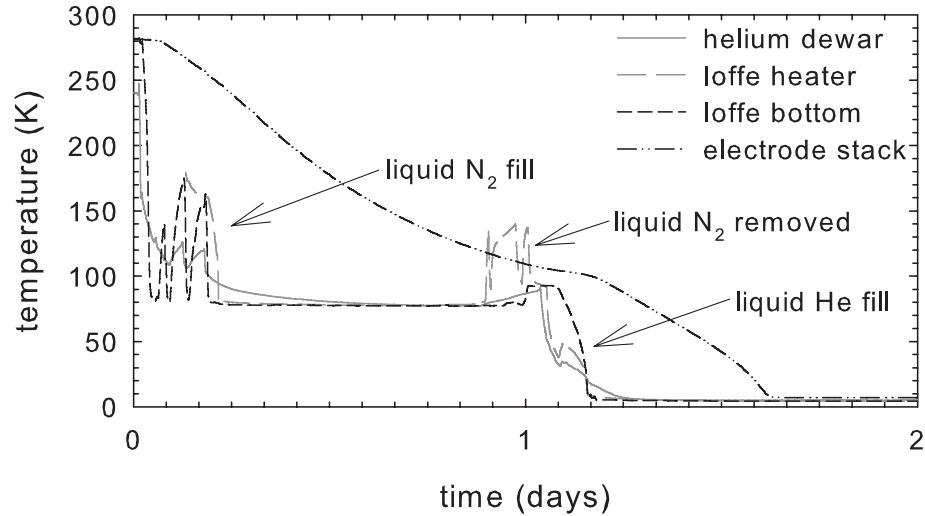


Figure 2.19: The typical cool-down procedure for the Penning-Ioffe trap.

depressurized and filled with liquid helium. Throughout this process, the Penning trap is cooled by thermal conduction between the electrode stack and the cryogen reservoir. The cooling of the electrode stack is often the limiting factor, since the electrodes are stood off from the metal parts of the trap by electrically insulating materials, which are typically also poor thermal conductors. For the apparatus that is only a Penning trap, the heat must also be conducted through the titanium vacuum enclosure that takes the place of the Ioffe trap (Section 2.3.7). Titanium is a moderately poor thermal conductor. Even at cryogenic temperatures, it takes about ten times longer for heat to propagate through titanium than it does for aluminum or copper, the other non-magnetic metals used in this region. The cool-down time for the Penning trap apparatus was initially 4 days, but was reduced to 2 days by thermally bridging the titanium vacuum can by clamping thick copper straps across it.

The Ioffe trap fills with liquid helium through a direct connection to the bottom

of the helium dewar. This brings the helium reservoir closer to the Penning trap electrode stack in the combined Penning-Ioffe trap. It also introduces a significant difference to the cooling procedure. After pre-cooling with liquid nitrogen, the Ioffe trap will also be filled with liquid nitrogen. Although the nitrogen in the dewar can be removed using the previous procedure, there is no direct path for a tube to the bottom of the Ioffe trap. To deal with this problem, a heater system was developed for boiling away the last amount of liquid nitrogen inside the Ioffe trap before filling it with liquid helium. Thin kapton-insulated flexible heaters were wrapped around the Ioffe trap and helium dewar, thermally anchored with a thin layer of vacuum grease, and secured with tight wraps of kapton tape. The 7 A current required to operate the heaters at full power are supplied by four simple retractable current leads that connect via a mini-banana jack/plug interface on the top of the helium dewar. The leads are not normally connected, since the copper wire carrying the current would be a significant heat load on the helium dewar. The heaters in either location can supply over 1 kW of heat with an area density of up to 5-10 W/in<sup>2</sup>, but they are typically operated at much lower powers by selecting the input voltage using a variable AC transformer. Cooling down the Penning-Ioffe trap typically takes a day and a half, as in Fig. 2.19.

The warm up procedure in either case involves boiling off the liquid helium, turning of the insert dewar, and introducing a small amount of dry nitrogen gas into the insert dewar vacuum space. As with the procedure for warming up the insert dewar, this causes a thermal short between the trap and the various layers of the insert dewar, including the room-temperature outer vacuum layer. Using just this procedure, the

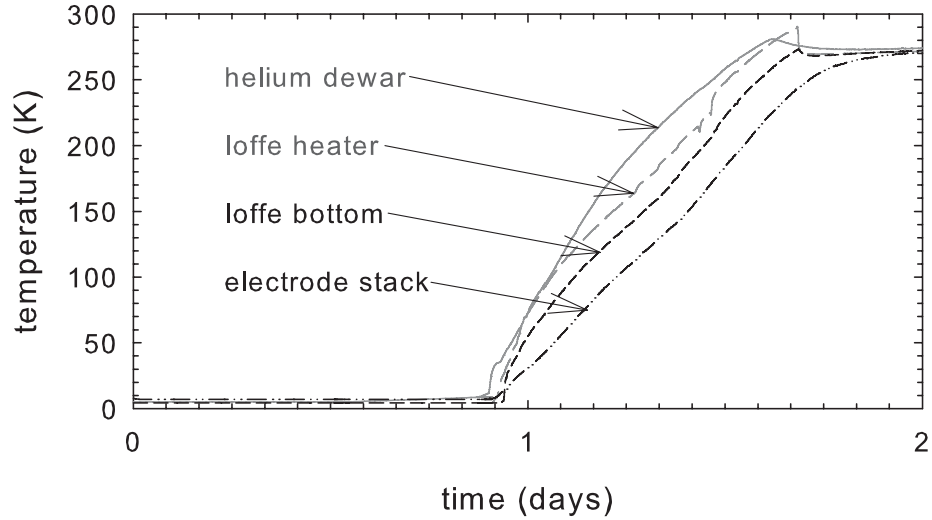


Figure 2.20: The Penning-Ioffe trap warm-up procedure using heaters.

trap can be warmed up in 2 days. The warm-up time can be reduced to one day if the heaters are used, as in Fig. 2.20.

In summary, the trap can be cooled down in as little as 1.5 days and warmed up in as little as 1 day using a heater system. This makes the theoretical minimum time required to swap our two traps about 3 days, which is still a significant sacrifice when we are taking antiproton beam. A serious limitation to the cooling and warming time is that the electrode stack is somewhat thermally insulated from the helium reservoir. The measured electrode stack temperature was often around 7 K, higher than the 4.2 K liquid helium temperature. This was due to the heat load from the micro-coax cables connected to the electrodes, and the problem was later alleviated by better heat sinking of the micro-coax to the helium dewar.

### 2.3.6 The Cryogenic, Two-Dimensional Translation Stage

Access into the electrode stack from outside the trap vacuum space is crucial for antihydrogen experiments. High-energy antiprotons have access into the Penning trap by passing through a series of thin titanium vacuum windows that are located below the electrode stack. Access from above the electrode stack is required for positrons, electrons, and laser light, each of which have their own particular requirements. Positron access requires having a small tube on-axis with the electrode stack (Section 4.2.2), electron loading optimally requires having a gold-plated optical window on-axis (Section 4.1.2), and laser access for antihydrogen cooling and spectroscopy requires placing a large-aperture optical window on-axis. Additionally, placing faraday cups or a phosphor screen above the electrode stack would allow plasma profile measuring capabilities. To meet all of these conflicting requirements, a two-dimensional translation stage was designed and constructed that can move various access windows on-axis with the electrode stack (Fig. 2.21). This “X-Y stage” operates at liquid-helium temperature, within the insert dewar vacuum space.

The X-Y stage sits in the region between the helium dewar and the Ioffe trap (Fig. 2.10). As it translates, it moves a 6" OD conflat flange that sits 5 inches above the top of the electrode stack. This double-sided titanium conflat flange separates the cryogenic Penning trap vacuum space from the positron-transfer vacuum space above it, and is connected to titanium edge-welded bellows on either side. The flange has five different vacuum window locations on it: a central 1-1/3" OD conflat flange, two 2-1/8" OD conflat flanges, and two indium-sealed flanges. By translating the position of the large flange in the horizontal plane, any one of these window locations

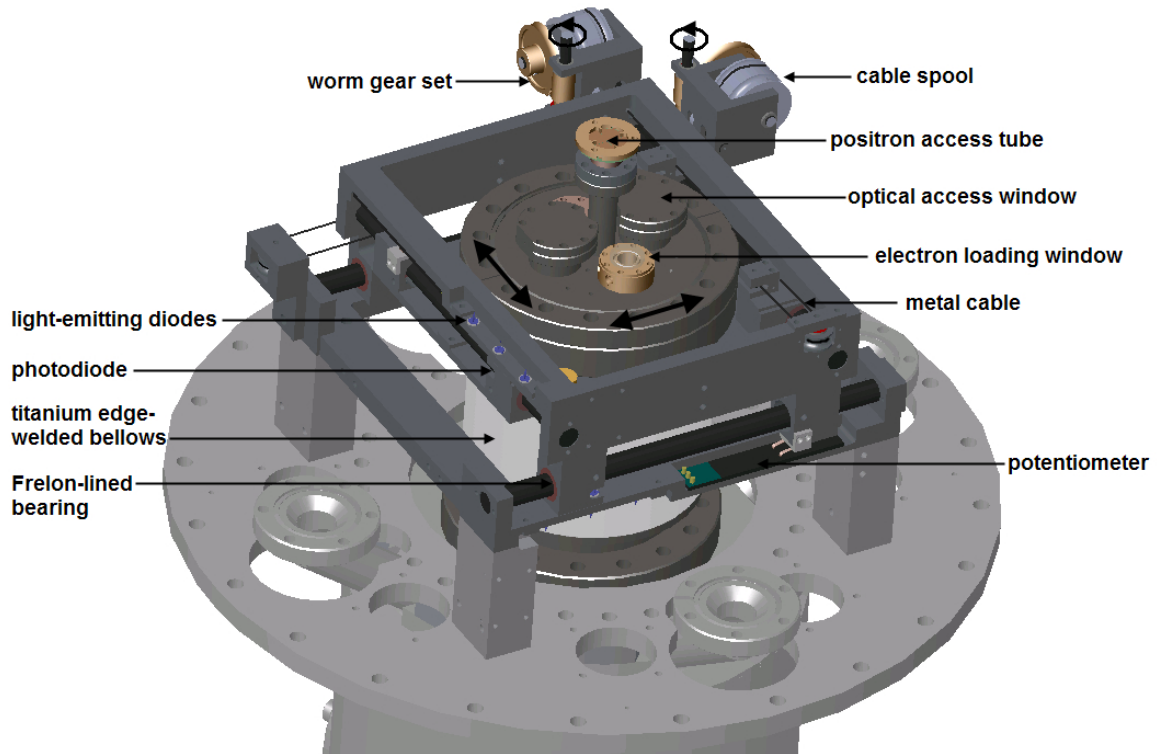


Figure 2.21: The cryogenic, two-dimensional translation stage is used to line up a variety of different objects with the central axis of the Penning trap, allowing a diverse range of particle loading, laser access, and diagnostic capabilities.

can be centered over the Penning trap symmetry axis. The total travel range of the X-Y stage is  $\pm 1.15''$  along the x-axis and  $\pm 1.26''$  along the y-axis.

### X-Y Stage Design Issues

The cryogenic vacuum environment posed some serious challenges in the design of the X-Y stage. Most commercial mechanical devices will cease up at cryogenic temperatures. This is in part due to differential thermal contraction of the materials, which can disrupt mechanical function if parts must fit together within tight tolerances. Liquid lubricants that are often used at room temperature stop functioning

because they freeze, and they are not compatible with a vacuum environment in any case. For each of the two axes of travel, the X-Y stage motion is guided by Frelon-lined aluminum bearings that slide along ceramic-coated aluminum shafts to either side of the edge-welded bellows. Frelon is a compound of Teflon, which maintains its intrinsic lubricating properties at cryogenic temperatures, allowing for equally smooth travel at cryogenic temperatures as at room temperature. For the stage to move properly, the distance between the bearings must match the distance between the two shafts. As such, differential thermal contraction must be avoided between the parts housing the bearings and the parts setting the shaft separation. This problem is minimized by forming the X-Y stage body entirely out of aluminum so that there are no material contraction mismatches, by using large solid pieces rather than bolting together a collection of small parts in order to minimize shifts in the part locations during cooling, and by heat-sinking each section of the X-Y stage together using flexible copper cables in order to avoid temperature gradients.

The initial design of the X-Y stage did not function properly at cryogenic temperatures, and some valuable lessons can be learned from the experience. The first lesson was that the difficulty of moving the stage scaled very strongly with the number of parallel shafts required to guide the motion. Sliding along a single shaft is very easy because the bearing is self-centering on the shaft. Sliding along two shafts is somewhat difficult because of the distance-matching problem just described. Sliding along three shafts is quite difficult in practice because it adds another dimension that must also be precisely matched. In the original X-Y stage design, the motion was driven by a nut that was threaded along a rotating lead screw, effectively adding a third

shaft to the system. The original design also involved bolting together a collection of small parts, which always fit together slightly differently each time that it was assembled. The location of the parts could be adjusted slightly so that the stage moved smoothly at room temperature, but the precise alignment was not maintained as the trap cooled down, causing the stage to not move properly. Another lesson learned from the experience was that friction in the stage motion at room temperature always gets worse as the stage cools down.

The final design for the X-Y stage avoids using the lead screw in favor of using cables to pull the stage back and forth. The first attempt at this design involved stringing the cables all the way up to the hat and pulling on them there. The cable paths were guided using homemade Bowden cables, commonly used as bicycle brake cables. This did not allow the XY stage to travel over its full range of motion because there was an unexpectedly large amount of friction in the system, and it was also difficult to maintain a constant path length between the hat and the X-Y stage. Metal cables were used instead of string because they were much less stretchy. The final X-Y stage design bypassed this problem by transmitting torque down to the X-Y stage and converting this torque into tension in the cables using gearboxes directly attached to the X-Y stage (Fig. 2.21). The stage is moved along a particular axis by rotating the shaft on the top of the gearbox, with the direction of the rotation determining the direction of the corresponding motion. This shaft couples into a worm drive system that amplifies the input torque by a factor of 50. The worm gear is coupled to a spool that the metal cable progressively winds around or unwinds from. To move the stage in either direction, two cables are connected to the spool

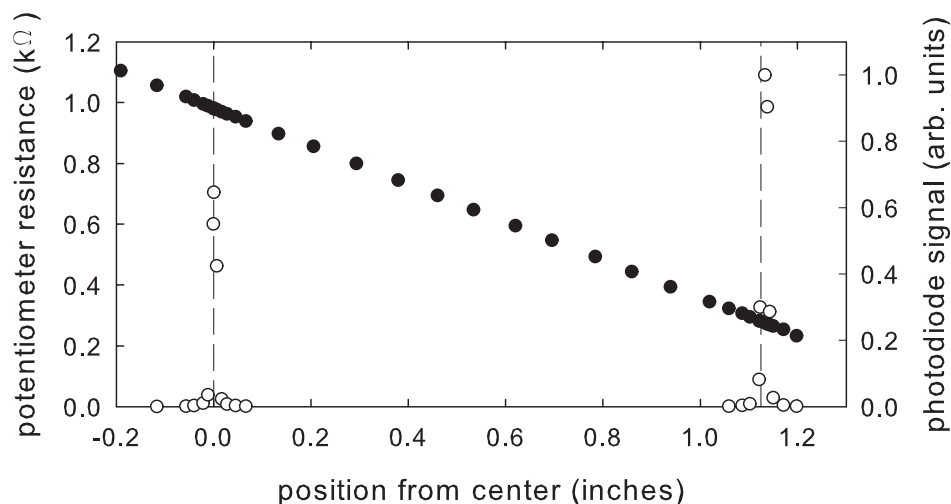


Figure 2.22: An example of the potentiometer resistance (solid points) and photodiode response (open points) measurements used to determine the position of the X-Y stage as it travels between two window locations. The vertical lines indicated the known window positions. The photodiode response is for a 1 mA current through the LEDs.

in opposite winding directions, and both of them are constantly under tension. One cable connects directly to the corresponding movable section of the stage, while the other is passed around a pulley before pulling on the stage from the opposite direction. One rotation of the gearbox shaft corresponds to a 2 mm translation of the stage.

The torque driving the X-Y stage is provided from above the hat through a rotational vacuum feedthrough. The output shaft connects to a telescoping double universal joint that couples into a thin-walled G10 tube that passes through the thermal isolation plates to the bottom of the helium dewar. A second set of telescoping double universal joints then couple these shafts to the shafts on the top of the gearboxes.

## Determining the Position of the X-Y Stage

The position of the X-Y stage is determined using two distinct methods for each axis of motion. One photodiode (Hamamatsu S2386-18K) is mounted into each of the two moving section of the stage, with a 0.014" diameter pinhole in front of it. As the section moves, the photodiode pinhole passes by three pinholes of the same diameter, each one of which marks the center position of one of the windows on the central vacuum flange, and each has a transmitting LED (Opto Diode Corp. OD-880W) behind it. The light from the LED is picked up on the photodiode, and by measuring the signal on the photodiode as a function of position, the location of the three windows along that axis can be identified. These particular photodiodes and LEDs were chosen because they were known to perform well at 4 K [61]. The second method for determining the position of the X-Y stage is to measure the resistance of a linear potentiometer. The potentiometer is formed from a pair of conductive plastic strips (taken from an ETI Systems LCPL200-5K potentiometer), and the metal brush connecting the two strips is connected to the moving section of the X-Y stage for each axis. This resistive measurement can be used to determine the position of the X-Y stage between the window locations once the resistance measurement has been calibrated.

An example of the two measurements used to determine the position of the X-Y stage is given in Fig. 2.22 as the stage positioned travels between two window locations. The measured potentiometer linear resistance is typically 0.63 k $\Omega$ /inch at room temperature and 0.77 k $\Omega$ /inch at 4 K. The behavior of the LEDs with temperature can be found in [61].

### Cautionary Remarks

It is worth noting a few cautionary remarks about using the X-Y stage. A differential pressure between the inside and the outside of the titanium edge-welded bellows can damage either the bellows or X-Y stage under certain circumstances. If the external pressure is higher, then there is a significant force on the bellows pushing them toward the on-center position. If the X-Y stage is being held off center by the cables, then these counteracting forces can potentially cause a leak in the bellows. Likewise, if the internal pressure is higher, which can arise if the trap is warmed up while inside the evacuated insert dewar, then there is a net force on the bellows pushing them off-center, which can likewise potentially lead to damage.

### 2.3.7 Vacuum Inside the Cryogenic Penning Trap

Cryo-pumping within a sealed vacuum enclosure that is cooled to 4 K can reduce the background gas pressure to unparalleled levels. This exceptionally good vacuum level is required for long antiproton and antihydrogen lifetimes within the trap, since background gas can cause antiproton annihilations. Within previous Penning traps used by the ATRAP collaboration, an observed antiproton lifetime in the trap longer than 1 month was used to derive an upper limit on the gas pressure of  $5 \times 10^{-17}$  Torr [62]. The new A-TRAP Penning-Ioffe trap utilizes a different positron loading method where positrons are transferred into the trap from an external accumulator. This requires a small hole on-axis with the Penning trap which the positrons can pass through Section 4.2.2. As such, our Penning trap vacuum enclosure is not completely sealed before it is cooled to cryogenic temperatures. Gas atoms from outside of the

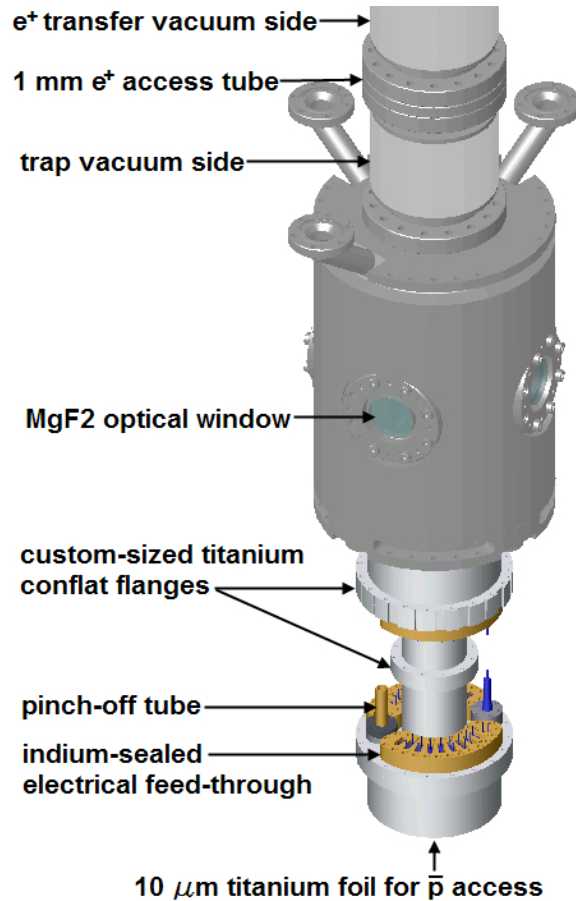


Figure 2.23: The Penning trap vacuum enclosure.

trap can enter through the 1 mm diameter, 1.3 cm long positron hole. Most gases will be efficiently cryo-pumped onto the cold surfaces of the trap, but hydrogen and helium gas could potentially accumulate within the trap over time. We observe no discernable antiproton loss after holding antiprotons within the Penning trap for 15 hours. From this observation, we can set an upper limit on the pressure within the trap of  $3 \times 10^{-16}$  Torr. It seems clear that the cold small-diameter pumping restriction and the good vacuum above the Penning trap are sufficient to decouple the Penning trap vacuum space from the non-cryogenic vacuum space outside.

The trap is made from entirely non-magnetic materials below the level of the helium dewar. This includes the vacuum enclosure for the Penning trap. Our non-magnetic vacuum enclosure is formed from titanium, including edge-welded titanium bellows above the electrode stack and the Ioffe trap vacuum enclosure. Titanium is sufficiently hard to form conflat flanges, which seal by compressing a copper gasket between two circular titanium knife-edges. Conflat flanges were used whenever possible to join the various pieces of the vacuum enclosure, since they are typically much easier to seal than the alternative indium seal that is commonly used in cryogenic experiments. We found that our titanium conflats are more difficult to properly seal than their stainless steel counterparts. It is however possible to consistently seal the flanges using a torque wrench. Several of our conflat flanges are a custom size (Fig. 2.23), due to the unique space requirements demanded by our Penning trap. For those conflat flanges, we fabricate custom-sized copper gaskets. An associated challenge is the choice of bolts used to fasten the conflat flanges. Titanium seems like an obvious choice because it is strong and matches the thermal contraction of the flanges. Pure titanium grades are soft enough that there would be a danger of stripping the bolts however, and most titanium alloys become brittle at cryogenic temperatures [63]. Titanium alloys with small amounts of the interstitials oxygen, carbon, and nitrogen tend to maintain higher ductility at cryogenic temperatures. Of the extra-low interstitial (ELI) grades of titanium, the Ti-5%Al-2.5%Sn ELI alloy has the best ductility properties at cryogenic temperatures, but we chose to use the Ti-6%Al-4%V ELI alloy for our bolts due to availability, which also has satisfactory properties at cryogenic temperatures [64].

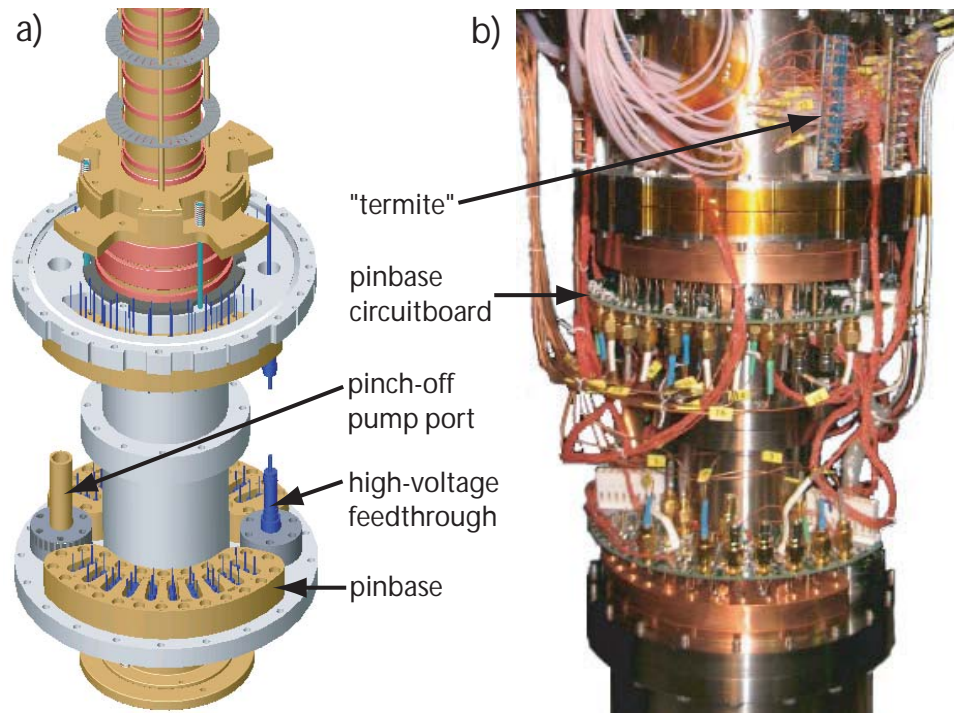


Figure 2.24: (a) A model of the electrical feed-throughs into the Penning trap vacuum space. (b) A photograph of the electrical connections for the Penning trap.

A number of vacuum seals are still formed using indium seals. The bottom of the Penning trap vacuum enclosure is formed by a small 10  $\mu\text{m}$  thick titanium foil, which is clamped onto an ring of indium sitting in a groove. Additionally, the electrical feed-throughs into the Penning trap vacuum space are brazed into a copper flange. Each of these four flanges has 30 electrical vacuum feed-throughs, and we collectively refer to these as the “pinbases” (Fig. 2.24a). The pinbases are also sealed by compressing a ring of indium into a groove. The feed-through pins are soldered to a circuit board that sits on top of the pinbases (Fig. 2.24b). The resistors and capacitors that form the filters in Fig. 2.5 and Fig. 2.6 are also mounted on these circuit boards. The electrical inputs for the electrode stack are carried from the hat down to the pinbases by micro-

coaxial cables and constantan wires. The micro-coax lines have SMA connectors that screw directly onto the board. The constantan wires are jumpered over to standard copper wires at several “terminals” located above the pinbases, and the copper wires plug into the circuit board.

The pump-out procedure for the Penning trap vacuum space involves pumping on both sides of the 1 mm positron hole, from above through the positron access valve, and on the Penning trap side through a copper “pinch-off” tube. The trap is roughed out slowly using a sorption pump so as not to shock the fragile titanium vacuum foil. Several torr of dry nitrogen gas are introduced to the trap and pumped away, and this cycle is repeated a few times to purge helium from the trap. The trap is then pumped down to the  $10^{-6}$  Torr range. When the desired pressure is reached, the trap vacuum is sealed by closing the positron access valve on top of the apparatus and by pinching shut the copper tube on the Penning trap side. The Penning trap is later cooled to cryogenic temperatures. As it is cooled, any residual gas in the trap is cryo-pumped onto the cold surfaces within the trap. To boost the cryo-pumping capacity of this trap, charcoal was placed inside the vacuum space, both above and below the cold positron tube.

# Chapter 3

## Particle Manipulations and Measurements

### 3.1 Particle Transfer

#### 3.1.1 Adiabatic Transfer

The simplest and most common method of transporting particles inside the trap involves moving the particles one electrode at a time by shifting the minimum of the axial confining potential onto a neighboring electrode. The voltages typically used for this are depicted in Fig.3.1. The particles begin in a 100 V well in a single electrode (solid curve). A 110V potential is applied to the neighboring electrode, shifting the particles along with the axial potential minimum into the neighboring electrode (dashed curve). The potential on the original electrode is then set to zero and the confining potential on the new electrode is reduced to 100V (dotted curve).

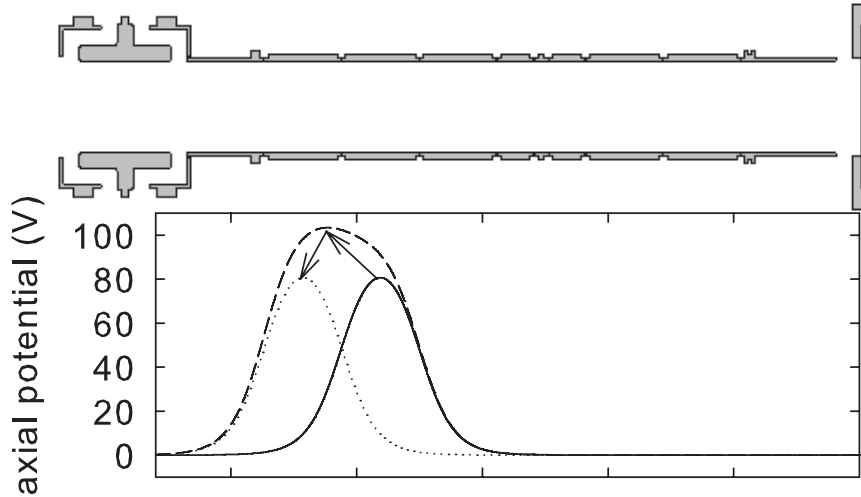


Figure 3.1: The potentials used to adiabatically transfer particles.

This process can be repeated as many times as necessary to move the particles to the desired trap location. We commonly refer to this technique as “adiabatic transfer” because the voltages are changed over time scales that are much longer than the  $\approx 1 \mu\text{s}$  axial bounce time of the particles, in order to minimize the heating of their axial motion. The slow voltage changes are assured by the  $RC = 1 \text{ ms}$  time constant of low-pass filters between the voltage supplies and the electrodes.

We can use our efficient detection of antiproton annihilations as a diagnostic of particle confinement within our electrodes. Under most circumstances, we are able to detect no antiproton loss during adiabatic transfer. However, if an electrode is misaligned, damaged, or has a poor or noisy electrical connection, particles will be lost as they pass through it. We can rapidly identify “lossy” electrodes to be avoided or repaired by adiabatically transferring antiprotons through the trap and efficiently detecting antiproton annihilations in real time. We are sensitive to as few as 20

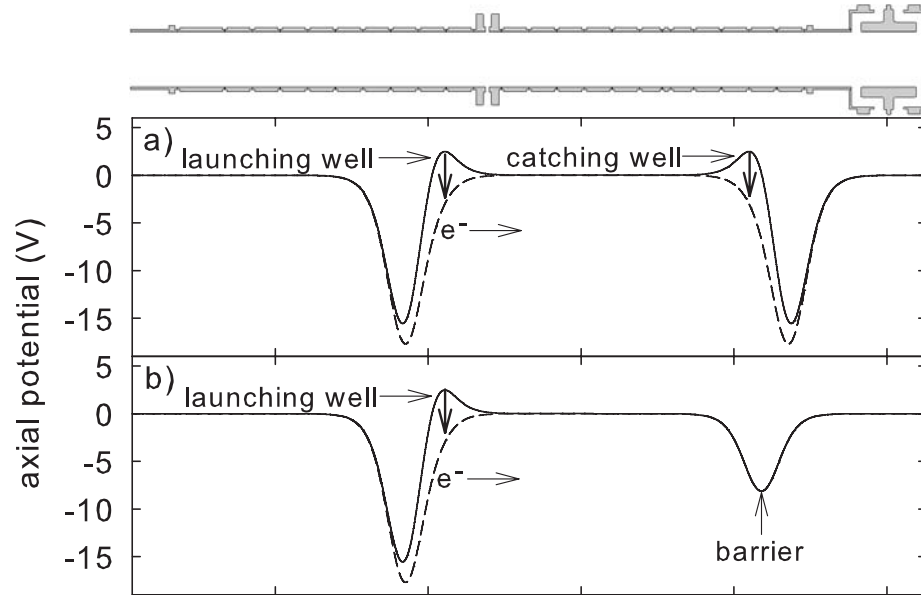


Figure 3.2: (a) Particles are transferred from a launching well to a catching well by matching the duration of a rapidly-applied voltage pulse (dashed curve) in both locations to the particle transit time. (b) The energy distribution of the particles launched from the well can be measured by varying the height of a barrier.

antiproton annihilations per second with a signal-to-background ratio of one. We take care to ensure that particles are not confined directly between two electrodes during adiabatic transfer, because we have found that this leads to more-rapid radial expansion of the confined plasma, and corresponding particle losses.

### 3.1.2 Pulse Transfer

We can also transfer particles between locations in the trap by launching and catching them using rapidly-applied voltage pulses. An example of the launching and catching potentials that can be used is depicted in Fig. 3.2a. Particles are launched out of their initial well by a rapidly-applied voltage pulse. An identical voltage pulse

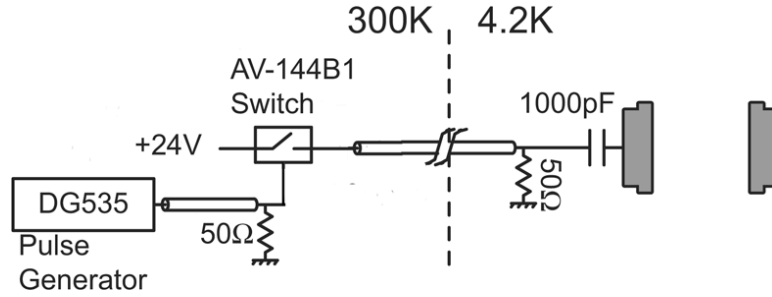


Figure 3.3: Electronics used to apply fast voltage pulses to the trap electrodes.

changes the catching well potential into a slope that slows the particles as they reach that location. Particles are captured in the catching well by timing the duration of this voltage pulse so that the sloped potential is transformed back into a confining potential just as the particles arrive.

The fast voltage pulses are applied to the trap electrodes using the circuit depicted in (Fig.3.3). An Avtech Electrosystems AV-144B1 saturated switch is used, which is specified to output a 20 V pulse into a 50  $\Omega$  load with a characteristic rise and fall time of 2.5 ns, which is roughly ten times faster than the typical axial oscillation frequency for positrons and electrons. The timing and duration of the pulse is controlled using a Stanford Research DG535 pulse generator. The pulse is transmitted into a 50  $\Omega$  stainless-steel micro-coax cable (Microstock UT-20-SS) that spans the 2.0 m distance between the room temperature and 4 K sections of the trap, and is 50  $\Omega$  terminated at the electrical feed-through into the trap vacuum. The rapid voltage pulse is capacitively coupled to the electrode so that it adds to the DC bias potential during short timescales. The saturated switch typically outputs a 24 V pulse that is divided down to 12 V at the electrode by the 50  $\Omega$  terminator.

The pulse transfer method outlined above has some potential advantages over adiabatic transfer. The transfer process is much more rapid, set by the time-of-flight of the particles. The particles can rapidly pass through lossy electrodes or electrodes containing other particles to reach parts of the trap that would otherwise be inaccessible using adiabatic transfer. Pulse transferring also allows us to separate particles or ions with the same charge but differing masses that are initially mixed together. Charges of differing mass have differing accelerations in an electric field, enabling us to separate electrons from antiprotons or positrons from ionized background gas by controlling the pulse timing.

A disadvantage of pulse transferring over adiabatic transferring is that it requires precise timing, which must be optimized experimentally for each given launching and catching well structure and separation distance. Even in the fully-optimized case however, the potentially large spatial and velocity distribution of the launched particles can lead to poor transfer efficiencies. Furthermore, the axial motion of the particles could potentially be heated by the rapidly-applied voltages. Nonetheless, pulse transferring can be used to transport small particle plasmas (less than 1 million particles) with nearly 100% efficiency [65].

Efficiently transferring larger plasmas is considerably more challenging however [65]. Larger plasmas launched during a single pulse have a larger axial energy distribution, so that not all of the particles are in the catching electrode at the same time. This is due to space charge effects. The electric field from the voltage pulse accelerates particles near the outside of the plasma first, while the plasma space charge screens out the field near the center of the plasma, causing a time lag between when

different particles can leave the well. Furthermore, the repelling space charge forces inside the plasma will cause it to spread out axially while in flight. These effects can be combatted to some extent by pulsing large plasmas out of a well in smaller bunches using a series of short pulses [65]. Alternately, it may be possible to capture particles more efficiently in a longer catching well by applying the catching pulse to multiple electrodes simultaneously.

Some preliminary experiments were performed in A-TRAP to determine if we could use pulse-transferring to separate positrons from ionized background gas that might be trapped in the same well, because these ions could cause positron heating that would suppress antihydrogen production. In principle, these ions could also be driven out by applying a low-frequency noise drive to the electrode that would be resonant with the ion's axial frequency, but such an approach would probably not be very effective for large plasmas due to space-charge screening. Because the positron plasmas in A-TRAP typically number in the tens of millions, we must use relatively large confining potentials to counteract the repulsive space charge of the plasma. Although the precise number of particles that can be confined with a given potential is dependent upon the electrode and plasma geometries, we typically find that we confine at most 4 million positrons per volt of axial well depth. Using larger potentials gives more stable particle confinement however, so we typically use several tens of volts to confine our positron plasmas, whereas in the past, a 2 V deep well was sufficient to confine the smaller number of positrons available, and a 6 V pulse was used to pulse-transfer them [65]. For us to pulse-transfer our positrons, we must either use larger voltage pulses or else use a series of small voltage pulses to transfer

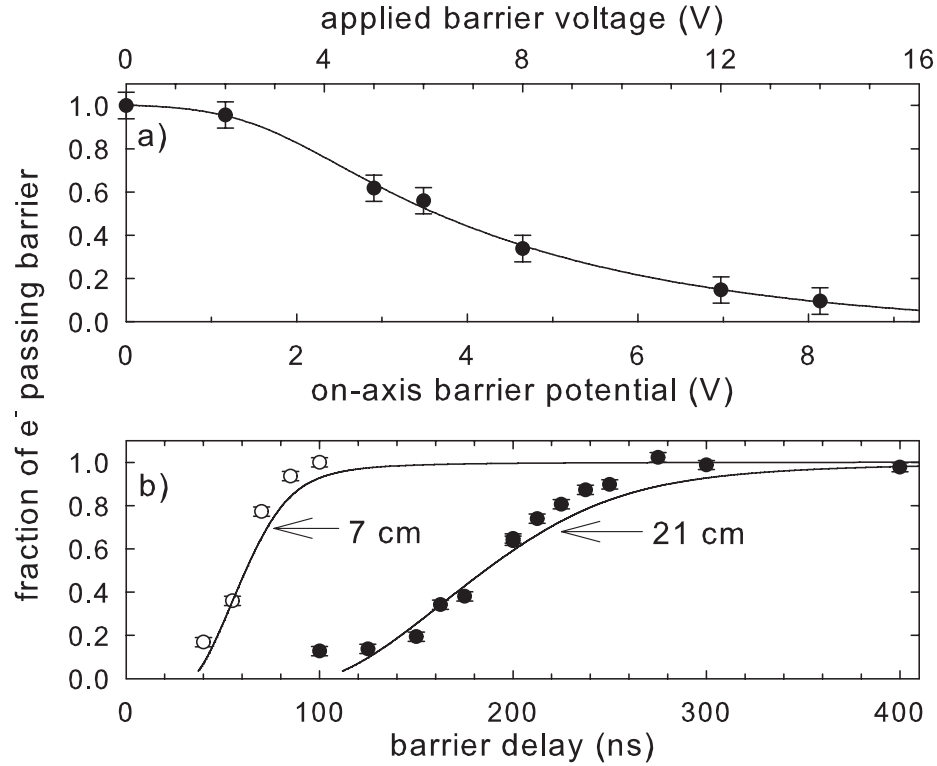


Figure 3.4: The fraction of 7 million pulse-launched electrons that (a) have sufficient energy to pass a given barrier potential, or (b) have passed a given distance before a barrier is applied at the given delay time. The curves drawn in figure (b) are directly derived from the fit curve in figure (a), demonstrating the agreement of the velocity and time distributions.

the particles.

We can determine the transit time and axial energy distribution of a pulse-launched plasma by using a barrier potential, as depicted in Fig. 3.2b. We can measure the energy distribution of the pulsed particles by varying the height of the barrier and measuring how many of the particles are able to pass the barrier and be counted as they strike the degrader. Our method of counting the charged particles will be discussed in the next section (Section 3.2.1). For 7 million electrons launched using a 12 V pulse, the resulting electron energy distribution can be derived from Fig. 3.4a.

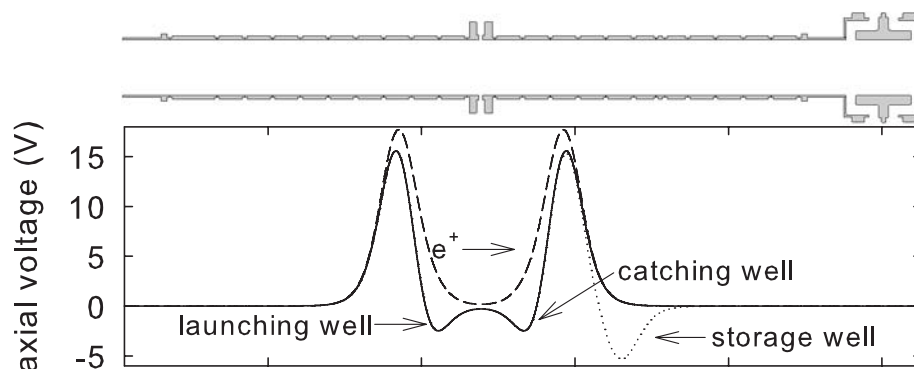


Figure 3.5: The potentials used to pulse separate positrons from ions. Positrons are transferred between two wells (solid curve) by a rapidly-applied voltage pulse (dashed curve). Multiple pulses can be used to extract the positrons from the launching well if the caught positrons are transferred to a storage well (dotted curve) between each pulse sequence.

The energy of the electrons vary over a voltage range that is comparable to both the pulse voltage and the voltage initially confining the plasma. Electrons on either end of this energy range would take between 10 and 20 ns to pass through a single radius-length electrode. By making the barrier large enough to reflect all of the particles, we can determine the time that the particles take to pass the barrier position by removing the barrier with a voltage pulse of a given duration after the particles are launched, and measuring the number of particles that are able to pass the barrier and be counted on the degrader as a function of pulse duration. The results of this experiment are depicted in Fig. 3.4b for two different barrier locations. The particle-transit times predicted from Fig. 3.4a are in good agreement with the temporal distribution of the electron pulse in Fig. 3.4b.

Because we can only capture particle in the catching well within a narrow time

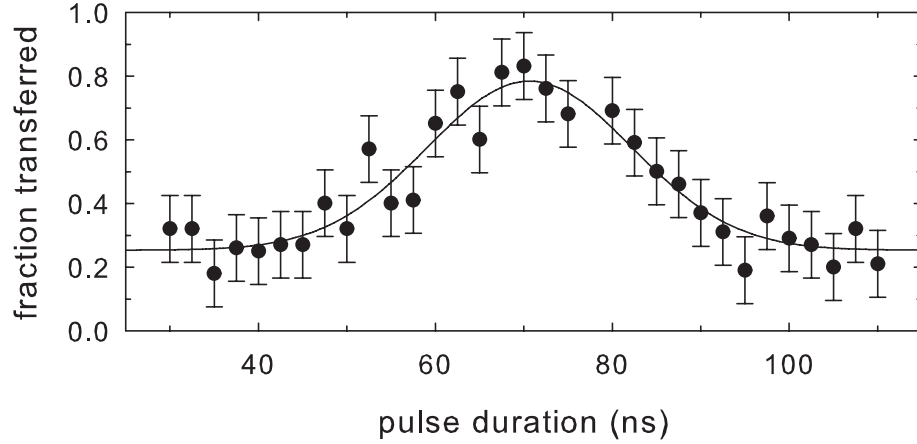


Figure 3.6: The efficiency of pulse-transferring 8 million electrons between two wells separated by 7 cm.

window, it is clear from Fig. 3.4b that the pulse-transfer efficiency falls off rapidly with distance. The ideal pulse-transfer potentials for separating positrons from ions places the launching and catching wells as close together as possible, as in Fig. 3.5. Inverted potentials were used to test the transfer efficiency with electrons. The maximum efficiency of transferring 8 million electrons with a single 12 V pulse was about 80%, as depicted in Fig. 3.6. Larger plasmas required deeper confining potentials, but could be transferred using multiple 12 V pulses by adiabatically transferring the caught electrons to a storage well (dotted curve in Fig. 3.5) and gradually lowering the launching well depth between each pulse. As many as 50 million electrons were transferred this way with efficiencies around 80%, and no indication that larger numbers could not be pulse-transferred similarly. Previous experiments suggest that pulse-transferring a million or less positrons using lower voltage pulses could likely be done in A-TRAP with greater efficiency [65], but this was not studied because we intend to

use much larger numbers of positrons in all future experiments. There are still many possibilities for optimizing the efficiency of pulse-transferring large positron plasmas, but time constraints prevented further investigations.

## 3.2 Particle Counting

There are several different methods used to determine the number of particles confined within the Penning trap. The method that will be discussed first in this section is ejecting the particles from inside the trap onto a Faraday cup electrode, and measuring the charge deposited on that electrode (Section 3.2.1). This method is accurate as long as the particles being counted do not in turn cause secondary charged particles to be emitted from the electrode, since those secondary particles would be included in the net charge deposited. For electrons, the emission of collisionally-excited secondary electrons is suppressed by applying voltages that strongly attract the electrons toward the Faraday cup. For positrons, the situation is somewhat more complicated, but the emission of secondary particles can nonetheless be suppressed with an appropriate choice of voltages (see discussion at the end of Section 3.2.1). We also attempted to measure the charge of several hundreds of thousands of antiprotons using this method, but the generation of secondary particles during the antiproton annihilation process is not understood well enough to make this an accurate calibration of the antiproton number at this time. As such, a discussion of these measurements will be delayed until Section 3.2.3, at which point they can be compared with our annihilation counting method.

The number of antiprotons in the trap is determined by detecting the charged

particles created when an antiproton annihilates after being released from the trap (Section 3.2.2). The number of annihilation signals detected can be converted into the number of antiprotons released from the trap if we know the annihilation detection efficiency. Presently, we rely upon Monte Carlo simulations to estimate our detection efficiency. Our ability to detect positron annihilations will also be briefly discussed in Section 3.2.2. Following that, the annihilation detection and charge counting methods will be compared for both positrons and antiprotons in Section 3.2.3. Finally, a nondestructive method of counting particles through rf detection of oscillating image charges will be discussed in Section 3.2.4, although this method can only accurately count particle plasmas numbering 5 million or less.

### **3.2.1 Destructive Charge Counting**

The primary method of determining the number of electrons or positrons in the trap is to pulse the particles onto a faraday cup and measure the net charge deposited. This is a “destructive” counting method because the particles that are being counted are lost from the trap. To determine the number of particles in the trap at a given time, we typically count the number of particles loaded using destructive charge counting and then load an identical particle plasma using the same loading procedure. Alternately, we can calibrate the linear relationship between the number of particles loaded and the number of particle pulses accumulated before loading the desired number. We therefore rely upon the high reproducibility (usually within 2%) and linearity of our electron and positron loading techniques. Since we lose any particles that are counted, this counting method is only practical because our particle loading

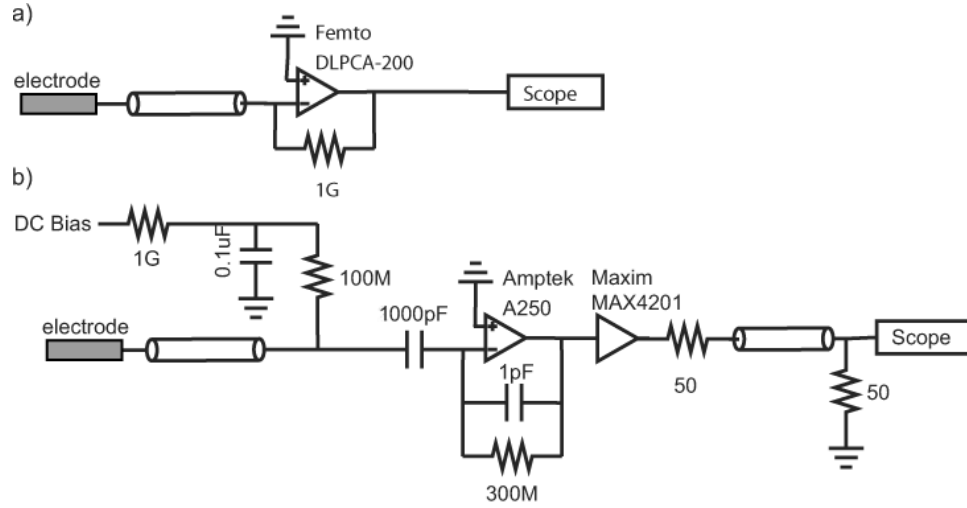


Figure 3.7: Schematic diagrams of the electronics used to measure (a) currents and (b) charges of particles striking an electrode [66].

rates are much faster than in previous experiments.

The electronics used to measure current or charge due to particles striking a Faraday-cup electrode is schematically depicted in Fig. 3.7. Currents can be measured using a (FEMTO DLPCA-200) current amplifier, which has a gain of  $10^9$  V/A and a 3 dB bandwidth of 1.2 kHz (Fig. 3.7a). This device is most useful for measuring the intensity of continuous beams of particles. The charge of particles confined within the trap is more sensitively measured using a charge-sensitive amplifier, by rapidly pulsing the particles onto the electrode (Fig. 3.7b) [66]. It should be noted that the amplifiers actually measure the net change in charge on the electrode, including the ejection of secondary electrons caused by the incoming energetic particles. We bias our Faraday-cup electrodes to electrically suppress the escape of secondary electrons, so that the charge counted only reflects the number of particles pulsed onto the Faraday cup. The charge-sensitive amplifier is basically an operational amplifier with

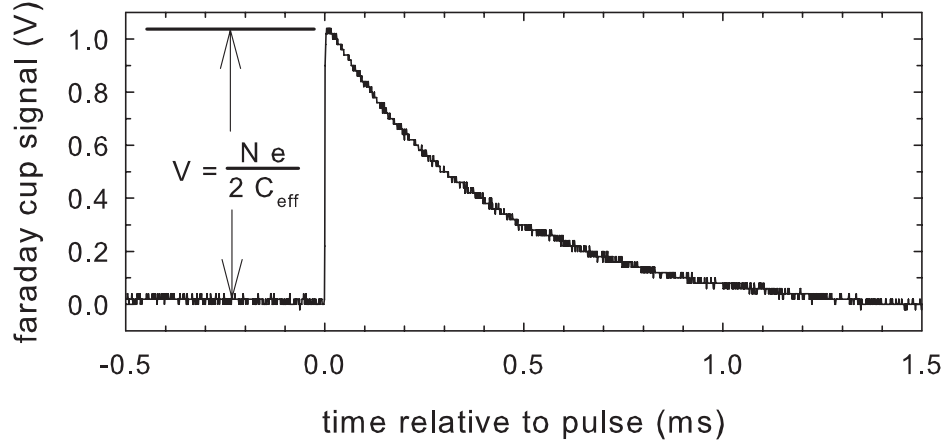


Figure 3.8: The voltage signal from a charge-sensitive amplifier caused by 28 million electrons pulsed onto the degrader.

a feedback capacitor  $C_f \sim 1$  pF. The output voltage of the amplifier is related to the input charge by  $V_{out} = q/C_f$ , and the charge stored by the feedback capacitor is drained away by a  $300$  M $\Omega$  resistor with a time constant of approximately  $300$   $\mu$ s to reset the amplifier for subsequent charge pulses.

The input charge at the amplifier is somewhat smaller than the charge collected on the electrode due to the capacitance of the coaxial cable and blocking capacitor before the amplifier (Fig. 3.7b). To account for this effect, we define the effective capacitance of the amplifier as:

$$C_{eff} = C_f \left( 1 + \frac{C_{cab}}{C_{blk}} \right) \quad (3.1)$$

where  $C_f \sim 1$  pF is the feedback capacitance,  $C_{blk} \sim 1000$  pF is the blocking capacitance, and  $C_{cab}$  is the capacitance of the cable joining the electrode and the amplifier. The value of  $C_{eff}$  is determined experimentally by applying calibrated charges to the cable input and measuring the voltage response on the oscilloscope. The amplifier

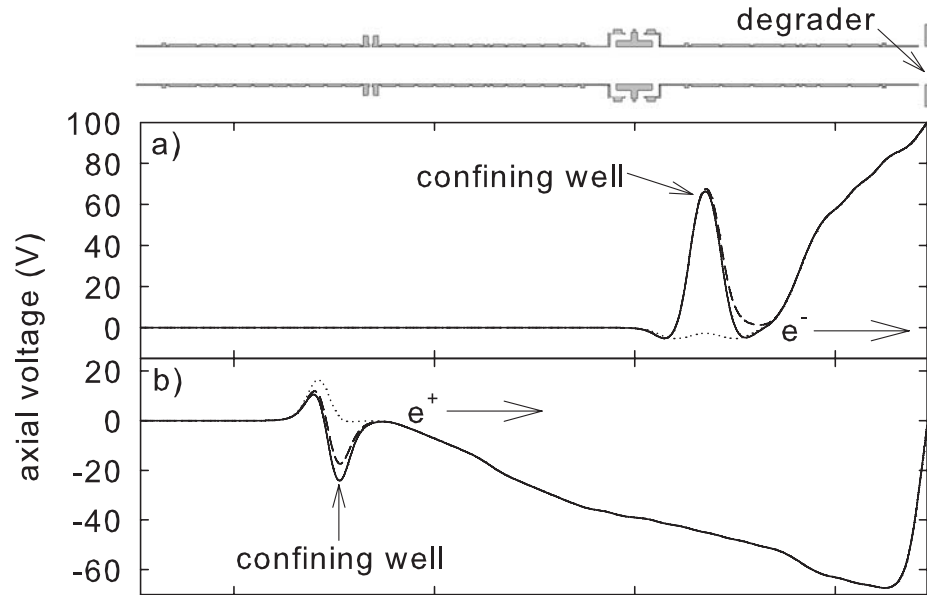


Figure 3.9: The potentials used for counting the charges of (a) electrons or (b) positrons that are pulsed onto the degrader.

output voltage is divided by two at the oscilloscope due to the input termination.

The voltage on the oscilloscope is then given by:

$$V = -\frac{Nq}{2C_{eff}} \quad (3.2)$$

where  $N$  is the number of particles and  $q$  is the charge of a particle. In this way, the charge striking the electrode can be measured accurately and used to determine the number of particles that were pulsed onto the electrode. The voltage signal from the charge-sensitive amplifier due to 28 million electrons is depicted in Fig. 3.8.

Particles in the Penning trap are pulsed out of their confining well using fast voltage pulses like those described in the previous section, and the faraday cup is typically the degrader, a beryllium foil at the end of the Penning trap (Fig. 3.9). The magnetic bias field lines are parallel to the trap central axis, and therefore direct the

particles from anywhere inside of the Penning trap onto the degrader. The potentials typically used to pulse the electrons or positrons onto the degrader are depicted in Fig. 3.9. Although we can pulse the particles onto the degrader using a single, large-voltage pulse, particle numbers exceeding roughly 50 million saturate our amplifier. As such, to count large numbers of particles, we typically use a sequence of small pulses that each eject a small fraction of the particles out of the confining well. If the confining potential is less than the repulsive space-charge potential of the plasma, particles will leak out until the potentials are in equilibrium. Using this principle, a fast-voltage pulse (dashed curve in Fig. 3.9) reduces the confining potential and allows some of the particles to escape to the degrader. The static confining potential is then reduced by a small increment, a second pulse is applied, and the process is repeated until no particles remain in the well (dotted curve). The total number of particles is simply the sum of the particles counted from each voltage pulse. A typical example of the number of electrons incrementally released as a function of the confining well voltage is provided in Fig. 3.10 for 185 million confined electrons.

There are some differences between the potentials used for charge counting electrons and positrons in Fig. 3.9. For electrons, the barrier on one side of the confining well is reduced to release the electrons. For positrons, the confining potential has a larger barrier to one side, and the overall depth of the well is reduced to release particles in the opposite direction. Although either of these methods yield identical results in the lower electrode stack, implementing the electron-counting type of potential in the upper electrode stack resulted in an inaccurately small particle counts. This was likely due to the fact that potentials applied to the shorter, radius-length electrodes

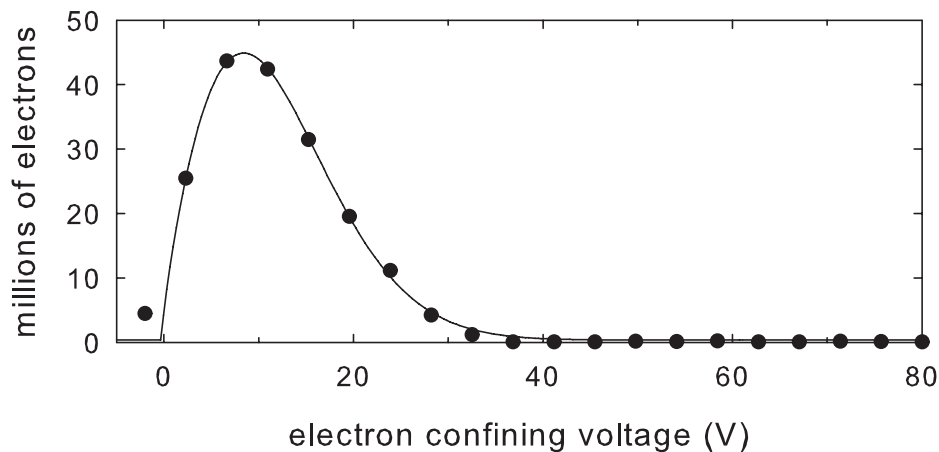


Figure 3.10: An example of incremental charge counting for 185 million electrons. The number of electrons released onto the degrader by a short voltage pulse is indicated as a function of the confining well voltage, which is incrementally decreased from 80 V to -2 V, as illustrated in Fig. 3.9a.

used in the upper stack significantly affect the potentials in neighboring electrodes as well, whereas this is not a major problem in the lower stack. Using the potential structures in Fig. 3.9 yielded consistent particle counts in both the upper and lower stacks.

For both electrons and positrons, the potentials directly in front of the degrader in Fig. 3.9 are meant to suppress the emission of secondary electrons, which would lead to inaccurate particle counting. Electrons released onto the degrader in Fig. 3.9a gain 100 eV of kinetic energy as they are accelerated by the potential ramp leading toward the degrader. Collisions between these energetic electrons and other electrons near the surface of the degrader will cause some electrons to be kicked off of the degrader. These secondary electrons will have energies that are less than 100 eV however, so they will be pulled back onto the degrader by the same potential that accelerated the

initial electrons. Consequently, only the electrons that are initially released from the trap will contribute to the total charge deposited on the degrader.

For positrons, a number of factors may potentially contribute to inaccurate charge counting. The positrons in Fig. 3.9b are initially accelerated toward the degrader, but then lose most of that energy in climbing the secondary-electron suppressing potential immediately in front of the degrader. As was the case with electrons, collisions between the positrons and electrons near the surface of the degrader can cause the emission of secondary electrons. The positrons arrive at the degrader with roughly 10 eV of energy or less however, so we expect that collisionally-excited secondary electrons will have less energy than this, and will be easily suppressed by the potential directly in front of the degrader. Another possibility is that some of the positrons may scatter back out of the degrader or be moderated by the degrader and emitted with an energy close to the negative work function for a positron in beryllium ( $\simeq -0.5$  eV) [67], although it seems unlikely that the degrader would moderate positrons very efficiently. In any case, any positrons that may be emitted from the degrader would be reflected back onto the degrader after reaching the potential barrier to the left in Fig. 3.9b. We must also consider the electrons emitted as a result of positron-electron annihilations inside the degrader. The annihilation will produce back-to-back 511 keV photons, and these can in turn cause energetic electrons to be emitted via Compton scattering or photoemission. A previous study suggested that these processes contribute to less than 1% of the secondary electrons emitted however [68].

A more concerning possibility arises if a positron annihilates with a core electron of a beryllium atom. This will result in the emission of an Auger electron as an

outer electron in the atom fills the core vacancy [68]. These Auger electrons have energies that peak at around 100 eV for beryllium, but the distribution also extends to lower energies as a result of the direction of the emitted electron and energy attenuation within the material [69, 70]. In retrospect, the potentials typically used to count positrons (Fig. 3.9b) may not have been sufficient to suppress the most energetic Auger electrons emitted. However, preliminary measurements suggest that the positron charge measurements were probably accurate nonetheless. If we apply voltages to encourage the emission of secondary electrons rather than suppress them, then we count 25% more positive charge deposited on the degrader as a result of secondary electron emission. These electrons are easily suppressed by a moderate voltage however, and there was no observed variation in the positive charge collected on the degrader as the magnitude of the electron-suppressing axial voltage was varied between 40 and 80 V. Although this voltage would not be sufficient to suppress the most energetic Auger electrons, we would have expected to see a variation in the charge measured due to the suppression of lower-energy Auger electrons if a significant number of Auger electrons were produced. We therefore believe that our positron counting method is accurate. An independent measurement of the positron and electron numbers using rf detection (Section 3.2.4) may be used to cross-calibrate the two charge measurements in the near future as further verification of their accuracy.

### 3.2.2 Annihilation Detection

When antiprotons escape the trap and come in contact with the trap walls, the resulting annihilations can be detected with high efficiency. Antiproton-proton anni-

ihilations have many possible decay channels, but the average product of an annihilation is three charged pions and two neutral pions [71]. The high-energy charged pions are detected as they pass through sets of scintillating detectors, where the energy deposited in the detectors produces a light signal that is converted into an electrical signal, which is then counted electronically. The annihilation signals are monitored continuously, and can therefore be used to detect real-time loss of antiprotons from the trap. The detector background rate due to cosmic rays and electrical noise sets a lower limit on the number of antiproton annihilations that can be counted in real time to a few tens of antiproton annihilations per seconds. Just a few antiprotons can be reliably detected however by ejecting the antiprotons from the trap over a time scale that is short in comparison to the detector background rate and detecting just the annihilation signals that are registered during the ejection time window. This results in an effectively background-free, high-efficiency method of detecting just a few antiprotons, which is an extremely important tool in the detection of antihydrogen formation [15].

The antiproton annihilation detectors are depicted in Fig. 3.11. They were built by members of the ATRAP collaboration from Forschungszentrum Jülich. The detectors consist of four layers of plastic scintillating fibers in the fiber ring located between the Ioffe-Penning trap and the bore of the superconducting solenoid, and two layers of plastic scintillating paddles on the exterior of the solenoid. The two inner fiber layers are each composed of 224 straight, 3.8 mm diameter fibers. The two outer fiber layers are composed of 168 helically-wound, 3.8 mm diameter fibers. In both cases, the fibers are tightly packed so that the fibers in the second layer sit in the gaps

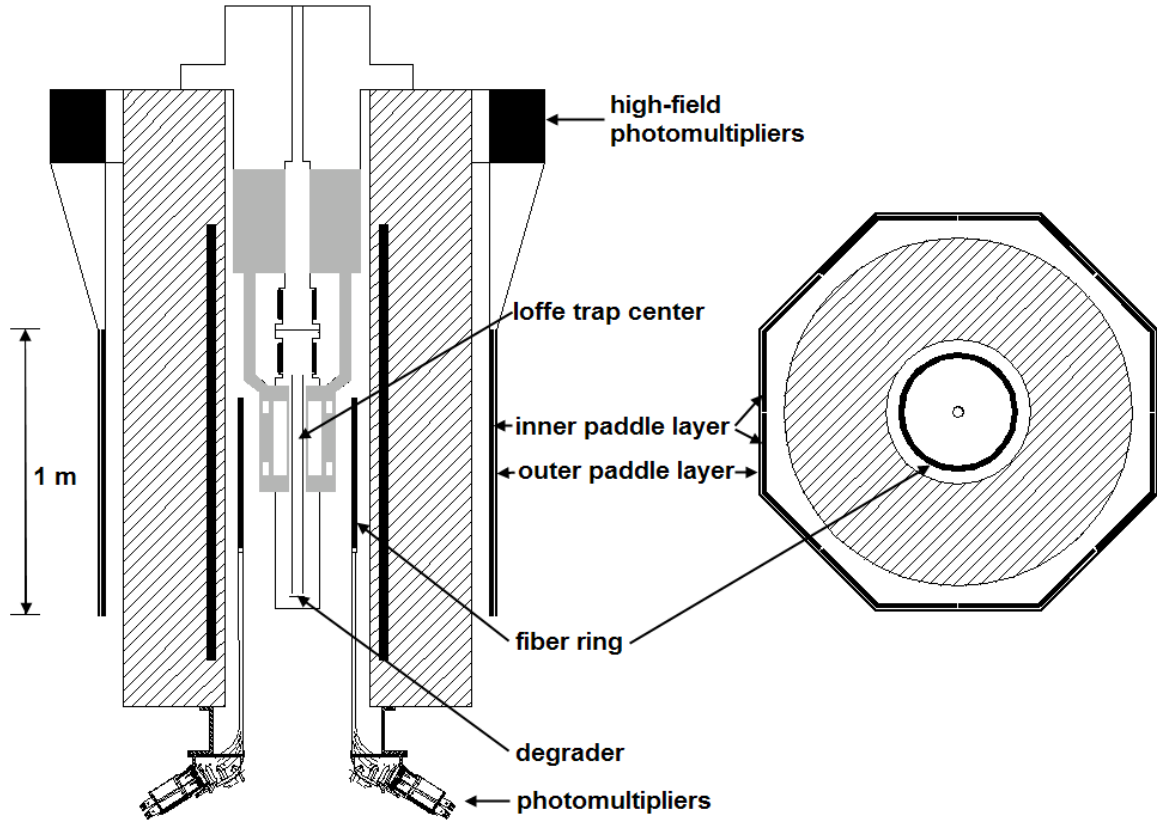


Figure 3.11: Scintillating fibers and paddles used to detect antiproton annihilations.

between the fibers in the first layer. The light signal from the fibers are guided into a number of 16-channel photomultipliers (Hamamatsu H6568) that surround the lower perimeter of the solenoid bore. Each fiber has its own corresponding photomultiplier channel. The outer scintillating paddles are arranged in an octagon pattern around the exterior of the solenoid. The outer of the two layers is composed of 8 large paddles, while the inner layer is composed of 16 paddles, two for each large paddle. The paddle layers are closely spaced, so that the vast majority of particle trajectories that pass through an inner paddle must also pass through the matching outer paddle. Coincidence of these two layers can therefore be used to reduce background counts

	Ioffe center	degrader
fibers	0.82	0.18
paddles	0.58	0.43
fiber-paddle overlap	0.58	0.03

Table 3.1: The solid angle acceptance of the detectors for a single particle originating at the indicated annihilation position [1].

due to noise. The light from the paddles are guided through plexiglass light guides into photomultipliers (Hamamatsu R2238) surrounding the upper perimeter of the solenoid. All of the photomultipliers are mounted within three-layer iron enclosures that screen out some of the magnetic field of the solenoid.

When the Ioffe trap is not installed around the Penning trap, two additional fiber rings can be inserted inside of the fiber ring in Fig.3.11 to allow for greater detection efficiency, better background discrimination, and some annihilation position resolution capabilities [1]. The inner of these two rings is also composed of two layers of straight fibers and two layers of helical fibers, while the outer one is composed of two straight fiber layers. When the Ioffe trap is installed however, there is not enough space for these additional fiber layers, so we operated in the configuration depicted in Fig. 3.11 most of the time.

### **Annihilation Detection Efficiency**

The efficiency of the detectors depend upon where the antiprotons annihilate, due to the solid angle subtended by the detectors for charged pion trajectories originating from the annihilation location. Because low-energy antiproton trajectories follow magnetic field lines, when we intentionally eject antiprotons from the trap, they leave

	Ioffe center	degrader
fiber multiplicity $\geq 1$		0.55
fiber multiplicity $\geq 2$	0.92	0.50
paddle	0.80	0.75
fiber-paddle coincidence	0.77	0.40

Table 3.2: Monte Carlo simulation predictions for the probability that a single antiproton annihilation at the indicated location in a 1 T field will be registered on the indicated detector or coincidence of detectors [1].

the trap along the central axis and annihilate on the degrader. Antiprotons are always counted using this well-established annihilation location. When the Ioffe trap is energized however, there will be significant radial loss within the center of the Ioffe trap due to antihydrogen production or radial antiproton transport along field lines. The fraction of the total solid angle subtended by the detectors for a single particle originating at either of these locations is given in Table 3.1 [1].

The overall detector efficiencies depend upon many factors, including the number of charged particles generated by the annihilation, their trajectories, generation of secondary particles, and energy loss within the detectors and in surrounding materials. A full calculation of the detector efficiencies was calculated using Monte Carlo simulations by ATRAP collaboration members from Jülich [1]. The simulations were done using the GEANT4 simulation tool-kit. The CHIPS event generator was chosen to simulate the particles produced by the annihilation of low-energy antiprotons on either gold or beryllium nuclei because its predictions were in reasonable agreement with existing experimental data. The objects surrounding the trap and detectors were approximated by models with realistic geometries and materials to account for energy attenuation and secondary particle generation. The calculated detector effi-

ciencies that resulted from these simulations are summarized in Table 3.2.

In reality, the signal from each of the detector photomultiplier is converted into a electronic logic signal if the photomultiplier output voltage exceeds a critical threshold voltage. These voltages are read out at 25 MHz, divided into 40 ns time bins. During each time bin, the signals from some channels are summed together and coincidences between various channels are also registered. In practice, not all of this data is recorded unless we explicitly want to look at a particular small region in time. Rather, these summed and coincidence detector counts are typically summed up into larger time bins that can be stored.

For the purposes of the following discussion, it is important to briefly define some of the various summation and coincidence logic operations that are recorded, which we commonly refer to as the different “detector channels”. A “fiber single” count is registered if there is a detection signal from at least one of the fibers. A “fiber double” count is registered if there is a signal from at least one of the straight fibers and at least one of the helical fibers in the fiber ring. A “paddle” count is registered if there is a signal from at least one of the large outer scintillating paddle in coincidence with a signal from one of the two smaller paddles from the inner layer that overlap it. This coincidence requirement between the outer and inner paddle layers within a 40 ns interval reduces background counts due to noise. We generally use the term “trigger” to refer to coincidence signals from the paddle and fiber detectors. A “trigger type 1” count is registered if the conditions for the “fiber double” and “paddle” counts are both satisfied within the 40 ns window. A “trigger type 2” count is registered if the “fiber double” condition is satisfied and a paddle multiplicity of at least two is measured

	Ioffe center	degrader	background (Hz)	S/N degrader (Hz)
fiber single	1.9	1.32	450-900	340-680
fiber double		0.45	30	70
paddle	0.80	0.75	350-450	470-600
trigger type 1	0.49	0.25	12	50
trigger type 2	0.21	0.11	3	30

Table 3.3: Absolute detector channel efficiencies, derived from the relative detector efficiencies and the assumption that the paddle detector efficiencies are equal to the derived Monte Carlo values. Also listed are the typical background count rates for each detector channel, and the antiproton annihilation rate that is required to equal the background noise rate (labeled S/N).

during the same 40 ns window. Having a paddle multiplicity of at least two means that there are signals from at least two of the large outer paddles in coincidence with each other, and for each of them, in coincidence with one of their corresponding smaller paddles.

The maximum count rate of each of these detector channels is one every 40 ns. As such, in order to avoid saturating our detectors, we always release our antiprotons from the trap slowly enough so that there is a small probability that two antiprotons will annihilate within the same 40 ns time window.

We can determine the relative detection efficiencies of these various detector channels by slowly releasing antiprotons from the trap and measuring the annihilations counted above background for each channel. In order to determine the overall efficiency of the detectors however, we presently rely upon Monte Carlo calculations. We plan to calibrate our detector efficiencies in the near future with an independent measurement of the number of antiprotons being released from the trap. It was initially hoped that this calibration could be done using the charge measurement method

discussed in Section 3.2.1, but the secondary particles generated by antiproton annihilations make it challenging to extract a reliable number of antiprotons from the charge measurements (Section 3.2.3). Until reliable experimental calibrations can be made, we assume that the Monte Carlo calculation of the “paddle” detector efficiency is approximately correct, since this detector is the simplest and most easily modeled of our detector channels. The resulting absolute detector efficiencies, based upon this assumption and the measured relative detection efficiencies between channels, are given in Table 3.3. The relative detector efficiencies for antiproton annihilations within the Ioffe trap were measured by energizing the quadrupole Ioffe trap with antiprotons held in the center and then allowing the antiprotons to be guided out radially along field lines to collide with the electrode walls. We believe that the excessively-high fiber detection efficiency is due to over-counting, although the cause of this over-counting has not yet been identified.

The detector channel background rates are also given in Table 3.3. Despite their lower detection efficiency, the coincidence detection channels are better for counting antiprotons over long timescales because they have a higher signal to noise ratio, and very steady background count rates over long periods of time. For the “trigger type 2” channel for example, an antiproton loss rate of just 20-30 per second would give a signal-to-background ratio of one.

### **Positron Annihilation Detection**

Positron annihilations are detected with low efficiency by the scintillating fibers, but not by the scintillating paddles. We can therefore distinguish between positron

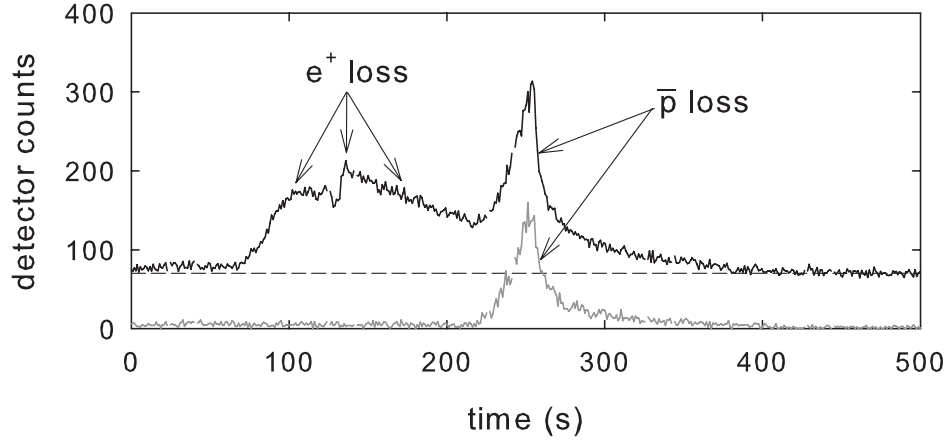


Figure 3.12: Demonstration that the detection fibers are sensitive to positron annihilations, but the paddle detectors are not. The black curve is one tenth of the fiber counts registered, and the gray curve is the trigger counts registered. The dashed lines indicates the fiber background count rate.

and antiproton losses, as demonstrated in Fig. 3.12, which depicts both the “fiber single” and “trigger type 2” detector channels while first positrons and then antiprotons are spilled out of the trap and annihilate. The large background of the “fiber single” channel and the poor detection efficiency do not make the fibers an ideal positron detector, but it is nonetheless useful when large numbers of positrons are being lost from the trap, for example when antihydrogen is being formed in the Ioffe trap.

### 3.2.3 Comparing Annihilation and Charge Counts

Because we can also measure the charge of positrons, we can use this independent measurement of the positron number to calibrate the positron annihilation detection efficiency of our “fiber single” detection channel. The results are depicted in Fig. 3.13, for both positron annihilations on the degrader and for radial loss along field lines

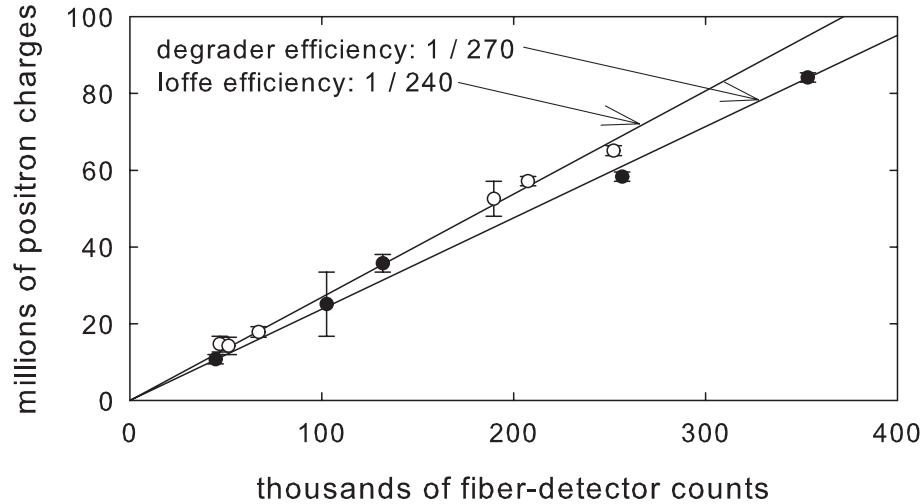


Figure 3.13: Positron detection efficiency calibration curve using direct comparison between fiber detector counts and positron charge measurements. This calibration was performed both for positrons annihilating on the degrader and for radial positron loss within the energized Ioffe trap.

within the energized Ioffe trap. In both cases, the positrons were released slowly enough to not saturate the detectors. Both counting mechanisms are destructive. We therefore loaded multiple positron plasmas and alternately counted their charge or spilled them out slowly, and relied upon the reproducibility of the loading procedure to determine the positron number in the later case. Surprisingly, the detection efficiency for positron annihilations on the degrader and inside the Ioffe trap are nearly identical, despite the larger solid angle factor for annihilations in the Ioffe trap. Perhaps the large amount of metal surrounding the Ioffe trap attenuates the 511 keV  $\gamma$ -rays produced by the positron annihilation sufficiently to cancel the solid angle effect. It should be noted that the positron detection efficiency may change somewhat over time, since the “fiber single” detection channel is very sensitive to the photomultiplier

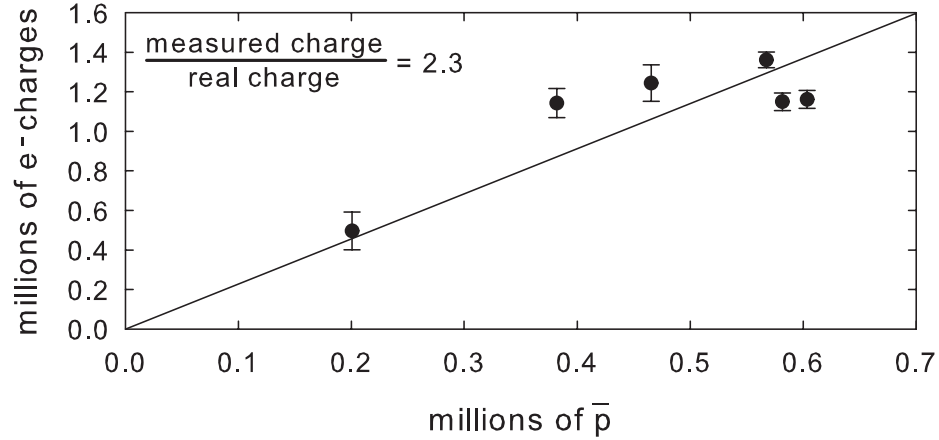


Figure 3.14: Comparison of detector channel counts with the net charge detected as antiprotons are pulsed onto the degrader.

bias voltages, detection thresholds, magnetic field, and other factors that change over time. The detector background rate has varied by as much as a factor of two during beam runs.

Using a similar method, we also compared the net charge collected when antiprotons are pulsed onto the degrader with the corresponding number of antiprotons derived from the calculated detection efficiencies in Section 3.2.2. The results are depicted in Fig. 3.14. Although the net charge detected on the degrader has the correct sign, it is not solely due to the deposited antiproton charges.

Antiproton capture and annihilation within a material is a complicated process that produces many energetic particles. This process has been studied theoretically [72] and experimentally [73, 74, 75] for a number of different materials. As low-energy antiprotons are slowed in a material, they are eventually captured in orbit around an atom. They then cascade down to lower energy levels by emitting X-rays and

Auger electrons, until they annihilate near the surface of the nucleus. The 1.9 GeV of energy that is released by the annihilation is converted primarily into pions and short lived mesons that in turn decay into pions. An average of 5 pions, including 3 charged pions, are produced with an average kinetic energy of 230 MeV. Some of these pions pass into the nucleus and are either scattered or absorbed, depositing energy. The resulting intra-nuclear cascade causes the emission of high-energy pions, protons, deuterons, tritons, and even some He nuclei. The Be nuclei may also undergo fragmentation. Further nucleons then evaporate off of the resulting heated nuclei. Many of these particles immediately leave the degrader, while others may be absorbed in the degrader or in nearby electrodes and produce secondary particles.

In order to determine the total charge deposited in the degrader, the charge of the particles leaving the degrader must be subtracted from the charge of the incoming antiprotons. We normally applied a voltage to the degrader that would suppress the emission of negative particles with up to 1 keV of energy, and there was no change in the charge measured when the voltage was reduced to 500 V, but we would expect that many of the particles emitted from the degrader would have much larger energies. Our measurements in Fig. 3.14 suggest that the total charge deposited on the degrader is approximately twice the charge of the antiprotons. The antiproton annihilation process within the degrader is not understood well enough for this to be a reliable method of determining the number of antiprotons released from the trap however. If it were, this would be a good method of calibrating our annihilation detectors.

Although the antiproton charge measurements can not be used to count antipro-

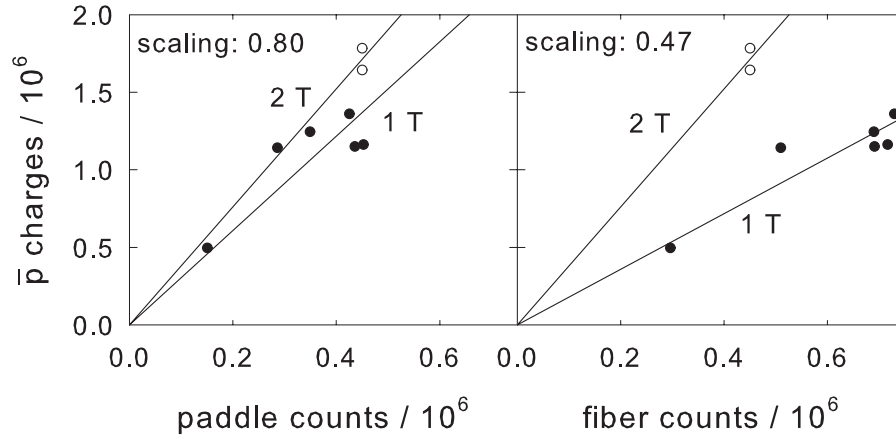


Figure 3.15: The relative detection efficiency of the fiber and paddle detectors at 1 T and 2 T.

tons, they can be used to compare the relative sizes of different collections of antiprotons. This technique was used to measure the relative efficiencies of our detectors at two different values of the magnetic field in the superconducting solenoid. As the magnetic field is changed, it can dramatically affect the operation of the fiber detector photomultipliers, which are close enough to the solenoid coils to experience a large fringing field. As shown in Fig. 3.15, the fiber detector efficiency deteriorates significantly as the magnetic field is increased. The paddle detector efficiency is much less sensitive to the field, primarily because the paddle photomultipliers are designed to operate in a larger magnetic field, and also because they are slightly further away from the solenoid coils.

### 3.2.4 Nondestructive RF Detection

Particles can be counted nondestructively through rf detection of the oscillating image charges induced on an electrode by the center-of-mass motion of the particles.

Previous ATRAP experiments in the first experimental zone at CERN relied heavily upon this method for counting electrons and positrons, largely because the positron accumulation rate was very slow and we could not afford to use destructive counting methods at the time. This counting method had the serious limitation that it could not accurately count more than about 5 million particles. Although we are able to use nondestructive rf detection in the new A-TRAP apparatus, the substantial increases in particle loading rates and the total number of particles typically used has made destructive counting methods highly advantageous, such that it is now almost exclusively used for counting particles. I shall nonetheless give a brief overview of nondestructive rf detection here. A more-complete review of the subject can be found in Ref.[66].

The particles being counted are confined in a potential generated in a three-electrode structure composed of a central “ring” electrode and a “compensation” electrode on either side. The geometry and relative voltages of the electrodes are optimized to minimize anharmonicities in the confining potential Table 2.2 [66, 57]. This establishes a well-defined center-of-mass frequency for the confined particles, although large plasmas may still sample anharmonic regions of the potential.

The axial, center-of mass oscillations of the confined particles produce oscillating image charges on the neighboring compensation electrode. The induced voltage on the compensation electrode in turn acts as a damping force back on the particle motion [76, 77]. When the resulting axial equation of motion of the particles is written in terms of the induced voltages and currents on the compensation electrode, the individual terms in the equation behave like inductive, resistive, and capacitive

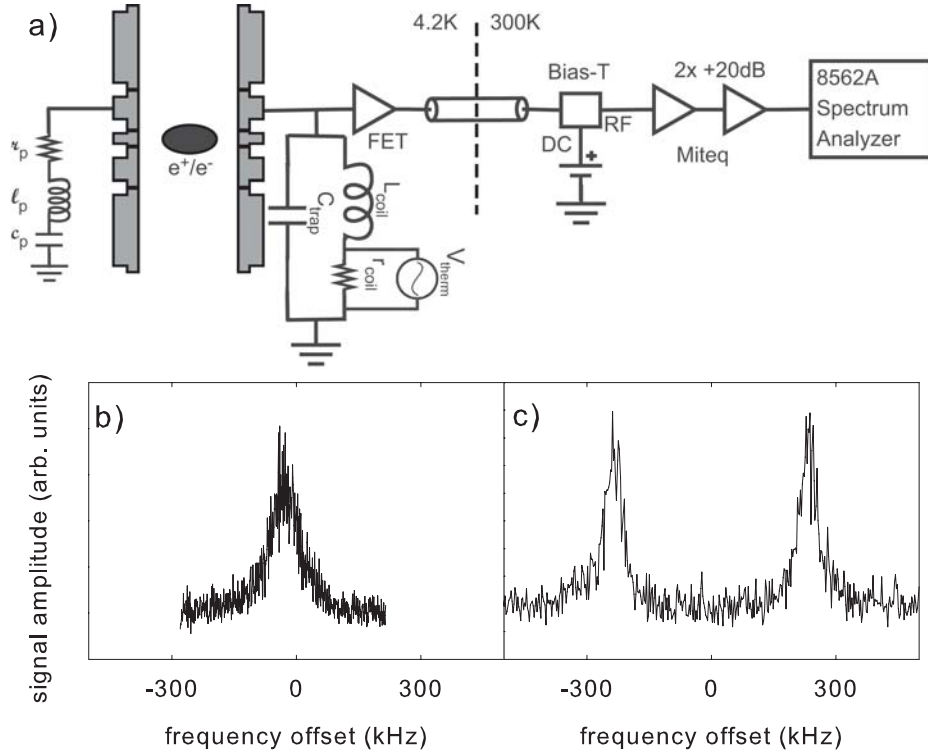


Figure 3.16: (a) The schematic of the electronic circuit used for nondestructive counting of particles [66]. The amplifier signal (b) without particles and (c) with 1 million positrons.

elements. The effect of the particle motion on the voltage of the compensation electrode is therefore equivalent to that of a LRC circuit with values  $l_p$ ,  $r_p$ , and  $c_p$  that are dependent upon the particle number, and with a resonant frequency equal to the particle axial frequency  $\omega_z$ .

The motion of the particles are coupled to an external  $LC$  circuit connected to the compensation electrode, which in turn is connected to a cryogenic amplifier that sends the signal to a spectrum analyzer, as depicted in Fig. 3.16a. In Fig. 3.16a,  $C_{trap}$  is the natural capacitance of the trap electrode and  $r_{coil}$  is the parasitic resistance of the inductive coil. When there are no particles in the trap, Johnson thermal

noise in  $r_{coil}$  drives the circuit and produces a resonant curve like that in Fig. 3.16b. When particles are in the trap, if we tune the particle axial frequency by adjusting the confining potential until  $\omega_z \approx \omega_{LC} = 1/\sqrt{L_{coil}C_{trap}}$ , then the effective particle LRC circuit shorts out the coupled circuit at frequencies near  $\omega_{LC}$ . The resulting power spectrum looks like a dip separating two peaks, as in Fig. 3.16c. The distance between the two peaks is proportional to  $\sqrt{N}$ , and can therefore be used to determine the particle number.

As particle numbers increase, the axial motion of the particles can be damped through coupling to the cyclotron motion or to plasma modes [78], and anharmonicity in the confining potential at large radii can alter the axial frequency, causing problems with nondestructive rf counting of large plasmas. The axial damping alters the  $\sqrt{N}$  dependence of the peak spacing, and the peaks can actually start getting closer together as the particle number continues to increase, as we observed experimentally [66]. This set the maximum number of particles that could be accurately counted in this way at around 5 million in previous experiments. Consequently, this technique was not used very extensively in the A-TRAP apparatus.

## 3.3 Particle Cooling

### 3.3.1 Radiative Cooling

Accelerating charged particles emit radiation, with the radiated power given by the Larmor formula [79]:

$$P_L = \frac{e^2}{6\pi\epsilon_0 c^3} \left| \ddot{\vec{r}} \right|^2 \quad (3.3)$$

$\gamma^{-1}$	$e^+$	$\bar{p}$
Magnetron	$1.5 \times 10^{18}$ s	$1.5 \times 10^{18}$ s
Axial	$2.2 \times 10^6$ s	$7.3 \times 10^{12}$ s
Cyclotron	2.6 s	$1.6 \times 10^{10}$ s

Table 3.4: Radiative damping time constants for particles in the Penning trap, assuming a 100 V confining potential in a radius-length electrode and a 1 T magnetic field.

Because a particle in a Penning trap is accelerated during its cyclotron, magnetron, and axial motion, the energy of each of these motions is damped by radiation [55]. For each of these motions, we can predict a corresponding damping time constant  $\gamma$  given by:

$$\frac{dE}{dt} = -P_L = -\gamma E \quad (3.4)$$

For the cyclotron motion, we can use the relations  $\ddot{\vec{r}} = \omega_c^2 \rho_c$  and  $E_c = \frac{1}{2} m \omega_c^2 \rho_c^2$ , to show that

$$\gamma_c = \frac{e^2 \omega_c^2}{3\pi \epsilon_0 m c^3} \quad (3.5)$$

which is the cooling rate due to cyclotron radiation. For the axial motion, we can use the relations  $E_z = \frac{1}{2} m \omega_z^2 z_{max}^2$  and  $\ddot{z} = -\omega_z^2 z_{max} \sin(\omega_z t)$  to find the average damping constant:

$$\gamma_z = \frac{e^2 \omega_z^2}{6\pi \epsilon_0 m c^3} \quad (3.6)$$

For the magnetron motion, we use the magnetron energy in Eq. 2.8c and  $\ddot{\vec{r}} = \omega_m^2 \rho_m$  to find that the magnetron energy exponentially decreases with the time constant:

$$\gamma_m = \frac{e^2}{3\pi \epsilon_0 m c^3} \frac{\omega_m^4}{\left(\frac{1}{2}\omega_z^2 - \omega_m^2\right)} \quad (3.7)$$

Typical values of these time constants are given in Table 3.4. Present cyclotron damping time constants are approximately 25 times longer than in all previous ATRAP

experiments, due to the fact that we now operate at a reduced magnetic field of 1 T in order to maximize our Ioffe trap depth.

Only the electron or positron cyclotron motion is radiatively damped on a sufficiently short timescale to be relevant for our experiments. For dense plasmas however, collisions between particles will exchange energy between the axial and cyclotron motion. The axial damping rate is therefore set by the rate at which collisions transfer axial energy into cyclotron energy, which is in turn rapidly radiated away.

The rate at which the axial and radial velocity components thermalize via collisions within an electron plasma in a magnetic field was calculated by Glinsky *et al.* [80]. In this model, the thermalization rate is given by:

$$\Gamma = n\bar{v}\bar{b}^2 I(\bar{k}) \quad (3.8)$$

where  $n$  is the electron or positron density,  $\bar{v} = \sqrt{2k_B T/m}$  is the thermal spread for the relative velocity distribution,  $\bar{b} = 2e/(4\pi\epsilon_0 k_B T)$  is twice the classical distance of closest approach, and  $\bar{k} = \omega_c \bar{b}/\bar{v} = (\bar{b}/\rho_c)/\sqrt{2}$  is a dimensionless term that depends upon the magnetic field strength. The dependence of this calculated thermalization rate on magnetic field is given by the function [80]:

$$I(\bar{k}) \simeq \exp\left(-\frac{5(3\pi\bar{k})^{2/5}}{6}\right) \left[ \frac{1.83}{\bar{k}^{7/15}} + \frac{20.9}{\bar{k}^{11/15}} + \frac{0.347}{\bar{k}^{13/15}} + \frac{87.8}{\bar{k}} + \frac{6.68}{\bar{k}^{17/15}} \right] \quad (3.9)$$

In a strong magnetic field, the thermalization rate is exponentially small because the total cyclotron action ( $J = \sum_j m v_{\perp j}^2 / 2\omega_c$ ) is an adiabatic invariant when the collision duration is much longer than the cyclotron period (when  $\bar{k} = \omega_c \bar{b}/\bar{v} \gg 1$ ). It is therefore worth noting that although the cyclotron cooling rate decreases as the magnetic field is decreased, the rate at which axial energy is converted into cyclotron

energy actually increases. The theoretical predictions from Eq. 3.8 and Eq. 3.9 are in good agreement with experimental measurements for  $10^{-6} \leq \bar{k} \leq 10^2$  [80].

Using the positron plasma parameters relevant for the antihydrogen production experiments discussed in Chapter 7,  $n = 4 \times 10^7 \text{ cm}^{-3}$ ,  $T = 4.2 \text{ K}$ , and  $B = 1 \text{ T}$ , we find  $\bar{k} = 124$ , and the calculated thermalization time constant is  $\Gamma^{-1} = 33 \text{ ms}$ . This suggests that our plasmas should be in very good thermal equilibrium with the 4.2 K trap, assuming that we allow sufficient time for cyclotron cooling. If we were to increase the magnetic field to 5 T, as was used in many previous ATRAP experiments, then  $\bar{k} = 620$  and Eq. 3.9 predicts that the time constant would be dramatically increased to 12 hours. Using such a calculation, some have suggested that the axial energy of our particles in previous experiments at 5 T should not have been in thermal equilibrium with the trap temperature [81]. However, it seems tenuous to assume that the form of Eq. 3.9 will continue to be accurate at such large values  $\bar{k}$ , without further experimental evidence. Previous experimental observations within our group using  $B = 5 \text{ T}$  suggest that energy is collisionally transferred between axial and cyclotron motion much more rapidly than indicated by Eq. 3.9, and that the axial motion should have been in thermal equilibrium for previous experiments as well [82].

Antiprotons do not cool via cyclotron radiation over timescales that would be relevant for our experiments. Consequently, both the antiproton cyclotron and axial motions are sympathetically cooled via collisions inside of an electron plasma. The axial motion of particles can also be damped by coupling to a cold external resistor, as discussed in Section 3.2.4, but this tends to be a slow process [83].

### 3.3.2 Sideband Cooling

The magnetron radius of a particle increases as energy is lost from the magnetron motion. Fortunately, the magnetron energy has a very long time constant for radiative decay, as indicated in Table 3.4. To decrease the magnetron radius of particles, we must actively add energy to the magnetron motion. The relatively low magnetron frequency makes direct coupling to the motion by external fields very weak. We can however excite the axial and magnetron motions simultaneously by applying a drive at frequency  $\nu_z + \nu_m$ , a technique commonly referred to as “sideband cooling” [55].

In a quantum mechanical picture, the applied drive frequency excites the axial and magnetron motion both by one energy level, and the axial energy then returns to its original level via spontaneous emission, causing only a net increase to the magnetron energy. In practice, the axial energy of the particles is typically damped by coupling the axial motion to an external resistor, as discussed in Section 3.2.4. The particles are stored in an electrode geometry with a very harmonic potential so that the axial frequency is well defined, and the sideband cooling drive is applied to a half-split electrode to meet the necessary symmetry requirement.

This technique is very effective for small numbers of particles, but becomes much less effective for dense plasmas, where the space charge screens external fields and the appropriate drive frequencies are not well defined. Because our typical electron and positron plasmas number in the tens of millions, sideband cooling was not extensively used in recent experiments. For dense plasmas like these, a more effective method for radially compressing the plasmas is to increase the plasma rotation frequency using a rotating wall potential [84]. A rotating wall potential can be applied to a

four-split electrode in either of two locations within the A-TRAP Penning trap, and the required electronic equipment has been set up for this process. There has been insufficient time to systematically develop this technique in our Penning traps thus far, but there are plans to do so in the near future.

# Chapter 4

## Particle Loading

### 4.1 Electrons

Electrons perform several critical functions in our experiments. Within the large magnetic field inside our Penning traps, they rapidly lose energy via cyclotron radiation and equilibrate with the cryogenic environment. This makes them ideal for collisionally-cooling more energetic charged particles, and they are key to both the antiproton and positron loading processes. Because electrons have the same mass and equal magnitude but opposite sign charge as positrons, they can be used to replicate processes involving positrons by simply reversing the sign of the confining electric potentials used in the two cases. Large numbers of electrons can be loaded more quickly and easily than positrons, so they are frequently used to test the stability of electron plasmas in various electrostatic field configurations and as diagnostics for our various plasma measurement and manipulation techniques before positrons are employed.

We capture electrons that are liberated from a photocathode via the photoelec-

tric effect using intense UV laser pulses, a technique that was recently developed by ATRAP and demonstrated for the first time in a cryogenic Penning trap [23]. It was first used in a completely sealed vacuum enclosure cooled to 4 K, and is therefore compatible with the extreme high-vacuum conditions that are desirable for long-term antimatter confinement. This technique allows us to load electrons much more rapidly and to accumulate larger numbers of electrons than was possible using previous electron-loading methods.

#### 4.1.1 Previous Methods for Loading Electrons

In earlier ATRAP experiments, we used a beam of electrons that tunneled out of a sharp field emission point (FEP) kept at 4 K and biased to approximately -700 V. This produced about a 10 nA ( $\sim 6 \times 10^{10}$  e<sup>-</sup>/s) beam that was constrained to move along the magnetic field line from the tip of the FEP. The electrons emitted were too energetic to trap directly, but were able to liberate cryo-pumped gas on the trap wall where the beam struck. A static potential well was applied in the trap, and electrons colliding with the liberated gas in the well volume could either lose enough energy in the collision to be captured or ionize the gas, freeing electrons with an energy low enough that they are captured. Collisions between the electron beam and the electrons already captured could then further accelerate the loading process.

The FEP loading procedure produced very energetic electron plasmas that then took a long time to cool and center in the trap, and it was difficult to reliably and reproducibly load more than 10 million electrons this way. Furthermore, the electron beam would collisionally heat any other particles already in the trap, ions generated

by the loading process could be captured with the particles, and the FEP loading efficiency decreased over time as all gas was gradually desorbed from surface that the electron beam struck. Another possible technique for loading electrons into a cryogenic Penning trap, thermionic emission of electrons from a hot filament, can cause a significant heat load on the trap and also causes the release of atoms and molecules that can be ionized and captured with the particles in the trap. The new photoemission loading technique avoids the pitfalls inherent in these methods.

### 4.1.2 Electrons Loaded from Photoemission

The apparatus used for loading electrons via photoemission is depicted in Fig. 4.1. A KrF excimer laser produces 248 nm light pulses with up to 18 mJ of energy and 2 MW peak power with a maximum repetition rate of 250 Hz. This light is directed through a lens and vacuum window into the room-temperature vacuum space above the Penning trap, where it is reflected by a 45° mirror to a vertical path aligned with the trap electrode stack 2 m below. Positrons pass along this same path to the trap from the positron accumulator, so the mirror can be retracted under remote-control when electrons are not being loaded to allow positrons to pass. It can then be repositioned with sufficient reproducibility to allow laser pulses to be sent down to the trap without optics realignment. In the cryogenic region of the apparatus directly above the electrode stack, the position of a 6" conflat flange with welded bellows on either side can be adjusted using a movable stage controlled from the outside of the apparatus (Section 2.3.6). This flange has a number of different windows on it, and by changing the position of the stage, either the photoemission assembly in Fig. 4.1

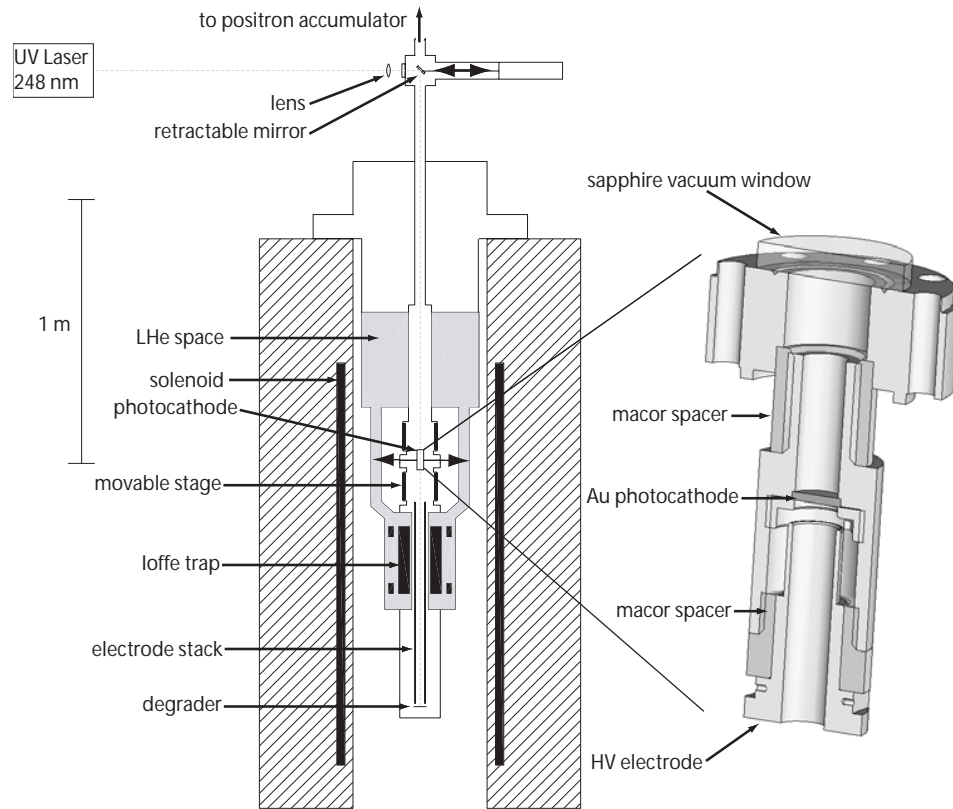


Figure 4.1: The apparatus for loading photoelectrons into the A-Trap Penning trap using excimer laser pulses.

or a small hole to allow positron access can be aligned with the central axis of the electrode stack (Fig. 2.21). Electrons were initially loaded using the photoemission assembly with the cryogenic vacuum space of the Penning trap completely sealed (without a hole for positrons), but at later dates the hole was typically left on-axis to allow either laser light or positrons to pass through it without moving the position of the flange.

When the photoemission assembly was on axis, the laser light was directed through a vacuum window onto a 6 mm diameter sapphire window with a 15 nm thick gold film evaporated onto it. The gold layer served as the photocathode from which the

electrons were emitted via the photoelectric effect. Gold was chosen despite its relatively low quantum efficiency because its photoemission is robust and reproducible even after being exposed to air, and because its 4.7 eV work function is less than the 5.0 eV energy of the photons from the excimer laser.

When the positron hole was on axis, light passed through the electrode stack to the degrader, a beryllium foil primarily used for slowing antiprotons, but that served also as the photocathode in this application. Although the positron hole was only 1 mm in diameter and 1.3 cm long, it was possible to pass sufficient light through it to produce large numbers of photoelectrons.

There were gold-plated faraday cups positioned around the top perimeter of both the photoemission assembly and the positron hole that allowed us to measure the charge of electrons emitted from the faraday cups if stray laser light hit them (Fig. 4.8). Along with measuring the charge emitted from the photocathode itself, this allowed us to determine the position of the laser beam 2 m within the cryogenic apparatus and to adjust the path of the beam from outside the apparatus onto either the center of the gold-plated window or through the positron hole.

The potentials used for loading electrons into the lower portion of the electrode stack are depicted in Fig. 4.2a for electrons emitted from the gold-coated window above the electrode stack, or alternately in Fig. 4.2b for electrons emitted from the degrader by incident light passing through the 1 mm hole. In either case, electrons are emitted during a narrow time window set by the duration of the laser pulse (about 10 ns), and with a narrow energy distribution of only a few eV. As the electrons approach the confining well, a potential barrier is briefly removed as they pass by

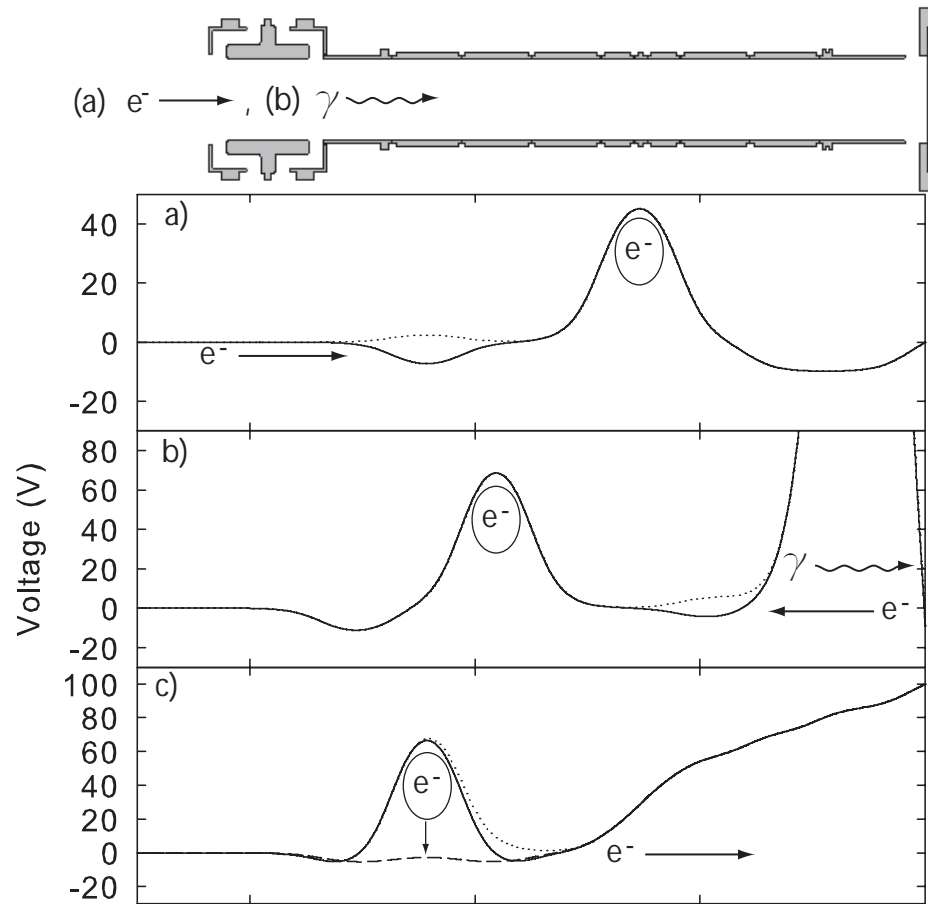


Figure 4.2: The potentials typically used to load electrons (a) from the photoemission assembly or (b) from the degrader. (c) The electrons are counted by sequentially pulsing them onto the degrader and measuring their charge.

using a voltage pulse from a saturated switch (dotted curves in Fig. 4.2a,b). This barrier is restored before they have time to reflect off of the potential behind the confining well and return in the opposite direction, trapping those electrons that have less energy than the barrier height. The delay between the laser pulse and the time when the barrier is restored is optimized to maximize the number of trapped electrons. Collisions between trapped electrons convert their axial energy to cyclotron

energy, which is lost via cyclotron radiation (Section 3.3.1), allowing the electrons to axially cool to the bottom of the confining well. Subsequent laser pulses can then be used to load more electrons in the same fashion while keeping those electrons already in the well. The electron-loading efficiency decreases as the magnetic field is reduced due to the increased cyclotron cooling time required. The 0.1 s time constant for cyclotron cooling at 5 T is reduced to 2.6 s at 1 T. Consequently, the laser repetition rate had to be reduced to 1 Hz to give optimal electron loading at this field, since faster repetition rates did not allow sufficient time for the confined electrons to cool before more energetic electrons were added.

The number of electrons that can be accumulated is ultimately limited by the depth of the confining well. The electrons will continue to fill the well until the potential of their space charge equals the axial confining potential, after which point any addition electrons will spill out axially. Our typical procedure for counting large numbers of particles takes advantage of this principle, and is depicted in Fig. 4.2c. The barrier separating the well from the ramp to the degrader is briefly reduced by a voltage pulse (dotted curve) to allow electrons near the top of the potential well to escape to the degrader, where their charge is counted (Section 3.2.1). The depth of the well is then decreased and the process is repeated in small increments until no electrons remain (dashed curve). This process allows us to determine the potential energy distribution of electrons in the well (Fig. 4.3), and the sum of the counts gives us the original number of electrons.

Up to 100 million photoelectrons are emitted during each laser pulse, and more than 10 million of these can be captured in the Penning trap. The specific number of

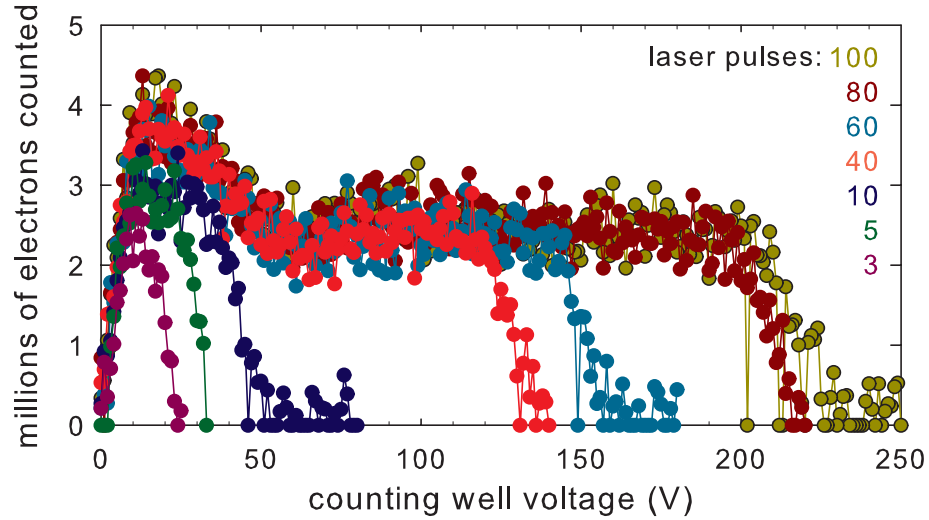


Figure 4.3: Electrons released as their confining well depth is incrementally decreased, showing the potential energy distribution of electrons loaded from various numbers of laser pulses.

electrons emitted is dependent upon the electric field at the surface of the photocathode, as depicted in Fig. 4.4a. At low electric fields, the space charge of photoelectrons near the surface of the cathode inhibit the emission of further electrons. By increasing the electric field that accelerates the electrons away, we rapidly overcome this effect and operate in a regime where the number of electrons emitted is roughly linear with the applied field. This is due to the Schottky effect, whereby the applied field opposes the potential confining the electron in the metal, effectively lowering the work function [85]. The 5.0 eV photons from the laser were consequently able to easily liberate electrons from the degrader with a sufficiently large field, even though the natural work function of beryllium is 5 eV.

Although the photocathodes can be independently biased to a given voltage, the majority of the electric field at the photocathode surface is generated by applying

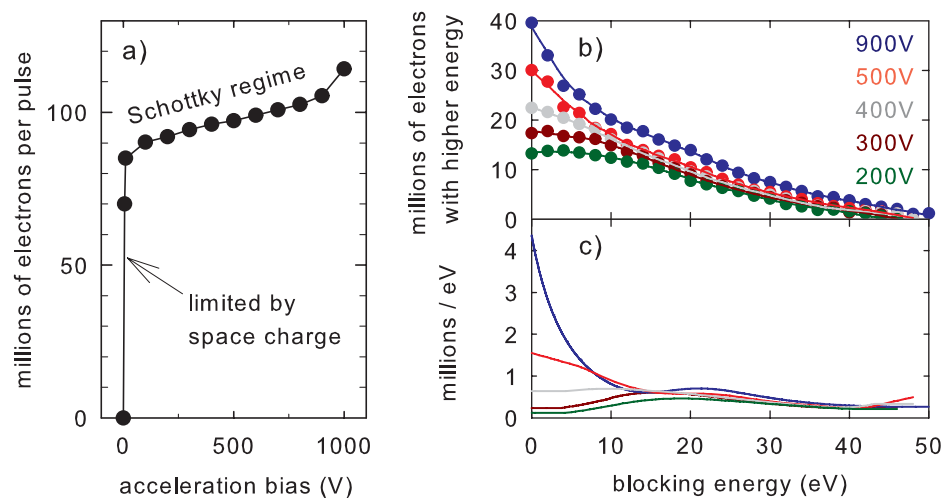


Figure 4.4: (a) Room temperature measurements demonstrate that more electrons are emitted as the bias accelerating them away from the gold photocathode is increased. (b) The number of emitted electrons that have more energy than a given blocking potential for various accelerating biases, and (c) the derivative of the curves indicate their energy distribution.

a large positive voltage to the ring electrode closest to it. For the photoemission assembly, this is the “HV electrode” in Fig. 4.1. Although electrons accelerate as they enter the electrode, they decelerate by the same amount as they leave it. By measuring the potential required to block electrons exiting the photocathode, we were able to determine the typical energy distribution of the photoelectrons, and found that more low-energy electrons are emitted by biasing the ring electrode to a large voltage (Fig. 4.4b,c).

The number of electrons confined in the Penning trap is linear with the number of laser pulses used, and up to 1 billion electrons have been loaded in this fashion (Fig. 4.5a). The particular loading efficiency depends upon the laser intensity and alignment however, both of which can vary over time. In order to obtain a well-defined

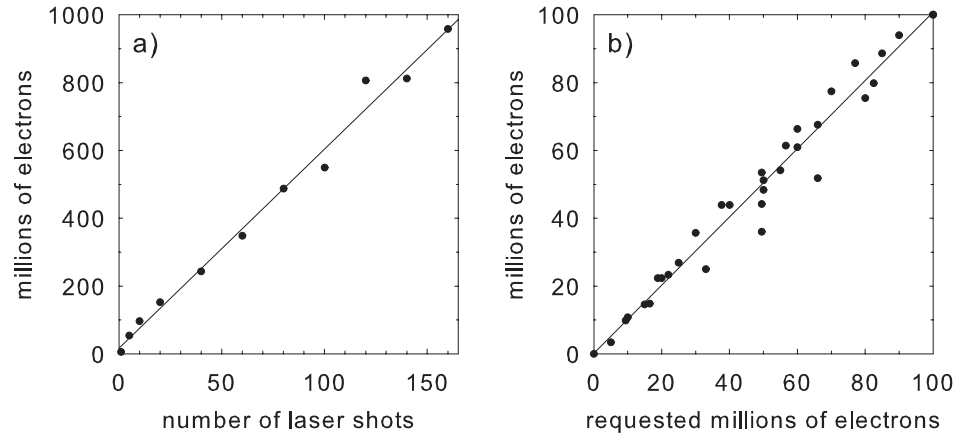


Figure 4.5: The number of electrons loaded is (a) linear with the number of laser pulses used, and (b) a lower linear loading rate that is insensitive to variations in laser intensity and alignment is achievable by lowering the electron confining potential to spill electrons above a certain number.

number of electrons that is independent of these fluctuations, an excessive number of electrons can be loaded and then reduced to a well-defined number by lowering the confining potential to a pre-calibrated value to spill out the extra electrons (Fig. 4.5b). As such, the electron loading procedure is very robust and reproducible.

## 4.2 Positrons

In order to form antihydrogen, we must accumulate large numbers of positrons. Positrons are readily emitted from some radioactive sources, and the large kinetic energy of the emitted positrons can be reduced by passing them through a thin moderator. The resulting positrons emerging from the moderator typically have a few eV of energy, characterized by the negative positron work function of the moderator material [67], but an additional energy-loss mechanism is required to confine

positrons inside a Penning trap. Positrons are presently trapped within a Penning trap geometry after losing energy through collisions with a buffer gas [86]. This is the first application of this method within the ATRAP collaboration, and it required the construction and testing of both an external positron accumulator and a positron guide for linking the accumulator to the cryogenic Penning trap, which will be the focus of this section.

### 4.2.1 Previous Method of Loading Positrons

Positrons were accumulated in previous ATRAP experiments by field ionizing strongly-magnetized Rydberg positronium in a static electric confining potential [9, 65]. The positronium was produced as a result of moderating positrons in a 2  $\mu\text{m}$  thick tungsten crystal in a strong magnetic field. This method had the substantial advantage that positrons could be loaded through a 10  $\mu\text{m}$  thick titanium window into a completely sealed vacuum enclosure, and it was therefore compatible with the lowest vacuum levels achievable by cooling such a vacuum enclosure to cryogenic temperatures [62]. Because no substantial external apparatus was required, it was also the first method that allowed the accumulation of substantial numbers of cold, trapped positrons. This method had several serious disadvantages however. The formation of Rydberg positronium was critically dependent upon an absorbed gas layer on the tungsten moderator, which was not well understood, and which also could be removed through various processes within the trap. The positron accumulation rate grew quadratically with magnetic field, making accumulation at low magnetic fields difficult. Most importantly, the positron accumulation rate was approximately

$7 e^+/\text{s} \cdot \text{mCi}$  [65], dependent upon the radioactive source strength, roughly a thousand times lower than the best loading rates reported using buffer-gas accumulators [10].

Our goal of producing antihydrogen within a Penning-Ioffe trap required being able rapidly load large numbers of positrons on a regular basis, and was therefore not compatible with the relatively-low loading rate of the Rydberg positronium ionization method. The best available alternative, buffer-gas accumulation of positrons, presented the associated challenge of isolating the relatively low vacuum of the accumulator from the extremely low vacuum of the cryogenic Penning trap while maintaining a path for positrons to be transported between the two. Introducing even small amounts of background gas into the Penning trap would greatly decrease the antiproton confinement times in the trap due to annihilations with background gas. As will be discussed, this potential problem was effectively avoided by separating the vacuum spaces by large distances and with a cryogenic pumping restriction.

### 4.2.2 Buffer Gas Positron Accumulation and Transfer

The positron accumulation and transfer system was designed, constructed, and tested by members of the ATRAP collaboration from York University. The design of the positron accumulator was based upon a previous design by Surko *et al.* [86]. This section will briefly describe the operation of our accumulator. A more thorough description of the apparatus can be found in [87].

The positron accumulator and transfer system are depicted in Fig. 4.6. The experimental zone at CERN that contains the superconducting solenoid and the A-TRAP Penning trap was not large enough to contain the positron accumulator as well. As

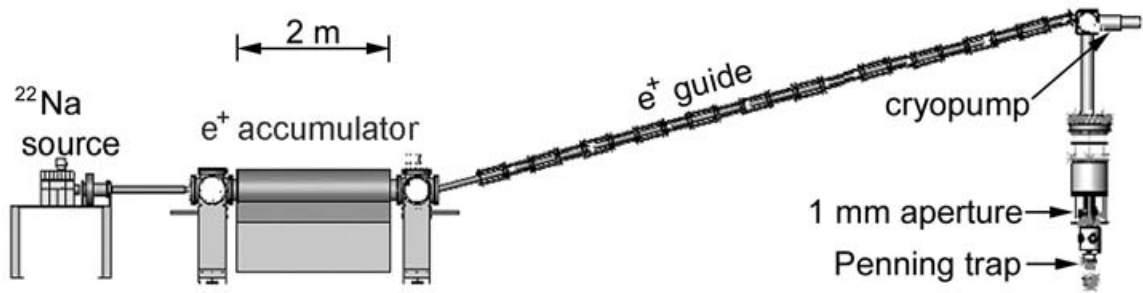


Figure 4.6: The positron accumulation and transfer system.

such, another experimental zone was established to contain the positron accumulator, and the two zones were linked by a 7 m long positron guide to deliver the positrons into the Penning trap.

A  $^{22}\text{Na}$  radioactive source is used to produce positrons during 90% of its radioactive decays. This isotope has a half life of 2.6 years, and strength of our source was roughly 40 mCi at the time of these experiments. The source is sealed in a titanium capsule, which is mounted inside a vacuum chamber that is surrounded by lead blocks to attenuate the radiation to safe background levels outside of the enclosure. Positrons emerge from the thin titanium window on the front of the source capsule, and a fraction of these have their kinetic energy reduced to roughly 15 eV after moderation within a solid neon moderator that is frozen onto a surface near the source window using a cryocooler. A solid neon moderator was chosen because of its high positron moderation efficiency [88, 89]. The moderated positrons are then guided from the source enclosure into the positron accumulator by the magnetic field of a solenoid wound on the vacuum tube connecting the two.

The positron accumulator is depicted in Fig. 4.7. The accumulator has a cylindri-

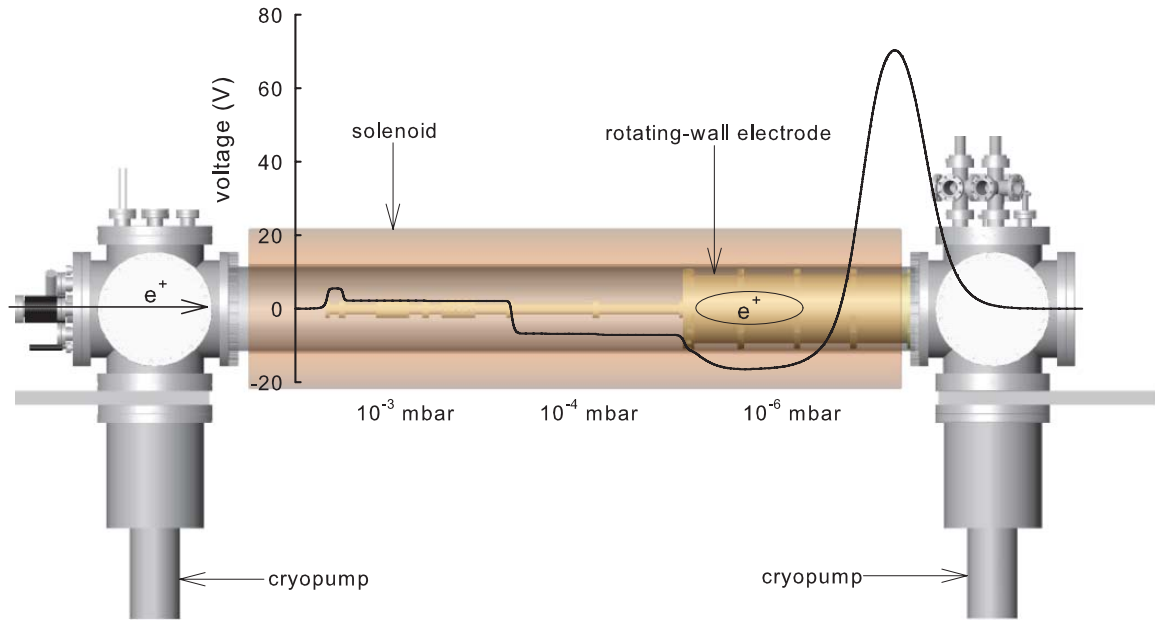


Figure 4.7: The buffer-gas pressures and electric potentials used to trap positrons in the positron accumulator.

cal Penning trap design, and is surrounded by a water-cooled solenoid that generates a 0.14 T field. The electrodes have incrementing diameters that also serve to regulate differential pumping across the accumulator length and establish three sections with differing pressure. Nitrogen buffer gas is introduced in the high-pressure section indicated, and is differentially pumped away by cryopumps on either side of the accumulator. Positrons from the source enter the accumulator from the left after passing a small voltage barrier. The pressure in the accumulator is regulated to optimize the probability that positrons entering the accumulator will lose kinetic energy through a collision with nitrogen gas during a single pass through the trap and will therefore be captured in the long well spanning all three sections of the accumulator. Additional collisions with background gas channel the positrons into deeper parts of the confin-

ing well until they are concentrated in the low-pressure section of the accumulator. Increasing the gas pressure beyond the minimum required level would be detrimental because it would lead to larger rates of positron annihilation and radial expansion of the confined positron plasma. Radial expansion of the positron plasma is suppressed by applying a rotating-wall potential to the split “rotating-wall electrode” indicated. In this way, 26 million positrons are typically accumulated during each 50 s accumulation cycle. At the end of each accumulation cycle, the positrons are launched down the positron guide toward the A-TRAP apparatus in a single bunch using a rapidly-applied voltage pulse.

The positron guide consists of a 7 m long vacuum pipe surrounded by solenoid windings and trim magnets. In addition to the magnetic field along the central axis of the pipe generated by the solenoid, 95 trim coils along the positron guide are independently controlled to cancel external magnetic fields within the building. Positrons will follow the magnetic field lines within the vacuum tube, and if these field lines intersect the walls of the tube, the positrons will annihilate. The annihilation signal is monitored as a function of time after the positrons are launched out of the accumulator, and the time delay of any annihilation signal can be used to determine the corresponding location of the annihilations. The trim coils can then be adjusted to redirect the field line until positrons reach the end of the guide. Because external fields within the building change as a function of time during the antiproton deceleration cycle, the positron transfer pulse has to be synchronized with the antiproton deceleration cycle for successful transfer.

The positron guide is sloped upward slightly to avoid the large fringing field of the

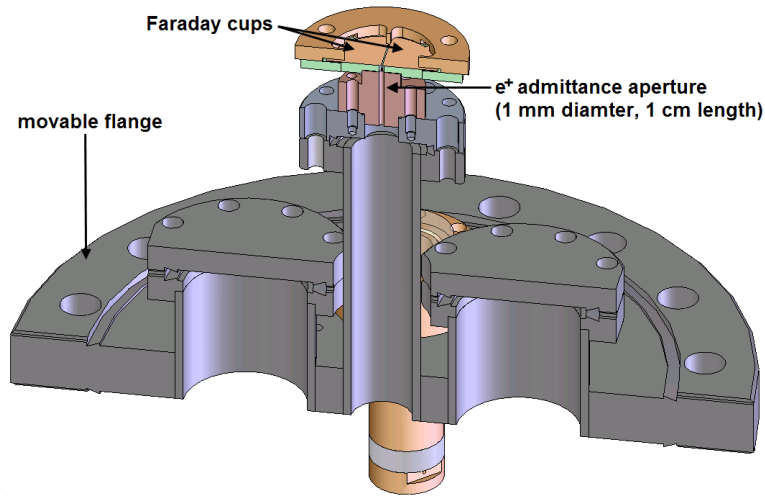


Figure 4.8: The positron-admitting aperture into the cryogenic Penning trap.

superconducting solenoid surrounding the A-TRAP apparatus, until the end of the guide is reached. At the end of the positron guide, the positrons make an abrupt  $105^\circ$  change in direction and are guided by the fringing field lines from the superconducting solenoid the rest of the way into the cryogenic Penning trap. An additional cryopump is also located at this abrupt bend in order to reduce the pressure in this region of the transfer line below the  $10^{-9}$  Torr level.

Once the positrons are on a downward trajectory into the superconducting solenoid, they transition into a 1 T magnetic field and are radially compressed. They have sufficient kinetic energy to overcome magnetic bounce forces due to the magnetic field gradient. The positrons pass through a set of vacuum bellows extending into the cryogenic region of the A-TRAP apparatus. Directly above the Penning trap electrode stack, there is an aperture that is 1 mm in diameter and 1.3 cm long that allows the positrons to enter into the Penning trap vacuum space (Fig. 4.8). The aperture is held

at a temperature of 4 K and is mounted on a vacuum flange that can be translated in both dimension of the horizontal plane using the XY translation stage described in Section 2.3.6. Most background gas passing through the aperture will tend to stick to the cold walls rather than bounce off of them, and the dimensions of the aperture are chosen to minimize line-of-sight paths for background gas into the Penning trap vacuum. Additionally, charcoal is mounted to the 4 K vacuum flange to maximize the cryopumping capacity around the positron aperture. This minimizes the gas that is transferred from the good vacuum in the positron transfer system into the exceptionally good vacuum of the Penning trap. We set an upper limit on the pressure inside the cryogenic Penning trap of  $3 \times 10^{-16}$  Torr based upon antiproton lifetime measurements, as discussed in Section 2.3.7. After the trap is initially evacuated and cooled, gas slowly leaks into the cold trap however, and this pressure may get worse with time.

The positrons can be steered through the aperture by measuring the charges collected on four Faraday cup quadrants above the positron aperture, as well as the charge of positrons passing through the aperture and striking the degrader below the electrode stack. The positron trajectory can be changed by varying the positron guide magnet currents, or the position of the aperture can be changed using the XY translation stage. Of the 26 million positrons launched out of the accumulator, more than 17 million typically reach the top of the positron aperture, and 10 million of these pass through the aperture into the electrode stack. The profile of the positron beam can be probed by measuring the positron charge collected on the degrader as a function of the position of the 1 mm aperture, as depicted in Fig. 4.9. Based on this

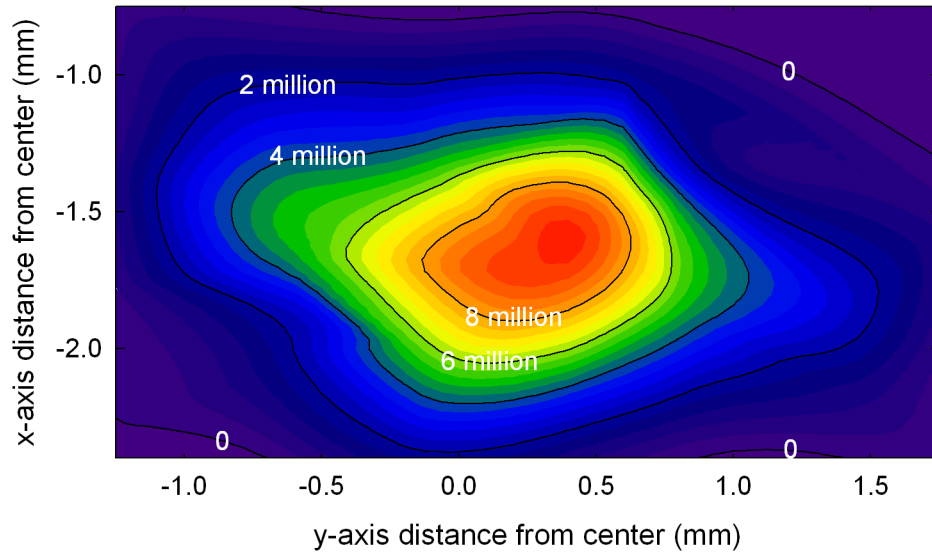


Figure 4.9: The number of positrons striking the degrader as a function of the position of a 1 mm diameter aperture.

data, the positron aperture diameter was subsequently expanded to 1.5 mm to allow greater positron transmission.

We measure that positrons arrive at the degrader approximately within a 500 ns wide time window and with a 10 eV energy spread. The majority of the upper electrode stack is utilized to capture these positrons in flight, while the lower electrode stack can be simultaneously utilized to load antiprotons. The potentials used for loading positrons into the Penning trap are depicted in Fig. 4.10. To confine the positrons in a single electrode, the axial kinetic energy of the positrons must be reduced by many eV within the 50  $\mu$ s positron loading cycle time. We find experimentally that the positrons cool much more rapidly and efficiently if they are collisionally cooled with electrons that are preloaded into the long positron catching well. We load 150 million electrons and transfer them into the nested well structure in Fig. 4.10.

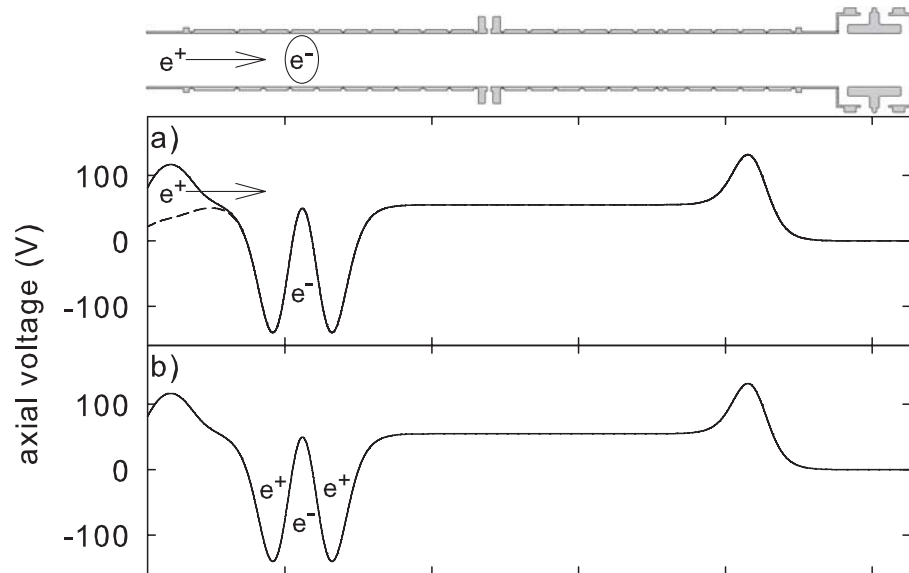


Figure 4.10: The potentials used for loading positrons into the Penning trap. (a) A barrier potential is removed by a voltage pulse (dashed curve) to allow the positrons to enter the trap, and (b) the positrons are trapped in the long well until they lose energy through collisions with electrons and cool into the side wells of a nested well structure.

Positrons are allowed to enter the electrode stack by briefly lowering a blocking potential at the entrance of the stack (Fig. 4.10a). The potential is restored before the positrons can reflect off of the lower potential and exit the stack, trapping the positrons. Axial energy is converted into cyclotron energy through collisions between positrons and electrons, and this cyclotron energy is lost via cyclotron radiation. The maximum rate at which electrons or positrons may come into thermal equilibrium with the trap temperature is set by the 2.6 s time constant for cyclotron cooling at 1 T (Section 3.3.1). The resulting low-energy positrons are cooled into confining wells on either side of electron plasma in a nested well structure (Fig. 4.10b).

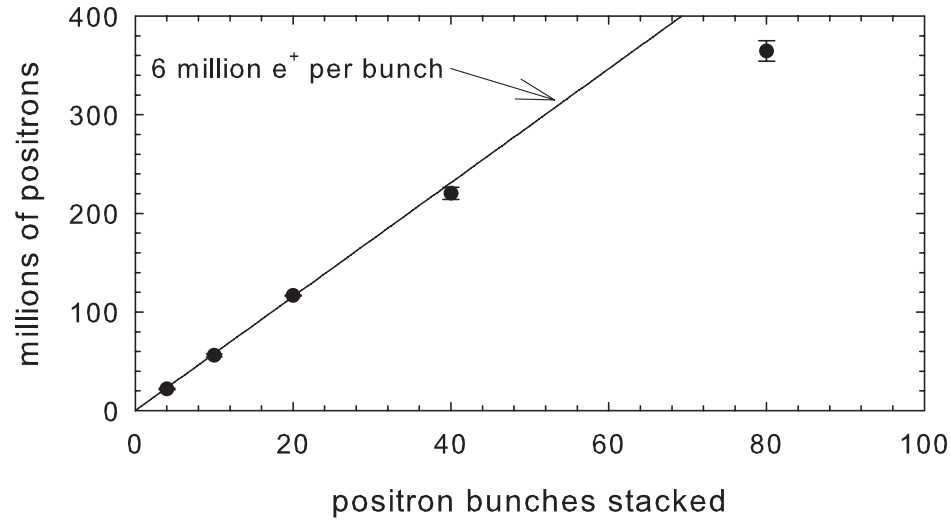


Figure 4.11: Positrons loaded into the Penning trap as a function of the number of positron bunches stacked.

Multiple bunches of positrons can be loaded using a single electron plasma by repeating the procedure outlined above. Once the desired number of positrons have been loaded, the electron plasma can be spilled out of the trap and the collected positrons can be unified in a confining potential in a single electrode. The number of positrons loaded is very linear with the number of positron bunches stacked, up to about 200 million positrons (Fig. 4.11). Approximately 6 million positrons are loaded per positron bunch from the accumulator, and as many as 360 million positrons have been loaded into the trap. Two bunches of positrons are loaded into the trap for each antiproton bunch that is loaded simultaneously.

## 4.3 Antiprotons

In order to form cold antihydrogen atoms, it is necessary to accumulate large numbers of cold antiprotons. We receive antiprotons from CERN with an initial kinetic energy of 5.3 MeV and subsequently reduce their energy by 10 orders of magnitude within a Penning trap until they are at equilibrium with the 4.2 K (0.345 meV) temperature of the trap. To do this, we utilize techniques initially developed by the TRAP collaboration [90], the predecessor of ATRAP. This involves slowing the antiprotons in matter [91], catching these slowed antiprotons within the Penning trap [7], and then further cooling them to 4.2 K through collisions with electrons [8]. By repeating this process for multiple bunches of antiprotons received from CERN, we are able to accumulate on the order of a million cold antiprotons [92]. These techniques have been used for antihydrogen experiments for a number of years [19], but this section will focus on recent antiproton accumulation results in a new apparatus that is compatible with magnetic trapping of antihydrogen atoms.

### 4.3.1 Antiproton Production and Delivery at CERN

Presently, the only source of low-energy antiprotons in the world is the Antiproton Decelerator (AD) at CERN, near Geneva, Switzerland. The antiproton production and deceleration process begins with the extraction of a bunch of roughly  $10^{13}$  protons with a momentum of 26 GeV/c from the Proton Synchrotron (PS) at CERN. These protons are directed onto an iridium target, producing approximately 35 million antiprotons at 3.5 GeV/c that are guided into the AD ring depicted in Fig. 4.12. In a series of steps, the antiprotons are then decelerated to 100 MeV/c (kinetic energy of

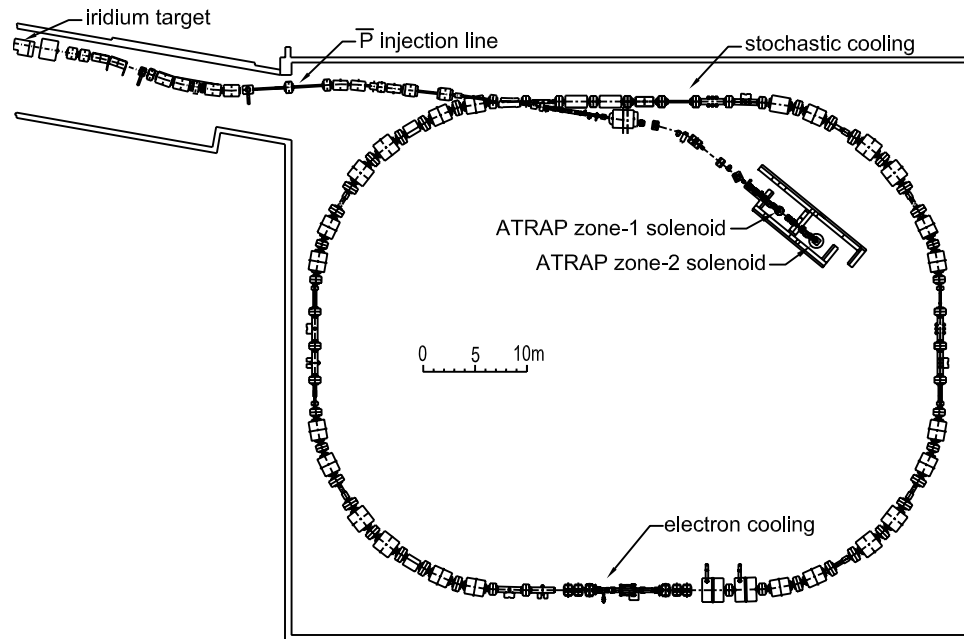


Figure 4.12: The Antiproton Decelerator storage ring at CERN.

5.3 MeV) over 100 seconds in the AD ring while employing first stochastic cooling and then electron cooling to maintain a small momentum spread in the beam. This typically results in a 200 ns duration bunch of 35 million antiprotons that can then be ejected from the ring toward our experiment. By setting the currents in the magnets leading up to our experiment, we can then direct the beam vertically up into either of the superconducting solenoids in our two different experimental zones, and steer the beam into a Penning trap in either location.

### 4.3.2 Antiproton Steering and Energy Tuning

In order to load the antiprotons into a Penning trap, the antiproton beam must be steered into the center of the trap electrodes. The beam trajectory is adjusted

by changing the currents in the steering magnets along the beam pipe leading up to our experiment, and the position of the beam with respect to the center of the electrodes is monitored using a parallel plate avalanche counter (PPAC) [93, 94]. The PPAC consists of two sets of anode-cathode pairs, each of which are biased to a 75 V potential difference and separated by a 1 atm layer of slowly-flowing argon gas. The cathodes are thin aluminum-coated mylar sheets and the anodes are similar sheets where the aluminum layer has been divided into 5 strips that are 2 mm wide with a 0.5 mm gap between each strip. The antiproton beam is initially on a horizontal path from the AD ring, but is steered to a vertical trajectory to match the symmetry axis of our trap. The PPAC is located below the electrode stack (Fig. 2.10), with the anode-cathode sheets oriented in the x-y plane perpendicular to the beam trajectory (Fig. 4.13). The aluminum strips on one anode sheet are oriented in the x direction, along the original path of the beam from the AD ring, while the strips on the other anode sheet are in the y direction. The aluminized-mylar and argon-gas layers are sufficiently thin to allow the antiprotons through the PPAC with only a minimal loss in their kinetic energy.

As the antiprotons pass through the PPAC, they are able to ionize the argon atoms that they collide with, and the liberated electrons are accelerated toward the anode strips by the applied electric potentials and are collected there. Under our typical operating conditions, the PPAC operates in a linear rather than an avalanche mode, and the number of electrons liberated in a certain region is simply proportional to the number of antiprotons passing through that region. The electrons are constrained to move along the vertical field lines of the superconducting solenoid. By measuring the

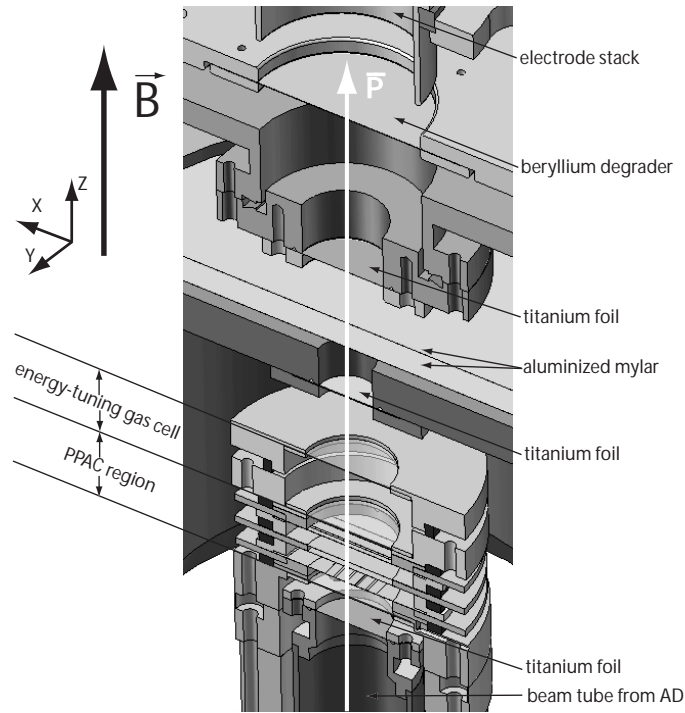


Figure 4.13: The path of antiprotons before entering the trap.

charge collected on each of the 5 x-axis and 5 y-axis anode strips, we are therefore able to determine the size and position of the antiproton beam for each bunch of antiprotons received. We are typically able to steer and focus the beam well enough to have nearly all of the antiprotons within a single 2 mm wide strip in both the x and y-axis near the center of the trap.

The number of ions generated in the PPAC is proportional to the intensity of the antiproton beam. Because of the small gaps between the anode strips however, not all of the charge is collected, and the total signal is dependent upon the beam profile and steering. As an alternate measure of the fluctuation in the intensity of the beam from shot to shot, we use a plastic scintillator placed inside of the zone. As a large portion

of the antiprotons annihilate upon entering the trap, some of the pions produced strike the scintillator and produce light that is measured by a photomultiplier. The integrated signal from the scintillator is proportional to the number of antiprotons in the bunch.

In order to load the antiprotons from the AD into a Penning trap, the kinetic energy of the incident antiprotons must also be reduced from 5.3 MeV down to just a few keV, at which point they can be confined by electrostatic potentials applied to the trap electrodes. The energy of the antiprotons is reduced through collisions with matter as they pass through a series of thin plastic and metal foils and a number of gas-filled regions [91], as depicted in Fig. 4.13. The two critical deceleration stages occur in a gas-filled energy-tuning cell and the final beryllium foil, called the degrader.

Immediately after passing through the PPAC, the antiprotons pass through a 16 mm long cell that is filled with a mixture of He and SF<sub>6</sub> gas at 1 atm. By changing the ratio of the two gasses, the density of the gas in the cell can be altered dramatically. This corresponds to a tunability in the energy lost by traversing antiprotons of approximately 0.6 MeV between an entirely He-filled or SF<sub>6</sub>-filled cell. The vast majority of the energy loss (approximately 3.6 MeV) occurs after this in the degrader, a 130 μm thick beryllium foil that the antiprotons pass through immediately before entering the trap. The optimal gas mixture for the energy tuning cell is empirically determined by measuring the antiproton trapping efficiency, as demonstrated in Fig. 4.14. If too much energy is lost before the antiprotons reach the degrader, they will stop in the degrader and annihilate. If too little energy is lost before the degrader, the antiprotons leaving the degrader will be moving too fast to be electrostatically

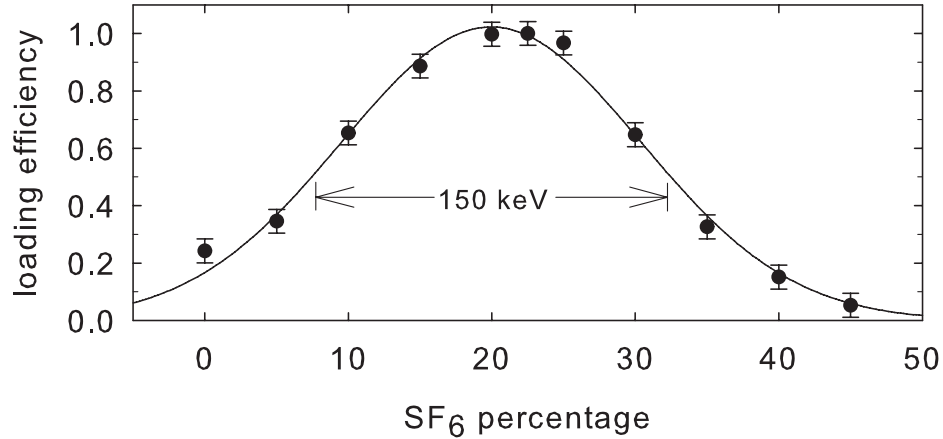


Figure 4.14: Optimization of the SF<sub>6</sub>-He gas mixture in the energy-tuning cell for antiproton loading in the A-TRAP Penning trap.

confined and will annihilate on the trap walls. Only the antiprotons that are slowed to less than a few keV of axial energy upon leaving the degrader can be trapped. If we compare that to the width of the antiproton energy distribution measured in Fig. 4.14, it is clear that even in the optimal case, only a very small fraction of the antiprotons from the AD will be slowed to within the appropriate energy range to be trapped.

### 4.3.3 Antiproton Trapping

The typical antiproton trapping procedure is depicted in Fig. 4.15. Antiprotons pass through the degrader at the bottom of the Penning trap (right side in the figure). The degrader is initially biased to 600 V to suppress the emission into the trap of secondary electrons liberated from the degrader by the antiprotons. A -5 kV reflecting

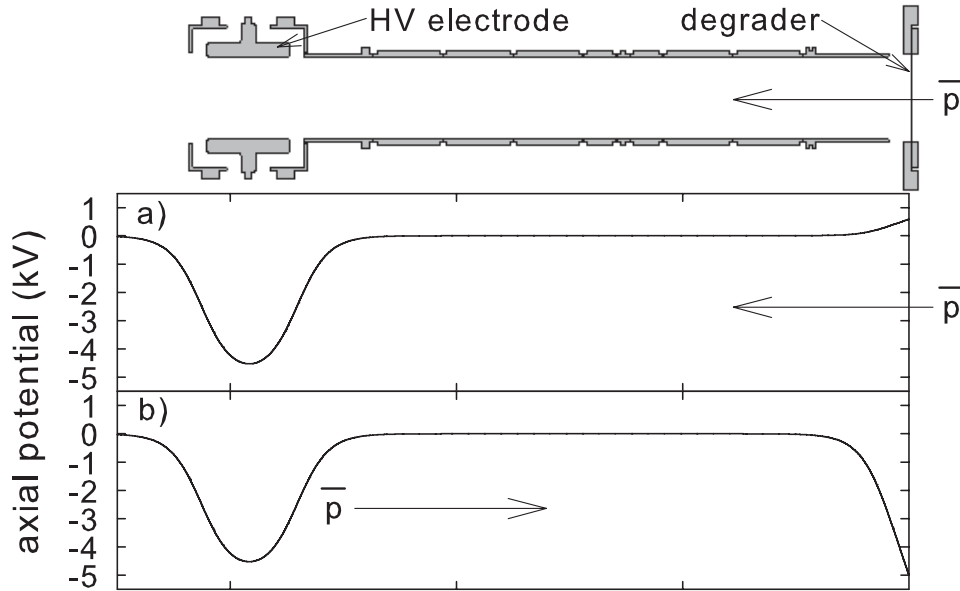


Figure 4.15: The typical antiproton catching procedure, demonstrating the potentials applied to the trap as (a) the antiprotons enter the trap through the degrader and (b) are confined by the applied electrostatic potentials.

potential is applied to the high-voltage (HV) electrode. Antiprotons that leave the degrader with an axial energy greater than 600 eV but less than 5.1 keV will enter the trap and be reflected back toward the degrader when they reach the HV electrode. Before the antiprotons can return to the degrader and annihilate, we switch the potential on the degrader to -5 kV in approximately 50 ns, confining the antiprotons in the trap. The high-voltage switching apparatus is described in detail in Ref.[95].

We switch the potential on the degrader at a fixed delay after we receive a warning signal from the AD that antiprotons have been ejected toward our experiment. We measure the trapping efficiency as a function of the delay time in order to optimize this parameter (Fig. 4.16). If the potential is switched too early, the antiprotons will be accelerated by the potential upon entering the trap and will have too much energy

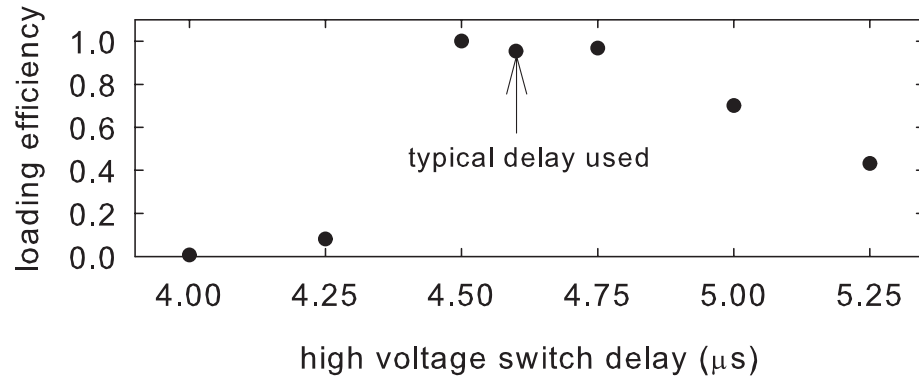


Figure 4.16: High voltage switch delay optimization for antiproton loading.

to be confined. If the potential is switched too late, the fast antiprotons reflected off of the HV potential will strike the degrader and annihilate before the trapping potential is applied.

At an arbitrary time later, we can then release the trapped antiprotons and count them using the annihilation detectors by ramping the potential on the degrader back up to 600 V in approximately 50 ms. By monitoring both the ramp voltage and detected annihilations as a function of time and correlating the two, we can also determine the axial energy distribution of the trapped antiprotons, as demonstrated in Fig. 4.17.

Because the axial energy distribution of antiprotons slowed by the degrader is very broad compared to the trappable energy range, one might naively expect to find that the trapped antiprotons have a uniform axial energy distribution, and consequently that the number of trapped antiprotons is simply linear with the trapping voltage applied. In reality, we predominantly trap low-energy antiprotons and the number

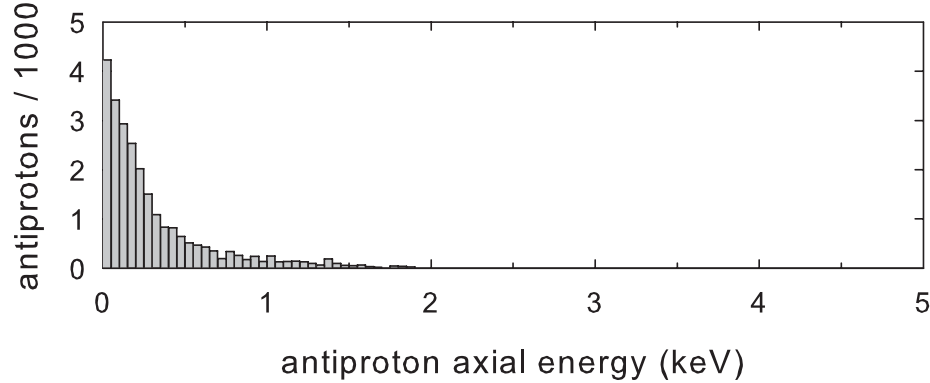


Figure 4.17: The axial energy distribution of a single bunch of antiprotons trapped in the A-TRAP Penning trap at 1 T. Most of the antiprotons entering the trap with more than 1 keV of axial energy are lost radially

of trapped antiprotons saturates at larger voltages. The voltage switching process is adequately fast to trap higher-energy antiprotons, so it must be concluded that the observed saturation effect is due to radial loss of the higher-energy antiprotons.

Radial confinement of the antiprotons is provided by the large magnetic field along the trap symmetry axis. As antiprotons leave the degrader, any velocity perpendicular to the magnetic field will result in cyclotron motion. If  $E_c$  is the corresponding cyclotron energy, the radius of the orbit is given by:

$$\rho_c = \frac{\sqrt{2E_c m}}{qB_0} \quad (4.1)$$

The cyclotron diameter as a function of energy for several relevant magnetic fields is plotted in Fig. 4.18.

If this diameter is too large, the antiproton will collide with the trap electrodes and annihilate. In the most simple model, for an antiproton starting in the center of the degrader, this occurs when the cyclotron diameter exceeds the radius of the

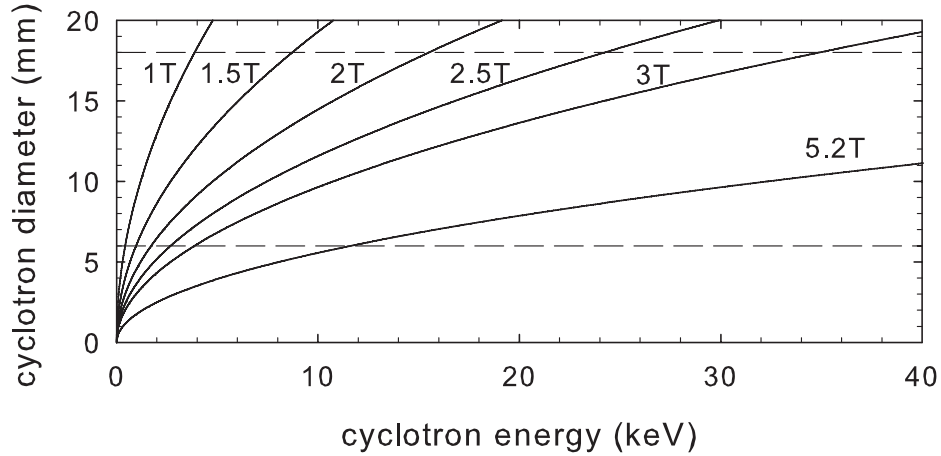


Figure 4.18: The antiproton cyclotron diameter as a function of radial energy for various magnetic fields. The dashed lines indicate the radii of the electrodes in the Penning traps used.

trap electrodes. In practice however, the spatial width of the beam, poor steering of the beam, or a slight misalignment of the magnetic field with the trap axis can all complicate this picture and can effectively reduce this cut-off diameter. In any case, the observed saturation in the antiproton trapping efficiency occurs for axial energies that are much less than the corresponding radial cut-off energies, suggesting that trapped antiprotons tend to have much more radial energy than axial energy.

More radially-energetic antiprotons can be captured by increasing either the magnetic field or electrode radius. Antiprotons were trapped in most previous ATRAP experiments in a 5.2 T field using Penning trap electrodes with a 6 mm radius. In order to magnetically confine antihydrogen atoms in a Ioffe trap though, it is desirable to decrease the axial magnetic field in order to maximize the radial magnetic trap depth (Eq. 2.13). Furthermore, it is not feasible in our present configuration to

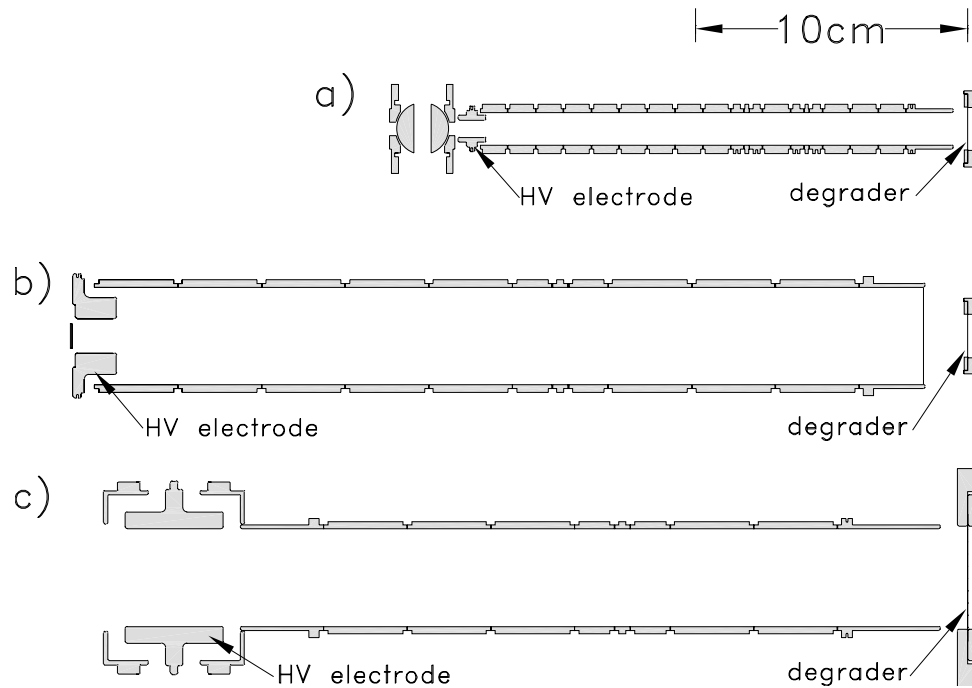


Figure 4.19: Cross sections of the antiproton trapping regions in the (a) Hbar, (b) X3, and (c) A-TRAP Penning traps. Trapped antiprotons are confined within the region bounded by the internal diameter of the cylindrical ring electrodes, and axially between the degrader and the high-voltage (HV) electrode.

increase the magnetic field while antiprotons are loaded and then decrease the field for antihydrogen trapping, because changing the field in the superconducting solenoids requires too much time. Consequently, if the axial magnetic field is reduced, the trap radius must also be increased in order to maintain the antiproton loading efficiency. It was therefore decided to increase the trap electrode radius by a factor of three (to 18 mm) in the new generation of Penning traps for antihydrogen trapping.

In order to study the effects of these changes, the antiproton-trapping efficiency was compared for various magnetic fields within three different trap configurations. The first trap studied was the Hbar trap initially used for antihydrogen production

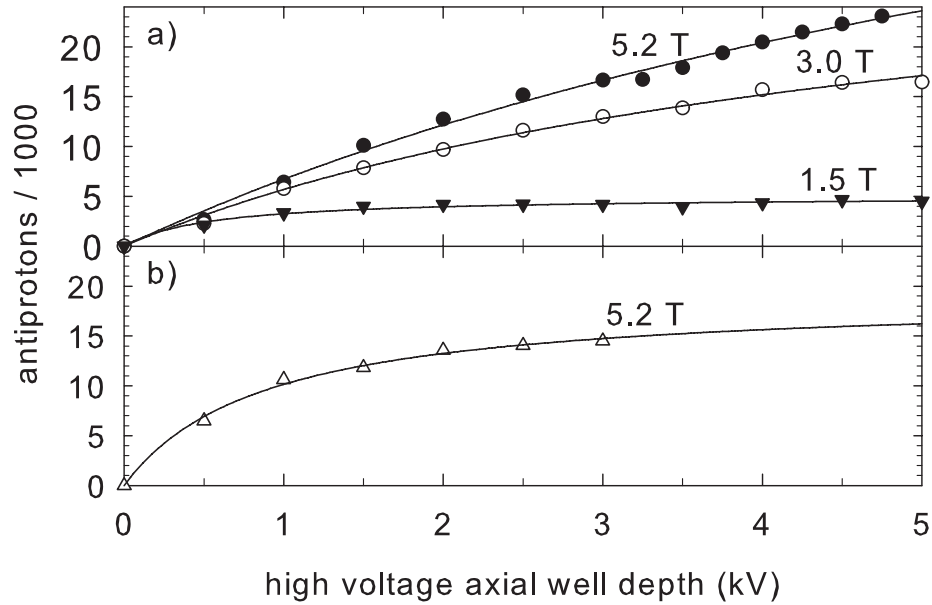


Figure 4.20: Antiprotons loaded as a function of axial trapping voltage in zone one. The data depicted compares the antiproton loading efficiency for several different magnetic field values (a) into the X3 trap, and (b) into the Hbar trap.

in the first experimental zone [66]. The electrodes in the Hbar trap had a radius of 6 mm. Next, the X3 (“times-three”) trap was used to study the effect of increasing the trap radius to 18 mm in the same zone. The X3 trap was then briefly transferred to the second experimental zone before the A-TRAP apparatus was finally installed there. The antiproton trapping regions of these traps are displayed in Fig. 4.19.

A comparison of the Hbar and X3 trapping efficiencies for various magnetic fields and trapping voltages is given in Fig. 4.20. Because the cyclotron radius is inversely proportional to the magnetic field, it is expected that antiproton trapping in Hbar at 5.2 T should be similar to trapping in the X3 trap at 1/3 the field (1.7 T). The axial energy distribution of trapped antiprotons in Hbar at 5.2 T is very similar to

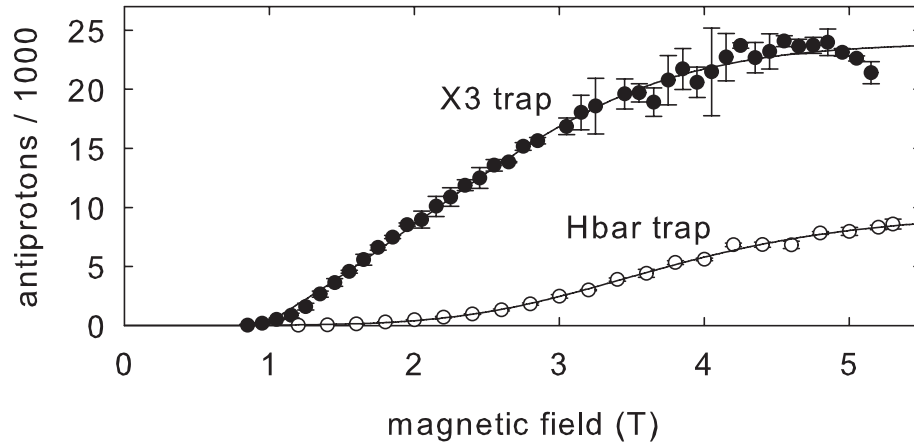


Figure 4.21: Antiprotons loaded as a function of magnetic field into either the X3 trap or Hbar trap in the zone one solenoid.

the energy distribution in the X3 trap at 1.5 T, but the number trapped is only about 1/3 of that in Hbar for unknown reasons. As expected, the number of trapped antiprotons in the X3 trap becomes more linear with the trapping voltage as the magnetic field is increased.

The number of antiprotons trapped in the Hbar and X3 traps at maximum trapping voltage was also measured as a function of magnetic field (Fig. 4.21). This data demonstrates that the X3 trap is capable of trapping antiprotons at lower magnetic fields than Hbar. Even for the X3 trap though, the number of antiprotons trapped effectively drops to zero at around 1 T.

The X3 trap was briefly transferred to the solenoid in the second experimental zone in order to compare the loading efficiency in the two zones. Unfortunately, the bias voltages applied to the photomultipliers for the particle detectors in that zone were still being optimized, so it was not possible to discern the number of antiprotons

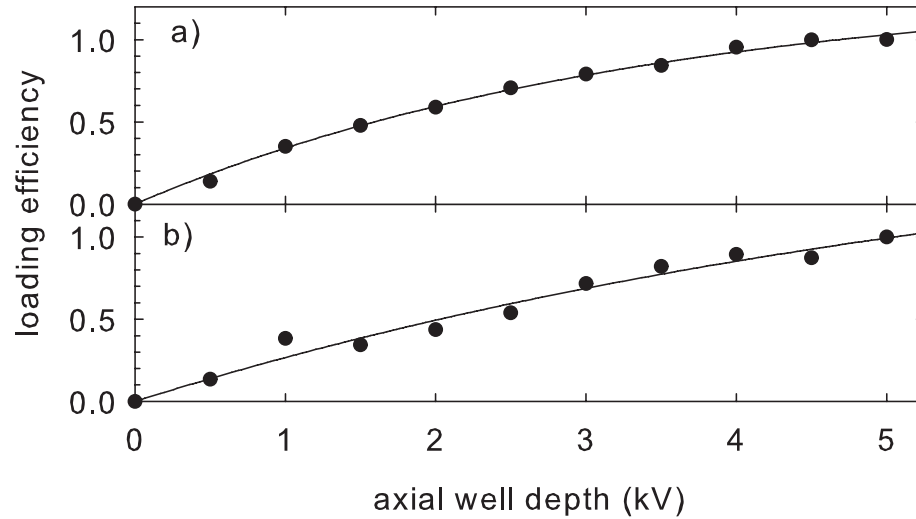


Figure 4.22: Comparison of the antiproton loading efficiency into the X3 trap with a 3 T axial field (a) in zone one and (b) in zone two as a function of axial trapping voltage.

being detected at that time. Nevertheless, it was possible to measure the axial energy distribution of the trapped antiprotons, and those results were consistent with those measured in the first zone at the same field (Fig. 4.22).

Similar data was acquired for the antiproton trapping efficiency as a function of trapping voltage and magnetic field in A-TRAP in the zone-two solenoid. The axial energy profile measured was consistent with that seen for the X3 trap (Fig. 4.23). However, roughly 10 times as many antiprotons are loaded into A-TRAP than into the X3 trap at 3 T. It should be noted that the A-TRAP measurements were made in the zone-two solenoid, while the X3 trap measurements were made in the zone-one solenoid. The annihilation detectors used in zone one were carefully calibrated by the TRAP collaboration by releasing a well-known number of antiprotons from a Penning

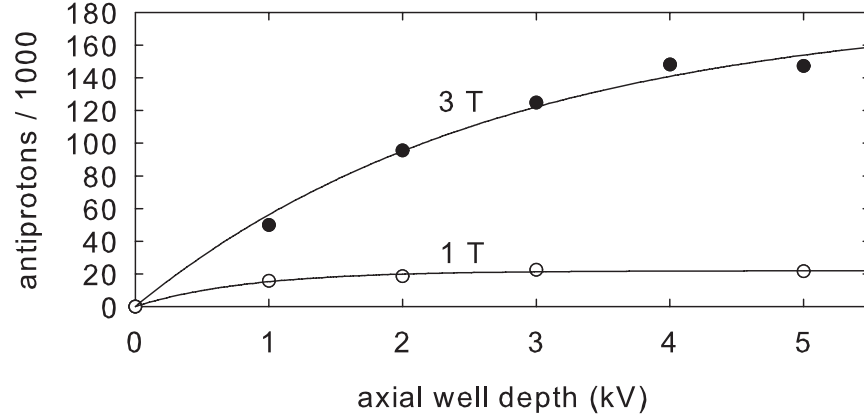


Figure 4.23: Antiprotons loaded as a function of axial trapping voltage in zone two into the A-TRAP Penning trap.

trap and measuring the detection efficiency [96], whereas the detectors in zone two are presently calibrated using Monte Carlo simulations of the detection efficiency (Section 3.2.2). Differences in the magnetic fields created by the two solenoids or in the accuracy of the two detector calibrations may contribute to the observed disparity between the trapping efficiencies in the two cases, but it is difficult to account for a factor of 10 from these possibilities alone. It remains unclear why there is such a large difference between A-TRAP and the X3 trap. These differences are further emphasized by the fact that we are able to continue loading antiprotons into A-TRAP at lower magnetic fields than was possible in either the Hbar or X3 traps (Fig. 4.24).

We find that approximately 7 times as many antiprotons are loaded into A-TRAP at 3 T than at 1 T (Fig. 4.24). This factor is based upon the number of annihilations counted using our paddle detectors, which are the annihilation detectors that are the least sensitive to changes in magnetic field (Section 3.2.3). It was assumed in Fig. 4.23

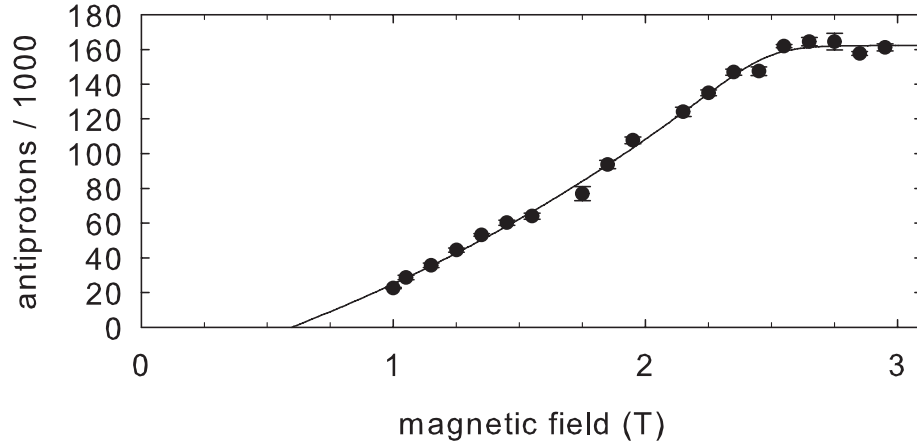


Figure 4.24: Antiprotons loaded as a function of magnetic field into A-TRAP in the zone two solenoid.

and Fig. 4.24 that the detection efficiency was the same at 3 T as it was at 1 T, while in reality, the detection efficiency should start to decrease slightly as the magnetic field is increased. Consequently, the factor of 7 difference estimated for the antiproton loading efficiencies at 1 T and 3 T should be considered a lower bound.

#### 4.3.4 Antiproton Cooling and Accumulation

After capturing the antiprotons in the Penning trap, we wish to reduce their energy from several keV down to thermal equilibrium with the trap walls at 4.2 K (0.345 meV), and confine them within a single electrode. To do this, we sympathetically cool the antiprotons via collisions with electrons. Electrons are able to lose their energy via cyclotron radiation much more rapidly than antiprotons (Section 3.3.1) and have the same charge as antiprotons, so that they are confined by the same potentials, making them ideal for collisional cooling.

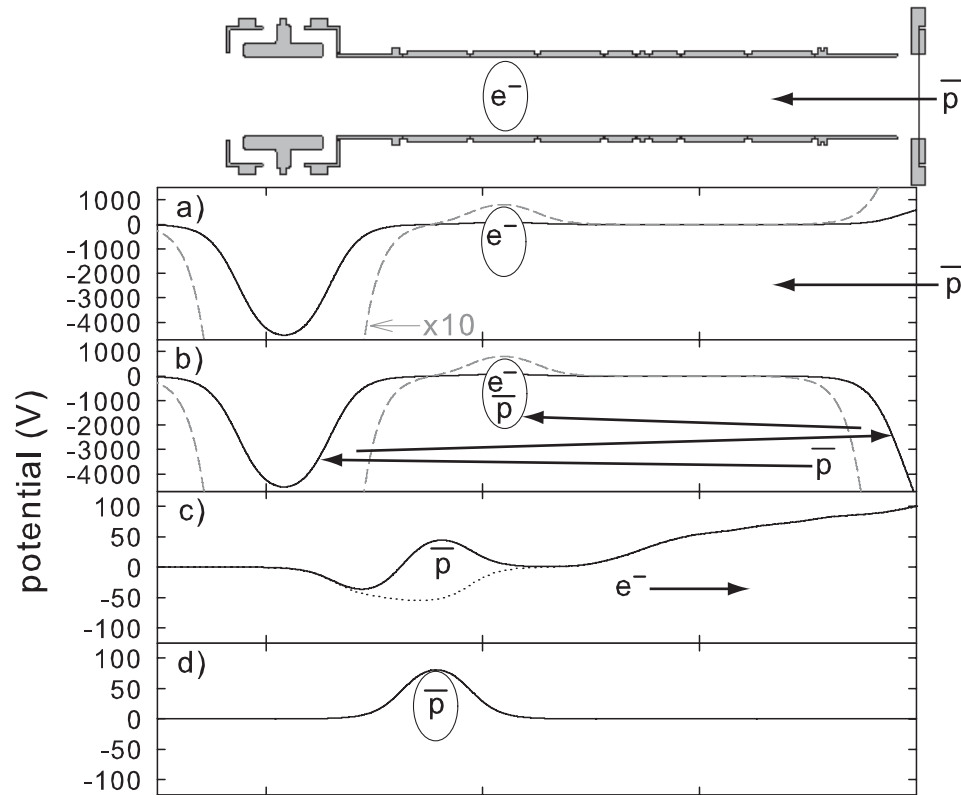


Figure 4.25: The typical antiproton stacking procedure, depicting the potentials applied to the trap as (a) the antiprotons enter the trap, (b) are confined and collisionally cool into the same potential well as the loaded electrons, (c) the electrons are expelled from the antiproton cloud by briefly removing the confining potential (dotted line), and (d) only a cold antiproton cloud remains.

The procedure employed for trapping and cooling multiple bunches of antiprotons from the AD is outlined in Fig. 4.25. The initial steps are similar to the antiproton trapping procedure described previously, but a cloud of electrons is positioned on an electrode within the antiproton confining region. Once the antiprotons are trapped, they are able to lose energy via collisions on each pass through the electrons, which in turn radiate the energy away via their excited cyclotron motion. The antiprotons rapidly cool into the same electrode that the electrons occupy, and any remaining

antiprotons that have not been cooled are released by ramping the degrader potential back to a positive value after a set delay time in preparation for the next antiproton bunch. Many bunches of antiprotons from the AD can be loaded in this fashion using the same electron cloud. Once a sufficient number of antiprotons have been accumulated, a 50 ns duration, 120 V pulse from a DEI HV1000 pulse generator temporarily inverts the potential confining the electrons and the antiprotons. The electrons are ejected to the degrader, but the pulse is sufficiently short that the antiprotons remain confined and are only minimally disturbed [19].

The charge deposited on the degrader by the electrons is measured, and a second pulse is used to confirm that all of the electrons have been removed from the antiproton cloud. If the electrons are not removed, we find that the antiprotons eventually become unstable and are lost, while solitary antiprotons tend to remain stable for long periods of time. The procedure initially employed to remove the electrons involved sequentially applying lower-voltage pulses from a saturated switch and lowering the depth of the potential well (similar to the procedure in Fig. 3.9a), but the large number of pulses required for this procedure appeared to disturb the antiprotons to the point where many were lost. Consequently, the final procedure adopted was to use a single 120 V pulse to eject the electrons.

As with the antiproton catching experiments described previously, tests of antiproton loading into a 36 mm diameter trap were initially performed using the X3 trap in the first experimental zone. Several parameters affecting the efficiency of this electron-cooling process were studied: the number of cooling electrons used, the confining voltage of the electrons, and the amount of time that the antiprotons are

allowed to cool.

In past experiments using the Hbar trap, we typically used only a couple million electrons to cool the antiprotons. Our studies with the X3 trap revealed that significantly larger numbers of electrons are required to efficiently cool antiprotons in larger-volume traps, especially at lower magnetic fields, as demonstrated by Fig. 4.26. For small numbers of electrons, a significant portion of the antiprotons are not cooled by the electrons within 50  $\mu$ s, and are released and counted. The number of cooled antiprotons appears to saturate for larger numbers of electrons. At high fields, this saturated value is slightly less than the number of antiprotons captured without electrons, suggesting that some portion of the antiprotons initially captured are lost due to collisions with the electrons. At lower fields however, the number of cooled antiprotons actually exceeds the number captured without electrons, suggesting that initial collisions within the electron cloud can actually assist in capturing a larger portion of the incident antiprotons.

For a given number of cooling electrons, increasing the voltage used to confine the electrons effectively increases the density of the electron plasma by squeezing it in the axial direction. The effect of this choice of voltage upon the number of antiprotons loaded was studied in the X3 trap for both multiple electron numbers (Fig. 4.27), and at multiple magnetic fields (Fig. 4.28). The results demonstrate that the antiproton loading efficiency initially increases with the voltage applied, followed by a more gradual decrease in efficiency as the voltage continues to increase. The decrease in the number of antiprotons cooled does not correspond to an increase in the number of hot antiprotons present, indicating that the antiprotons are actually

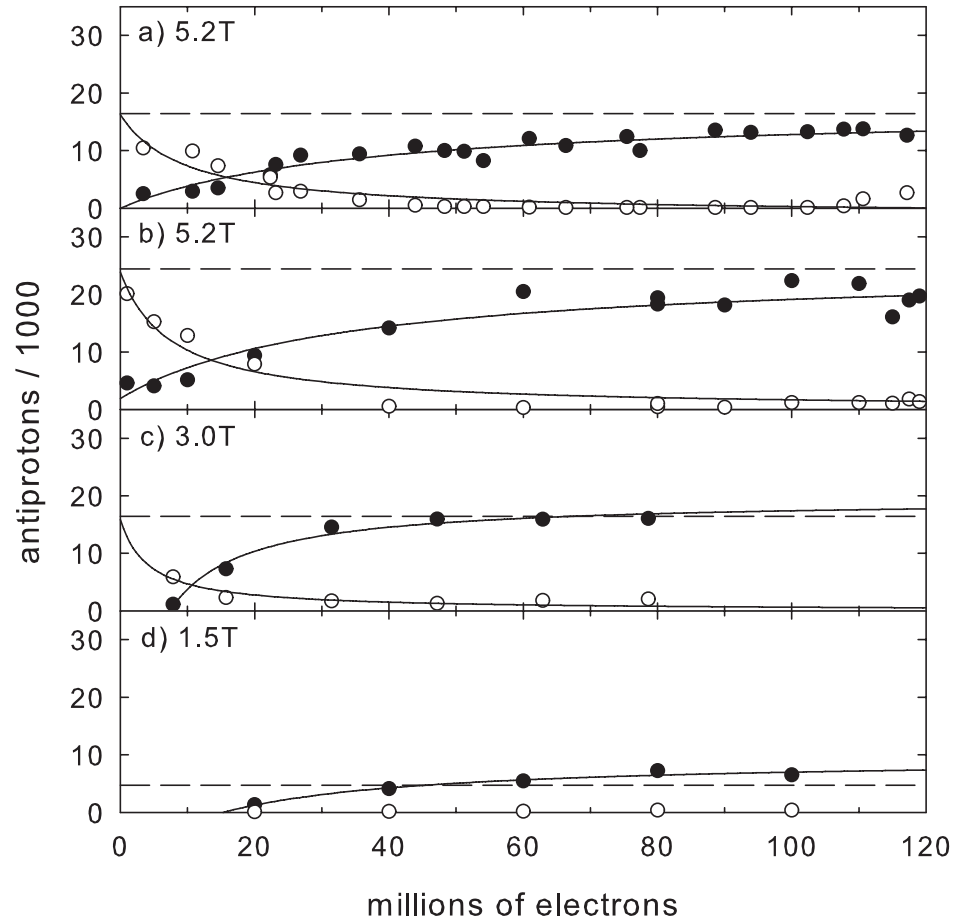


Figure 4.26: The number of cold antiprotons (closed circles) and hot antiprotons (open circles) in the X3 trap 50 s after their initial capture using a 3 kV trapping potential at (a) 5.2 T or a 5 kV potential at (b) 5.2 T, (c) 3.0 T, or (d) 1.5 T for various numbers of cooling electrons. The dashed line in each case indicates the number of hot antiprotons trapped without electrons.

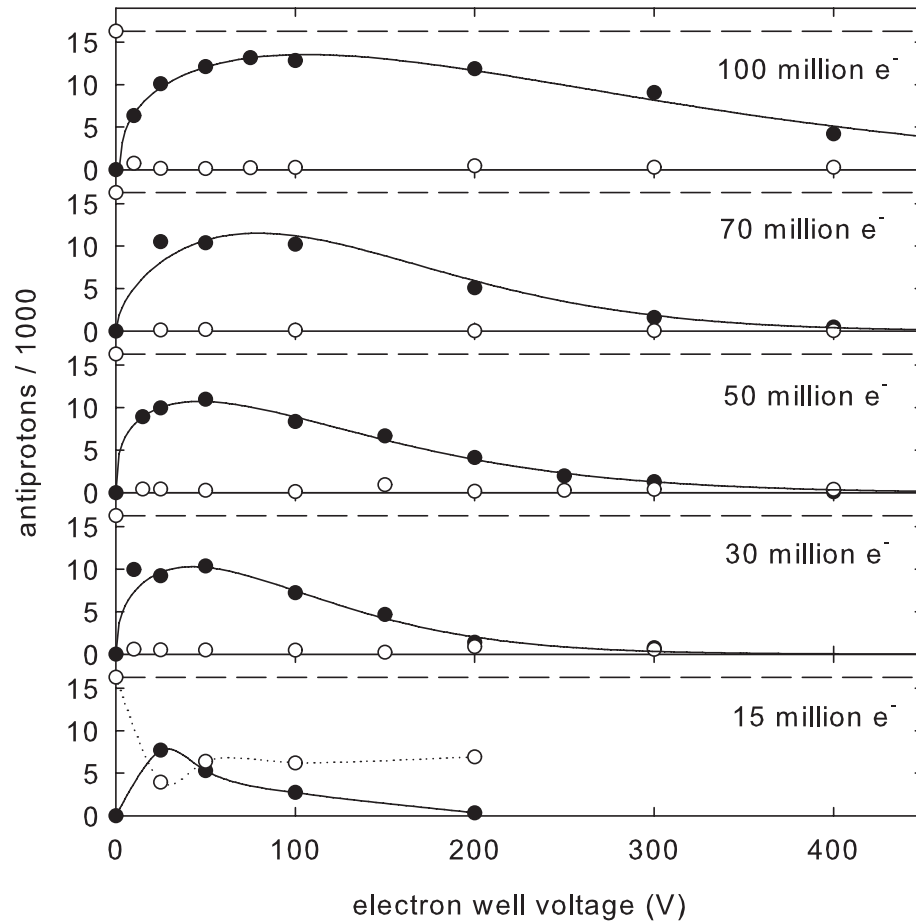


Figure 4.27: The number of cold antiprotons (closed circles) and hot antiprotons (open circles) as a function of electron confining potential in the X3 trap at 5.2 T using a 3 kV trapping potential and the number of cooling electrons indicated. The dashed lines indicate the number of hot antiprotons trapped without electrons.

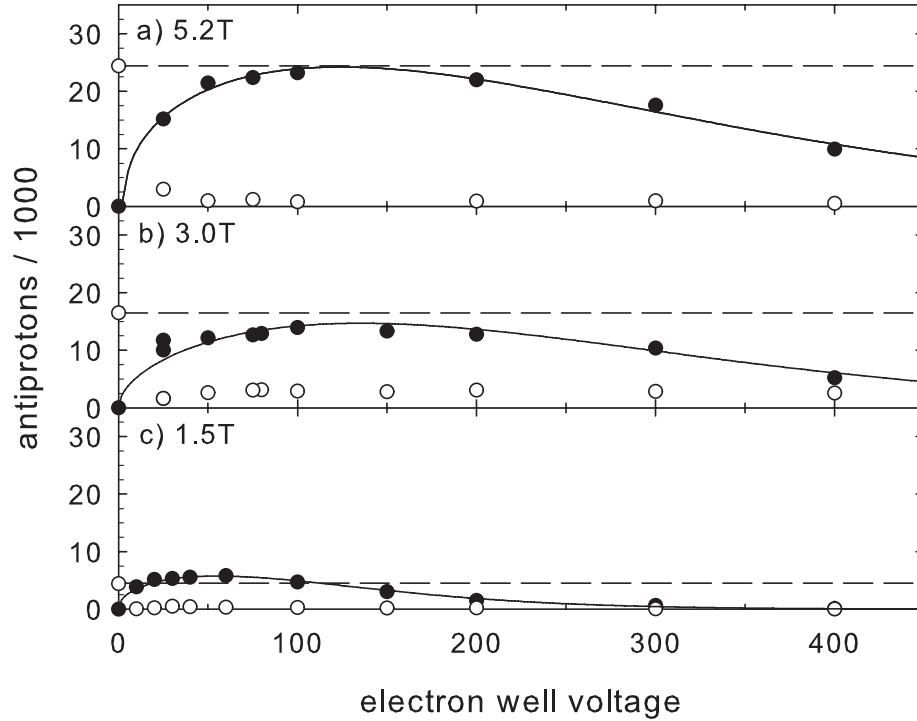


Figure 4.28: The number of cold antiprotons (closed circles) and hot antiprotons (open circles) as a function of electron confining potential in the X3 trap using a 5 kV trapping potential and 100 million electrons at (a) 5.2 T, (b) 3.0 T, and (c) 1.5 T. The dashed lines indicate the number of hot antiprotons trapped without electrons.

lost from the trap for a non-optimal choice of voltage. The peak in the antiproton loading efficiency appears to become more pronounced for small numbers of cooling electrons and low magnetic fields.

The amount of time required to electron cool the captured antiprotons is another important parameter, since we have to be ready to receive a new bunch of antiprotons from the AD every 100 s. Measurements in the X3 trap revealed that the amount of time required to cool the antiprotons into the same electrode as the electrons was

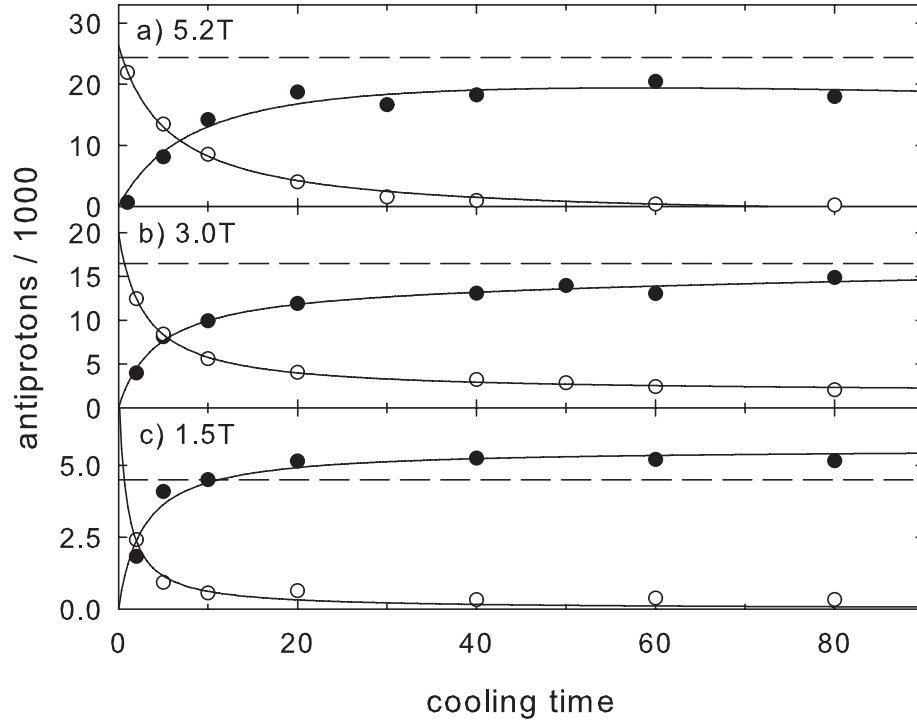


Figure 4.29: The number of cold antiprotons (closed circles) and hot antiprotons (open circles) in the X3 trap as a function of time after the antiprotons are confined using a 5 kV trapping potential and 100 million electrons at (a) 5.2 T, (b) 3.0 T, and (c) 1.5 T. The dashed lines indicate the number of hot antiprotons trapped without electrons.

largely invariant with the magnetic field (Fig. 4.29), suggesting that this time constant is mainly set by the frequency of collisions with the electrons rather than the cyclotron cooling time of the electrons. The measured cooling time constant ranged from 4–8 s, far shorter than the AD cycling time.

The number of antiprotons loaded into the X3 trap was linear with the number of antiproton bunches captured, as demonstrated in Fig. 4.30. In one case, as many as 1.2 million antiprotons were loaded at 3 T in 100 consecutive bunches from the AD.

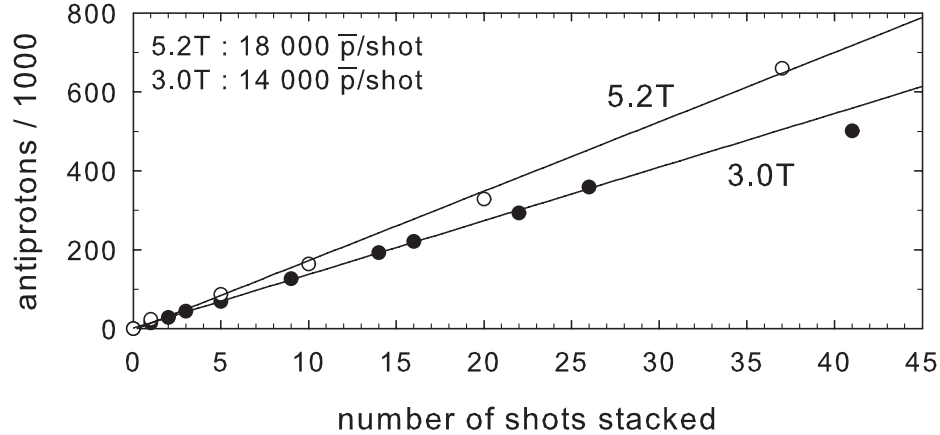


Figure 4.30: Antiprotons loaded into the X3 trap per bunch from the AD.

The goal of the experiments just outlined was to better predict and understand the efficiency of loading antiprotons into the A-TRAP apparatus in the second experimental zone, since the two traps have very similar geometries. As soon as A-TRAP became functional, antiprotons were loaded into the trap under similar conditions. Although some studies were briefly performed at higher magnetic fields, A-TRAP was almost always used with a bias magnetic field of 1 T because this allowed for a much larger magnetic trap depth from the Ioffe trap. By contrast, the X3 trap had effectively zero loading efficiency at this field. Even in A-TRAP however, loading antiprotons at this low of a field presented some substantial challenges.

As the magnetic field is lowered, the time required for the electrons to lose energy and come into thermal equilibrium with the cold trap electrodes increases. The electron's cyclotron energy is lost via cyclotron radiation with a time constant given

by (Section 3.3.1):

$$\tau_c = \frac{3\pi\epsilon_0 m^3 c^3}{e^4 B^2} \approx \frac{2.6T^2}{B^2} s \quad (4.2)$$

while the axial energy is only reduced when collisions between electrons convert axial energy to cyclotron energy, which can take substantially longer [97]. To compensate for the increased cooling time required at 1 T, we allowed the electrons to cool for 5 to 10 minutes after loading them before we began loading antiprotons. During this time, the electrons were kept in a 600 V deep potential in order to increase the electron collision frequency. Although this procedure was not previously employed at larger magnetic fields, we found that it was essential at 1 T. If this procedure was not followed, it often resulted in the antiprotons that were loaded into the electron cloud becoming unstable and being lost from the trap within the first few antiproton bunches from the AD. When this happened, the only solution was to allow the electrons to cool for a longer period of time before starting to load antiprotons.

We empirically determined that using roughly 380 million cooling electrons in a 100 V potential provided the most efficient and stable antiproton loading at 1 T in A-TRAP. With these settings, it was possible to consistently load 35,000 cooled antiprotons per bunch, or about 0.1% of the antiprotons initially ejected from the AD. By comparison, typically 27,000 antiprotons were trapped without electrons at this field, so the cooling electrons gave a clear boost to the antiproton capture efficiency. Up to 0.6 million antiprotons were loaded at 1 T and 1.7 million at 2 T in A-TRAP by stacking consecutive bunches from the AD, as demonstrated in Fig. 4.31. The quoted numbers of antiprotons loaded into A-TRAP rely upon the accuracy of Monte Carlo simulations used to determine the efficiencies of our annihilation

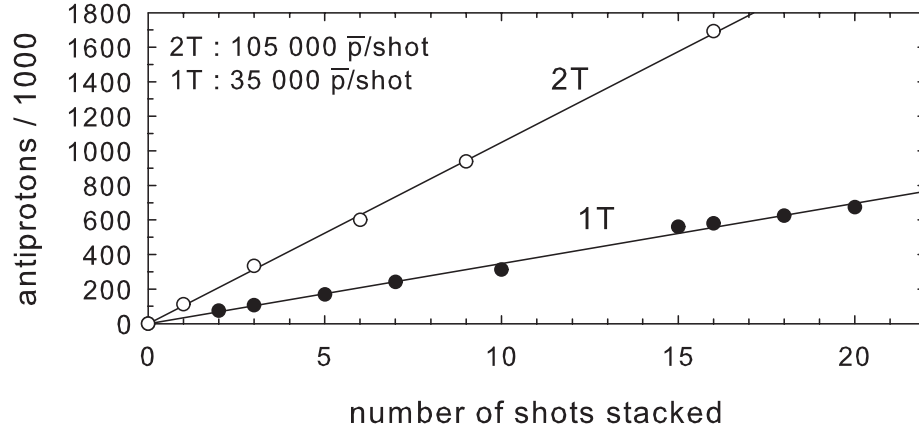


Figure 4.31: Antiprotons loaded into A-TRAP per bunch from the AD.

detectors (Section 3.2.2). More accurate calibrations of our detection efficiencies are planned for the near future.

### 4.3.5 Future Improvements to Antiproton Loading

A clear boost to the antiproton loading efficiency can be gained by increasing the magnetic bias field, but the field would then need to be reduced before antihydrogen-trapping experiments were performed in order to allow for the largest Ioffe trap depth possible. A small superconducting solenoid directly around the antiproton catching region of A-TRAP awaits installation. It should turn on and off quickly in order to temporarily increase the field in that region by several tesla as the antiprotons are being loaded. It remains to be seen if the relative inhomogeneity of the field generated by this small solenoid will cause problems with antiproton loading. Additionally, initial experiments suggest that a significant portion of the antiprotons loaded at the

larger field may be lost as the field is reduced back to 1 T, and it may be necessary to actively reduce the antiproton cloud radius in order to prevent this.

The number of captured antiprotons saturates for low axial trapping potentials at 1 T, but if the magnetic field is increased, trapping potentials greater than 5 kV could capture larger numbers of antiprotons. A high-voltage switch that can apply larger potentials is currently in construction.

The number of electrons used to cool antiprotons was varied in the studies outlined here, but the shape and density of the electron plasma could only be varied by changing the electron-confining potential. Better control and diagnostics of the electron plasma in the future using a rotating wall, mode diagnostic, and imaging techniques could potentially lead to improved and more reliable antiproton loading. These techniques are currently in development.

Finally, the inefficiency of capturing antiprotons largely derives from the fact that we are only able to capture antiprotons within a small range of energies from a much broader energy distribution. The energy broadening of the antiprotons is mostly due to the slowing process within the degrader, and it is expected that if the incident antiproton energy were reduced so that we could use a thinner degrader, then the antiprotons would leave the degrader with a much narrower energy distribution and our catching efficiency would increase. To this end, there is a proposal to add a smaller decelerating ring to the AD complex within the upcoming years to further reduce the antiproton energy before delivering them to the experiments.

## Chapter 5

# Non-neutral Plasmas

In order to produce large amounts of antihydrogen, it is necessary to confine large numbers of charged particles. In the regime in which we normally operate, the single-particle theory of motion in a Penning trap is no longer a sufficient description because the space charge of the particles significantly alter the trap potential. In this case, it is appropriate to describe the particles as forming a non-neutral plasma in the sense that the dimensions of the volume that the particles occupy is much larger than the Debye length, the characteristic length scale over which electric fields are screened in a plasma  $\lambda_d \equiv \sqrt{\epsilon_0 kT / ne^2}$ , typically some tens of  $\mu\text{m}$ , where  $T$  is the temperature and  $n$  is the density of the plasma. The physics of such plasmas in a Penning trap is well understood and studied [84]. This section will summarize this theory and compare its predictions with the plasmas observed in our apparatus.

## 5.1 Plasmas in a Cylindrical Trap

The Lagrangian of a particle with charge  $q$  in an arbitrary electromagnetic field is [98]:

$$\mathcal{L}(\vec{r}, \vec{v}, t) = \frac{m}{2}v^2 + q\phi(\vec{r}, t) + q\vec{v} \cdot \vec{A}(\vec{r}, t) \quad (5.1)$$

For the uniform axial magnetic field,  $\vec{B} = B\hat{z}$ , and cylindrically-symmetric electric potential of the Penning trap, the vector potential is  $\vec{A} = B\rho\hat{\theta}/2$  and  $\phi = \phi_t(\rho, z)$ . The canonical momenta,  $p_\alpha \equiv \partial\mathcal{L}/\partial v_\alpha$ , in cylindrical coordinates are then given by:

$$p_\rho = m\dot{\rho}, \quad p_z = m\dot{z}, \quad p_\theta = m\rho^2\dot{\theta} + qA_\theta(\rho)\rho = m\rho^2\dot{\theta} + \frac{q}{2}B\rho^2 \quad (5.2)$$

If we now consider a plasma of  $N$  particles of the same charge, then to a good approximation, the Hamiltonian governing the motion of the particles is [84]:

$$\begin{aligned} H &= \sum_{j=1}^N \frac{m}{2}v_j^2 + \sum_{j=1}^N q\phi(\vec{r}_j) \\ &= \sum_{j=1}^N \left( \frac{p_{\rho_j}^2}{2m} + \frac{p_{z_j}^2}{2m} + \frac{[p_{\theta_j} - \frac{q}{2}B\rho_j^2]^2}{2m\rho_j^2} \right) + \sum_{j=1}^N q[\phi_t(\rho_j, z_j) + \phi_p(\rho_j, z_j)] \end{aligned} \quad (5.3)$$

where the electric potential is now the superposition of the trap potential without any particles,  $\phi_t$ , and the mean-field potential of the plasma itself,  $\phi_p$ . A non-relativistic Hamiltonian suffices because  $|v_j|/c \ll 1$ . This treatment also neglects the interaction energy of the particles with the image charges induced in the electrodes of the Penning trap. This is a small effect if the charges are far away from the electrode walls, but may become more important for large plasmas.

The Hamiltonian is invariant with time, so the total plasma energy is conserved. The cylindrical symmetry of the apparatus ensures that both  $\phi_t$  and  $\phi_p$  are cylindrically symmetric. The rotational invariance of the Hamiltonian then ensures that the

total canonical angular momentum of the plasma is conserved:

$$\text{const} = P_\theta \equiv \sum_{j=1}^N m\rho_j^2 \dot{\theta}_j + \frac{q}{2} B \rho_j^2 \quad (5.4)$$

The first term is the mechanical angular momentum of the particles, while the second term is the angular momentum associated with the magnetic field. The second sum is much larger than the first for our typical plasmas, so that:

$$\text{const} = P_\theta \simeq \sum_{j=1}^N \frac{q}{2} B \rho_j^2 \quad (5.5)$$

In other words, the mean square radius of the plasma is constant with time.

In principle, some particles can still move out radially if other particles consequently decrease their radius. To set a limit on what fraction of particles might be lost from a plasma through such processes, consider a spheroidal plasma of uniform density (this approximation will be justified later) with a radius of 1 cm. The most extreme case imaginable involves transporting particles from a radius of 1 cm out to the electrode walls at 1.8 cm, until all of the remaining particles are concentrated on the central axis. To conserve angular momentum, only 18% of the initial particles could be transported out to the electrode walls in this fashion. This should be regarded as an extreme upper bound for this example plasma geometry, and we would expect that radial particle transport through angular-momentum conserving processes would lead to far fewer particle losses than this in reality.

Although angular momentum is ideally conserved in the plasma, in practice, small misalignments of the electrode symmetry axis with the magnetic field, defects or charged patches on the electrode surface, and any slits or holes placed in electrodes can all break the perfect cylindrical symmetry of the system. This causes small

torques on the plasma that lead to long term particle loss. Nevertheless, particle plasmas can be kept in our Penning trap for many hours.

We wish to determine the thermal equilibrium state of the confined plasma. If the correlations between the charged particles are sufficiently small, the thermal equilibrium states can be described by a single particle distribution function. The particles are considered uncorrelated if the coulomb energy between neighboring charges is less than the random thermal energy, if  $\Gamma = e^2/(4\pi\epsilon_0 akT) < 1$  where  $a$  is given by  $4\pi n_0 a^3/3 = 1$  and  $n_0$  is the particle density. For plasmas in our experiment, the density is sufficiently small to satisfy this condition.

The distribution function must be expressible in terms of the constants of motion of the system from Liouville's theorem [99], in terms of the energy and angular momentum in this case. The specific distribution function here for fixed values of  $N$ ,  $H$ , and  $P_\theta$  is given by [84, 100]:

$$f(\vec{r}, \vec{v}) = \frac{N \exp \left[ -\frac{1}{kT} (h + \omega_r p_\theta) \right]}{\int d^3\vec{r} d^3\vec{v} \exp \left[ -\frac{1}{kT} (h + \omega_r p_\theta) \right]} \quad (5.6)$$

where  $h$  and  $p_\theta$  are the single particle Hamiltonian and canonical angular momentum:

$$h = \frac{m}{2} v^2 + q\phi(\rho, z); \quad p_\theta = m\rho^2\dot{\theta} + \frac{q}{2} B\rho^2 \quad (5.7)$$

Plugging Eq.(5.7) in Eq.(5.6) yields the distribution:

$$f(\vec{r}, \vec{v}) = n(\rho, z) \left( \frac{m}{2\pi kT} \right)^{3/2} \exp \left[ -\frac{1}{2} m \frac{(\vec{v} + \omega_r \rho \hat{\theta})^2}{kT} \right] \quad (5.8)$$

where the plasma density is given by

$$n(\rho, z) = n_0 \exp \left[ -\frac{q\phi(\rho, z) + \frac{1}{2} m\omega_r (\omega_c - \omega_r) \rho^2}{kT} \right] \quad (5.9)$$

and  $\omega_c = qB/m$  is the cyclotron frequency. The velocity distribution in Eq.(5.8) is a Maxwell-Boltzman distribution in a rotating reference frame. The implication is that the mean velocity of the particles in the plasma is  $v_\theta = -\omega_r \rho \hat{\theta}$ , describing a shear-free, rigid rotation of the plasma at frequency  $\omega_r$ . This rotation is in the  $-\hat{\theta}$  direction for positive charges and  $\hat{\theta}$  direction for negative charges, and the value of  $\omega_r$  is determined by the conserved values of  $N$ ,  $E$ , and  $P_\theta$  when the particles are loaded.

It is instructive to consider a reference frame that rotates at the same frequency as the plasma. This will give insight into the physical significance of the terms in Eq.(5.9). The Hamiltonian in a frame that rotates with frequency  $-\omega_r \hat{\theta}$  is [101]:

$$H_R = H + \omega_r P_\theta \quad (5.10)$$

Adding  $\omega_r P_\theta$  to Eq.(5.3), after some algebra, results in [84]:

$$\begin{aligned} H_R = & \sum_{j=1}^N \left( \frac{p_{\rho_j}^2}{2m} + \frac{p_{z_j}^2}{2m} + \frac{[p_{\theta_j} - \frac{m}{2} (\omega_c - 2\omega_r) \rho_j^2]^2}{2m\rho_j^2} \right) \\ & + \sum_{j=1}^N \left[ q\phi_t(\rho_j, z_j) + q\phi_p(\rho_j, z_j) + \frac{1}{2}m\omega_r (\omega_c - \omega_r) \rho_j^2 \right] \end{aligned} \quad (5.11)$$

Comparing this with the Hamiltonian in Eq.(5.3), we can identify the terms that are added in the rotating frame. The effective magnetic field in the rotating frame is reduced due to the fictitious Coriolis force, and the cyclotron frequency is replaced by the vortex frequency  $\omega_v = \omega_c - 2\omega_r$  [84]. The effective single-particle potential in the rotating frame becomes:

$$q\phi_R(\rho, z) = q\phi_t(\rho, z) + q\phi_p(\rho, z) + \frac{1}{2}m\omega_r (\omega_c - \omega_r) \rho^2 \quad (5.12)$$

where  $-m\omega_r^2 \rho^2/2$  is the potential due to the fictitious centrifugal force and  $m\omega_r \omega_c \rho^2/2 = qB\omega_r \rho^2/2$  is the effective potential to account for the  $q\vec{v} \times \vec{B}$  force on the particles rotating through the magnetic field. Although  $\phi_t(\rho, z)$  is an axially-confining potential,

it is anti-confining in the radial direction, as are  $\phi_p(\rho, z)$  and  $-m\omega_r^2\rho^2/2$ . It is only the  $qB\omega_r\rho^2/2$  term that increases with increasing radius, and it is therefore this term that provides the radial confinement of the plasma in the co-rotating frame where the plasma is stationary.

In the low temperature limit where  $T \rightarrow 0$ , demanding a finite plasma density in Eq. 5.9 requires that

$$q\phi(\rho, z) + \frac{1}{2}m\omega_r(\omega_c - \omega_r)\rho^2 = 0 \quad (5.13)$$

inside of the plasma. This is simply the condition that total potential inside the plasma is zero in the co-rotating frame. Put another way, the charges will arrange themselves into an equilibrium state where the net force on the charges is zero within the plasma in the co-rotating frame.

Plugging Eq.(5.13) into Eq.(5.9) implies that the the density is constant,  $n_0$ , inside of the plasma, and zero outside of the plasma boundary, in the zero temperature limit. For some small finite temperature, there will be a more gradual transition on the boundary over a distance proportional to the Debye length,  $\lambda_d \equiv \sqrt{\epsilon_0 kT/ne^2}$ . Eq.(5.13) also implies that the total lab-frame potential is independent of  $z$ .

$$\phi(\rho) = \phi_t(\rho, z) + \phi_p(\rho, z) = -\frac{m}{2q}\omega_r(\omega_c - \omega_r)\rho^2 \quad (5.14)$$

The potential inside of the plasma must also satisfy Poisson's equation:

$$\nabla^2\phi(\rho) = -\frac{qn_0}{\epsilon_0} \quad (5.15)$$

Plugging Eq.(5.14) into Eq.(5.15) then gives the result:

$$n_0 = \frac{2\epsilon_0 m\omega_r(\omega_c - \omega_r)}{q^2} \quad (5.16)$$

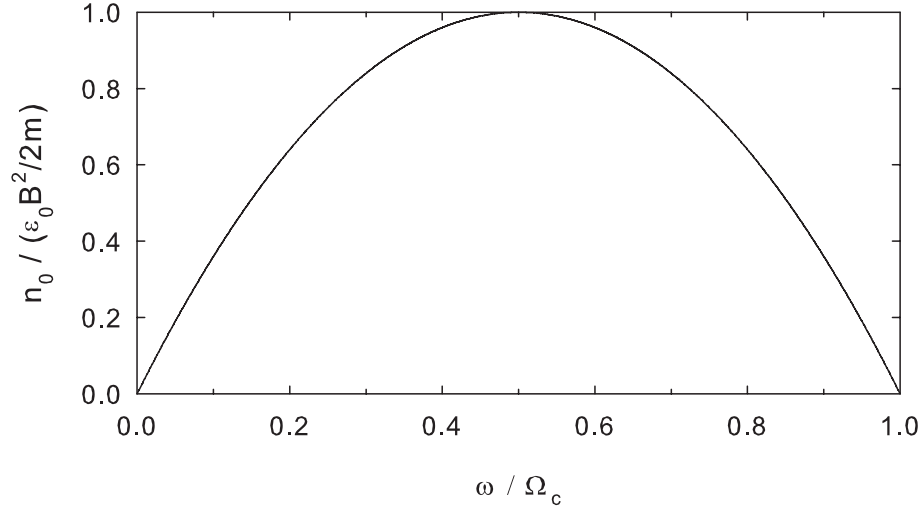


Figure 5.1: The plasma density as a function of plasma rotation frequency.

This is often written in terms of the plasma frequency, given by:

$$\omega_p^2 \equiv \frac{q^2 n_0}{\epsilon_0 m} = 2\omega_r (\omega_c - \omega_r) \quad (5.17)$$

The density of the plasma is therefore determined by the rotation frequency of the plasma (Fig. 5.1). The maximum theoretical density of the plasma is  $n_0 = \epsilon_0 B^2 / 2m$  when  $\omega_r = \omega_c / 2$ . For an electron plasma in a 1 T field, this maximum density is  $5 \times 10^{12} \text{ cm}^{-3}$ . We operate in a regime where  $\omega_r \ll \omega_c / 2$ , with plasma densities typically five orders of magnitude less than this limit.

It is important to note that the results thus far are valid for any cylindrically-symmetric trap potential. We shall now consider the plasma shape for an ideal quadratic potential in a Penning trap.

## 5.2 Plasmas in a Quadratic Electric Potential

Let's now assume that the trap potential is perfectly quadratic:

$$\phi_t(\rho, z) = \frac{m\omega_z^2}{2q} \left( z^2 - \frac{1}{2}\rho^2 \right) \quad (5.18)$$

This is the lowest-order axially-confining potential possible that satisfies the requirement  $\nabla^2\phi_t = 0$ . In the cylindrical electrode geometry used here, the real trap potential will also include higher-order components (Section 2.1.2), but the electrode geometry is chosen to make the potential quadratic (to a good approximation) near the center of the trap.

Plugging Eq.(5.18) into Eq.(5.14), the potential due to the plasma space charge is then:

$$\phi_p(\rho, z) = -\frac{m\omega_z^2}{2q} \left( z^2 - \frac{1}{2}\rho^2 \right) - \frac{m}{2q}\omega_r(\omega_c - \omega_r)\rho^2 \quad (5.19)$$

to exactly cancel the effective potential of the trap in the reference frame rotating with the plasma. Using the result in Eq.(5.17), this simplifies to:

$$\phi_p(\rho, z) = -\frac{m\omega_z^2}{2q} \left[ z^2 + \frac{1}{2} \left( \frac{\omega_p^2}{\omega_z^2} - 1 \right) \rho^2 \right] \quad (5.20)$$

This is simply a quadratic potential, which is the potential generated by a spheroidal distribution of uniform charge-density [102]. Since this solution must be unique by the uniqueness theorem for Poisson's equation, the equilibrium shape of the plasma in a quadratic trap potential is therefore a spheroid.

The number of particles in the spheroidal plasma is related to its dimensions by:

$$N = \frac{4}{3}\pi n_0 z_p \rho_p^2 \quad (5.21)$$

where  $\rho_p$  is the radius and  $z_p$  is the axial half-length of the spheroidal plasma.

If we define the aspect ratio of the spheroid as  $\alpha \equiv z_p/\rho_p$ , then this quantity can be related to the plasma frequency and the axial frequency by [103]:

$$\frac{\omega_z^2}{\omega_p^2} = \frac{Q_1^0\left(\frac{\alpha}{\sqrt{\alpha^2-1}}\right)}{\alpha^2-1} \quad (5.22)$$

where  $Q_1^0$  is the Legendre function of the second kind:

$$Q_1^0(z) \equiv \frac{z}{2} \ln\left(\frac{1+z}{z-1}\right) - 1 \quad (5.23)$$

We now have enough information to fully describe a plasma based upon just a few parameters. The mass and charge of the particles in the plasma are known. The frequencies  $\omega_z(V)$  and  $\omega_c(B)$  are then derived from the electrode voltage and magnetic field of the Penning trap, and are also well known. It is also relatively simple to determine the number of particles in the plasma, either by destructively measuring the charge of the plasma, or by loading a well calibrated number of particles to begin with. Once we have these parameters, it is sufficient to know just one of the remaining parameters,  $\alpha$ ,  $\rho_p$ ,  $z_p$ ,  $n_0$ ,  $\omega_p$ , or  $\omega_r$  to completely describe the spheroidal plasma. A possible method of determining one of the remaining variables is to measure the frequencies at which the plasma oscillates, which will now be discussed briefly.

### 5.3 Spheroidal Plasma Dynamics

When the plasma is disrupted slightly from its equilibrium position, the resulting collective motion of the particles can be characterized as a superposition of distinct modes with oscillatory frequencies that depend upon the equilibrium shape of the plasma. The modes are classified by integers  $(l, m)$ , with  $l > 0$  and  $|m| < l$ . The

$m = 0$  modes are cylindrically symmetric, while the  $m \neq 0$  modes are not. The frequencies of these modes have been analytically calculated in the low-temperature limit for spheroidal plasmas in a quadratic electric potential [104]. In this ideal case, the frequency of a given  $(l, 0)$  mode,  $\omega_l$ , is given by:

$$1 - \frac{\omega_p^2}{\omega_l^2} = \frac{k_2 P_l(k_1) Q_l'(k_2)}{k_1 P_l'(k_1) Q_l(k_2)} \quad (5.24)$$

where

$$k_1 = \frac{\alpha}{\sqrt{\alpha^2 - 1 + \frac{\omega_p^2}{\omega_l^2}}}, \quad k_2 = \frac{\alpha}{\sqrt{\alpha^2 - 1}}, \quad (5.25)$$

The  $(1,0)$  mode is the center-of-mass mode, corresponding to the entire plasma oscillating axially about the equilibrium position while maintaining its equilibrium shape. For a perfectly quadratic electric potential, the frequency of this motion is identical to the axial oscillation frequency of a single particle,  $\omega_1 = \omega_z$ . The  $(2,0)$  mode is the quadrupole mode, which corresponds to the plasma having a spheroidal shape with an oscillating aspect ratio. The motions described by some of the higher order modes are depicted in Fig. 5.2, along with their frequencies in relation to  $\omega_z$ .

Knowledge of  $\omega_z$  and the frequency of one higher-order mode is sufficient to determine the density and aspect ratio of the plasma using Eq.(5.24). This provides us with the previously missing piece of information that allows us to fully describe the spheroidal plasma in an ideal Penning trap. Because the Penning trap used is not ideal however, this spheroidal description is only approximately correct. A more accurate description of the plasmas will be discussed in the next section.

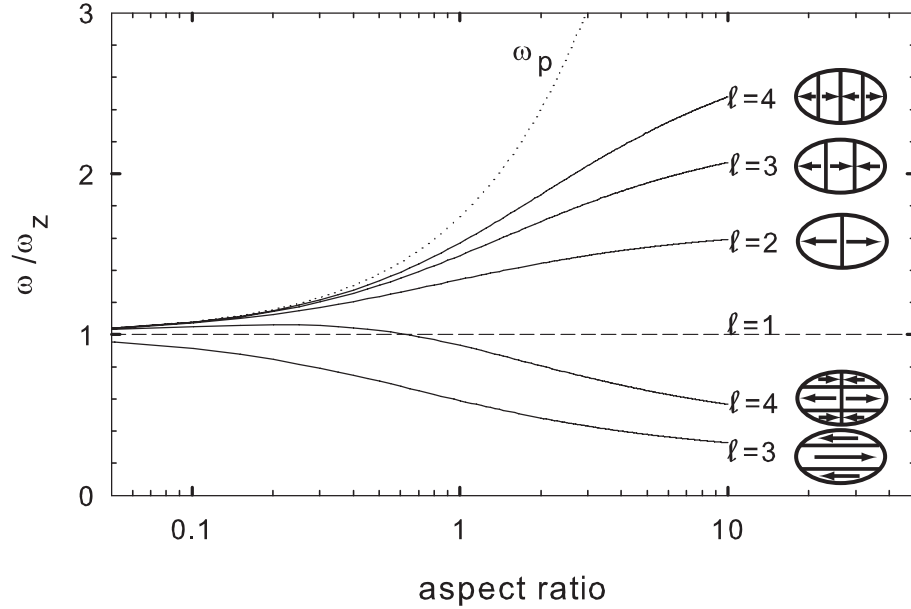


Figure 5.2: Frequencies of the lowest-order cylindrically-symmetric ( $m = 0$ ) modes as a function of the plasma aspect ratio [105], scaled to the center of mass ( $l = 1$ ) mode frequency. The plasma oscillations corresponding to each mode are depicted. The plasma frequency is also plotted (dotted curve).

## 5.4 Plasmas in Non-ideal Potentials

The cylindrical electrodes in our Penning trap do not form a perfect quadrupole electric potential (Section 2.1.2). Consequently, the non-neutral plasmas confined within our electrodes are not perfect spheroids. The shape of the plasmas must self-consistently solve Eq. 5.9 and Eq. 5.15. In order to determine the equilibrium shape of the confined plasmas, we use the computer code *equilsor2* provided to us by Spencer *et al.* [106]. The axially-symmetric mode frequencies are determined for these equilibrium plasma shapes within realistic confining potentials using the *rattle* 2D particle-in-cell computer code, also provided by Spencer *et al.* [107, 108].

The *equilzor2* and *rattle* codes were used to determine equilibrium plasma shapes and mode frequencies for a range of values of particle number, plasma density, and confining voltage in order to identify the geometry of our plasmas using measurements of the mode frequencies. Because our primary interest is the density and geometry of positron plasmas used for antihydrogen production, these computations were carried out assuming that the plasma is confined in a radius-length electrode with 18 mm radius, which is the size of electrodes within the Ioffe trap in the upper electrode stack.

The mode frequencies predicted by *rattle* have some interesting differences with the analytical frequency predictions for an ideal quadrupole confining potential. The first-order difference between the two is that the *rattle* results predict that the center-of-mass (COM) oscillatory mode frequency is dependent upon the plasma geometry, while for an ideal quadrupole potential, the COM frequency is equal to the single-particle axial oscillation frequency for all plasma geometries. The COM frequencies predicted by *rattle* are shown in Fig. 5.3.

The COM frequency of the plasma is determined exclusively by the confining potential from the electrodes, since the total force on the plasma due to the space charge potential is zero by Newton's third law. The plasma has an approximately uniform density, and by the definition of the COM mode, the plasma retains its equilibrium shape throughout the oscillation. As such, when the plasma is displaced axially from its equilibrium position and the restoring forces on the particles are summed, most of the forces cancel due to symmetry arguments, and only the particles on the extended edge of the plasma contribute to the total restoring force. The

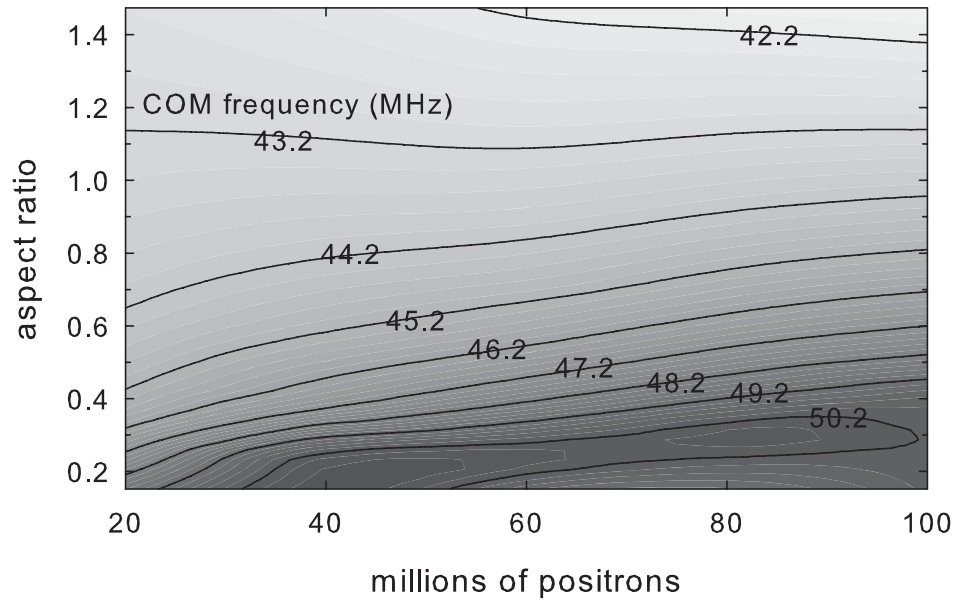


Figure 5.3: The plasma center-of-mass (COM) oscillation frequency as a function of particle number and plasma aspect ratio. The plasma is confined by a 100 V potential on a single radius-length electrode. The axial oscillation frequency of a single particle near the center of the trap would be 43.2 MHz.

COM frequency therefore depends upon the restoring potentials sampled along the boundary of the plasma.

The dependence of the COM frequency upon the plasma geometry arises from the anharmonicity of the trapping potential in our cylindrical electrodes. Near the central axis of the trap, the real confining potential within a cylindrical radius-length electrode is slightly less steep than the corresponding ideal quadrupole potential (Fig. 5.4a). Far off-axis however, the real confining potential is more steep than in the corresponding ideal quadrupole potential (Fig. 5.4b). Consequently, if the diameter of the plasma is much larger than its axial length, then the net axial confining potential that the plasma experiences will be larger than the value for a single particle near

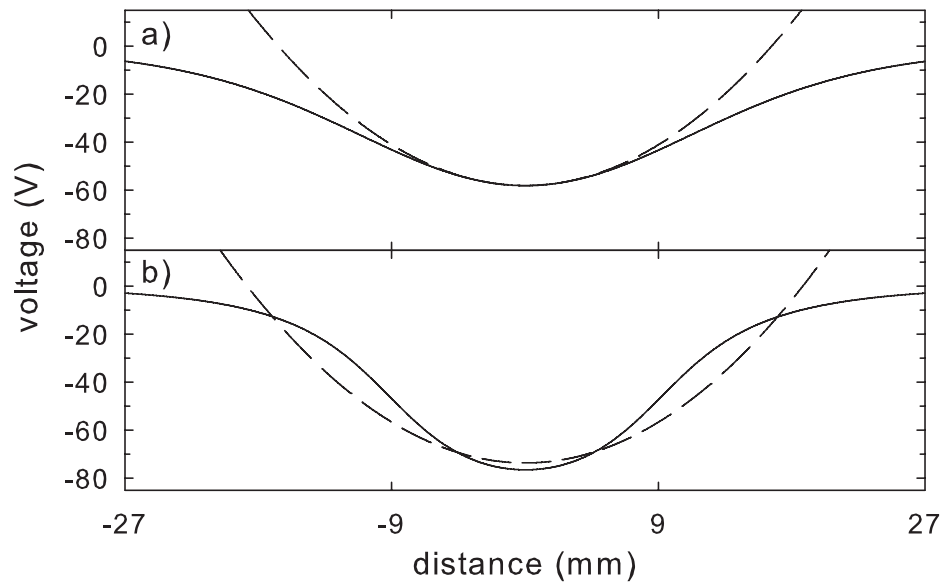


Figure 5.4: The axial confining potential due to a 100 V potential applied to a 18 mm-radius-length electrode (solid curve) compared to the corresponding ideal quadrupole potential (dashed curve), both (a) on the central axis of the electrode and (b) 12 mm off-axis.

the center of the trap. If the axial length is much larger than the diameter, then the opposite is true.

The computations in Fig. 5.3 indicate that the COM frequency equals the ideal value when plasmas have an aspect ratio of about 1.1, while aspect ratios that are larger or smaller than this value alter the COM frequency in the expected way. The sensitivity of the COM frequency to the plasma aspect ratio increases as the particle number increases, due to the resulting increase in both plasma dimensions. This also explains previous observations that the COM frequencies of our plasmas drift over time as our plasmas slowly expand and particles are lost. Other groups have experimentally observed variations in the COM frequency that become more pronounced as the particle number or plasma radius increases [109, 110], while these variations

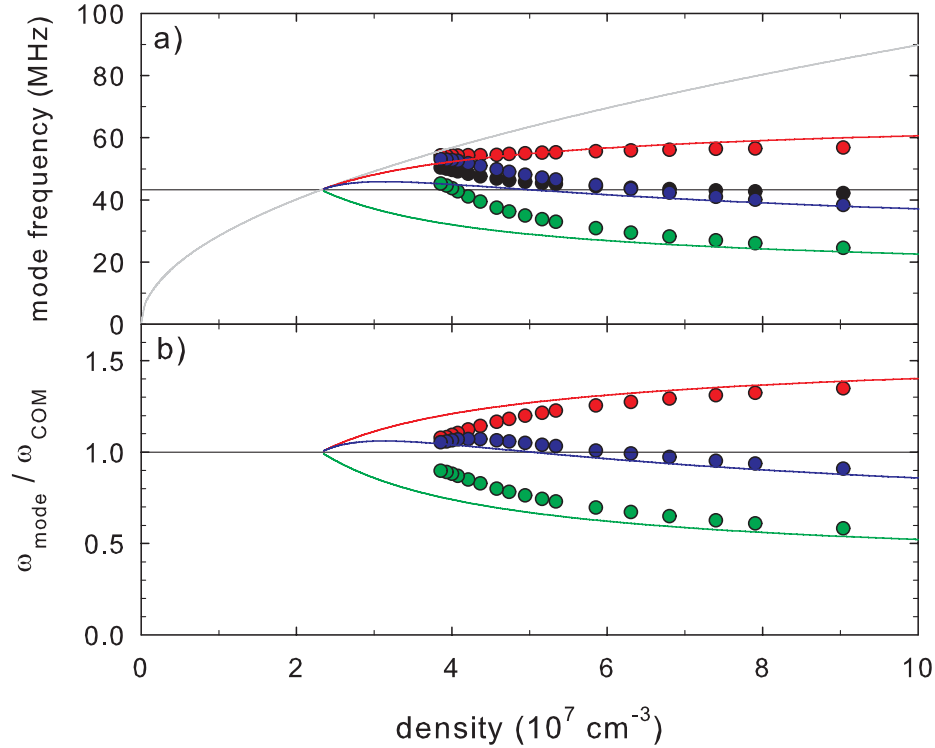


Figure 5.5: (a) The points indicate calculations of the frequency of the COM mode (black),  $(l, m) = (2, 0)$  mode (red), lower  $(l, m) = (3, 0)$  mode (green), and lower  $(l, m) = (4, 0)$  mode (blue) of a non-spheroidal plasma as a function of plasma density, for 60 million positrons in a 100 V well in a radius-length electrode. The solid curves indicate the corresponding predictions assuming a spheroidal plasma in a perfect quadrupole potential, as well as the plasma frequency (gray). (b) When the frequencies are scaled to the COM frequency, the two predictions can be directly compared.

are not observed in a more ideal quadrupole trap [110].

As the COM frequency changes, so do all of the other mode frequencies, as demonstrated by the numerically calculated mode frequencies in Fig. 5.5a. If all of the mode frequencies are scaled to the COM frequency, as in Fig. 5.5b, then we can make a more direct comparison between the analytical predictions for the mode frequencies in an

ideal potential and the realistic mode frequencies predicted by the *rattle* calculations. If we measure a set of mode frequencies, Fig. 5.5b demonstrates that the mode frequencies calculated for an ideal potential can not be used to accurately determine the plasma parameters. Doing so would predict that the plasma is less dense and has a smaller aspect ratio than it does in reality. The plasmas that we typically load do not closely resemble spheroids, as will be discussed further in the following section. The ideal and the realistic mode frequencies agree more closely however for high-density, low-aspect ratio plasmas, when the plasma is more tightly confined near the center of the electrode.

## 5.5 Plasma Mode Frequency Detection

So far, we have used only very simple electronics to measure the frequencies of plasma modes within the Penning trap, as schematically depicted in Fig. 5.6. A RF signal generator outputs a constant sine wave at a given probe frequency. This signal passes into a pair of attenuators that are switched off for a 10  $\mu\text{s}$  duration, converting the CW output of the signal generator into a 10  $\mu\text{s}$  duration pulse. This pulse is applied to the electrode neighboring the plasma-confinement electrode. The response of the plasma to the applied pulse is determined by measuring the voltage induced on the opposite neighboring electrode due to the induced image charges from the oscillating plasma. This voltage is in turn amplified and read out on a spectrum analyzer, which operates in zero-span mode to measure the amplitude of the signal oscillating at the probe frequency as a function of time. The response of the plasma to the input signal can be measured as a function of frequency by repeating this

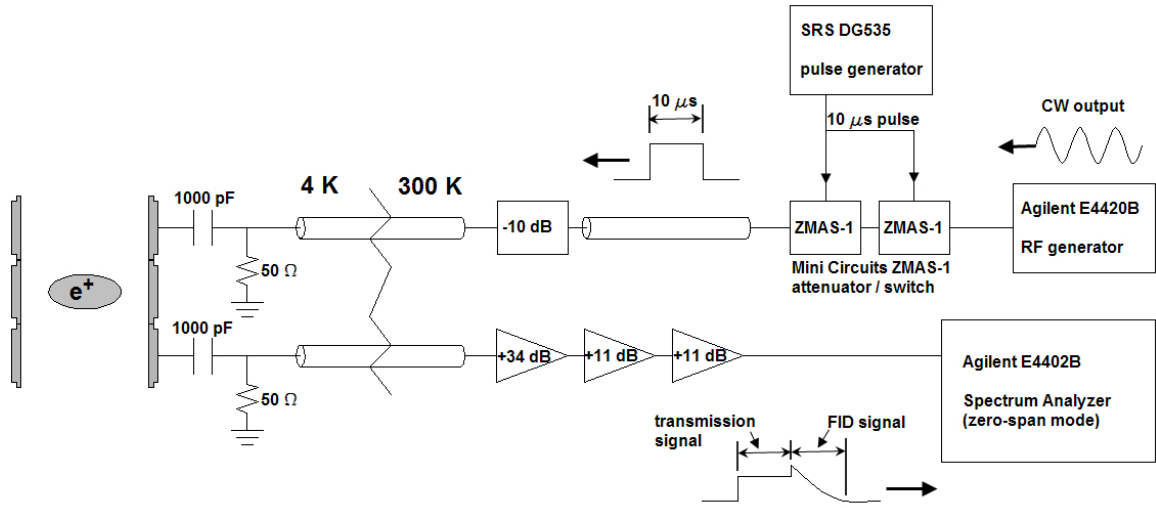


Figure 5.6: The circuit used to detect plasma mode frequencies.

sequence for a range of frequencies at discrete intervals.

Without any particles in the trap, some portion of the signal will be transmitted between the two electrodes. When a plasma is present, the shape of the response signal is altered if the probe frequency is resonant with a plasma mode frequency. While scanning the probe frequency, we measure the amplitude of the free induction decay (FID) signal following the pulse, which is due to the decay of the excited plasma mode oscillation. We also record the amplitude of the transmitted signal during the 10  $\mu\text{s}$  pulse duration, which indicates resonances at the same frequencies as the FID signal. An example of the plasma mode detection signal for a plasma containing 60 million positrons is shown in Fig. 5.7. This scan clearly identifies three plasma mode frequencies, which is what we typically see.

These three mode frequencies, from highest to lowest frequency respectively, correspond to the  $(l, m) = (2, 0)$  quadrupole stretch mode, the center-of-mass (COM)

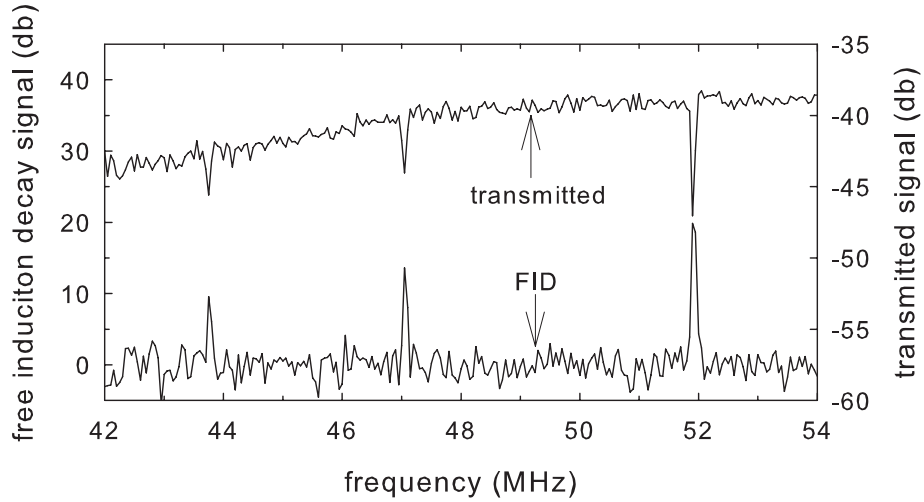


Figure 5.7: The plasma mode detection signal for 60 million positrons stored in a single radius-length electrode with a 100 V confining potential.

oscillation mode, and the  $(l, m) = (2, 1)$  azimuthally asymmetric quadrupole mode that describes the central axis of the plasma precessing about the magnetic field direction [111, 112]. This last mode is not an axially symmetric mode, and therefore its frequency can not be predicted for our realistic plasma geometry using the *rattle* code. However, if we choose one particular ratio of mode frequencies predicted from our rattle simulations, we find the remaining ratios of mode frequencies can be predicted accurately from the analytical solutions for an ideal quadrupole potential. We identify the low-frequency mode as the  $(2, 1)$  mode because the ratio of the mode frequency to the COM frequency is in remarkable analytic agreement with the ratio of the COM and quadrupole mode frequencies.

The shape of the plasma corresponding to the mode scan in Fig. 5.7 is shown in Fig. 5.8. This demonstrates that our plasmas do not closely resemble the spheroidal shape predicted for a perfect quadrupole electrostatic potential, but rather have more

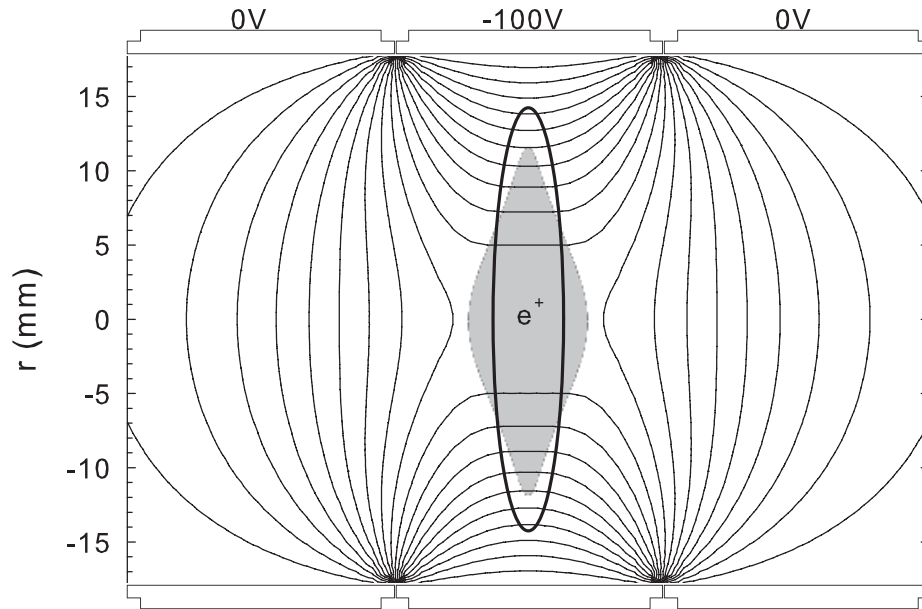


Figure 5.8: The shape of the plasma corresponding to the mode scan in Fig. 5.7 (gray profile), and the corresponding equipotential contours. The black ellipse indicates the spheroidal plasma shape that would be predicted from the mode frequencies for a perfect quadrupole confining potential.

of a diamond shape. For comparison, the black ellipse in Fig. 5.8 is the plasma cross section that would have been predicted from the measured mode frequencies if we assumed a perfectly quadrupole potential. The plasma in Fig. 5.8 corresponds to 60 million positrons with a density of  $4 \times 10^7 \text{ cm}^{-3}$ . Identical positron plasmas were loaded at the start of each antihydrogen experiment described in Chapter 7.

In the future, we hope to expand our capabilities at measuring our plasma geometries by pulsing the plasmas onto phosphor screens and imaging them. An alternate method, measuring the charge collected on aperture faraday cups of various radii, was tested in the past and found to be consistent with plasma geometries derived from mode measurements [113, 66].

## Chapter 6

# Particle Stability in a Combined Penning-Ioffe Trap

The most straightforward approach to confining antihydrogen for spectroscopy would be to superimpose the magnetic gradients needed to trap antihydrogen atoms on the uniform magnetic field of the Penning trap used to store the positrons and antiprotons from which antihydrogen is formed. A quadrupole Ioffe trap is the simplest form of magnetic trap that is compatible with the static magnetic field of the Penning trap, but the radial field of a Ioffe trap breaks the cylindrical symmetry that assures confinement of the charged antiprotons and positrons in the Penning trap. In the single particle picture, there are still stable particle orbits below a critical cut-off radius if radially-transporting resonance frequencies are avoided [114]. For dense plasmas, these radially-transporting resonances lead to a diffusive loss of particles [115, 116]. It was suggested that these loss processes may make it impossible to confine positrons and antiprotons in a Penning trap with a superimposed quadrupole-Ioffe field for a

long enough time to form antihydrogen [115, 117, 25]. High-order multipole Ioffe traps reduce the effects of these radial losses [118], but have associated disadvantages for the eventual goal of antihydrogen spectroscopy. ATRAP demonstrated that confinement of positrons and antiprotons in a Penning trap with a superimposed quadrupole-Ioffe field is possible for a sufficiently long time to form antihydrogen [24]. This chapter will summarize the key issues and experimental results surrounding this topic.

## 6.1 Single Particle Stability

Combining the radial magnetic field from a quadrupole Ioffe trap with the axial bias field,  $B_0\hat{\mathbf{z}}$ , of a Penning trap results in the magnetic field of a combined Penning-Ioffe trap given by:

$$\vec{B} = B_0\hat{\mathbf{z}} + \beta(x\hat{\mathbf{x}} - y\hat{\mathbf{y}}) \quad (6.1a)$$

$$= B_0 [\hat{\mathbf{z}} + (x\hat{\mathbf{x}} - y\hat{\mathbf{y}})/R_0] \quad (6.1b)$$

where  $\beta$  is the radial gradient of the Ioffe field and  $R_0 = B_0/\beta$  is the characteristic radius when the radial magnetic field equals the axial magnetic field. The magnetic field lines in a combined Penning-Ioffe trap take the shape depicted in Fig. 6.1.

The low-energy charged particles in the trap form tight cyclotron orbits around these magnetic field lines and are constrained to travel along them. In the absence of any electric field, a particle starting at a given radius in the X-Y plane in Fig. 6.1 with some initial velocity in the Z direction will follow a single field line and be exponentially transported outward in the X direction until it collides with the trap electrodes, while a particle moving in the -Z direction will be exponentially transported outward

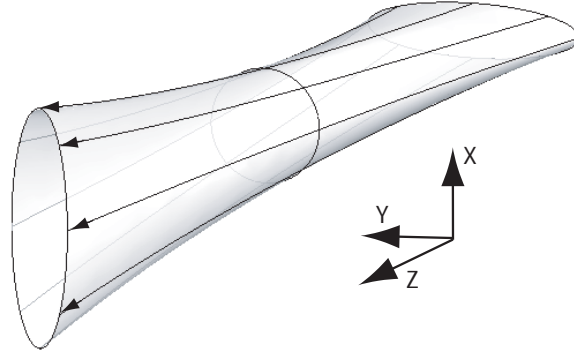


Figure 6.1: Straight field lines from the axial bias field are distorted by the radial field of the quadrupole Ioffe trap, such that field lines passing through a circle in the X-Y plane form the shape depicted.

in the Y direction. This basic principle makes it difficult to move particles over long distances within a Penning-Ioffe trap. For the purposes of future discussions, it will be convenient to depict only the X-Z or Y-Z planes, where the field lines lie strictly in the planes and this radial transport problem is most pronounced. The field lines then take the form:

$$\rho = \rho_{z=0} \exp(\pm\beta z/B_0) \quad (6.2)$$

Adding to this magnetic field an ideal quadrupole electrostatic confining potential, the potential energy of a charge is given by:

$$W = q\Phi = \frac{m\omega_z^2}{2} \left[ z^2 - \frac{x^2 + y^2}{2} \right] \quad (6.3)$$

The equations of motion of the particle are then:

$$\ddot{z} = -\epsilon^2\omega_c^2 z + \frac{\omega_c}{R_0} (y\dot{x} + x\dot{y}) \quad (6.4a)$$

$$\ddot{x} = \frac{1}{2}\epsilon^2\omega_c^2 x - \omega_c\dot{y} - \frac{\omega_c}{R_0} y\dot{z} \quad (6.4b)$$

$$\ddot{y} = \frac{1}{2}\epsilon^2\omega_c^2 y + \omega_c\dot{x} - \frac{\omega_c}{R_0} x\dot{z} \quad (6.4c)$$

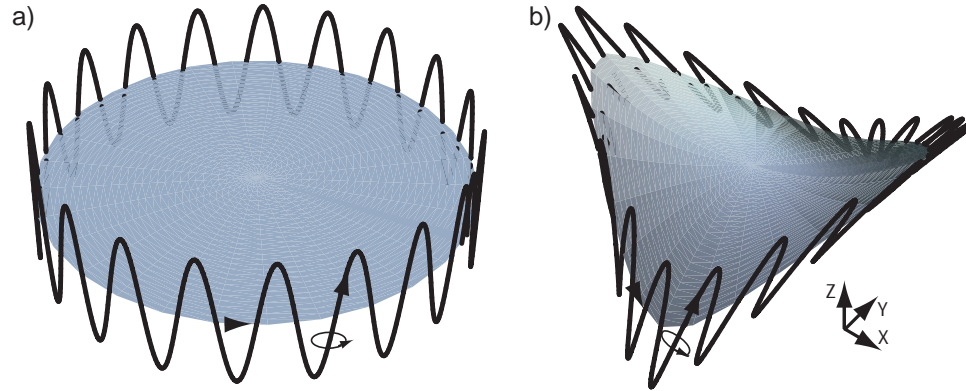


Figure 6.2: The motion of a charged particle in a Penning trap (a) without and (b) with a radial Ioffe field [114].

where  $\omega_c = |e|B_0/m$ , and  $\epsilon = \omega_z/\omega_c$ . For  $\rho \ll R_0$ , the nonlinear terms can be neglected, so that the motion of a charge near the center of the trap is approximately described by the three uncoupled oscillations in an ideal Penning trap. The frequencies of these oscillations differ by  $\epsilon$  from each other, where  $\epsilon \ll 1$  for our trap, so that  $\omega_m \ll \omega_z \ll \omega_c$ .

The general solution of the particle motion for small  $\epsilon$  preserves these three distinct oscillations with the same frequency hierarchy, each one of which is associated with a different adiabatic invariant [114]. The motions described by these oscillations differ from those in an ideal Penning trap however, as depicted in Fig.6.2. The cyclotron motion becomes perpendicular to the local magnetic field, and the magnetic moment  $M \approx mv_c^2/2B$  is an adiabatic invariant as the cyclotron velocity and magnetic field magnitude vary. The “axial” oscillations occur along the local magnetic field line, and  $J \approx E_z/\omega'_z$  is an adiabatic invariant of the motion as the axial energy  $E_z$  and the oscillation frequency along the field line  $\omega'_z$  change with the particle radius. Particular magnetron orbit must lie on an electric equipotential since the magnetron

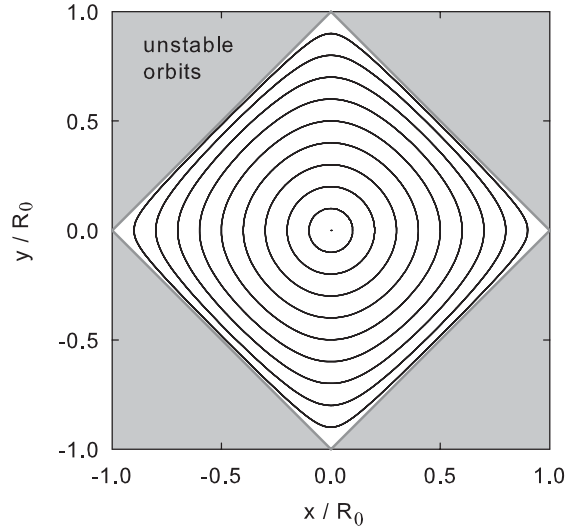


Figure 6.3: The projections of stable magnetron orbits in an ideal Penning-Ioffe trap onto the X-Y plane [114].

kinetic energy is much smaller than the potential energy. It must also lie on a stable equilibrium point of the axial motion, satisfying the condition  $\vec{E} \cdot \hat{\mathbf{B}} = -\nabla\Phi \cdot \hat{\mathbf{B}} = 0$ . Pictorially, these stable equilibrium points are located where the magnetic field lines are tangent to the equipotential curves. Using Eq. 6.1a and Eq. 6.3, this condition is satisfied on the curve:

$$z = \frac{x^2 - y^2}{2} \quad (6.5)$$

The magnetron orbit on a given equipotential is then given by the intersection of this curve with the equipotential curve in Eq. 6.3. The projection of these stable orbits onto the X-Y plane are depicted in Fig. 6.3. The magnetic flux  $\Phi_m$  enclosed by these magnetron orbits is another adiabatic invariant, so that a Penning trap magnetron orbit will transition to the Penning-Ioffe magnetron orbit with the same flux if the radial Ioffe field is turned on slowly.

Stable magnetron orbits only exist for  $B_0 > \beta(x + y)$ , establishing a maximum cut-off radius  $\rho_{cut} = R_0$ . Beyond that radius, there is no longer a restoring electric potential along the magnetic field line. Note that this is the maximum radial extent of the Penning-Ioffe magnetron orbit, but the radius changes throughout the orbit. A more useful figure of merit is the maximum magnetron radius in the initial Penning trap that will remain confined as the Ioffe fields is turned on slowly. Using the invariance of the flux through the magnetron orbit, we find that this maximum radius is  $\rho_{cut} = \sqrt{4/3\pi} R_0 \approx 0.65 R_0$  for a charged particle in an ideal Penning-Ioffe trap [119].

If the electrostatic potential is not a perfect quadrupole, then Eq. 6.5 is no longer the explicit solution to the condition  $-\nabla\Phi \cdot \hat{\mathbf{B}} = 0$ , but there is still a simple stability condition for realistic Penning-Ioffe traps. The equipotential curves of a confining potential in a cylindrical ring electrode intersect the edge of the electrode. As such, any particle moving along a field line that intersects a neighboring electrode will experience a confining electric potential, while those moving along a field line that intersects the confining electrode itself will be constantly accelerated toward the electrode and lost. In the plane where the field lines are maximally diverging, this simple axial confinement condition establishes an effective maximum cut-off radius for particles. Particles will be lost from the trap if they are at a radius in the electrode central plane that is larger than:

$$\rho_{cut} = \rho_0 \exp(-\beta z_0 / B_0) \quad (6.6)$$

where  $\rho_0$  and  $z_0$  are respectively the electrode radius and half-length.

The curves in Fig. 6.4a depict the electric equipotentials and magnetic field lines in the A-Trap Penning-Ioffe trap with the maximum 375 mK magnetic trap depth

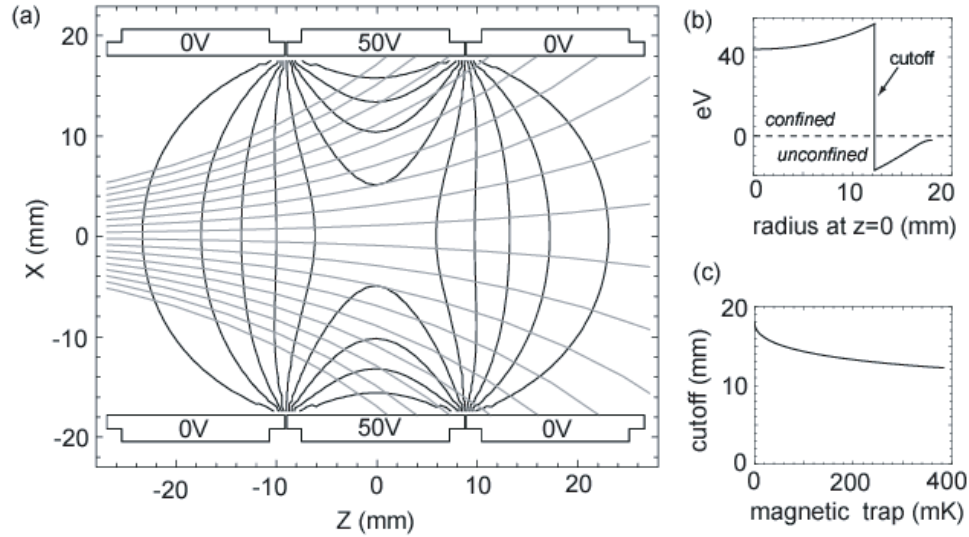


Figure 6.4: (a) The cross section of cylindrical ring electrodes, displaying the electric equipotentials (black) and magnetic field lines (gray) in the A-Trap Penning-Ioffe trap at the full 375 mK magnetic trap depth. (b) The corresponding electrostatic well depth for a charge moving along the field line that crosses  $Z=0$  at the indicated radius. (c) The cutoff radius in the Penning-Ioffe trap as a function of the total magnetic trap depth.

applied ( $\beta\rho_0/B_0 = 0.78$ ). The magnitude of the confining potential seen by a particle moving along a field line at a given radius is shown in Fig. 6.4b, demonstrating the sharp cut-off radius beyond which particles are no longer confined. The cut-off radius as a function of Ioffe trap depth is given in Fig. 6.4c, including the effect of the mirror coils that boost the axial field.

The cut-off radius in Eq. 6.6 has been identified by others [120], and has been referred to in some papers as “ballistic loss” [25]. The single-particle loss mechanism in all of these cases is identical to that described previously for a particle in an ideal Penning-Ioffe trap though [114], and was just applied to a non-ideal electric confining potential. As for the case in an ideal Penning-Ioffe trap, this effective cut-off radius does not exactly corresponding to the initial magnetron radius of the particle before

the Ioffe field is turned on, but it is a reasonable approximation. This maximum cut-off radius has been used to measure the radial distribution of trapped antiprotons by measuring the number of antiproton annihilations as a function of Ioffe field as the Ioffe trap is turned on [121]. Although such a method could in principle be used in the experiments described here, the slow ramp rate of our Ioffe trap makes such measurements challenging.

In order for the single-particle orbits to remain stable in the radial Ioffe field, the resonance  $\omega'_z = 2\omega'_m$  that couples the modified axial and magnetron motions must be avoided. When this resonance condition is satisfied, the particle's "axial" oscillations along field lines will be timed with its magnetron rotation onto the alternately radially converging and diverging magnetic field planes in Fig.6.1 in such a way that the particle's radius will be either constantly increasing or decreasing, depending upon the relative phase of the axial and magnetron oscillations. The magnetron motion transfers energy into the axial motion by resonantly driving the particle up and down in the Z direction as it rotates around the orbit in Fig.6.2b, causing the magnetron radius to grow until the particle is lost. Large magnetron orbits also have Fourier components at odd harmonics of  $\omega'_m$ , resulting in additional resonances at  $\omega'_z = 2N\omega'_m$ , where  $N > 1$  is an odd integer, although these resonances typically occur only over a very narrow range of magnetron radius. For the trap configurations considered here, these resonant conditions can be easily avoided in the single particle limit, but they become a more serious problem in dense plasmas, as discussed in the next section.

## 6.2 Diffusive Losses in Plasmas

In dense plasmas, particles arrange themselves into a distribution that cancels the “axial” electric field along magnetic field lines inside the plasma. As such, the parameter equivalent to the single particle axial frequency becomes the particle bounce frequency within the borders of the plasma, which is dependent upon both the thermal distribution of the particles and the geometry of the plasma. Likewise, the single-particle magnetron frequency must be replaced by the rigid plasma rotation frequency  $\omega_r$ . With these modifications, the resonant condition described in the single particle case is still relevant here,  $\omega'_z = 2\omega_r$ . The thermal distribution of axial-bounce frequencies assures that some fraction of the particle population will be resonant with this condition.

An additional complication is that frequent collisions between particles can knock a particle from one radial trajectory to a nearby one. The combined effects of these collisions and the axial frequency thermal distribution can be described by a random-walk radial-diffusion process. Gilson *et al.* [115, 116] proposed that the diffusion coefficient should be approximately given by

$$D = \frac{64z_p^3\rho^2\omega_r^2\beta^2}{\pi^4 B_0^2} \sqrt{\frac{m}{2\pi kT}} \exp\left[\frac{-\omega_r^2}{2\omega_T^2}\right] \quad (6.7)$$

where  $\rho$  is the particle radius,  $z_p$  is the plasma half-length, and

$$\omega_T = \frac{\pi}{4z_p} \sqrt{\frac{kT}{m}} \quad (6.8)$$

is half the mean thermal axial bounce frequency in the plasma. It should be noted that the plasma length, which affects the distribution of axial bounce frequencies within the plasma, is treated as a constant in Eq. 6.7. In reality, the length of our

plasma changes substantially as a function of radius (Section 5.5), so a more complete picture would replace  $z_p$  with  $z_p(\rho)$  for particles at different radii. The particles will diffuse radially until they reach the cut-off radius  $\rho_{cut}$  (Eq. 6.6), beyond which they are lost. If we make the simplifying assumption that the plasma is a uniform-density cylinder, then to first order, we can estimate the particle loss time constant from Fick's law as [66]:

$$\tau \approx 0.2 \frac{\rho_{cut}^2}{D} \quad (6.9)$$

Although this approximation is overly simplistic, it does demonstrate that the diffusive particle loss is strongly dependent upon the cut-off radius imposed by the diverging magnetic field lines within the Ioffe trap.

Initial experiments conducted by Gilson and Fajans [115, 117] demonstrated that the scaling of the diffusion coefficient with  $\omega_r, \beta, B_0$ , and  $z_p$  showed excellent agreement with Eq. 6.7, while the scaling with  $kT$  did not. These experiments typically used plasmas with much larger  $z_p$  and  $kT$ , and much smaller  $B_0$  than used in our experiments however. A subsequent experiment more closely replicated our trap conditions [25], and demonstrated rapid particle loss due to the particle cut-off radius followed by slower diffusive loss over the course of minutes. The results of this paper shall be discussed further later in comparison with our measurement. The particle losses were sufficiently dramatic in this case to convince the ALPHA collaboration to use an octupole Ioffe trap rather than a quadrupole [118, 122]. The relative merits and disadvantages of quadrupole and higher-order Ioffe traps will now be briefly discussed.

### 6.3 Comparing Quadrupole to Higher-Order Ioffe Traps

The radial magnetic field in a Ioffe trap is produced by passing currents through vertical bars with alternating current directions. The simplest Ioffe field is produced by a quadrupole trap with four bars, while higher-order Ioffe fields can be produced with additional bars. I shall focus here on comparing quadrupole Ioffe traps and Octupole Ioffe traps, which use eight current bars. Both of these designs were considered for the ATRAP Ioffe trap, but a quadrupole design was eventually chosen.

The combined field of an ideal Ioffe trap and a static bias field has the general form

$$\vec{B}(\rho) = B_0 \hat{z} + B_w \left( \frac{\rho}{\rho_0} \right)^{n-1} [\hat{\rho} \cos(n\theta) - \hat{\theta} \sin(n\theta)] \quad (6.10)$$

where  $B_w$  and  $\rho_0$  are the field and radius at the electrode wall, and  $2n$  is the number of current bars forming the radial Ioffe field ( $n=2$  for quadrupoles,  $n=4$  for octupoles). Octupole fields have four maximally-divergent magnetic field planes. Field lines in these planes propagate outward like

$$\rho(z) = \frac{\rho_{z=0}}{\sqrt{1 - 2 \frac{B_w}{B_0} \frac{\rho_{z=0}^2}{\rho_0^2} \frac{z}{\rho_0}}} \quad (6.11)$$

The corresponding cut-off radius for particles following these field lines is

$$\rho_{cut} = \frac{\rho_0}{\sqrt{1 + \frac{B_w}{B_0} \frac{2z_0}{\rho_0}}} \quad (6.12)$$

where  $z_0$  and  $\rho_0$  are the confining electrode half-length and radius. The normalized cut-off radius  $\rho_{cut}/\rho_0$  for both quadrupole and octupole fields as a function of  $B_w/B_0$  for radius-length electrodes ( $z_0 = \rho_0$ ) is depicted in Fig. 6.5.

An octupole field has a larger cut-off radius than a quadrupole field with the same trap depth. Consequently, a larger fraction of particles will remain confined as

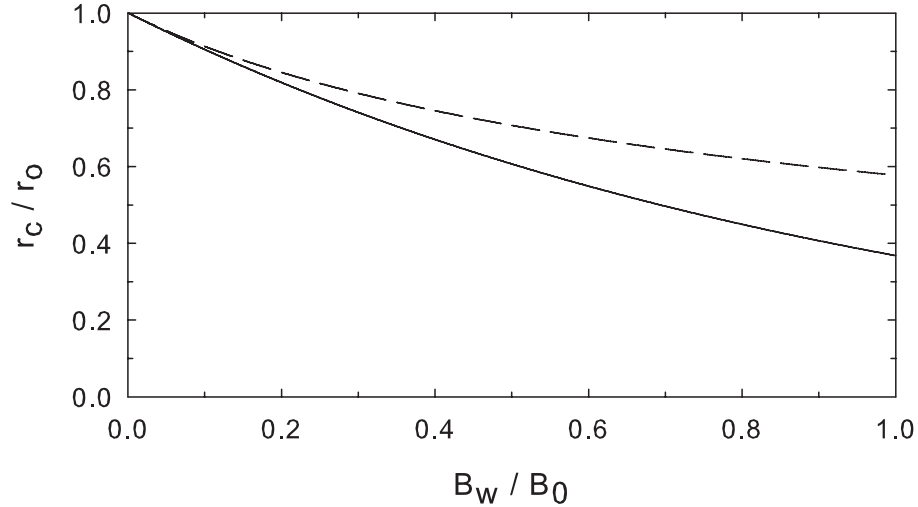


Figure 6.5: The normalized cut-off radius  $\rho_{cut}/\rho_0$  for both quadrupole (solid curve) and octupole (dashed curve) fields as a function of  $B_w/B_0$  for radius-length electrodes ( $z_0 = \rho_0$ ).

the Ioffe field is turned on for the octupole than for the quadrupole. Furthermore, diffusive loss is strongly suppressed for octupole Ioffe traps compared to quadrupole traps, because the radial field that causes this loss scales as  $(\rho/\rho_0)^3$  inside an octupole and as  $(\rho/\rho_0)$  inside a quadrupole.

Superconducting Ioffe traps of various multipole geometries can achieve similar radial field magnitudes at the radius of the Ioffe trap windings,  $R_t$ . This can be seen by noting that the current density required to produce the field  $B_t$  at  $R_t$  for a general multipole is [118]

$$J = \frac{2B_t}{\mu_0} \sin(n\theta) \quad (6.13)$$

and in turn that the maximum  $J$  achievable in superconducting windings is limited by the field at the windings. If we assume that quadrupole and octupole superconducting Ioffe traps can attain the same field  $B_t$  at  $R_t$ , we can then pose the related question of

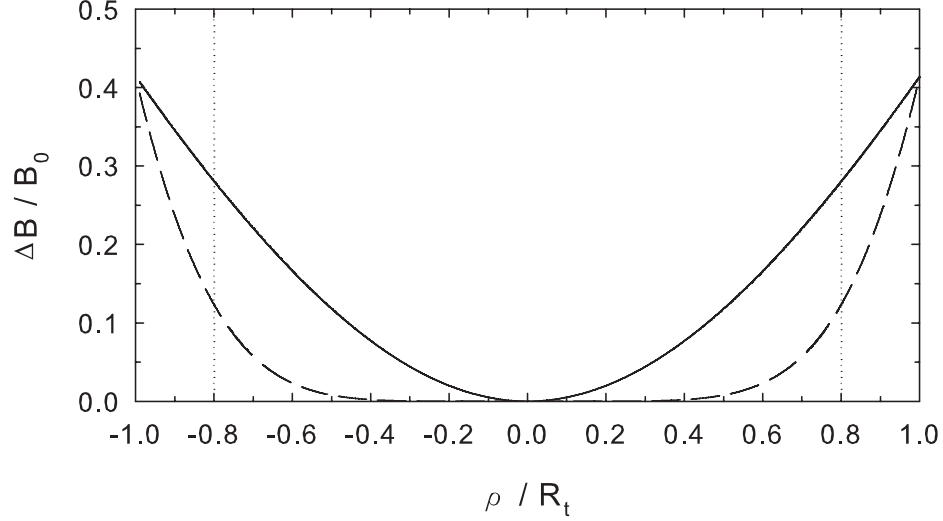


Figure 6.6: The normalized magnetic field magnitude  $\Delta B/B_0$  as a function of radius for both a quadrupole (solid curve) and octupole (dashed curve) Ioffe trap. The radius is normalized to the trap winding radius  $R_t$ , and it is assumed that  $B_t = B_0$  for both traps. The dotted lines represent the electrode radius at an arbitrarily-chosen location.

what magnetic trap depths can be achieved for atoms in Ioffe traps of either variety.

The confining potential seen by atoms in a Ioffe trap is proportional to the magnetic field magnitude. The trap depth at a given radius relative to the trap center is therefore proportional to  $\Delta B = |\vec{B}(\rho)| - |\vec{B}(\rho = 0)|$ . For a quadrupole Ioffe trap, this quantity has the form

$$\Delta B = \sqrt{B_0^2 + B_t^2 \left(\frac{\rho}{R_t}\right)^2} - B_0 \quad (6.14)$$

While for an octupole trap, it has the form

$$\Delta B = \sqrt{B_0^2 + B_t^2 \left(\frac{\rho}{R_t}\right)^6} - B_0 \quad (6.15)$$

These two functions are plotted in Fig.6.6, assuming the  $B_t = B_0$  for both traps.

The dotted lines in Fig.6.6 represent an arbitrarily-chosen electrode radius. Because

the electrode radius marks the maximum boundary for confined atoms, this figure demonstrates that the maximum realizable trap depth can be significantly larger for quadrupole traps than for octupole traps, even for otherwise identical trap geometries and fields at the Ioffe windings.

This marks one advantage of quadrupole Ioffe traps over octupole traps. Octupole Ioffe traps can only be effective if the superconducting windings are very close to the electrode inner diameter, which brings about serious constructional challenges, particularly for conventional coil-winding techniques on machined forms. However, using less-traditional winding techniques in conjunction with explicit efforts to minimize the space between the electrodes and the windings can allow effective octupole traps if great care is taken [122].

Another clear advantage of quadrupole traps is that they confine trapped atoms to a smaller volume near the center of the trap than octupoles do, allowing for much better overlap of trapped antihydrogen atoms with cooling and spectroscopy lasers. Furthermore, there tends to be more room for radial laser access ports to pass through a quadrupole Ioffe trap than there is in an octupole, simply because there are fewer current-carrying bars, and therefore more space available between them as well. It has also been proposed that trapped Rydberg antihydrogen atoms with large magnetic moments could cool by spontaneously decaying to lower energy levels while near the turning points of their motion inside the Ioffe trap [48], an effect that would be more pronounced within a quadrupole field.

A combination of these factors encouraged us to build a quadrupole Ioffe trap rather than a higher-order multipole Ioffe trap. Stability measurements with this Ioffe

trap will be outlined in the next section.

## 6.4 ATRAP Experimental Results

For our quadrupole Ioffe trap to be capable of trapping antihydrogen atoms, we had to first verify that sufficient numbers of positrons and antiprotons could be kept within the combined Penning-Ioffe trap long enough to form antihydrogen. As such, this was one of our first experiments when the apparatus became operational [24]. We expected to compete with both the immediate loss of particles outside of the cut-off radius (Eq. 6.6) as the Ioffe field was turned on, and the slower diffusive loss of particles (Eq. 6.7), which we expected to be suppressed for low particle densities.

For the antiproton stability tests, we electron-cooled the antiprotons in the lower electrode stack in a 1 T field (Fig. 6.7b). Successive bunches of antiprotons were stacked until we had loaded the desired number. The electrons were then separated from the antiprotons by removing the antiproton confining potential for a short enough time that the electrons could escape, but not the antiprotons. The resulting antiprotons were then moved from their initial loading position to the center of the deenergized Ioffe trap 0.4 m away (Fig. 6.7b) by adiabatically transferring them through 18 ring electrodes (Section 3.1.1). Some unexpected antiproton losses were observed during this process, possibly because of an elevated pbar temperature that was unfortunately present at the time. After adiabatically transporting them, the antiprotons could be held in the center of the deenergized Ioffe trap for an arbitrarily long time with no noticeable losses. At any point, they could be released from the trap onto the degrader, and their annihilations could be counted with high efficiency

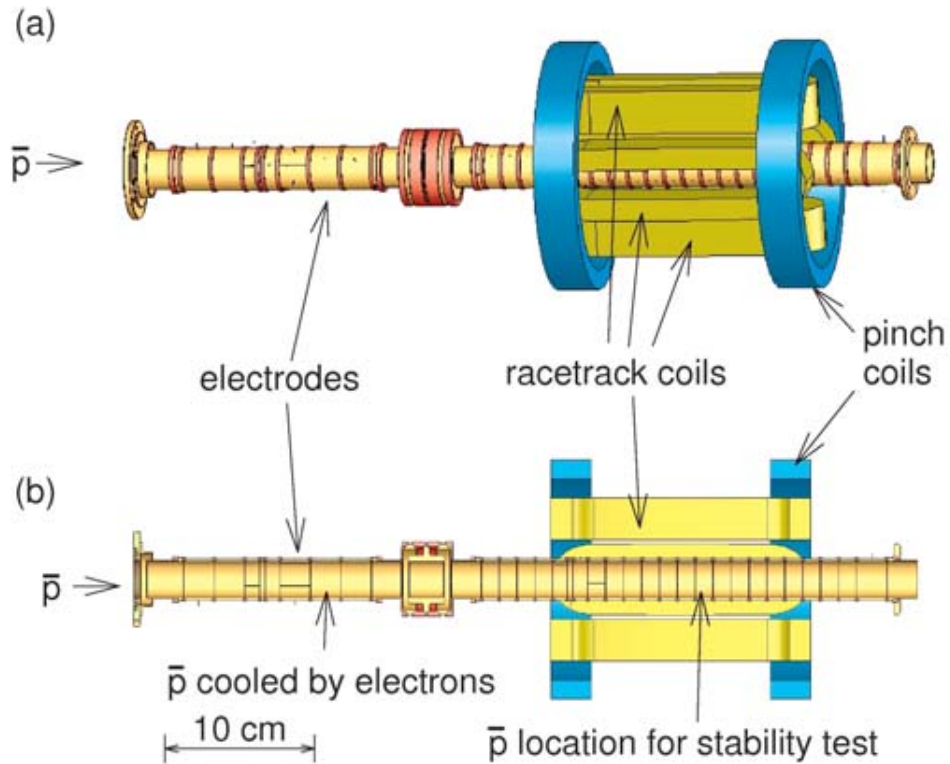


Figure 6.7: Exterior (a) and cutaway (b) view of the Penning-Ioffe apparatus used for particle stability measurements. A 1T bias field along the central axis of the electrode stack is produced by a large external solenoid (not depicted). Two pinch coils add an axially-confining gradient to the bias field. The radial quadrupole Ioffe field is produced by four racetrack coils.

(Section 3.2.2).

Axial confinement in the Ioffe trap was produced by a pair of pinch coils, while the radially-confining quadrupole field was produced by four racetrack coils (Fig. 6.7a). The trap was designed so that 69 A in the racetrack coils and 80 A in the pinch coils produced a radial gradient of  $\beta = 93$  T/m, a radial-to-axial field ratio of  $\beta r_0/B_0 = 0.78$ , and a 375 mK magnetic trap depth for low-field-seeking ground-state antihydrogen in a 1 T external field. Significantly larger radial-to-axial field ratios could be achieved by not energizing the pinch coils, because they added an additional

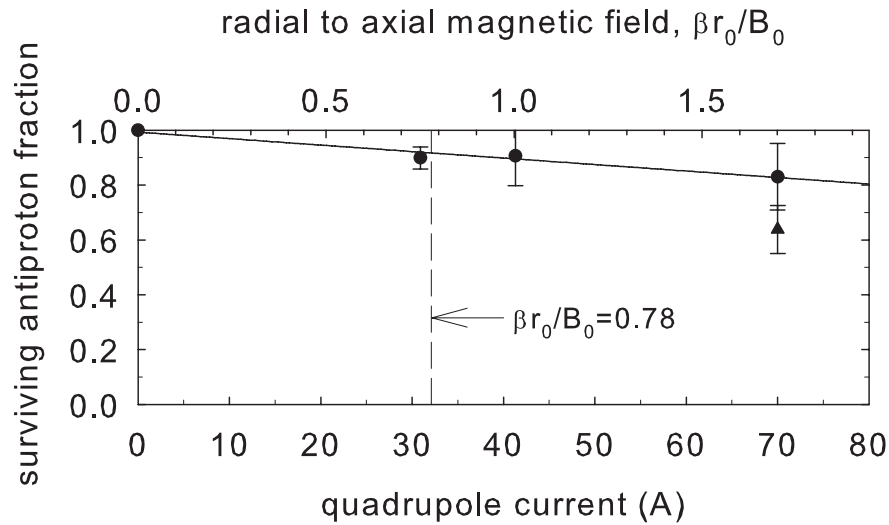


Figure 6.8: The fraction of about 90 000 (circles) and 280 000 (triangle) trapped antiprotons that survive a quadrupole Ioffe field that is ramped up to a given current, held 300 s, and ramped back down. The dashed line indicates the radial to axial field ratio corresponding to the maximum trap depth when both the quadrupole the pinch coils are energized.

1.2 T to the axial magnetic field at the center of the Ioffe trap. As such, we energized only the quadrupole field for the antiproton stability tests in order to push the radial field to as high of a limit as possible with our Ioffe trap.

After antiprotons were centered in the Ioffe trap, the quadrupole field was ramped up over about 10 minutes at 0.1 A/s, held constant for 5 minutes (long enough to make antihydrogen), and then ramped back down again at the same rate. The antiprotons were held in a 50 V deep well in a radius-length electrode during this process. The antiproton annihilation detectors continuously monitored antiproton losses. After the Ioffe field was back at zero, the surviving antiprotons were released onto the degrader and counted. The fraction of the antiprotons that survived this process is shown in Fig. 6.8.

The loss of antiprotons was roughly linear with the applied quadrupole field. The

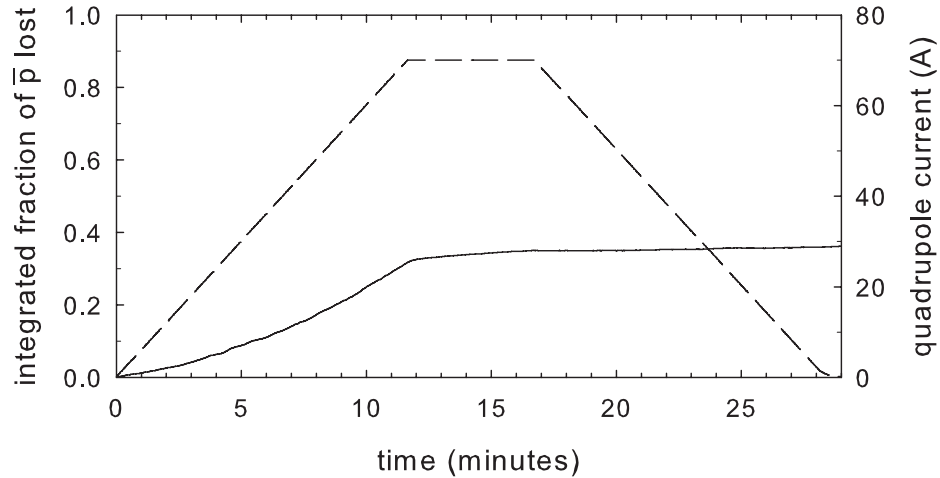


Figure 6.9: The integrated fraction of antiprotons lost (solid curve) and the quadrupole current (dashed curve) as a function of time.

antiproton losses observed were almost entirely while the quadrupole current was being turned on, with negligible losses after the maximum field was reached, as shown in Fig. 6.9 for the most extreme antiproton loss observed. This suggests that the antiproton losses were simply due to the cut-off radius imposed by the field (Eq. 6.6), and that diffusive losses were negligible in comparison for the numbers of antiprotons considered. For the largest radial field applied, this cut-off radius was 7.7 mm, while it was 12.2 mm for the maximum trap depth achievable if the pinch coils are also energized. The relatively small fraction of antiprotons lost in Fig. 6.8 suggests that the majority of the antiprotons were located at smaller radii than this. The losses observed could be further suppressed if the antiproton cloud radius were reduced using a rotating wall potential, a technique that other groups have demonstrated [123, 124].

A second requirement for forming antihydrogen in the Ioffe trap is that positrons must be confined in the Ioffe field in sufficient quantities and for a sufficient time to

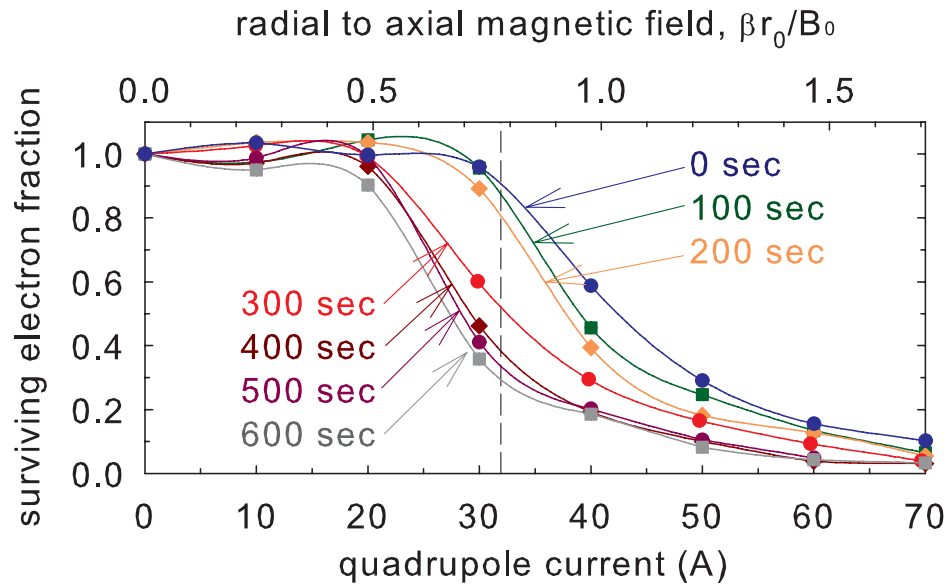


Figure 6.10: The fraction of 36 million electrons that survive a radial Ioffe quadrupole field that is ramped up to a given value, held for the time indicated, and ramped back down. The electrons were held in a 50 V potential in a radius-length electrode.

mix with the antiprotons. To test this, we initially used electrons instead of positrons because they should have the same behavior but are easier to load into the trap. We expect that these electrons cool to a 4.2 K equilibrium temperature via synchrotron radiation. The experiment began by loading 36 million electrons and adiabatically transferring them to the center of the deenergized Ioffe trap. The electrons were held in a 50 V well in a single radius-length electrode. The quadrupole Ioffe field was slowly ramped on, held constant for a given time, and then ramped back down. The surviving number of electrons was then counted by pulsing them onto the degrader and measuring their charge. The results are shown in Fig. 6.10.

These results suggested that sufficient numbers of positrons could be held within the Ioffe trap field long enough to form antihydrogen. We observed significant diffusive

loss of the electrons as they were being held in a constant quadrupole field, in contrast with the antiproton results. Some of the electron loss observed was certainly due to loss of particles outside of the quadrupole cut-off radius, but it is difficult to separate this loss from the diffusive loss in our results because the time required to turn on the quadrupole field ( $T_{ramp} \approx 10 I_{quad}$  in seconds) was comparable to the time that the particles were then held at field. A faster-ramping Ioffe trap would make the distinction between these loss mechanisms more clear.

It is relevant at this time to compare these results with the most similar measurements previously reported. Fajans *et al.* reported severe electron losses in a Penning-quadrupole-Ioffe trap that was similar to ours, using similar numbers of electrons [25]. We could compare the results in Fig.6.10 directly with the corresponding results in this paper (Fig.3b in Ref.[25]). Although the two results may qualitatively seem similar, they are actually quite different. We can begin by comparing the radial cut-off loss in the two cases. Because the quadrupole ramp time was just a few seconds in Ref.[25], compared to hundreds of seconds in our case (0.1 A/s ramp rate), they were able to distinguish between cut-off loss and diffusive loss much more easily. The immediate radial cut-off losses observed in Ref.[25] for high values of  $\beta r_0/B_0$  exceeded our combined losses due to both the cut-off radius and subsequent radial diffusion as we held the electrons for 10 minutes at full field, and additionally for over 10 minutes as the current in the quadrupole was ramped up to full field and back down. The diffusive losses observed in Ref[25] were also much larger than our observations. For example, in our case, more than half of the electrons that survived to reach the full quadrupole current still remained 5 minutes later, even for the most extreme radial

fields. In Ref.[25], the number of electrons in the trap 5 minutes after turning on the quadrupole was very small for all but modest radial fields (fields corresponding to an antihydrogen trap depth of less than 50 mK in our case). If taken at face value, the conclusion to draw from the results in Ref.[25] would be that we could not confine any positrons long enough to make antihydrogen at the Ioffe trap depths that we intended to use. As demonstrated by Fig. 6.10, we showed that this is simply not the case for our experiments.

The discrepancies between the two published results [25, 24] must be due to differences in electrode geometries and electron plasma parameters. An obvious difference is that the electrons in Fig.3b of Ref.[25] were stored inside a pair of radius-length electrodes, while the electrons in our experiments were stored in a single radius-length electrode. Increasing the effective length of the electrode that the particles are stored in decreases the quadrupole cut-off radius. For example, when  $\beta r_0/B_0 = 1$ , we find from Eq. 6.6 that our normalized cut-off radius  $\rho_{cut}/\rho_0$  has the value 0.61, while the corresponding normalized cut-off radius in Ref.[25] would be reduced to  $(0.61)^2 = 0.37$ . Furthermore, increasing the length of the plasma leads to increased radial diffusion rates, as will be discussed in a moment. These factors could help to explain the discrepancies between the results. Other factors that may have contributed include the fact that in Ref.[25], the electrode radius and magnetic bias field were smaller than in our experiments. The electron temperature in Ref.[25] was estimated to be between 1 and 0.0004 eV (4.2 K), although they were unable to measure electron temperatures below 0.05 eV. We believe that the temperature of our electrons was close to 4.2 K because they were allowed to cool for time periods that were

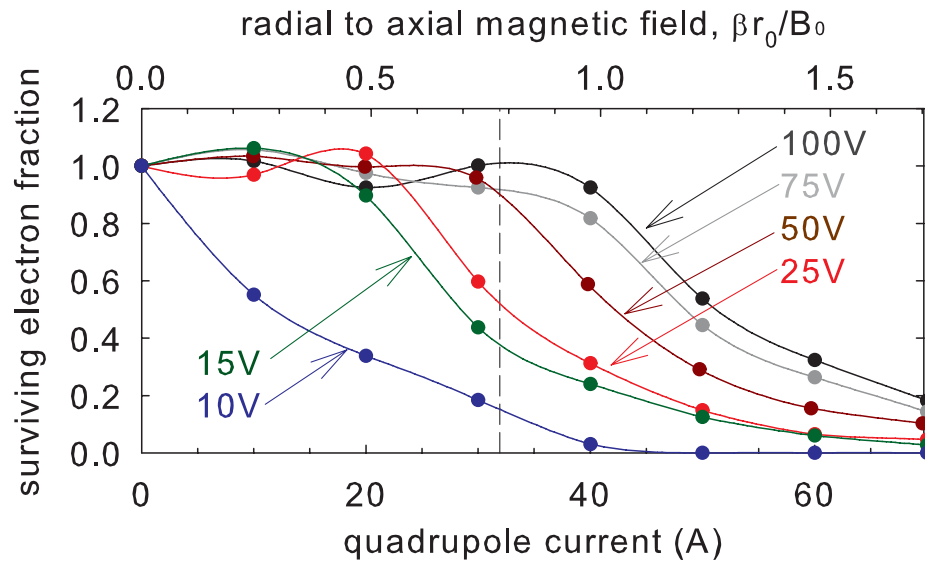


Figure 6.11: The fraction of 36 million electrons that survive a radial Ioffe quadrupole field that is ramped up to a given value and then ramped immediately back down. The electrons were held in a radius-length electrode with the indicated voltage.

much longer than the cyclotron time constant (2.6 s). Their electron loading method was different than ours, and the decreased magnetic field used (0.4 T for Fig.3b in Ref.[25]) would lead to a longer cyclotron cooling time constant (16 s). The voltage used to confine the electrons in Ref.[25] was not specified.

The voltage used to confine the electrons plays an important role in determining the radial diffusion rate. Experimental evidence of this can be found in Fig.6.11 and Fig.6.12. For Fig.6.11, electrons were confined in a radius-length electrode with a given voltages while the quadrupole field was ramped up to a specified current and then immediately ramped back down. For Fig.6.12, the quadrupole current was additionally held at its target value for 5 minutes before ramping it back down.

This data demonstrates that lower confining voltages result in a smaller fraction of the electrons surviving the applied quadrupole field. Because the quadrupole cut-off

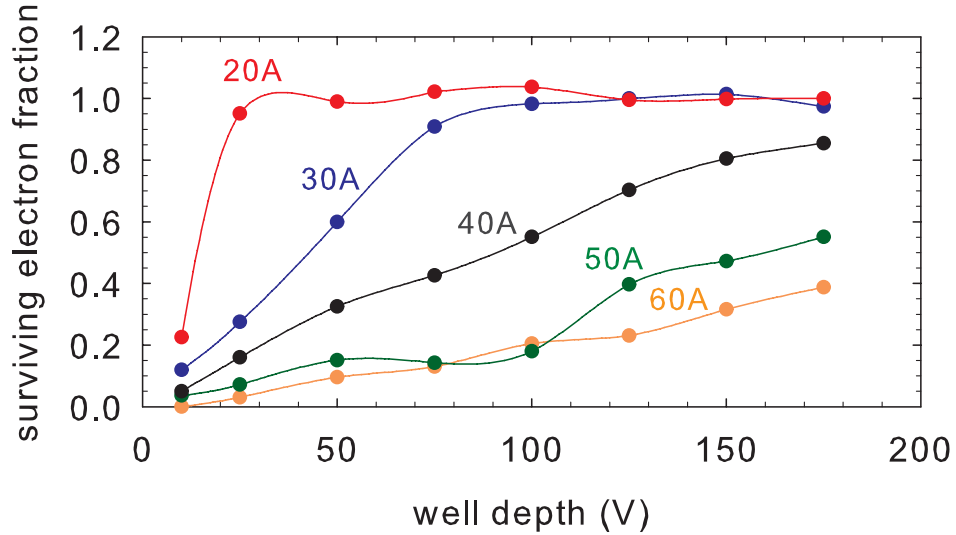


Figure 6.12: The fraction of 36 million electrons that survive a radial Ioffe quadrupole field that is ramped up to the indicated value, held for 5 minutes, and ramped back down. The electrons were held in a radius-length electrode with the indicated voltage.

radius for low-energy electrons is not determined by the specific confining potential, this increased loss of electrons for smaller confining voltages is almost certainly due to a corresponding increase in the diffusion coefficient in Eq. 6.7. This relationship can be easily understood. As the voltage confining a plasma is decreased, the radius of the plasma remains approximately constant due to conservation of angular momentum, but the length of the plasma increases. From Eq. 5.21, for a fixed plasma radius, we find that the plasma length is related to the plasma density as  $n_0 \propto 1/z_p$ . From Eq. 5.16, assuming  $\omega_r \ll \omega_c$ , we find that the relation between plasma density and rotation frequency is  $n_0 \propto \omega_r$ . Therefore,  $\omega_r \propto 1/z_p$  for a fixed plasma radius. If we plug this relation into Eq. 6.7, then we see that if  $z_p$  and  $\omega_r \propto 1/z_p$  are varied while keeping  $N, \rho_p, \beta, B_0$ , and  $T$  constant, as we expect to be the case when we load identical electron plasmas and only vary the voltage confining these plasmas,

then  $D \propto z_p$ . So the diffusive loss rate is roughly proportional to the length of the plasma in this case, and consequently related to the confining voltage as well. We can determine how the plasma length increases as the confining voltage is decreased for a fixed radius from Eq. 5.22. This simple model helps to explain the trend of the data shown in Fig. 6.11 and Fig. 6.12.

In summary, confining particles in long electrodes is undesirable because it leads to a reduced cut-off radius, and generally results in longer plasma lengths and correspondingly larger diffusive losses. Additionally, for a given electron plasma, using small plasma confinement voltages is undesirable because it results in longer plasma lengths and correspondingly larger diffusive losses. The plasma parameters are related to each other and to the diffusive loss rate in a complicated fashion however, so if we consider the general case where all of the plasma parameters can be varied, it becomes much more difficult to predict which optimal plasma geometry would minimize particle loss in the quadrupole Ioffe field.

The results in Fig. 6.8 and Fig. 6.10 demonstrated that sufficient numbers of antiprotons and positrons could be confined within a quadrupole Ioffe trap long enough to form antihydrogen. The stability of these particles in the Ioffe trap could potentially be optimized by varying the electrostatic confining potential and plasma parameters, but the complicated interrelations of these parameters makes this process challenging to implement. Even if positrons and antiprotons can be independently confined within the Ioffe trap, there are additional challenges to forming antihydrogen from these constituents. For example, the most common way of forming antihydrogen involves passing antiprotons through a positron plasma in a nested well structure.

This transport of antiprotons over a relatively large distance within the quadrupole Ioffe field could lead to large losses of antiprotons due to radial transport along field lines. Antihydrogen formation inside of a Penning-Ioffe trap will be covered in the next chapter.

## Chapter 7

# Antihydrogen Production within a Penning-Ioffe Trap

An important step toward magnetically confining antihydrogen is demonstrating that antihydrogen can be formed within a combined Penning-Ioffe trap. Antihydrogen formation within a Penning trap has been demonstrated for two different methods: via cooling antiproton axial motion through collisions with positrons in a nested Penning trap [15, 16, 14], and via a laser-controlled charge exchange process [22]. Confining the antihydrogen produced requires adding the radial magnetic field of a Ioffe trap to the constant axial field of the Penning trap. The resulting distortion of the magnetic field poses some serious challenges for either of the demonstrated antihydrogen production methods. The radial magnetic field reduces the radius within which particles can be confined and leads to diffusive radial expansion of the particle plasmas (Chapter 6), making it more difficult to confine antiprotons and positrons within the combined Penning-Ioffe trap. ATRAP demonstrated that the particle confinement within our

quadrupole Ioffe field was nonetheless sufficiently long for antihydrogen production (Section 6.4) [24], and similar confinement was also demonstrated using higher-order Ioffe traps [125, 126]. In addition to confining the particles in the Penning-Ioffe trap, the antiprotons and positrons must interact with each other to form antihydrogen. Antihydrogen production via positron cooling of antiprotons requires that the antiprotons have sufficient energy to pass through the positron plasma in the center of the nested well potential. This transport of antiprotons across several electrode lengths can in principle lead to direct loss of the antiprotons along radially-diverging magnetic field lines before antihydrogen can form. This radial loss can be minimized if the antiprotons are given the minimum amount of energy required to interact with the positrons however, which was the goal of our antihydrogen production experiments within a quadrupole Ioffe trap. This chapter describes the first reported production of antihydrogen within a combined Penning-Ioffe trap [5], which marks a significant step toward the goals of confinement and spectroscopy of antihydrogen.

## 7.1 Antihydrogen Production Procedure

The antihydrogen production experiments were done using the A-TRAP Penning-Ioffe trap described in Chapter 2. This trap is depicted in Fig. 7.1, with antihydrogen formation taking place in the center of the Ioffe trap at the location indicated.

The first step in any antihydrogen formation experiment is accumulation of antiprotons and positrons. We typically began by taking 10 minutes to calibrate the number of positrons being captured in our Penning trap from the positron accumulator. This was required because the positron accumulation efficiency decreased

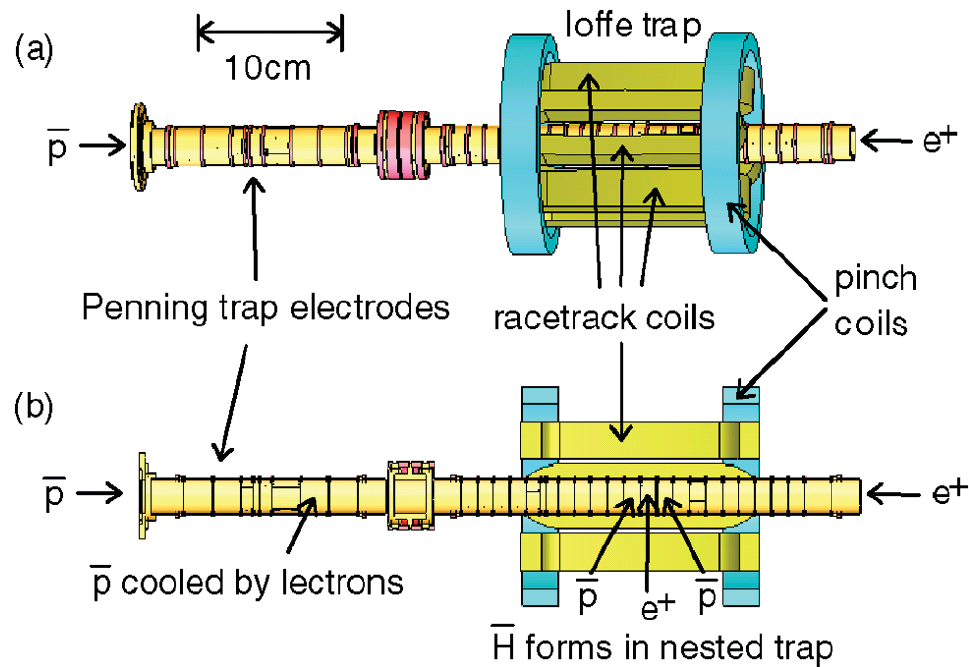


Figure 7.1: (a) Exterior and (b) cross section view of the Penning-Ioffe apparatus used to produce antihydrogen. A 1T bias field along the central axis of the electrode stack is produced by a large external solenoid (not depicted). Two pinch coils add an axially-confining gradient to the bias field. The radial quadrupole Ioffe field is produced by four racetrack coils.

slightly over time as the frozen neon positron moderator deteriorated slowly after being formed. (Improved instrumentation makes this first step no longer necessary.) After this calibration, 10 minutes were taken to accumulate and cool 150 million electrons required for efficient positron capture, and 400 million electrons for cooling antiprotons. This includes an intentional 5 minute wait time while holding the electrons in a 600 V well to let their motion cool via cyclotron radiation (Section 3.3.1). They are held in a deep well to maximize the particle density and frequency of collisions which convert axial energy to cyclotron energy, and the wait time accounts for the reduced cyclotron cooling rate at 1 T. Without introducing this wait time, we found that antiprotons loaded into a 1 T field often became unstable. During the

subsequent 15 minutes, we trap and cool 0.2 million antiprotons in the lower electrode stack using 9 injections from the AD, simultaneously accumulate 60 million positrons in the upper electrode stack, remove the cooling electrons from the trap, and let the positrons cool in a -600 V well for 5 minutes. We then adiabatically transfer the antiprotons and positrons into the center of the deenergized quadrupole Ioffe trap.

The procedure following this was meant to produce antihydrogen within the Ioffe trap, while minimizing the axial energy of the antiprotons passing through the positrons, in order to both produce slower antihydrogen atoms and to minimize radial loss of antiprotons along curving magnetic field lines. The procedure is outlined in Fig. 7.2. The potentials confining the antiprotons and positrons are first slowly transformed into the nested well structure, with the antiprotons sitting at an elevated potential above the nested well (Fig. 7.2a). The antiprotons are then launched into the nested well by rapidly lowering the barrier confining the antiprotons using a 1.75  $\mu\text{s}$  voltage pulse (Fig. 7.2b). The axial energy of the antiprotons is cooled through collisions with the positrons confined in the center of the nested well. Approximately half of the antiprotons are lost during the process, either due to antihydrogen formation or radial loss of antiprotons. Roughly 100 antihydrogen atoms are also detected during this process, but the antiprotons in the detection well are discarded, since these are produced before the Ioffe field is applied. The purpose of this step is to give the initially cold antiprotons some kinetic energy so that they can interact with the positrons in a subsequent step.

The antiprotons will continue to pass back and forth through the positrons until they have lost sufficient energy through collisions to be confined within one of the

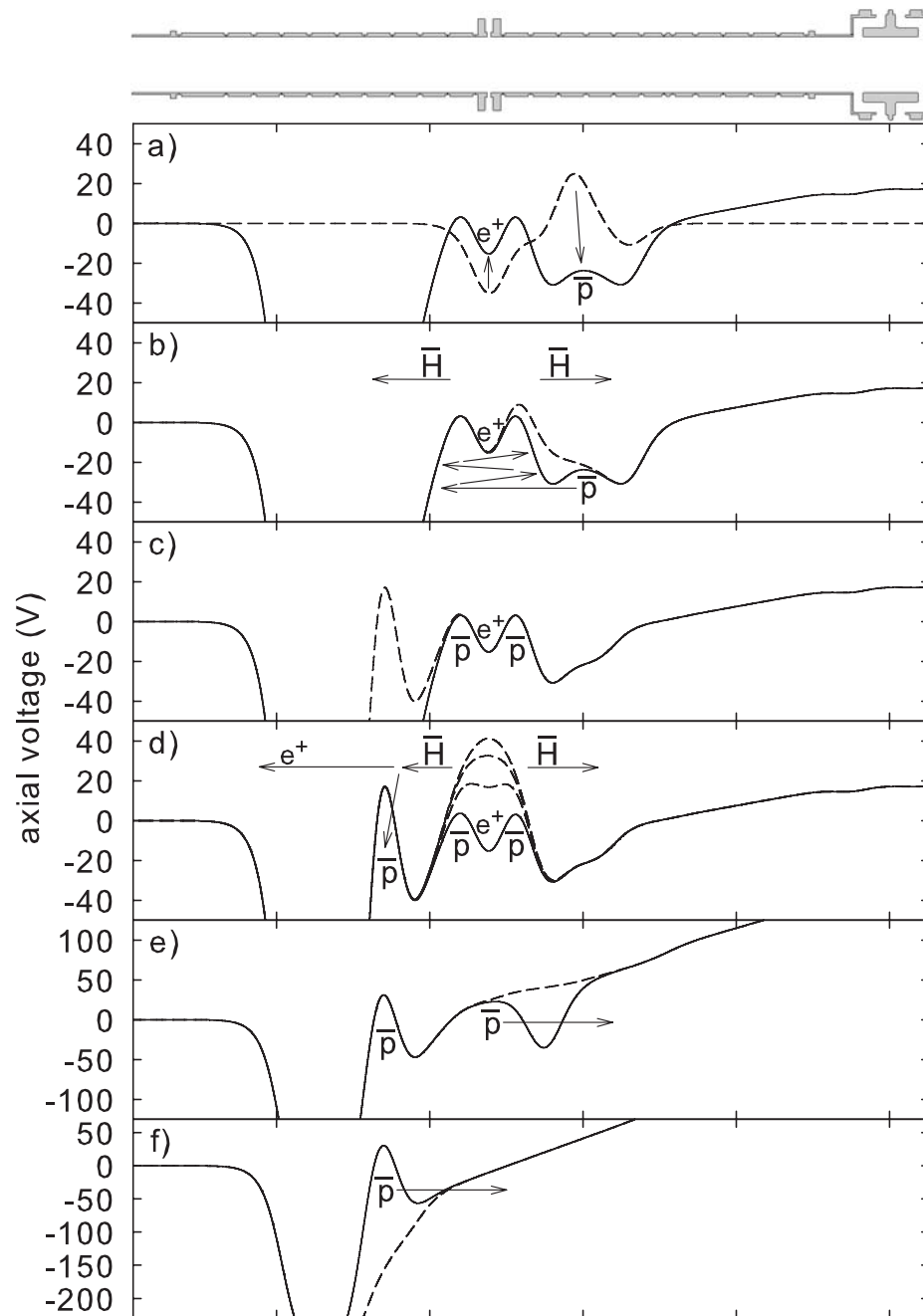


Figure 7.2: The potentials used for antihydrogen production and detection. (a) The nested well structure is formed. (b) The antiprotons are pulsed into the nested well and cooled by the positrons. (c) The Ioffe trap is turned on, and then the antihydrogen detection well is established (dashed curve). (d) The positron confining potential is reduced, allowing antiprotons to pass through the positrons and form antihydrogen, some of which is field ionized by the detection well. (e) The remaining antiprotons are counted. (f) The antiprotons in the detection well from ionized antihydrogen are counted.

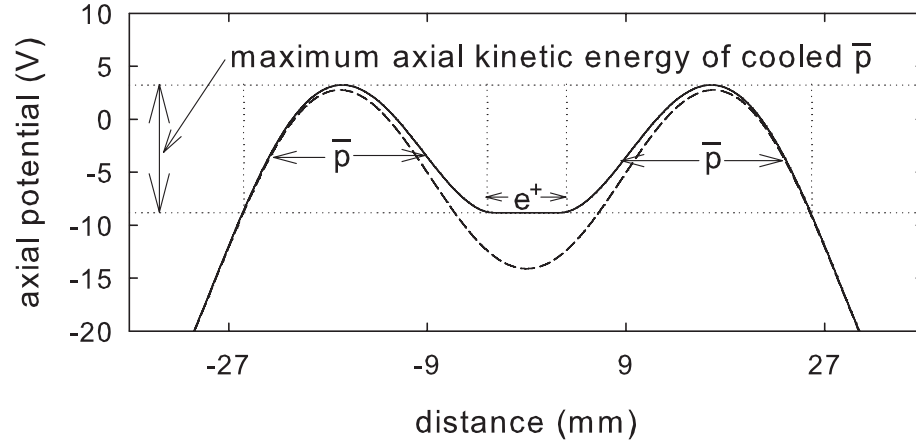


Figure 7.3: The vacuum axial potential within the nested well (dashed curve) is altered by the space charge potential of the positron plasma (solid curve). The flattened section of this potential indicates the axial extent of the plasma. Antiprotons passing through the positron plasma lose energy through collisions until they are confined within one of the two side wells, setting a maximum limit on the equilibrium antiproton kinetic energy.

side wells to either side of the positrons in the nested well structure. Once the antiprotons stop interacting with the positrons, their cooling mechanism is lost. There is some evidence that collisions between antiprotons in these side wells can continue to decrease the average antiproton energy via a process similar to evaporative cooling [65], but this occurs at a much slower rate. The axial energy range of the cooled antiprotons is determined by the total potential within the nested well, including the space charge potential of the positrons, as illustrated by Fig.7.3 for antiprotons on the central trap axis.

Using our antiproton annihilation detectors, we can monitor the antiproton cooling process by watching the steady decline in annihilations after the antiprotons are launched into the nested well. Once the antiprotons have cooled into the side wells,

corresponding to very few annihilations, the Ioffe trap is turned on (Fig. 7.2c). The current in the Ioffe trap is ramped up at a rate of 0.1 A/s, taking about 14 minutes to reach the full Ioffe trap depth. Usually less than 5% of the antiprotons are lost as the Ioffe trap is being turned on. The antihydrogen detection well is formed only after the desired Ioffe trap depth has been reached (dashed curve in Fig. 7.2c).

At this point, the antiprotons are brought back into contact with the positrons within the Ioffe trap field by slowly increasing the voltage on the electrode confining the positrons (Fig. 7.2d). This brings the flat potential marking the extent of the positron plasma in Fig. 7.3 closer to the bottom of the antiproton confining wells. Antiprotons that previously had slightly too little kinetic energy to interact with the positrons are then allowed to pass through the positron plasma and form antihydrogen atoms. This further cools the antiprotons toward the bottoms of the side wells, so the positron confining voltage must be continually decreased to keep the antiprotons in contact with the positrons without adding further energy to the antiprotons. The potential confining the positrons will eventually become small enough that the positrons will start leaking out of the center of the nested well axially, at which point the escaping positrons will follow radially-diverging magnetic field lines and be lost from the trap. We continue to increase the voltage on the center electrode until all of the positrons are lost and the antiprotons remaining in the two side wells are joined in the central electrode (dashed curves in Fig. 7.2d). We change the voltage slowly so that the antiprotons have sufficient time to cool and stay nearly in equilibrium with the decreasing confining potential. The total voltage ramp process take 11 minutes.

After this is done, the Ioffe trap is ramped back down to zero field in 1 minute.

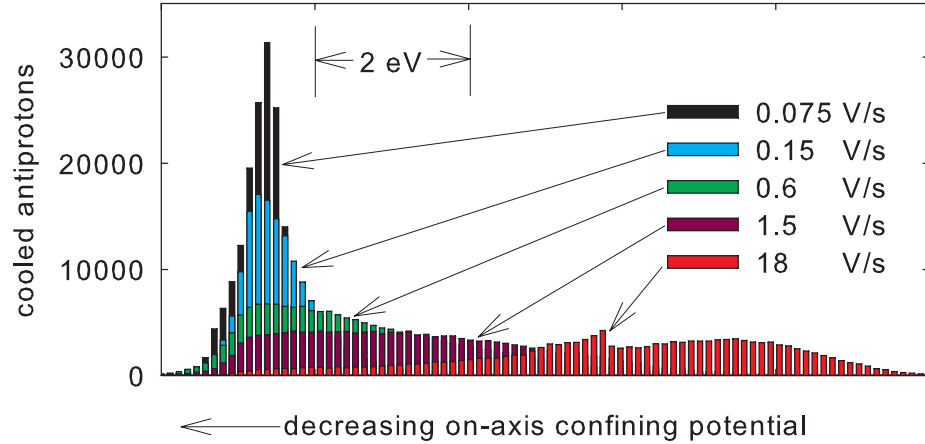


Figure 7.4: After antihydrogen is produced, the axial energy distribution of antiprotons remaining in the nested well is determined by recording the depth of the antiproton confining potential as the antiprotons escape. This energy distribution is depicted after the positron confining voltage is increased at several different rates. The antiprotons are cooled more efficiently to the bottom of the nested well using slower rates.

The antiprotons remaining in the nested well are released onto the degrader and their annihilation signals are counted (Fig. 7.2e). We gain valuable diagnostic information about the cooling of the antiprotons as the positron confining well depth is decreased. The energy distribution of the antiprotons remaining in the nested well after antihydrogen experiments with no Ioffe field on are shown in Fig. 7.4, for several trials where the positron confining voltage is increased at various rates. The antiprotons are clearly cooled to the bottom of the nested well more efficiently if the voltage is increased slowly, giving the antiprotons more time to cool.

The final step of the antihydrogen formation experiment is to release the antiprotons captured in the detection well from field ionized antihydrogen atoms and count the resulting annihilations (Fig. 7.2f). The antihydrogen detection well is depicted in

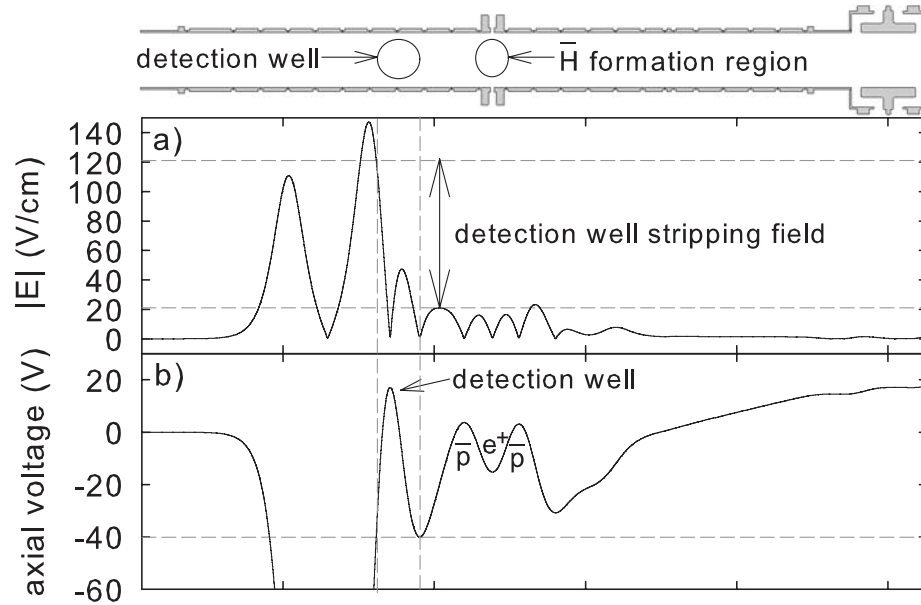


Figure 7.5: The on-axis (a) electric field magnitude and (b) potential within the Penning trap. If antihydrogen atoms passing through the detection well are field ionized between 20 and 120 V/cm, then the antiproton stripped from the antihydrogen atom will be captured in the detection well.

more detail in Fig. 7.5. Some fraction of the antihydrogen atoms originating from the nested well will pass through the detection well region. Those atoms passing through the detection well that are field ionized by fields between 20 and 120 V/cm will have their stripped antiproton captured within the detection well.

This means that only very highly excited antihydrogen atoms will be ionized and detected [127]. These large radius atoms within a strong magnetic field are best described classically in the guiding center approximation [39], which is discussed in detail in [66]. The field ionization threshold of a guiding center atoms is generally a rather complicated function of the atomic state and both the radial and axial electric field, but in this context, the ionization field can be approximated in terms of the

atom radius,  $\rho$ , as [127]:

$$\mathcal{E}_z > 3.60 \text{ V/cm} \left( \frac{\mu\text{m}}{\rho} \right)^2 \quad (7.1)$$

Therefore, we are able to detect antihydrogen atoms with a radius ranging between 0.17-0.42  $\mu\text{m}$ .

Field ionization is a very robust detection method. The detection well is designed in such a way that only antiprotons from stripped antihydrogen atoms can be captured within the detection well. Antiprotons with sufficient kinetic energy to escape from the nested well will leave the trap to the right in Fig. 7.5 before being able to gain sufficient energy to reach the detection well. Even if an antiproton did enter the detection well, it would bounce back out again because there is no means for the antiproton to lose energy while passing through the detection well. Trials of the antihydrogen production experiment without positrons in the nested well confirmed that no antiprotons were captured in the detection well in that case. Because the antiprotons from ionized antihydrogen atoms can be stored and released during an interval of time that is short compared to the detector background count rate, the field ionization method is effectively a background-free detection mechanism that is sensitive to very small numbers of antihydrogen atoms [15]. The field ionization detection method has previously been used to probe the velocity [20] and state distribution [16, 66] of antihydrogen atoms, although we had insufficient time in these experiments to perform similar measurements.

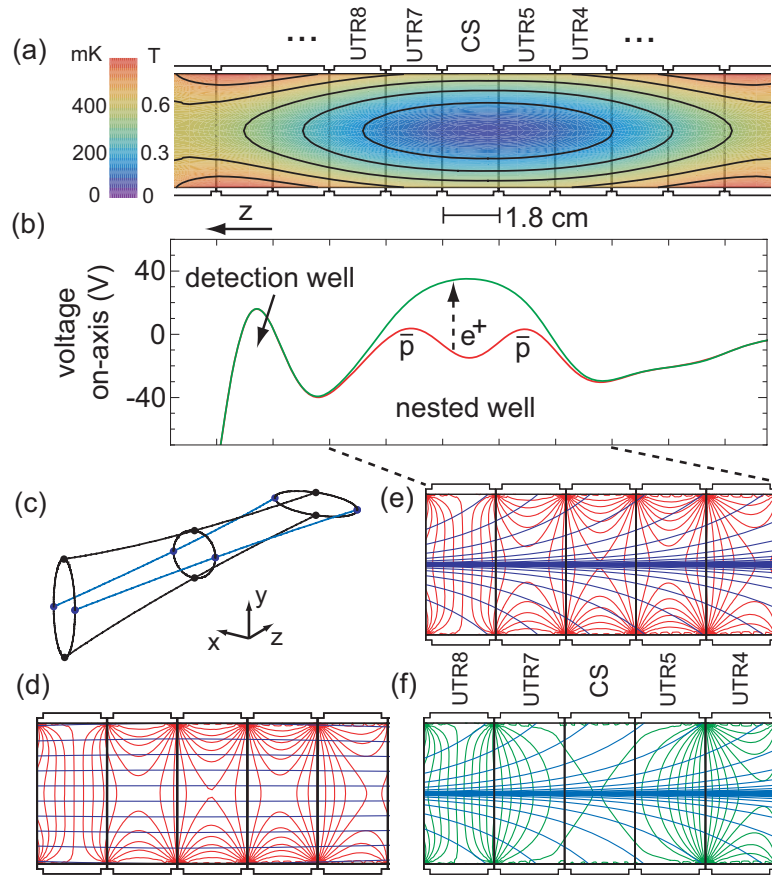


Figure 7.6: (a) The well depth contours for ground state antihydrogen atoms within the electrodes inside the Ioffe trap. (b) Potentials seen by particles on-axis before (red) and after (green) antihydrogen production, and (d-f) the corresponding equipotential contours. Magnetic field lines (blue) that are (d) parallel to the trap axis without the radial Ioffe field are (c,e-f) redirected when the Ioffe field is on.

## 7.2 Effects of the Ioffe Field on the Antiprotons

The electric and magnetic fields within the combined Penning-Ioffe trap lead to complex particle motions, and can result in particle loss on the Penning trap electrodes. The fields within the Penning-Ioffe trap are depicted in Fig. 7.6. Antihydrogen atoms in low-field-seeking ground states see the magnetic field magnitude contours

in Fig. 7.6a. The motion of charged particles are governed by the electric potentials in Fig. 7.6(b,d-f). The antiprotons interact with the positrons in the nested well (red) while the positron confining well depth is reduced to prolong the interaction until no positrons remain (green). The charged particles move along magnetic field lines (blue), which are initially parallel to the trap axis without the radial Ioffe field (Fig. 7.6d), but are distorted when the Ioffe field is on (Fig. 7.6c). The field lines in Fig. 7.6(e-f) correspond to the maximum Ioffe trap depth, viewed in the plane where the field lines are maximally-diverging. The picture is further complicated by the space charge potential of the positrons, which generally flattens the potential near the center of the nested well as in Fig. 7.3, but is omitted from this figure for simplicity.

Although antiprotons pass from one side of the nested well to the other as they are allowed to interact with the positrons within the Ioffe field, this does not necessarily mean that they are radially lost along field lines during the process. Whether or not an antiproton collides with an electrode and annihilates depends upon not only the trajectory of the field line, but also the electric potential within the trap and the axial kinetic energy of the particle. This point is illustrated in Fig. 7.7, for the simple case of antiprotons with 18 eV of energy inside the nested well potential in the Ioffe trap field. We consider the “axial” trajectory of antiprotons along field lines in the maximally-diverging plane (y-z plane in Fig. 7.6c). On time scales that are much longer than the “axial” oscillation period, the magnetron motion of the antiproton will also rotate it through other planes where the magnetic field lines have different trajectories than in Fig. 7.7, but this figure represents the worst of these cases. As illustrated, if an antiproton is traveling along a field line that intersects the central

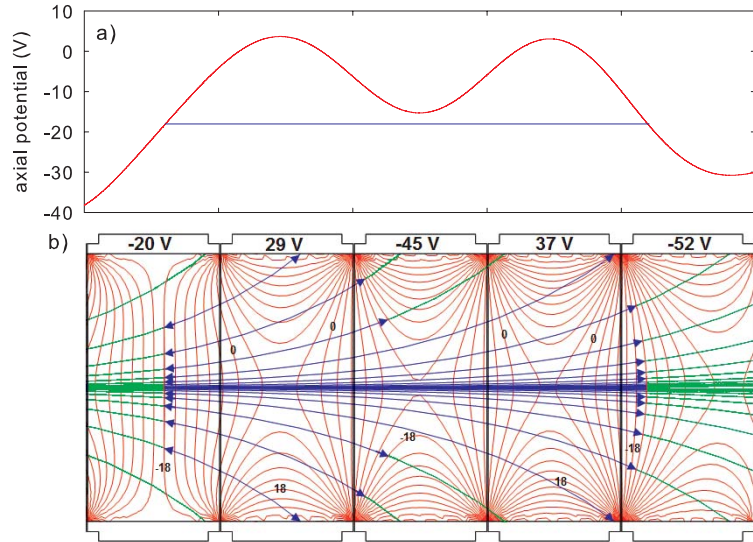


Figure 7.7: (a) The on-axis potential within the nested well (red) and the corresponding range of motion of antiprotons with 18 eV of energy (blue). (b) The corresponding antiproton trajectories (blue) of 18 eV antiprotons along magnetic field lines (green). Antiprotons following energetically allowed trajectories that intersect the electrodes are lost.

electrode of the nested well, it will be unable to annihilate on that electrode unless it has sufficient energy to overcome the electric repelling force (over 45 eV for this example). However, lower-energy antiprotons can pass from one side of the nested well to the other near the central axis, where the potential barrier is lower. This illustrates the fundamental point that antihydrogen can be formed within a nested well structure without severe radial loss of antiprotons, as long as the antiprotons are given only the minimal amount of energy required to interact with the positrons. The primary goal of the procedure outlined here was to minimize the energy of the antiprotons interacting with the positrons.

The antiprotons can have very complicated motions on time scales that span many “axial” oscillation periods. The  $\vec{E} \times \vec{B}$  drift magnetron motion of the antiprotons

within the nested well can rotate the antiprotons through planes where the magnetic field lines are alternately radially-diverging and radially-converging. The space charge of the positrons also significantly affects the potential in the center of the nested well, and collisions between antiprotons and positrons can reduce the axial energy of the antiprotons. Recent calculations simulated the motion of antiprotons being cooled by positrons in a realistic nested well potential within an octupole Ioffe trap field [128]. The simulations started the antiprotons at various radii in the axial center of the nested well with a large axial kinetic energy, and monitored the kinetic energy and radius of the antiprotons over time. The antiproton motion was often chaotic, and it was observed that when antiprotons started at larger radii, their kinetic energy was lost through positron collisions much more slowly when the radial Ioffe field was on than when it was off. The kinetic energy of the antiprotons was related to the radius of their motion, since the antiprotons could convert electric potential energy into kinetic energy by changing their radius along field lines. Although the radius of the antiprotons fluctuated greatly when the Ioffe field was on, the average radius of the antiprotons decreased slowly over time as they were cooled by the positrons. It was predicted that higher velocity antihydrogen atoms would be produced when the Ioffe field was on, as a result of the large fluctuations in antiproton radius and kinetic energy. It was also speculated however that the radial compression of the antiprotons caused by positron cooling within the Ioffe field could potential boost antihydrogen production. The large radial and kinetic energy fluctuations could be minimized by concentrating the antiprotons close to the central axis and minimizing their axial extent. These simulations are not directly applicable to the antihydrogen

production method described here, since the antiprotons in our case were initially confined in the two sides of the nested well with very little kinetic energy, and we were using a quadrupole Ioffe field, but the general observations about the behavior of the antiproton motion might carry over to our situation as well.

We can monitor antiproton annihilations throughout the antihydrogen formation process. Annihilations are minimal as the Ioffe trap is being turned on, but then become considerable as the positron confining well depth is decreased and the antiprotons are allowed to pass through the center of the nested well and interact with the positrons again. Some of these annihilations are clearly associated with antihydrogen production. The antiproton losses abate as the positrons begin to spill over the top of the nested well structure. By the time that the on-axis confining potential disappears for the positrons, most have them have left the trap, although positron losses detected later in the process indicate that a few positrons remain confined off-axis, where there are still non-zero confining potentials. After most of the positrons have left the trap, a second period of antiproton losses begin as the central potential of the nested well is inverted and the antiprotons in either side well are joined together in the center. Since there are very few positrons in the trap at this point, it must be concluded that these final antiproton annihilations correspond to direct radial loss. As the central potential in the nested well is inverted and the antiprotons sit in a flat potential spanning three electrodes within the Ioffe field, we would expect that the antiprotons that are located at large radii or have large amounts of axial kinetic energy will be lost radially along magnetic field lines. This expectation is confirmed by Fig. 7.8, which depicts the energy distribution of antiprotons remaining

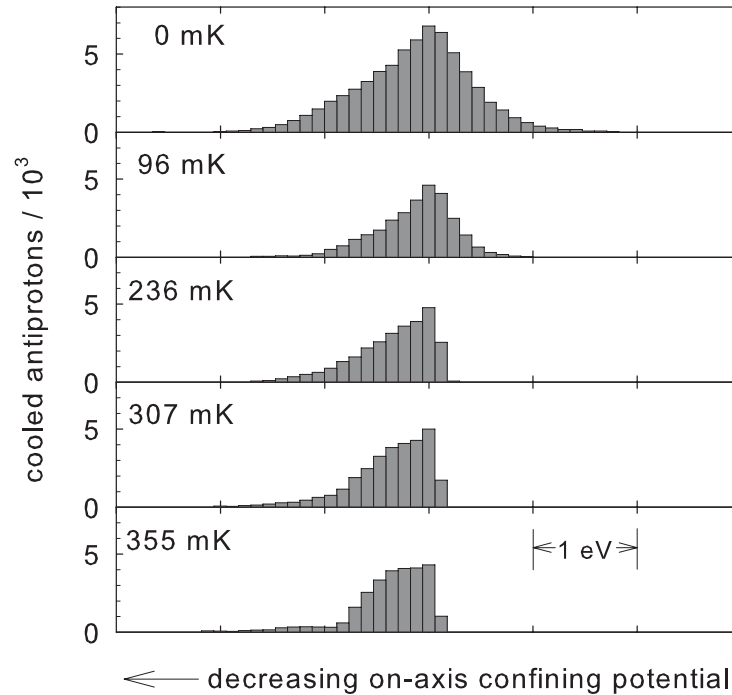


Figure 7.8: The energy distribution of antiprotons released from the green well in Fig. 7.6b after antihydrogen formation, at the Ioffe trap depths indicated. Antiprotons with larger axial energy (right side of distribution) and antiprotons at larger radii (left side of distribution) are lost at large Ioffe trap depths.

after antihydrogen production experiments using various Ioffe trap depths.

### 7.3 Experiment Results

The number of antihydrogen atoms ionized in the detection well as a function of Ioffe trap depth are given in Fig. 7.9a. The trap depth is given in temperature units for antihydrogen atoms in low-field-seeking ground states, and the antihydrogen number is normalized to the average number of antiprotons used in the antihydrogen production experiment within the Ioffe trap. The number of antihydrogen atoms

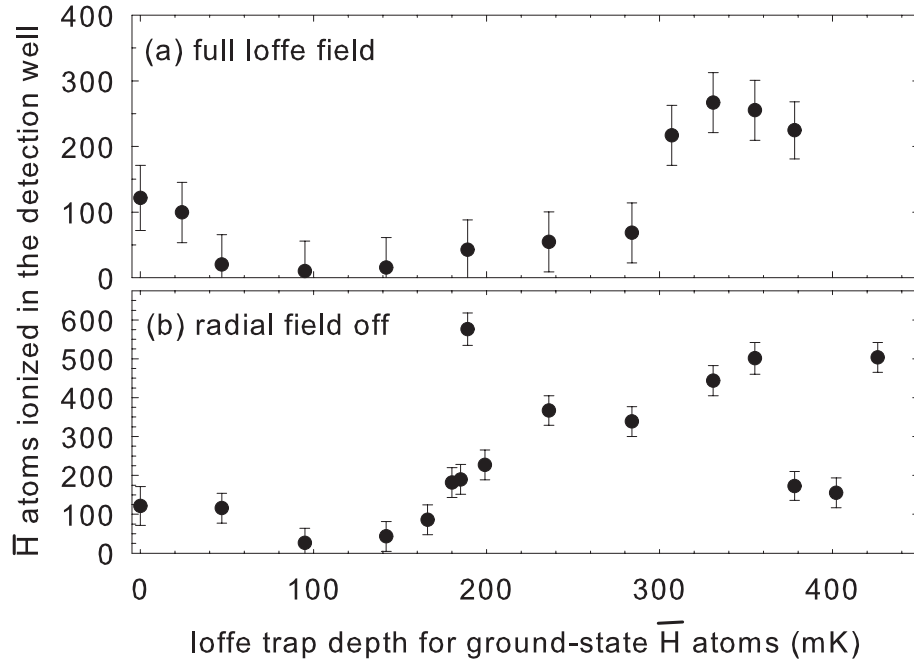


Figure 7.9: (a) The number of antihydrogen atoms ionized in the detection well per trial within the Ioffe trap and (b) within only the axial field of the Ioffe trap, as a function of the trap depth. The antihydrogen numbers are normalized to an average of 0.1 million antiprotons per antihydrogen production and detection trial, with reproducibility error bars.

detected initially decreases with increasing Ioffe trap depth, but then is enhanced for Ioffe trap depths greater than 300 mK. One possible cause for this behavior is that the Ioffe pinch coils, which provide axial confinement for the antihydrogen atoms, boost the axial magnetic field within the antihydrogen production region from 1 to 2.2 T. This could reduce the positron plasma radius, leading to a denser plasma, or may increase the antihydrogen production via another, yet unidentified, mechanism.

To investigate the effect of the increased magnetic field caused by the pinch coils, we repeated the experiments without the radial Ioffe field (Fig. 7.9b). The two data sets show similar trends, but more antihydrogen atoms are produced when only the

Ioffe pinch coils are used. The sharp features in Fig. 7.9 are reproducible, but are not yet understood. In all trials, about 1% of the antiprotons lost from the nested well during the antiproton formation process form atoms that we detect.

The number of antihydrogen atoms detected was significantly enhanced when a noise signal was applied to heat the antiprotons as the positron well depth was decreased, with as many as 1700 antihydrogen atoms detected in a single trial. The noise drive allows the antiprotons to continue interacting with the positrons after being cooled by them, which is a variation of the “driven” antihydrogen production method previously demonstrated by ATRAP [16].

There was an additional suggestion that antiprotons and positrons could not likely be successfully mixed to form antihydrogen within a quadrupole Ioffe field, even if the constituent particle plasmas could be individually confined for a long enough time to perform the experiment [25, 122, 125]. The radial magnetic field within a quadrupole Ioffe trap can potentially lead to antiproton losses along field lines within a single pass through the nested well, but we have demonstrated that these losses can be suppressed by limiting the energy of the antiproton. These results show that large amounts of antihydrogen can be produced with relative ease within a quadrupole Ioffe trap.

Once antihydrogen had been produced within the Ioffe trap, the next logical step was to search for antihydrogen atoms that were trapped by the confining magnetic field. The fastest mechanism at our disposal for releasing antihydrogen from the trap is to ramp the Ioffe field down in 1 minute, with the rate limited by quench-protection diodes inside the Ioffe trap. A signal equal to our detector background

would be produced by 20 trapped antihydrogen atoms per second leaving the trap. We observed no trapped antihydrogen signal above background for these experiments, but there is significant room for improvement in future experiments.

## 7.4 Future Prospects for Antihydrogen Confinement

The future success of magnetically confining antihydrogen will depend upon the properties of the antihydrogen produced. The 375 mK trap depth quoted for our Ioffe trap is for antihydrogen atoms in low-field-seeking ground states. All of the antihydrogen observed so far has been in highly excited states [16, 19], although we do not have a means of detecting more tightly bound atoms. Antihydrogen atoms will only feel a confining potential from the Ioffe trap if they are in a low-field-seeking (LFS) state ( $-\vec{\mu} \cdot \vec{B} > 0$ ). Monte Carlo simulations suggest that only a small fraction of the highly excited antihydrogen atoms will be in LFS states [44], and if they start in a LFS state, there is no guarantee that they will stay in one as they decay toward the ground state. These highly excited states can have much larger magnetic moments however, and consequently larger trap depths for the same magnetic confining field. It has been suggested that this may lead to a cooling mechanism for converting highly-excited antihydrogen atoms with more than 375 mK of energy to bound ground state atoms if the excited atoms decay near the turning points in the confining field [48]. Furthermore, the diamagnetic energy shift ( $\Delta E \propto B^2$ ) may play a significant role in trapping highly-excited antihydrogen states, although it would not be a significant factor as the atom decays to lower levels.

In addition to the state of the antihydrogen produced, the kinetic energy of the

atoms is also critical. Measurements of the velocity of the highly-excited antihydrogen observed suggested that the atoms were moving far too rapidly to be confined [20], although a recent reinterpretation of the results suggests that there should be some antihydrogen moving slowly enough to be trapped [21]. The primary factor determining the velocity of the antihydrogen is the initial energy of the antiproton passing through the positron plasma, since it is much more massive than the positron. There is clearly a benefit to producing antihydrogen with antiprotons that have as low of an energy as possible. However, even if the antiprotons have a 4 K temperature distribution after being cooled by electrons to equilibrium with the trap temperature, only a small fraction of the antihydrogen would be expected to have an energy less than the 375 mK trap depth. Clearly, there will be some challenges to overcome in order to trap antihydrogen, and there are still many unanswered questions regarding how difficult it will be.

One approach to the problem is to produce as much antihydrogen as possible in the hopes that at least some of the atoms will be trappable. The highest-efficiency antihydrogen production mechanism demonstrated by ATRAP is the driven production method in a nested well [16]. In this method, RF signals resonant with the antiproton axial oscillation frequency are applied to the electrode confining the antiprotons, heating their motion until they have sufficient energy to interact with the positrons. The positrons cool them into the opposite side well, at which point the procedure is repeated until most the antiprotons have been depleted by the antihydrogen formation process. This method can most likely be directly applied to antihydrogen production within a Penning-Ioffe trap, since the antiprotons can be heated slowly

enough that they have just barely enough energy to interact with the positrons. This method should in principle be able to produce very cold antihydrogen as well.

Another promising option is to produce antihydrogen via a resonant charge exchange process between antiprotons and Rydberg positronium, a method previously demonstrated by ATRAP [22]. Although this method produces fewer antihydrogen atoms, it has the advantage that it does not require transporting charged particles within the Ioffe trap field. It may also produce colder antihydrogen, since the antiprotons can be kept stationary and cold inside a confining well. There are plans to attempt this method within our Ioffe-Penning trap in the near future.

There are multiple options available for producing antihydrogen, and a great deal of room for optimization of these processes. The Penning-Ioffe trap is also being modified in order to lower the base temperature of the electrode stack, which should allow for cooler positrons and electrons, which in turn are used to cool the antiprotons, and may lead to a colder antihydrogen energy distribution. Finally, a new Ioffe trap is under construction that will provide a larger trap depth, and will be able to be turned on and off much more rapidly, allowing for faster antihydrogen production experiments and increased sensitivity to trapped antihydrogen atoms. It is expected that the new trap will be able to turn off sufficiently fast to be able to detect a single trapped antihydrogen atom above the detector background rate.

# Chapter 8

## Conclusion

Preceding the results presented here, there were significant developments in forming antihydrogen and determining the properties of the antihydrogen produced. Antihydrogen was most-frequently formed during the positron cooling of antiprotons within a nested Penning trap [11], either by launching the antiprotons into the nested well with an elevated energy [15, 14], or by resonantly adding energy to the antiprotons to make them interact with the positrons [16], which significantly boosted the antihydrogen production efficiency. A background-free field-ionization detection technique was used to probe the state-distribution [16, 19] and velocity [20] of the highly-excited atoms observed. A second method for forming antihydrogen using a laser-controlled two-step charge exchange process was also demonstrated [22], which has the potential of forming colder antihydrogen atoms with a narrower state distribution. Although these experiments were extremely successful, the apparatus used was not compatible with a magnetic trap required to confine the antihydrogen atoms.

A combined Penning-Ioffe trap was constructed for confinement and spectroscopy

of antihydrogen. This new trap required much more space than was previously available, so a new experimental zone was commissioned at CERN. This new zone included a superconducting solenoid with a 20 inch bore and a 3 T maximum magnetic field, and a large pulse-tube-cooled cryostat that provides a cryogenic vacuum environment for the trap. Two identical Penning traps were built, composed of 36 stacked cylindrical ring electrodes that each have independent electrical connections for static voltages and high-frequency signals, allowing diverse experimental capabilities. A quadrupole superconducting Ioffe trap was built that has a 375 mK trap depth within the Penning trap electrodes for low-field-seeking ground-state antihydrogen atoms, and has optical access along all three axes. A two-dimensional cryogenic translation stage allows access for particles, laser light, and diagnostic equipment on the central axis of the Penning trap. The Penning-Ioffe trap can be thermally cycled to 4 K and back to room temperature within 3 days, and can be maintained at 4 K for 6 days without replenishing the liquid helium reservoir, in spite of the size of the trap and the many electrical and vacuum connections required between room temperature and cryogenic portions of the apparatus. The Penning-Ioffe trap is constructed from completely non-magnetic materials, including a vacuum enclosure that is primarily titanium. Although the cryogenic vacuum space of the Penning trap is connected to a room-temperature vacuum system for positron access through a small hole, the vacuum within the Penning trap is sufficient to store antiprotons for 15 hours with no detectable loss due to annihilations with background gas, corresponding to a pressure lower than  $3 \times 10^{-16}$  Torr.

Significant improvements were made to the rate at which all particles could be

loaded into the Penning trap, increasing the amount of antihydrogen that can be produced. Previously, electrons were loaded from a field emission point, typically requiring a 10 minute procedure to load 5 million electrons, and loading more than 10 million electrons was unreliable. Using a new technique, electrons were loaded into the Penning trap via photoemission from a gold-plated window using UV laser pulses [23]. Up to 10 million electrons were captured per laser pulse, linearly accumulating as many as 1 billion electrons in the trap using more laser pulses. The 400 million electrons used to efficiently cool antiprotons typically required only a couple of minutes to load.

A buffer gas positron accumulator was constructed, and linked to the Penning trap by a 7 m long positron guide. Approximately 26 million positrons are accumulated every 50 seconds, and 6 million of these are successfully transferred into the Penning trap after traveling through the positron guide and passing through a 1 mm diameter tube at the top of the electrode stack. This corresponds to an accumulation rate of  $3000 \text{ e}^+/\text{s}$  mCi within the Penning trap, 400 times faster than the best accumulation rate realized by ATRAP in the past via the positronium-ionization loading method [9]. The number of positrons accumulated was linear with the number of positron bunches transferred, and up to 360 million positrons have been accumulated in this way.

The depth of the Ioffe trap decreases substantially as the bias field of the Penning trap is increased, which consequently means that antiprotons must be loaded into the Penning trap using a much lower magnetic field than previously demonstrated. The antiproton loading efficiency drops dramatically with the magnetic field, but 35

thousand antiprotons can still be accumulated at 1 T for each 100 s AD cycle, and as many as 0.6 million antiprotons have been accumulated at this field. At 2 T, the corresponding numbers are 100 thousand and 1.7 million. This is to be compared with 15 thousand antiprotons per AD cycle at 5 T that was typical for previous traps. The success of loading antiprotons at reduced magnetic fields was in part due to using larger radius electrodes in the Penning trap, and optimizing the parameters of the electrons used to cool the antiprotons.

The radial field of the quadrupole Ioffe trap destroys the cylindrical symmetry that guarantees particle confinement in a Penning trap [129]. Single particles can nonetheless have stable orbits within a combined Penning-Ioffe trap below a critical cut-off radius as long as certain resonance conditions are avoided [114]. Within dense plasmas, the adiabatic invariants that guarantee stable particle confinement break down. The resonance conditions cannot be completely avoided, leading to diffusive radial expansion of the plasma [115, 116]. A combination of the single particle cut-off radius and plasma diffusion effects led to some controversy about whether or not particles could be confined in a Penning-Ioffe trap long enough to form antihydrogen [25]. We conclusively demonstrated that positrons and antiprotons could be confined within a Penning-Ioffe trap long enough to form antihydrogen [24]. We found that only about 10% of 0.1 million antiprotons were lost for radial fields corresponding to our maximum Ioffe trap depth, and diffusive losses were negligible due to the low antiproton density. Diffusive particle losses were observed for electrons, but these losses could largely be suppressed by confining the particles with large voltages in electrodes with short lengths. For example, negligibly small losses were observed

when 36 million electrons were held in a well depth greater than 100 V while the radial field is ramped up to a value corresponding to the maximum Ioffe trap depth over 5 minutes, held at field for 5 minutes, and then ramped back down in 5 minutes.

An additional point that was under some contention was whether or not antihydrogen could be formed within a quadrupole Ioffe field [25]. Energetic charged particles traveling any substantial distance through the Ioffe trap can be transported radially along magnetic field lines and lost by colliding with the electrodes. In a more complete picture that takes into account the electric potentials and particle energy however, particles can be transported over several electrodes without being transported outward to the electrodes. We produced large amounts of antihydrogen via positron cooling of antiprotons within a quadrupole Ioffe field [5], using a method which emphasizes minimizing the length of the nested well and the wells confining the particles, compensating for the slow particle cooling rate at low magnetic fields, and prolonging the interaction of the antiprotons with the positrons using a new method which minimizes the energy of the antiprotons traveling through the positron plasma. Instead of reducing the antihydrogen production efficiency, we found that the number of antihydrogen atoms detected actually increases as the Ioffe trap depth is increased. This appears to be associated with the boost in the magnetic field in the antihydrogen production region caused by the Ioffe trap pinch coils. No trapped antihydrogen atoms were observed, but we would be insensitive to small numbers of trapped atoms, since it takes roughly 1 minute to switch off the Ioffe trap and release trapped atoms, and the background count rate of our annihilation detectors corresponds to an antiproton signal of 20 atoms/s.

The results presented for antihydrogen formation within a Penning-Ioffe trap are preliminary, and the antihydrogen production process can undoubtedly be greatly optimized. Previous results suggests that resonantly driving the antiproton axial motion to prolong interactions between antiprotons and positrons could substantially boost antihydrogen production [16], and it seems likely that this scheme could be directly implemented within a combined Penning-Ioffe trap. Whether or not antihydrogen will be trapped within the Ioffe trap field depends upon the internal states and velocity distribution of the atoms produced. Although some initial measurements [16, 20, 19] and theoretical calculations [44] seem unfavorable, there are still many unanswered questions surrounding this issue, and other theoretical calculations give more favorable prospects for success [21, 48]. A second method for producing antihydrogen, a laser-controlled charge-exchange process [22], may in principle produce slower antihydrogen atoms, and would be ideally suited for antihydrogen production within a Ioffe trap field. There are plans to attempt this method within the Penning-Ioffe trap in the near future as well. In addition to optimizing the antihydrogen production procedure, another key element to successfully trapping antihydrogen atoms is optimizing the Ioffe trap itself. To this end, a new Ioffe trap is presently under construction that will have a larger trap depth, and can be turned off much more rapidly in order to detect even single trapped antihydrogen atoms.

The results outlined here represent significant progress toward the goal of confining antihydrogen atoms for precision spectroscopy. The new Penning-Ioffe trap constructed should provide a versatile platform for a range of diverse experiments. Although much work remains to be done, there are many promising prospects for

magnetically confining antihydrogen atoms within the near future.

# Bibliography

- [1] Zhongdong Zhang, Ph.D. thesis, Ruhr-Universität Bochum, 2007.
- [2] G. Gabrielse, *Hyperfine Interact.* **44**, 349 (1988).
- [3] J. Walz and T. Hänsch, *General Relativity and Gravitation* **36**, 561 (2004).
- [4] G. Gabrielse, in *Fundamental Symmetries*, edited by (P.Bloch, P. Paulopoulos, and eds.) R. Klapisch (Plenum, New York, 1987), pp. 59–75.
- [5] G. Gabrielse, P. Laroche, D. Le Sage, B. Levitt, W. S. Kolthammer, R. McConnell, P. Richerme, J. Wrubel, A. Speck, M. C. George, D. Grzonka, W. Oelert, T. Sefzick, Z. Zhang, A. Carew, D. Comeau, E. A. Hessels, C. H. Storry, M. Weel, J. Walz, and A. T. R. A. P. Collaboration, *Phys Rev Lett* **100**, 113001 (2008).
- [6] G. Baur, G. Boero, S. Brauksiepe, A. Buzzo, W. Eyrich, R. Geyer, D. Grzonka, J. Hauffe, K. Kilian, M. Lo Vetere, M. Macri, M. Moosburger, R. Nellen, W. Oelert, S. Passaggio, A. Pozzo, K. Rohrich, K. Sachs, G. Schepers, T. Sefzick, R.S. Simon, R. Stratmann, F. Stinzinger, and M. Wolke, *Phys. Lett. B* **368**, 251 (1996).
- [7] G. Gabrielse, X. Fei, K. Helmerson, S. L. Rolston, R. L. Tjoelker, T. A. Trainor, H. Kalinowsky, J. Haas, and W. Kells, *Phys. Rev. Lett.* **57**, 2504 (1986).
- [8] G. Gabrielse, X. Fei, L. A. Orozco, R. L. Tjoelker, J. Haas, H. Kalinowsky, T. A. Trainor, and W. Kells, *Phys. Rev. Lett.* **63**, 1360 (1989).
- [9] J. Estrada, T. Roach, J. N. Tan, P. Yesley, and G. Gabrielse, *Phys. Rev. Lett.* **84**, 859 (2000).
- [10] D. P. van der Werf, L. V. Jørgensen, T. L. Watson, M. Charlton, M. J. T. Collier, M. Doser, and R. Funakoshi, *Applied Surface Science* **194**, 312 (2002).
- [11] G. Gabrielse, S. L. Rolston, L. Haarsma, and W. Kells, *Phys. Lett. A* **129**, 38 (1988).

- [12] G. Gabrielse, D. S. Hall, T. Roach, P. Yesley, A. Khabbaz, J. Estrada, C. Heimann, and H. Kalinowsky, *Phys. Lett. B* **455**, 311 (1999).
- [13] G. Gabrielse, J. Estrada, J. N. Tan, P. Yesley, N. S. Bowden, P. Oxley, T. Roach, C. H. Storry, M. Wessels, J. Tan, D. Grzonka, W. Oelert, G. Schepers, T. Sefzick, W. Breunlich, M. Cargnelli, H. Fuhrmann, R. King, R. Ursin, J. Zmeskal, H. Kalinowsky, C. Wesdorp, J. Walz, K. S. E. Eikema, and T. Haensch, *Phys. Lett. B* **507**, 1 (2001).
- [14] M. Amoretti, C. Amsler, G. Bonomi, A. Bouchta, P. Bowe, C. Carraro, C. L. Cesar, M. Charlton, M. J. T. Collier, M. Doser, V. Filippini, K. S. Fine, A. Fontana, M. C. Fujiwara, R. Funakoshi, P. Genova, J. S. Hangst, R. S. Hayano, M. H. Holzscheiter, L. V. Jorgensen, V. Lagomarsino, R. Landua, D. Lindelof, E. L. Rizzini, M. Macri, N. Madsen, G. Manuzio, M. Marchesotti, P. Montagna, H. Pruyss, C. Regenfus, P. Riedler, J. Rochet, A. Rotondi, G. Rouleau, G. Testera, A. Variola, T. L. Watson, and D. P. van der Werf, *Nature* **419**, 456 (2002).
- [15] G. Gabrielse, N. S. Bowden, P. Oxley, A. Speck, C. H. Storry, J. N. Tan, M. Wessels, D. Grzonka, W. Oelert, G. Schepers, T. Sefzick, J. Walz, H. Pittner, T. W. Hänsch, and E. A. Hessels, *Phys. Rev. Lett.* **89**, 213401 (2002).
- [16] G. Gabrielse, N. S. Bowden, P. Oxley, A. Speck, C. H. Storry, J. N. Tan, M. Wessels, D. Grzonka, W. Oelert, G. Schepers, T. Sefzick, J. Walz, H. Pittner, T. W. Hänsch, and E. A. Hessels, *Phys. Rev. Lett.* **89**, 233401 (2002).
- [17] R. van Roijen, J. J. Berkhout, S. Jaakola, and J. T. M. Walraven, *Phys. Rev. Lett.* **61**, 931 (1988).
- [18] C. L. Cesar, D. G. Fried, T. C. Killian, A. D. Polcyn, J. C. Sandberg, I. A. Yu, T. J. Greytak, D. Kleppner, and J. M. Doyle, *Phys. Rev. Lett.* **77**, 255 (1996).
- [19] G. Gabrielse, *Adv. At. Mol. Opt. Phys.* **50**, 155 (2005).
- [20] G. Gabrielse, A. Speck, C. H. Storry, D. Le Sage, N. Guise, D. Grzonka, W. Oelert, G. Schepers, T. Sefzick, H. Pittner, J. Walz, T. W. Hänsch, D. Comeau, and E. A. Hessels, *Phys. Rev. Lett.* **93**, 073401 (2004).
- [21] T. Pohl, H. R. Sadeghpour, and G. Gabrielse, *Physical Review Letters* **97**, 143401 (2006).
- [22] C. H. Storry, A. Speck, D. Le Sage, N. Guise, G. Gabrielse, D. Grozonka, W. Oelert, G. Scheppers, T. Sefzick, J. Walz, H. Pittner, M. Herrmann, T. W. Hänsch, D. Comeau, and E. A. Hessels, *Phys. Rev. Lett.* **93**, 263401 (2004).

- [23] B. Levitt, G. Gabrielse, P. Laroche, D. Le Sage, W.S. Kolthammer, R. McConnell, J. Wrubel, A. Speck, D. Grzonka, W. Oelert, T. Sefzick, Z. Zhang, D. Comeau, M.C. George, E.A. Hessels, C.H. Storry, M. Weel, and J. Walz, *Physics Letters B* **656**, 25 (2007).
- [24] G. Gabrielse, P. Laroche, D. Le Sage, B. Levitt, W.S. Kolthammer, I. Kulanishvili, R. McConnell, J. Wrubel, F.M. Esser, H. Glueckler, D. Grzonka, G. Hansen, S. Martin, W. Oelert, J. Schillings, M. Schmitt, T. Sefzick, H. Soltner, Z. Zhang, D. Comeau, M.C. George, E.A. Hessels, C.H. Storry, M. Weel, A. Speck, F. Nillius, J. Walz, and T.W. Haensch, *Phys. Rev. Lett.* **98**, 113002 (2007).
- [25] J. Fajans, W. Bertsche, K. Burke, S. F. Chapman, and D.P van der Werf, *Phys. Rev. Lett.* **95**, 155001 (2005).
- [26] T. D. Lee and C. N. Yang, *Phys. Rev.* **104**, 254 (1956).
- [27] C. S. Wu, E. Ambler, R. W. Hayward, D. D. Hoppes, and R. P. Hudson, *Phys. Rev.* **105**, 1413 (1957).
- [28] M. Gell-Mann and A. Pais, *Phys. Rev.* **97**, 1387 (1955).
- [29] J. H. Christenson, J. W. Cronin, V. L. Fitch, and R. Turlay, *Phys. Rev. Lett.* **13**, 138 (1964).
- [30] F. Wilczek, *Sci. Am.* **278**, 30 (1998).
- [31] G. Lüders, *Ann. Phys.* **2**, 1 (1957).
- [32] Robert G. Sachs, *The Physics of Time Reversal* (The University of Chicago Press, Chicago, 1987).
- [33] R. Carosi, P. Clarke, D. Coward, D. Cundy, N. Doble, L. Gagnon, V. Gibson, P. Grafström, R. Hagelberg, G. Kessler, and et al., *Phys. Lett. B* **237**, 303 (1990).
- [34] R. S. Van Dyck, Jr., P. B. Schwinberg, and H. G. Dehmelt, *Phys. Rev. Lett.* **59**, 26 (1987).
- [35] G. Gabrielse, A. Khabbaz, D. S. Hall, C. Heimann, H. Kalinowsky, and W. Jhe, *Phys. Rev. Lett.* **82**, 3198 (1999).
- [36] R. Bluhm, V. A. Kostelecký, and N. Russell, *Phys. Rev. Lett.* **82**, 2254 (1999).
- [37] M. Niering, R. Holzwarth, J. Reichert, P. Pokasov, Th. Udem, M. Weitz, T. W. Hänsch, P. Lemonde, G. Santarelli, M. Abgrall, P. Laurent, C. Salomon, and A. Clairon, *Phys. Rev. Lett.* **84**, 5496 (2000).

- [38] C. Zimmerman and T. Hänsch, *Hyperfine Interact.* **76**, 47 (1993).
- [39] M. Glinsky and T. O'Neil, *Phys. Fluids* **B3**, 1279 (1991).
- [40] P. O. Fedichev, *Phys. Lett. A* **226**, 289 (1997).
- [41] L. I. Men'shikov and P. O. Fedichev, *Sov. Phys. JETP* **108**, 144 (1995).
- [42] E. M. Bass and D. H. E. Dubin, *Phys. Plas.* **11**, 1240 (2004).
- [43] F. Robicheaux and J. D. Hanson, *Phys. Rev. A* **69**, 010701 (2004).
- [44] F. Robicheaux, *Phys. Rev. A* **73**, 033401 (2006).
- [45] F. Robicheaux, *Phys. Rev. A* **70**, 022510 (2004).
- [46] M. Amoretti, et al., *Phys. Lett. B* **583**, 59 (2004).
- [47] T. Topçu and F. Robicheaux, *Phys. Rev. A* **73**, 043405 (2006).
- [48] T. Pohl, H. R. Sadeghpour, Y. Nagata, and Y. Yamazaki, *Phys. Rev. Lett.* **97**, 213001 (2006).
- [49] C L Taylor, Jingjing Zhang, and F Robicheaux, *J. Phys. B* **39**, 4945 (2006).
- [50] J. L. Hurt, P. T. Carpenter, C. L. Taylor, and F Robicheaux, *J. Phys. B* **41**, 165206 (2008).
- [51] A. Speck, C. H. Storry, E.A. Hessels, and G. Gabrielse, *Phys. Lett. B* **597**, 257 (2004).
- [52] M. L. Wall, C. S. Norton, and F. Robicheaux, *Phys. Rev. A* **72**, 052702 (2005).
- [53] E. A. Hessels, D. M. Homan, and M. J. Cavagnero, *Phys. Rev. A* **57**, 1668 (1998).
- [54] M. Amoretti, C. Amsler, G. Bonomi, P. D. Bowe, C. Canali, C. Carraro, C. L. Cesar, M. Charlton, A. M. Ejsing, A. Fontana, M. C. Fujiwara, R. Funakoshi, P. Genova, J. S. Hangst, R. S. Hayano, L. V. Jorgensen, A. Kellerbauer, V. Lagomarsino, E. Lodi Rizzini, M. Macri, N. Madsen, G. Manuzio, D. Mitchard, P. Montagna, L. G. C. Posada, H. Pruys, C. Regenfus, A. Rotondi, H. H. Telle, G. Testera, D. P. Van der Werf, A. Variola, L. Venturelli, Y. Yamazaki, and N. Zurlo ATHENA Collaboration, *Physical Review Letters* **97**, 213401 (2006).
- [55] L. S. Brown and G. Gabrielse, *Rev. Mod. Phys.* **58**, 233 (1986).
- [56] M. Kretschmar, *Eur. J. Phys.* **12**, 240 (1991).

- [57] G. Gabrielse, L. Haarsma, and S. L. Rolston, *Intl. J. Mass Spec. Ion Proc.* **88**, 319 (1989), *ibid.* **93**, 121 (1989).
- [58] Harold J. Metcalf and Peter van der Straten, *Laser Cooling and Trapping* (Springer, New York, 1999).
- [59] Y. V. Gott, M. S. Ioffe, and V. G. Tel'kovskii, *Nuc. Fusion* 1962 Suppl. Pt. **3**, 1045 (1962).
- [60] D. E. Pritchard, *Phys. Rev. Lett.* **51**, 1336 (1983).
- [61] G. Michel, K. Dohlen, J. Martignac, J. Lecullier, P. Levacher, and C. Colin, *Applied Optics* **42**, 6305 (2003).
- [62] G. Gabrielse, X. Fei, L. A. Orozco, R. L. Tjoelker, J. Haas, H. Kalinowsky, T. A. Trainor, and W. Kells, *Phys. Rev. Lett.* **65**, 1317 (1990).
- [63] *Cryogenic Engineering*, edited by B. A. Hands (Academic Press, Orlando, Florida, 1986).
- [64] M. Chabaud-reytier, F. Kircher, and B. Levesy, *International Cryogenic Materials Conference* (Plenum, New York, 2002), Vol. 48, pp. 76–83.
- [65] N. Bowden, Ph.D. thesis, Harvard University, 2003.
- [66] A. Speck, Ph.D. thesis, Harvard University, 2005.
- [67] P. J. Schultz and K. G. Lynn, *Rev. Mod. Phys.* **60**, 701 (1988).
- [68] A. Weiss, R. Mayer, M. Jibaly, C. Lei, D. Mehl, and K. G. Lynn, *Phys. Rev. Lett.* **61**, 2245 (1988).
- [69] F. Staufenbiel, G. Schiwietz, K. Czerski, M. Roth, and P. L. Grande, *Nuc. Inst. Meth. B* **230**, 426 (2005).
- [70] J. J. Lander, *Phys. Rev.* **91**, 1382 (1953).
- [71] Claude Amsler, *Rev. Mod. Phys.* **70**, 1293 (1998).
- [72] A. S. Iljinov, V. I. Nazaruk, and S. E. Chigrinov, *Nucl. Phys. A* **382**, 378 (1982).
- [73] P. Hofmann, F. J. Hartmann, H. Daniel, T. Von Egidy, W. Kanert, W. Markiel, H. S. Plendl, H. Machner, G. Riepe, D. Protic, K. Ziock, R. Marshall, and J. J. Reidy, *Nucl. Phys. A* **512**, 669 (1990).

- [74] H. S. Plendl, H. Daniel, T. Von Egidy, F. S. Haninger, F. S. Hartmann, P. Hofmann, Y. S. Kim, H. Machner, G. Riepe, J. Jastrzebski, A. Grabowska, W. Kurcewicz, P. Lubinski, A. Stolarz, A. S. Botvina, Ye. S. Golubeva, A. S. Iljinov, V. G. Nedorezov, A. S. Sudov, and K. Ziock, *Phys. Scr.* **48**, 160 (1993).
- [75] W. Markiel, H. Daniel, T. Von Egidy, F. J. Hartmann, P. Hofmann, W. Kanert, H. S. Plendl, K. Ziock, R. Marshall, H. Machner, G. Riepe, and J. J. Reidy, *Nucl. Phys. A* **485**, 445 (1988).
- [76] D. J. Wineland and H. G. Dehmelt, *J. Appl. Phys.* **46**, 919 (1975).
- [77] G. Gabrielse, *Phys. Rev. A* **29**, 462 (1984).
- [78] X. Feng, M. Charlton, M. Holzscheiter, R. A. Lewis, and Y. Yamazaki, *J. Appl. Phys.* **79**, 8 (1996).
- [79] J. D. Jackson, *Classical Electrodynamics, 3rd Edition* (John Wiley and Sons, Inc., New York, 1975).
- [80] M. Glinsky, T. O'Neil, M. N. Rosenbluth, K. Tsuruta, and S. Ichimaru, *Phys. Fluids B* **4**, 1156 (1992).
- [81] F Robicheaux and J. Fajans, *J. Phys. B* **40**, 3143 (2007).
- [82] G. Gabrielse, private communication.
- [83] S. L. Rolston and G. Gabrielse, *Hyperfine Interact.* **44**, 233 (1988).
- [84] D. H. E. Dubin and T. M. O'Neil, *Rev. Mod. Phys.* **71**, 87 (1999).
- [85] T. Srinivasan-Rao, J. Fischer, and T. Tsang, *Journal of Applied Physics* **69**, 3291 (1991).
- [86] C. M. Surko, M. Leventhal, and A. Passner, *Phys. Rev. Lett.* **62**, 901 (1989).
- [87] D. Comeau, Ph.D. thesis, York University, 2008.
- [88] A. Mills and E. Gullikson, *Appl. Phys. Lett.* **49**, 1121 (1986).
- [89] R. G. Greaves and C. M. Surko, *Canad. J. Phys.* **74**, 445 (1996).
- [90] G. Gabrielse, *Adv. At. Mol. Opt. Phys.* **45**, 1 (2001).
- [91] G. Gabrielse, X. Fei, L. A. Orozco, S. L. Rolston, R. L. Tjoelker, T. A. Trainor, J. Haas, H. Kalinowsky, and W. Kells, *Phys. Rev. A* **40**, 481 (1989).

- 
- [92] G. Gabrielse, N. S. Bowden, P. Oxley, A. Speck, C. H. Storry, J. N. Tan, M. Wessels, D. Grzonka, W. Oelert, G. Schepers, T. Sefzick, J. Walz, H. Pittner, and E. A. Hessels, *Phys. Lett. B* **548**, 140 (2002).
- [93] P. Oxley, Ph.D. thesis, Harvard University, 2003.
- [94] Herbert Stelzer, *Nuc. Inst. Meth.* **133**, 409 (1976).
- [95] J. Estrada, Ph.D. thesis, Harvard University, 2002.
- [96] X. Fei, Ph.D. thesis, Harvard University, 1990.
- [97] B. R. Beck, J. Fajans, and J. H. Malmberg, *Physics of Plasmas* **3**, 1250 (1996).
- [98] L. D. Landau and E. M. Lifshitz, *The Classical Theory of Fields*, 4th ed. (Pergamon Press, New York, 1975).
- [99] L. D. Landau and E. M. Lifshitz, *Statistical Physics*, 2nd ed. (Pergamon Press, New York, 1969).
- [100] Ronald C. Davidson and Nicholas A. Krall, *Phys. Fluids* **13**, 1543 (1970).
- [101] L. D. Landau and E. M. Lifshitz, *Mechanics (Third Edition)* (Pergamon Press, New York, 1976).
- [102] Leaf Turner, *Phys. Fluids* **30**, 3196 (1987).
- [103] D. H. E. Dubin, *Phys. Fluids B* **5**, 295 (1993).
- [104] D. H. E. Dubin, *Phys. Rev. Lett.* **66**, 2076 (1991).
- [105] M. D. Tinkle, R. G. Greaves, C. M. Surko, R. L. Spencer, and G. W. Mason, *Phys. Rev. Lett.* **40**, 352 (1994).
- [106] R. L. Spencer, S. N. Rasband, and R. R. Vanfleet, *Phys. Fluids B* **5**, 4267 (1993).
- [107] G. W. Mason, R. L. Spencer, and J. A. Bennett, *Phys. Plas.* **3**, 1502 (1996).
- [108] Johnny K. Jennings, Ross L. Spencer, and K.C. Hansen, *Phys. Plas.* **2**, 2630 (1995).
- [109] M. Amoretti, G. Bonomi, A. Bouchta, P. D. Bowe, C. Carraro, C. L. Cesar, M. Charlton, M. Doser, A. Fontana, M. C. Fujiwara, R. Funakoshi, P. Genova, J. S. Hangst, R. S. Hayano, L. V. Jorgensen, V. Lagomarsino, R. Landua, E. L. Rizzini, M. Macri, N. Madsen, G. Manuzio, G. Testera, A. Variola, and D. P. van der Werf, *Phys. Plas.* **10**, 3056 (2003).

- [110] M. D. Tinkle, R. G. Greaves, and C. M. Surko, *Phys. Plas.* **2**, 2880 (1995).
- [111] J. J. Bollinger, D. J. Heinzen, F. L. Moore, W. M. Itano, D. J. Wineland, and D. H. E. Dubin, *Phys. Rev. A* **48**, 525 (1993).
- [112] C. S. Weimer, J. J. Bollinger, F. L. Moore, and D. J. Wineland, *Phys. Rev. A* **49**, 3842 (1994).
- [113] A. Speck, G. Gabrielse, P. Laroche, D. Le Sage, B. Levitt, W.S. Kolthammer, R. McConnell, J. Wrubel, D. Grzonka, W. Oelert, T. Seifzick, Z. Zhang, D. Comeau, M. C. George, E.A. Hessels, C. Storry, M. Weel, and J. Walz, *Phys. Lett. B* **650**, 119 (2007).
- [114] T. M. Squires, P. Yesley, and G. Gabrielse, *Phys. Rev. Lett.* **86**, 5266 (2001).
- [115] E. Gilson and J. Fajans, in *Non-neutral Plasma Physics IV*, edited by F. Anderegg, L. Schweikhard, and C. F. Driscoll (AIP, New York, 2002), Vol. 606, p. 378.
- [116] E. Gilson, Ph.D. thesis, University of California at Berkeley, 2001.
- [117] E. P. Gilson and J. Fajans, *Phys. Rev. Lett.* **90**, 015001 (2003).
- [118] J. Fajans and A. Schmidt, *Nuc. Inst. Meth. A* **521**, 318 (2004).
- [119] P. Yesley, Ph.D. thesis, Harvard University, 2001.
- [120] J. Fajans, N. Madsen, and F. Robicheaux, *Physics of Plasmas* **15**, 032108 (2008).
- [121] G. B. Andresen, W. Bertsche, P. D. Bowe, C. C. Bray, E. Butler, C. L. Cesar, S. Chapman, M. Charlton, J. Fajans, M. C. Fujiwara, R. Funakoshi, D. R. Gill, J. S. Hangst, W. N. Hardy, R. S. Hayano, M. E. Hayden, A. J. Humphries, R. Hydromako, M. J. Jenkins, L. V. Jorgensen, L. Kurchaninov, R. Lambo, N. Madsen, P. Nolan, K. Olchanski, A. Olin, R. D. Page, A. Povilus, P. Pusa, F. Robicheaux, E. Sarid, S. Seif El Nasr, D. M. Silveira, J. W. Storey, R. I. Thompson, D. P. van der Werf, J. S. Wurtele, and Y. Yamazaki, *Physics of Plasmas* **15**, 032107 (2008).
- [122] W. Bertsche, A. Boston, P.D. Bowe, C.L. Cesar, S. Chapman, M. Charlton, M. Chartier, A. Deutsch, J. Fajans, M.C. Fujiwara, R. Funakoshi, G. Gomboroff, J.S. Hangst, R.S. Hayano, M.J. Jenkins, L.V. Jørgensen, P. Ko, N. Madsen, P. Nolan, R.D. Page, L.G.C. Posada, A. Povilus, E. Sarid, D.M. Silveira, D.P. van der Werf, Y. Yamazaki (ALPHA Collaboration), B. Parker, J. Escallier, and A. Ghosh, *Nuclear Instruments and Methods in Physics Research A* **566**, 746 (2006).

- 
- [123] G. B. Andresen, W. Bertsche, P. D. Bowe, C. C. Bray, E. Butler, C. L. Cesar, S. Chapman, M. Charlton, J. Fajans, M. C. Fujiwara, R. Funakoshi, D. R. Gill, J. S. Hangst, W. N. Hardy, R. S. Hayano, M. E. Hayden, R. Hydomako, M. J. Jenkins, L. V. Jørgensen, L. Kurchaninov, R. Lambo, N. Madsen, P. Nolan, K. Olchanski, A. Olin, A. Povilus, P. Pusa, F. Robicheaux, E. Sarid, S. Seif El Nasr, D. M. Silveira, J. W. Storey, R. I. Thompson, D. P. van der Werf, J. S. Wurtele, and Y. Yamazaki, *Phys. Rev. Lett.* **100**, 203401 (2008).
- [124] N. Kuroda, H. A. Torii, M. Shibata, Y. Nagata, D. Barna, M. Hori, D. Horváth, A. Mohri, J. Eades, K. Komaki, and Y. Yamazaki, *Phys. Rev. Lett.* **100**, 203402 (2008).
- [125] G. Andresen, W. Bertsche, A. Boston, P. D. Bowe, C. L. Cesar, S. Chapman, M. Charlton, M. Chartier, A. Deutsch, J. Fajans, M. C. Fujiwara, R. Funakoshi, D. R. Gill, K. Gomberoff, J. S. Hangst, R. S. Hayano, R. Hydomako, M. J. Jenkins, L. V. Jørgensen, L. Kurchaninov, N. Madsen, P. Nolan, K. Olchanski, A. Olin, A. Povilus, F. Robicheaux, E. Sarid, D. M. Silveira, J. W. Storey, H. H. Telle, R. I. Thompson, D. P. van der Werf, J. S. Wurtele, and Y. Yamazaki, *Phys. Rev. Lett.* **98**, 023402 (2007).
- [126] M. Amoretti, C. Canali, C. Carraro, M. Doser, V. Lagomarsino, G. Manuzio, G. Testera, and S. Zavatarelli, *Phys. Lett. A* **360**, 141 (2006).
- [127] D. Vrinceanu, B. E. Granger, R. Parrott, H. R. Sadeghpour, L. Cederbaum, A. Mody, J. Tan, and G. Gabrielse, *Phys. Rev. Lett.* **92**, 133402 (2004).
- [128] J. Zhang, C. L. Taylor, J. D. Hanson, and F. Robicheaux, *J. Phys. B* **40**, 1019 (2007).
- [129] T. M. O’Neil, *Phys. Fluids* **23**, 2216 (1980).